Abrupt Climate Change and Glacial Terminations

Emily Louise Deaney

Thesis submitted for the Degree of Doctor of Philosophy
Cardiff University

September 2015

ABRUPT CLIMATE CHANGE AND GLACIAL TERMINATIONS

The Earth's system has witnessed abrupt climate changes throughout its history. It is widely understood that the pacing of the large-scale glacial-interglacial cycles (tens to hundreds of thousands of years) of the Pleistocene Epoch (~2 million years) are not simply the result of changes in the incoming solar insolation (orbital forcing) alone and as such, this large-scale variability calls upon feedback mechanisms in order to explain the magnitude of such changes.

This thesis investigates the shorter millennial scale events (thousands of years) and their role in determining the magnitude of glacial-interglacial cyclicity.

In order to investigate this, in this thesis three sediment cores will be used, ODP Site 1063 and ODP Site 983 in the North Atlantic and ODP Site 1089 in the South Atlantic. Datasets from these core locations provide insights in to the magnitude and duration of millennial scale variability across terminations 1, 2 and 5. The two regions studied here (North and South Atlantic) are important regions for recording changes in ocean circulation, specifically the Atlantic Meridional Overturning Circulation.

Upper water column reconstructions from the North and South Atlantic based on both planktonic foraminiferal faunal assemblage reconstructions and paired $\delta^{18}O$ and Mg/Ca analysis provide insight into the abrupt changes in ocean dynamics across glacial cycles. Additionally with the use of neodymium isotope analysis, changes in the deep North Atlantic, likely the result of changes in the Meridional Overturning Circulation, have also been identified. Importantly, this data provides evidence that the timing of the resumption of the Atlantic Meridional Overturning Circulation following glacial conditions is integral in determining the extent of deglacial CO_2 release.

The work presented here suggests that rather than it being the magnitude of millennial scale events determining the magnitude of glacial-interglacial climate variability, instead, it is the relative timing of the millennial scale events that plays a role in controlling the magnitude of glacial-interglacial cyclicity.

ACKNOWLEDGEMENTS

Firstly, I would like to thank my supervisors; Stephen Barker, Ian Hall, Jenny Pike and Tina van de Flierdt. A special mention should go to Steve for the continued support and guidance he has given me throughout my Ph.D. I would also like to say a special thank you to Tina for being the positive voice of reason I needed and for being on my side all the way.

I am very grateful to Lukas Jonkers, thank you for providing me with all the support that I needed and for being the best sounding board anyone could ask for – I simply can not thank you enough.

I would also like to thank all those I have shared an office or lab with during this project. To name but a few; Sarah, Miriam, Rebekah, Henry, Chris, Scott, Jamie, Rachel, Miros, Sam, Anna - I could not have got through this without the endless cups of tea you shared with me…you know who you are! All the members of the Earth and Ocean Sciences 'Rock Solid' football team deserve a mention – thank you all for being wonderful team-mates and friends, it is safe to say Rock Solid will always be a part of my life. I would also like to mention Paola Moffa-Sanchez and Margit Simmons for allowing me to bend their ears at the drop of the hat – you have both been a fantastic support to me and I will forever be in your debt for that.

This project would not have been possible without the technical support of so many; in particular with heartfelt gratitude to Anabel Morte-Rodenas, Sandra Nederbragt, Katharina Kreissig, Barry Coles, and Torben Struve.

Finally, I would like to thank my family. My Grandparents, Rob and Jo, Janet and Don, for supporting me through my prolonged university career. My brothers, Edward and Tom, for always making me laugh and for providing some much needed technical support. My truly wonderful parents, Mark and Juliet, for supporting me both emotionally and financially – quite simply this wouldn't have been possible without you both, so thank you. Finally to Jack – you have been everything I could have asked for and so much more besides, thank you.

COMMONLY USED SYMBOLS AND ABBREVIATIONS

NADW	North Atlantic Deep Water
LNADW	Lower North Atlantic Deep Water
AABW	Antarctic Bottom Water
AAIW	Antarctic Intermediate Water
GNAIW	Glacial North Atlantic Intermediate Water
ACC	Antarctic Circumpolar Current
NAC	North Atlantic Current
T2	Termination 2
SST	Sea Surface Temperature
G-IG	Glacial-Interglacial
ODP	Ocean Drilling Program
AMOC	Atlantic Meridional Overturning Circulation
D-O	Dansgaard–Oeschger events
MAT	Modern Analogue Technique
$CaCO_3$	Calcium carbonate
MIS	Marine Isotope Stage
$\delta^{18}O_c$	$\delta^{18}O$ of calcite
$\delta^{18}O_{sw}$	$\delta^{18}O$ of seawater

CONTENTS

1 INTRODUCTION; ABRUPT CLIMATE CHANGE AND GLACIAL TERMINATIONS 5
1.1 Ocean circulation 7
1.1.1 The Atlantic Meridional Overturning Circulation 8
1.1.2 Deep Water Formation in the North Atlantic (NADW) 9
1.1.3 Atlantic Limb of Antarctic Waters 10
1.2 The Bipolar Seesaw 10
1.2.1 The Bipolar Seesaw and D-O Events 11
1.3 The Thermal Bipolar Seesaw 12
1.3.1 Evidence for the Thermal Bipolar Seesaw Model 15
1.4 Scientific Objectives of Thesis 16
1.5 Outline of Thesis 17

2 TERMINATION 5 (T5); AN 'EXTREME' TERMINATION? 21
2.1 Introduction 21
2.1.1 Motivation for this Study 22
2.2 Oceanographic Setting of the Core Location 23
2.3 Materials and Methodology 26
2.3.1 Foraminiferal Analysis 26
2.3.1.1 Planktonic Foraminifera as Environmental Indicators/Proxies 27
2.3.1.2 Environmental Preferences of Indicator Species 30
2.3.2 Calcium Carbonate Analysis 31
2.4 Results 32
2.4.1 Sea Surface Temperature Estimates 32
2.4.2 Modern Analogue Technique SST Reconstruction 32
2.4.3 % Neogloboquadrina pachyderma SST Reconstruction 32
2.5 New Splice from ODP Site 1089 33
2.6 Age Model 36
2.7 Evaluation of Foraminiferal Asemblages/Dissolution 37
2.8 Evaluation of SST Estimates 46
2.9 SST and Faunal Assemblage Analysis and Results 47
2.9.1 Confirming Alignment of South Atlantic Cores across Termination 1 52
2.9.2 SST Reconstructions from the South Atlantic (t5) 54
2.9.3 Synthesis of Planktic Records across Terminations 1, 2 and 5 at ODP Site 1089 55
2.10 North and South Atlantic Expression of the Bipolar Seesaw; is T5 Extreme? 60
2.11 Deep Water/Preservation Proxies 62
2.11.1 Benthic $\delta^{13}C$ 62
2.11.2 Preservation 64
2.12 Alternative Age Model for ODP Site 1089 (T5) 68
2.13 Conclusion 71

3 LATE RECOVERY OF THE AMOC EXPLAINS LARGER AMPLITUDE OF CO_2 CHANGE ACROSS THE PENULTIMATE DEGLACIATION 73
3.1 Introduction 73
3.2 Materials and Methodology 77

3.2.1 Study Location and Oceanograhpic Setting 77
3.3 Proxy Records from ODP Site 1063 78
3.3.1 Sediment Processing 78
3.3.2 Calcium Carbonate Analysis 79
3.3.3 Foraminiferal Assemblage Analysis 79
3.4 Introduction to Stable Isotopes 83
3.4.1 Test Run to Determine Cleaning Methodology for $\delta^{18}O$ and $\delta^{13}C$ Analysis (Ultrasonification vs. Non-ultrasonification) 84
3.4.2 Results of Test Run for Planktonic Stable Isotope Analysis 85
3.4.3 Planktonic Stable Isotope Analysis 86
3.4.4 Benthic Stable Isotope Analysis 87
3.5 Theory of Neodymium Isotopes 89
3.5.1 Neodymium Isotope Systematics 90
3.5.2 Neodymium Signal in the Modern Oceans 91
3.5.3 Neodymium Methodology 92
3.5.4 Sample Composition 93
3.6 Age Model 95
3.7 Results 98
3.8 Discussion 101
3.9 Conclusion 105

4 VERY RAPID ATTAINMENT OF INTERGLACIAL CONDITIONS AT THE ONSET OF MIS 11 107
4.1 Introduction 107
4.2 Oceanographic Setting of the Core Location 109
4.3 Methodological Background 109
4.3.1 Introduction to Stable Isotope Analysis 109
4.3.2 Introduction to Mg/Ca 110
4.3.3 Globorotalia inflata Ecology and Mg/Ca Paleothermometry 111
4.4 Materials and Methodology 113
4.4.1 Stable Isotope Analysis 113
4.4.2 Mg/Ca Analysis 114
4.4.2.1 A Study of Potential Biases in the Mg/Ca Signal from Silicates 115
4.4.2.2 A Study of Potential Biases in The Mg/Ca Signal of *G. inflata* 116
4.4.2.3 Results of the Cleaning Test (Coarse Silicate Removal Stage vs. Non-coarse Silicate Removal Stage) 116
4.4.2.4 Results for Different wall Appearances of *G. inflata* (Translucent vs. Opaque) 119
4.4.3 Conclusion of Experiments to Test the Cleaning Protocol and Encrustation Variability 123
4.5 Analysis of Contamination of Samples 123
4.6 Age Model 128
4.7 Results 129
4.8 Discussion 131
4.8.1 The MIS 11 Interglacial in the North Atlantic (ODP Site 983) 131
4.8.2 Thermocline Changes 132
4.8.3 North Atlantic Temperature Changes Across MIS 11 and the Holocene 134
4.8.4 Timings of Peak Interglacial Conditions Relative to Changes in Benthic $\delta^{18}O$ 137
4.8.5 Extreme Nature of Termination 5 138

4.9 Conclusions 140

5 SYNTHESIS AND CONCLUSIONS 143
5.1 Summary of Chapters 143
5.1.1 Termination 5 (T5); an 'extreme' termination? 143
5.1.2 Late recovery of the AMOC explains largers amplitude of CO_2 change across the pemultimate deglaciation 144
5.1.3 Very rapid attainment of interglacial conditions at the onset of MIS11 144
5.2 Limitations of the interpretations of the proxy results 146
5.3 Limitations of the paleoceanographic results 147
5.4 Synthesis 148
5.5 Conclusions 151
5.6 Future Work 153
5.6.1 Methodological Future Work 153
5.6.2 Theoretical Future Work 154

6 REFERENCES 157

7 APPENDIX 183
7.1 Appendices for Chapter 2 183
7.2 Appendices for Chapter 3 198
7.3 Appendices for Chapter 4 213

1 INTRODUCTION; ABRUPT CLIMATE CHANGE AND GLACIAL TERMINATIONS

The Pleistocene Epoch (~2 million years) has seen variations in Earth's climate on both orbital (tens to hundreds of thousands of years) and millennial timescales (thousands of years) (Hays et al., 1976; Imbrie et al., 1993; Raymo et al., 1998; Loulergue et al., 2008; Barker et al., 2009). Despite significant research, the underlying mechanisms to explain this climate variability remain unknown. Milankovitch, (1941) suggested that changes in Earth's orbital geometry would cause significant variations in climate, an idea that was later suggested could be the case (Hays et al., 1976). However, the difficulty with Milankovitch's theory (1941) is the observation that the dominant mode of variability (the glacial-interglacial (G-IG) cycles of the last Pleistocene) displays a ~100kyr periodicity (Hays et al., 1976) but the forcing during this period (caused by changes in the shape of the Earth's orbit around the sun, eccentricity) is almost negligible (Raymo, 1997). As such there must be a non-linear response of the climate system whereby a relatively small change in amount of insolation reaching the surface of the Earth is amplified resulting in the large G-IG variability of the Pleistocene.

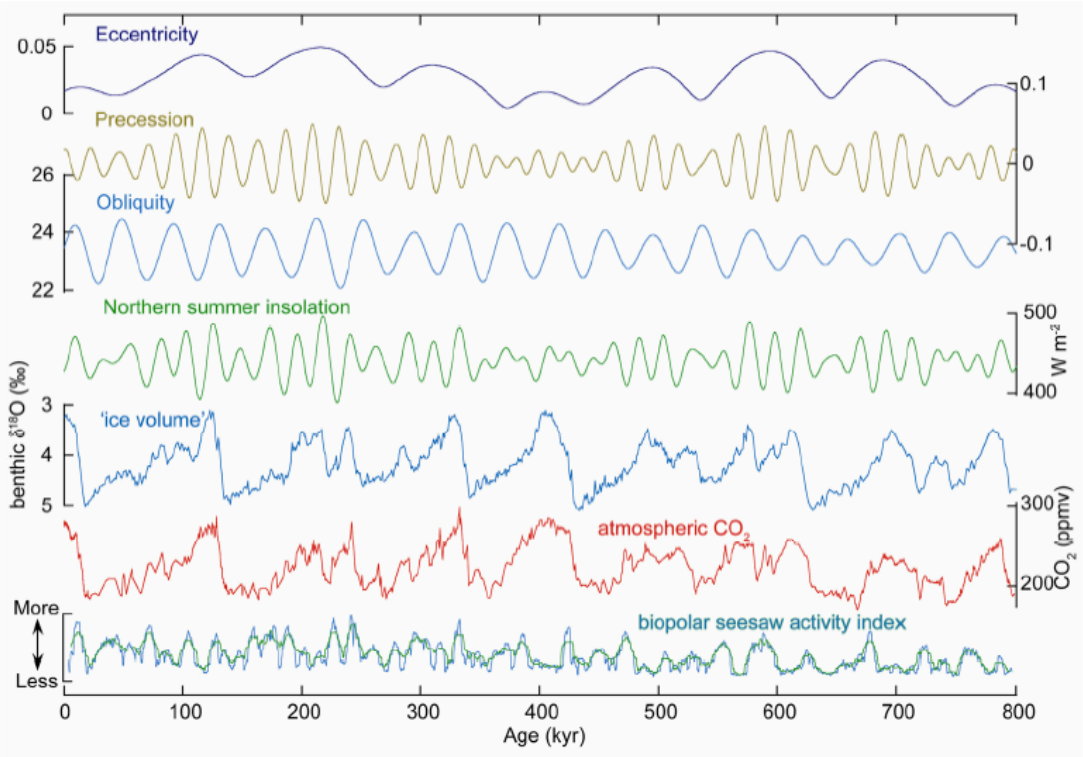

Figure 1.1 The orbital parameters (eccentricity, precession and obliquity) cannot be combined in any simple way (e.g. July at 65°N) to explain the ~100kyr glacial cycles of the Late Pleistocene (described here using benthic $\delta^{18}O$ as an ice volume proxy (Lisiecki and Raymo, 2005)). The CO_2 record for the same period (Lüthi et al., 2008) gives us a clue that feedbacks in the climate system may help to explain the amplitude of glacial terminations. An enhanced 'bipolar seesaw' activity (here reflected by a running window of the standard deviation of the first differential of the Antarctic temperature record minus its orbital timescale variability (Barker et al., 2011)) is recorded during intermediate states and the transitions between states, suggesting that millennial-scale activity (most probably involving ocean circulation changes) plays an integral role in major climate transitions.

The overall pattern of this 'glacial-interglacial' (G-IG) variability is a gradual, step-wise build-up of ice sheets followed by a relatively rapid collapse of ice sheets (Broecker and Donk, 1970). The asymmetry of the foraminiferal benthic $\delta^{18}O$ record (a crude proxy for continental ice volume change) suggests that there is a prolonged build up of ice sheets over a period of ~90kyr, followed by a shorter interval (~10kyr) of relatively fast ice sheet decay during deglaciation (Lisiecki and Raymo, 2005).

The last five glacial cycles (spanning the last ~430kyr) show a relatively uniform 'saw-tooth' pattern (Lisiecki and Raymo, 2005). Aligned with the saw tooth-pattern of G-IG variability in the foraminiferal benthic $\delta^{18}O$ record is the record of atmospheric CO_2 (Lüthi et al., 2008) (Figure 1.1). This record shows the same asymmetric pattern of G-IG variability, whereby there is a prolonged decrease in atmospheric CO_2 (~90kyr) followed by a rapid increase (~10kyr) inline with rapid ice sheets decay. However, the amplitude of CO_2 change (Lüthi et al., 2008) across the glacial terminations is quite variable (Ruddiman, 2003). For example, the change in CO_2 across the most recent deglaciation (Termination, T1) was ~80 ppmv compared to a rise of ~95 ppmv across T2 (Lüthi et al., 2008) (Figure 1.1). Thus, although the overall G-IG variability appears to have occurred consistently over the last 5 glacial cycles, there are details in the millennial scale record that vary from one cycle to the next, whereby CO_2 acts as an amplifier of climate variability, possibly providing a feedback mechanism to the climate system.

Most recent attempts to explain the amplitude of G-IG CO_2 variability call on several distinct mechanisms or processes with variable (and often opposing) effects on CO_2 (Archer et al., 2000; Köhler et al., 2005; Brovkin et al., 2007). These shorter-term, millennial scale (thousands of years) mechanisms can occur simultaneously and thus influence the glacial termination by adding and/or removing CO_2 from the atmosphere. Listed below are some of the mechanisms that contribute the most significantly in terms of alteration to the pattern of CO_2 outgassing/drawdown from the ocean across the transition from glacial to interglacial conditions as described by Köhler et al., (2005); the increase in Southern Ocean vertical mixing rates (>30 ppmv); decreases in alkalinity and carbon inventories (>30 ppmv); the reduction of the biological pump (~20 ppmv); the rise in ocean temperatures (15–20 ppmv); the resumption of ocean circulation (15–20 ppmv); coral reef growth (<5 ppmv). In order to record such large changes in atmospheric CO_2 on G-IG timescales we need to invoke changes in one (or more) of the readily available stores of carbon. The deep ocean is the largest store of readily available carbon on G-IG timescales (Broecker and Denton, 1989; Post et al., 1990). As such, in order to record such large changes in atmospheric CO_2 values across glacial terminations, changes in ocean circulation involving the deep ocean must therefore be involved.

Recently (Barker et al., 2009) and others (e.g. Cheng et al., 2009; Wolff et al., 2009) have built upon earlier suggestions (Broecker and Denton, 1989; Imbrie et al., 1993) in understanding the connection between millennial scale climate change and glacial terminations. Specifically, these authors (Barker et al., 2009; Cheng et al., 2009) have considered the interplay between millennial-scale climate variability, involving changes in ocean circulation and the bipolar seesaw (Stocker and Johnsen, 2003) and the transition from glacial to interglacial conditions. Here we build upon these ideas with the aim of better understanding the role of millennial scale events in longer timescale climate transitions, glacial terminations.

1.1 OCEAN CIRCULATION

Ocean circulation (Figure 1.2) is driven by a combination of processes, notably wind forcing and density gradients within the ocean that alter the mixing of water bodies (e.g. Dickson and Brown, 1994; Rahmstorf, 2002). Changes in the strength of the ocean

circulation, notably the Atlantic Meridional Overturning Circulation (AMOC), play a major role in controlling Earth's climate variability, primarily through the redistribution of heat, but also nutrients and notably CO_2 (Rahmstorf, 2002). Ocean circulation is a key player in the global climate system (Rahmstorf, 2002) as its response to orbital forcing (insolation) appears to be non-linear, given modest changes in incoming insolation result in large G-IG climate transitions (Figure 1.1).

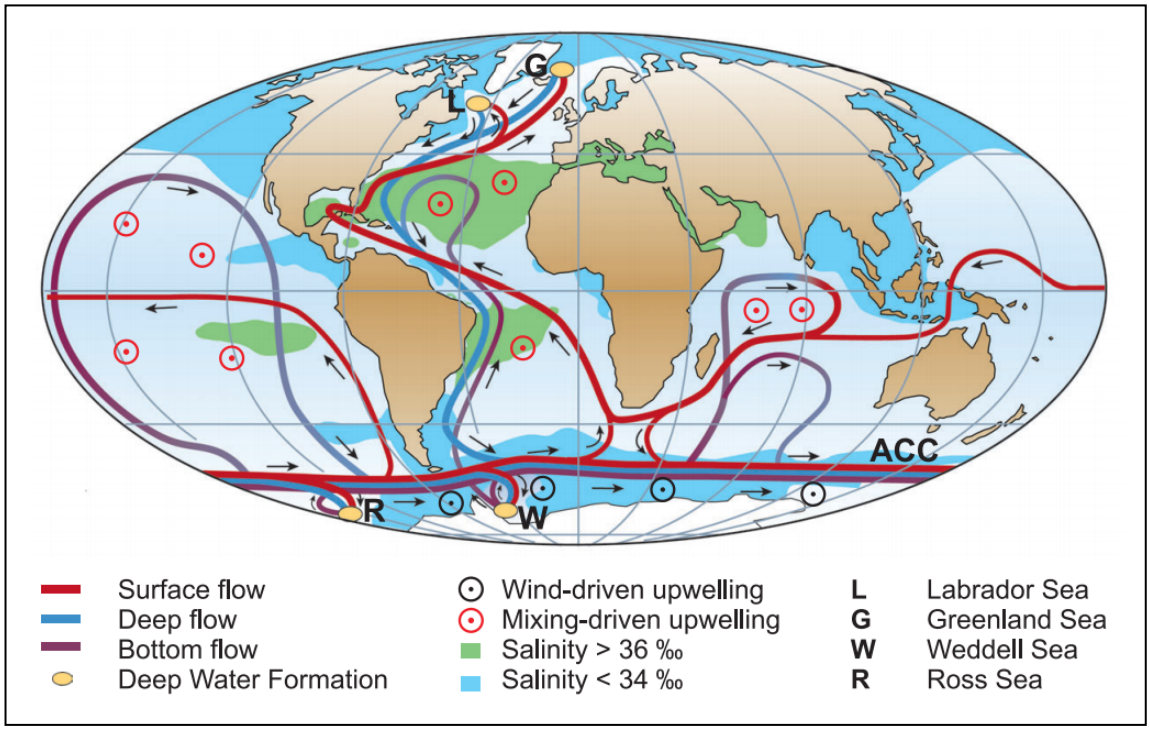

Figure 1.2. Schematic representation of the global thermohaline circulation. The main deep-water formation sites are shown in orange. Figure adapted from Rahmstorf (2002) in Elias and Mock, (2013).

1.1.1 THE ATLANTIC MERIDIONAL OVERTURNING CIRCULATION

The AMOC represents the bodies of ocean circulation in the Atlantic Ocean and contributes to maintaining a warm climate in the NW of Europe (Hansen and Østerhus, 2000). The AMOC is the Atlantic component of ocean circulation which when simplified comprises of warm salty surface subtropical waters moving northwards via the North Atlantic Current (NAC). As the waters of the NAC flow northwards they releases latent heat and eventually sink to ultimately form North Atlantic Deep Water (NADW) (Dickson and Brown, 1994). NADW and the NAC are key components of the global Thermohaline Circulation (THC), transferring carbon between surface and deep

ocean reservoirs (Dickson and Brown, 1994; Hansen and Østerhus, 2000). The thermohaline circulation is the part of the ocean circulation which is driven by density differences (Rahmstorf, 1996). As the surface waters move away from the equatorial Atlantic, they cool which results in an increase in density, subsequently the waters sink to form NADW (Dickson and Brown, 1994; Rahmstorf, 1996, 2002). As such, deep-ocean currents are driven by differences in the density of water, which in turn is controlled by temperature and salinity (Rahmstorf, 1996).

As well as northern hemisphere originated NADW filling the Atlantic abyss there is also Antarctic Bottom Waters (AABW) originating in the South Atlantic. These two water masses occupy the deep Atlantic Ocean and depending on the state of the AMOC, which varies temporally, the proportions of NADW and AABW occupying the deep ocean, also varies (Keigwin et al., 1994).

1.1.2 DEEP WATER FORMATION IN THE NORTH ATLANTIC (NADW)

Deep water in the North Atlantic is principally formed by convection of the northward flow of warm, saline surface waters from the lower latitudes in the North Atlantic (North Atlantic Current). Deep-water formation in the North Atlantic in the modern ocean occurs in both the Labrador and Nordic Seas, where the NAC cools, becomes denser and sinks to form deep water (Dickson and Brown, 1994).

The deep water formed in the Nordic Seas overflows the Greenland-Scotland Ridge and produces Iceland-Scotland Overflow Water (ISOW), Denmark Straits Overflow Water (DSOW) and to a lesser extent Wyville-Thompson Overflow Water (WTOW) that flow southwards at depth (Dickson and Brown, 1994; McCartney, 1992). These three overflows are the main constituents of the ‘deep western boundary current’ (McCartney, 1992), which flows southwards to become Lower North Atlantic Deep Water (LNADW). LNADW flows around the south of Greenland where it combines with Labrador Sea Water (LSW), which is shallower and overlies LNADW. These two water masses flow along the Labrador margin as NADW (Schmitz and McCartney, 1993). The volume of LSW, and its contribution to NADW, is important because of the contribution of NADW and the relative strength of the AMOC (Dickson and Brown, 1994).

1.1.3 ATLANTIC LIMB OF ANTARCTIC WATERS

Antarctic Bottom Water (AABW) is formed in the Weddell and Ross Seas from surface water cooling in polynyas (created by cold surface wind blowing off the Antarctic continent) and also below the ice shelf (Fofonoff, 1957; Jacobs et al., 1970). Increased sea ice production during colder periods (both seasonally and also on longer time scales) results in saltier surface waters and thus increased density of seawater and hence increased AABW formation (Jacobs et al., 1970). As the AABW flows away from the Antarctic margin some of it flows northwards into the abyssal Atlantic. AABW is denser than the NADW and thus flows along the deepest part of the Atlantic below the NADW (centred at about 2.5-3km depth) reaching a latitude of about 40°N (Orsi et al., 1999).

As highlighted in this section the oceans play an important role in taking up and releasing carbon in G-IG timescales. In order to understand what causes the transition from glacial to interglacial conditions and thus what drives G-IG variability we need to understand the millennial scale events and the feedback of these mechanisms and their contribution to G-IG variability.

1.2 THE BIPOLAR SEESAW

On millennial time scales ice core records from Greenland and Antarctica have recorded an asynchronous relationship between climate indicators in the northern and southern hemispheres (Figure 1.3) (Stuiver and Grootes, 2000, Jouzel et al., 2007). We can explain this asynchronicity via the mechanism of the bipolar seesaw, caused by variability in the Atlantic Meridional Overturning Circulation (AMOC) (Stocker and Johnsen, 2003). The modern day AMOC pattern transporting warmer waters northwards and deep-water formation in the North Atlantic has not always been the case (McManus et al., 1999, 2004). During the last glacial period, it has been suggested that the formation of NADW was further south and its penetration into the deep Atlantic reduced by the presence of southerly sourced deep waters to the abyss (Curry and Oppo, 2005). Furthermore, simulations from models (Weber et al., 2007) suggest that the strength of AMOC could also have been reduced. This slowdown of AMOC results in a warmer climate signal in the South Atlantic as the warmer waters are ‘held’ there as a

result of a reduction in deep water formation. Conversely, the North Atlantic cools as the slowdown of the AMOC stops warmer waters moving northwards (McManus et al., 2004). The mechanism of the bipolar seesaw (see section 1.2.1 The Bipolar Seesaw and D-O Events below) is the mechanism by which we are able to explain the asynchronicity between the signals observed when comparing the North and South Atlantic on millennial timescales (Figure 1.3).

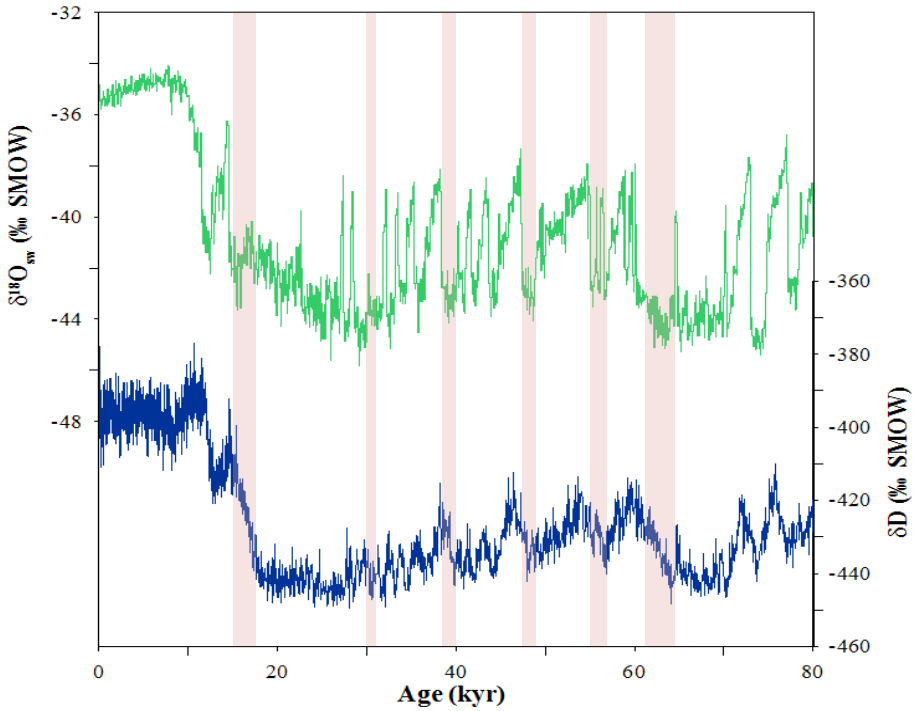

Figure 1.3. Comparison of the climatic signal recorded in Greenland (NGRIP $\delta^{18}O$ (NGRIP Members, 2004) with the South Atlantic EDC deuterium (Jouzel et al., 2007). Pink boxes indicate cold periods in the northern hemisphere and associated warming events in the southern hemisphere.

1.2.1 THE BIPOLAR SEESAW AND D-O EVENTS

The last glacial and deglacial periods of Earth's history are characterised by millennial-scale variability, ice core records (Stuiver and Grootes, 2000) reveal repeated oscillations between cold, stadial conditions and warmer interstadial conditions. These repeated oscillations in Greenland; the so-called Dansgaard-Oeschger (D-O) oscillations are extremely fast (decades or less), transitions characterised by millennial scale variability in the North Atlantic. In contrast to the abrupt D-O variability typical of northern hemisphere, high latitude temperature records, ice core records from Antarctica reveal a different mode of millennial-scale variability (Jouzel et al., 2007).

The 'Antarctica' signal is more gradual in nature, warming and cooling over thousands of years (Jouzel et al., 2007) and is approximately out of phase with its northern counterpart (Blunier and Brook, 2001). Due to the large rapid oscillations, it has been argued that D-O variability must involve changes in deep ocean circulation in order to explain the amplitude of variability (Barker et al., 2010), more specifically, changes in the Atlantic ocean circulation (AMOC) (Broecker et al., 1990; Bond et al., 1993) and the bipolar seesaw (Stocker and Johnsen, 2003).

1.3 THE THERMAL BIPOLAR SEESAW

As described the bipolar seesaw can account for the asynchronous nature of the climate records between the two hemispheres, however, this mechanism does not explain the differences in amplitude and rate of change of the signals when comparing the two hemispheres. One hypothesis to explain the relationship between the abrupt D-O oscillations in the northern hemisphere (Greenland) and the muted signal in the southern hemisphere (Antarctica) is that the Southern Ocean acts as a heat reservoir (Stocker and Johnsen, 2003). Due to the size of the Southern Ocean it takes a while for it to warm up/cool down and hence the signal recorded in Antarctica appears damped. Figure 1.4 shows the conceptual model proposed by Stocker and Johnsen, (2003).

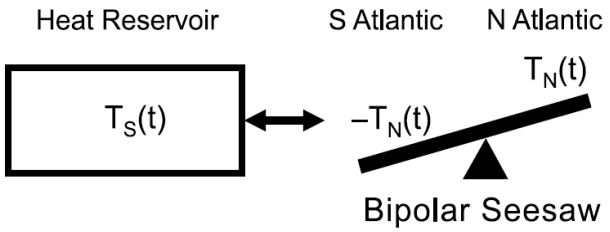

Figure 1.4. Schematic of the thermal bipolar seesaw model. $T_N(t)$ represents the temperature recorded in the North Atlantic and $-T_N(t)$ the temperature in the South Atlantic. $T_S(t)$ refers to the heat reservoir, the Southern Ocean. Simply, the bipolar seesaw mechanism suggests that there is an equal and opposite counterpart to millennial scale climate variability recorded in the North Atlantic, in the South Atlantic and the temperature recorded in the ice cores from Antarctica (e.g. Jouzel et al., 2007) is dampened as a consequence of the heat reservoir of the Southern Ocean. Taken from Stocker and Johnsen, (2003).

Stocker and Johnsen (2003) compiled a synthetic record of southern hemisphere climate variability based on a northern hemisphere signal and the asynchronous relationship between the northern and southern hemispheres (bipolar seesaw) (Figure 1.5). Based on their thermal bipolar seesaw model, Stocker and Johnsen, (2003) predict that in the South Atlantic, the exact opposite response to abrupt climate variability in the North Atlantic must occur. Recently authors have identified the southern hemisphere counterpart to these D-O event in the South Atlantic (TN057-21; 41.1°S, 7.8°W in 4981m water depth) (Barker et al., 2009), providing evidence for the thermal bipolar seesaw (Figure 1.6) playing an important role in determining the expression of the extent of millennial scale climate variability recorded in ice core in Antarctica (Jouzel et al., 2007).

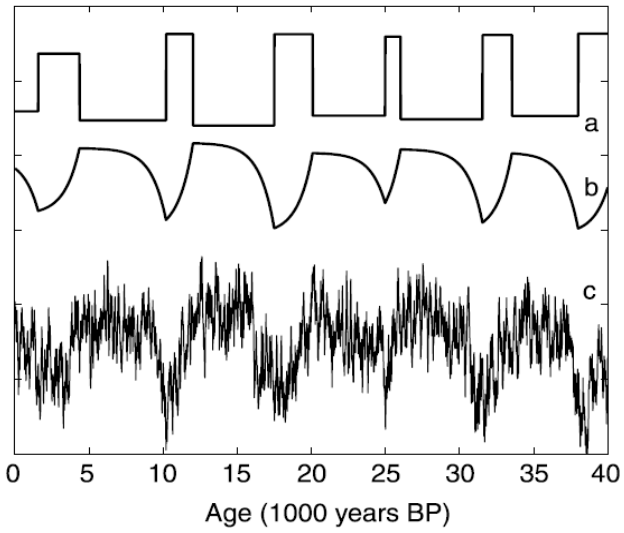

Figure 1.5. Simplified model of thermal bipolar seesaw; a) northern hemisphere signal; b) southern hemisphere signal; and c) synthetic signal output from the South Atlantic based on the northern hemisphere climate variability based on the thermal bipolar seesaw model (Stocker and Johnsen, 2003).

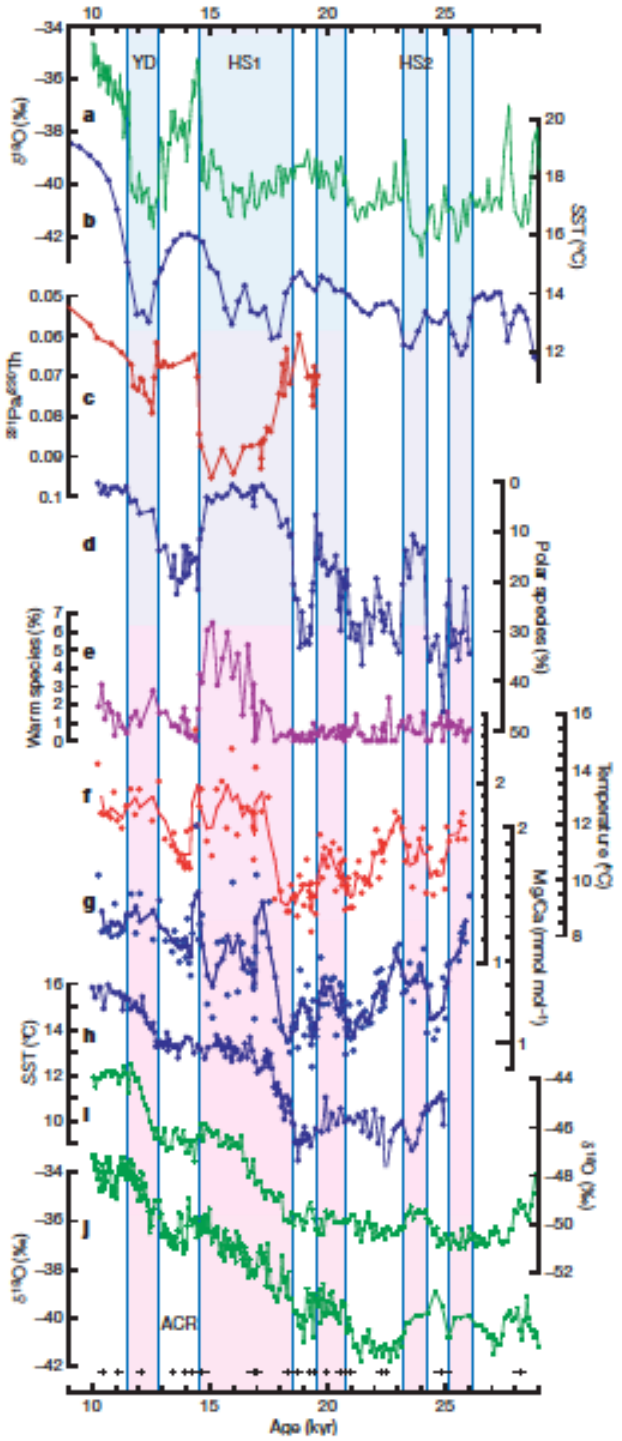

Figure 1.6 Deglacial records from TNO57-21 plus other proxy records for temperature and circulation within the Atlantic Ocean. a, Greenland temperature (GISP2 ice core) (Stuiver and Grootes, 2000); b, North Atlantic SST (core SU8118) (Bard et al., 2000); c, AMOC strength derived from sedimentary $^{231}Pa/^{230}Th$ ratio (McManus et al., 2004) (higher values indicate a reduced AMOC); d, polar foraminiferal species in TNO57-21 (Barker et al., 2009); e, warm species (Barker et al., 2009); f, Mg/Ca ratio (and calculated calcification temperature) in G. bulloides,

adjusted to account for dissolution (Barker et al., 2009); g, measured Mg/Ca ratio in G. bulloides (solid lines in f and g are three-point running means) (Barker et al., 2009); h, southeast Pacific SST (Lamy et al., 2007); i, j, Antarctic temperature (EDML (EPICA Community Members, 2006) and Byrd (Johnsen et al., 1972; Blunier and Brook, 2001) ice cores, respectively). Black symbols at the bottom indicate dating control points (calendar age uncertainty is 1s) (Barker et al., 2009). Shaded boxes represent periods of warmth or warming in the south according to the records from Barker et al., (2009). Figure taken from (Barker et al., (2009).

1.3.1 EVIDENCE FOR THE THERMAL BIPOLAR SEESAW MODEL

A record of deglacial climate variability from the Southern Ocean (site TN057-21) has provided evidence of the thermal bipolar seesaw expressed as the instantaneous response of the South Atlantic to changes in the North Atlantic. The record from the South Atlantic evidencing the instantaneous response of the southern hemisphere to northern hemisphere climate variability highlights the crucial role of the bipolar seesaw in climate variability in both the north and south hemispheres and the importance of the Southern Ocean as a heat reservoir. Barker et al., (2009) identified surface ocean changes at this study site that were equally as abrupt in nature as those previously only seen in the northern hemisphere (Figure 1.4 and Figure 1.6).

As previously mentioned the deep ocean acts as a store for carbon and as such changes in ocean circulation patterns can be linked to changes in atmospheric CO_2 levels (Broecker and Denton, 1989; Post et al., 1990). As such, changes in the overturning circulation and thus the bipolar seesaw contribute to atmospheric CO_2 variability, linking Antarctic temperatures and atmospheric carbon dioxide levels on both orbital (Petit et al., 1999) and millennial timescales (Ahn and Brook, 2008). Ahn and Brook, (2008) identify this relationship by showing that during Antarctic warm events there is an increase in the carbon dioxide levels. During cold events in the northern hemisphere warming occurred in Antarctica (Figure 1.7), linking CO_2 release during Antarctic warm events with changes in the strength of the overturning circulation, the bipolar seesaw (Stocker and Johnsen, 2003; Ahn and Brook, 2008).

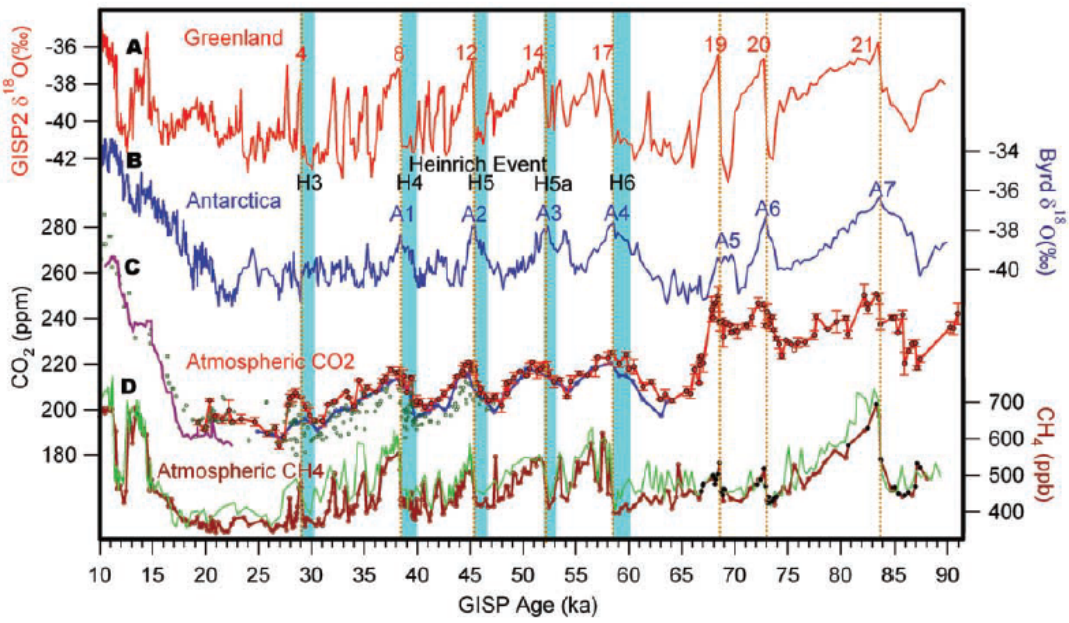

Figure 1.7. Atmospheric CO_2 and climate indicators during the last glacial period (Ahn and Brook, 2008). A) Greenland temperature proxy $\delta^{18}O_{ice}$ (Grootes et al., 1993), red numbers denote D-O events; B) Byrd station, Antarctica temperature proxy $\delta^{18}O$ice (Blunier and Brook, 2001), A1 to A7, Antarctic warming events (Blunier and Brook, 2001); C) atmospheric CO_2 concentrations, red dots (Ahn and Brook, 2008) and green circles (Stauffer et al., 1998) are from Byrd ice cores. Vertical brown dotted lines, abrupt warming in Greenland (Ahn and Brook, 2008); D) CH_4 concentrations from Greenland (green) (Blunier and Brook, 2001) and Byrd ice cores (brown) (Blunier and Brook, 2001; Ahn and Brook, 2008).

1.4 SCIENTIFIC OBJECTIVES OF THESIS

Having introduced, at the beginning of this chapter, the idea that glacial-interglacial cyclicity cannot be explained by orbital forcing alone and that internal feedbacks are required to amplify the orbital forcing in this thesis the following questions are considered;

- Are all terminations equal? Does each termination respond the same way to being orbitally forced?

- Are abrupt changes in ocean circulation a persistent feature of terminations? If so, do they matter and how? Do we observe the same changes in ocean circulation patterns across each of the terminations?

- Are the relationships between ocean circulation, CO_2 and glacial terminations consistent between different terminations? And as such are we able to unravel the complexities of the relationships and interactions of them?

To answer these questions the following scientific objectives are considered in this thesis:

- The main scientific objective of this work was to understand the impact of the timing, magnitude and sequence of millennial scale events across glacial terminations 2 and 5.

- To this end, in this thesis, with the use of planktonic foraminiferal faunal changes across Termination 5 (T5) in the surface ocean of the South Atlantic (ODP Site 1089), changes in oceanography during this interval will be assessed. These changes will be compared to changes during the same interval in the North Atlantic.

- As described above, deep-water formation is a key component of the overturning circulation in the Atlantic. The changes in deep-water formation will be assessed in the North Atlantic (ODP 1063) across Termination 2. This core location is near to a major site of NADW formation thus it is essential to be able to characterise the changes in deep-water formation and be able to understand the sequence of events across the termination too. This is important because of the relationship between deep-water formation and the drawdown of CO_2, in this thesis we are able to characterise these changes across Termination 2.

1.5 OUTLINE OF THESIS

The overall aim of this study is to improve our understanding of glacial terminations and the forcing mechanisms that drive the glacial, interglacial variability. To this end

we aim to characterise and understand millennial scale temperature changes in the surface and deep waters during glacial terminations.

Chapter 2 outlines the work carried out in the Southern Ocean/South Atlantic region across Termination 5 (T5). This study seeks to understand the millennial and sub-millennial scale changes across the glacial transition approximately 425kyr ago and puts this termination in to a wider perspective by comparing it to the subsequent terminations, T2 (approximately 130kyr) and T1 (approximately 14kyr). The oceanographic conditions during this termination have been reconstructed using a number of proxies, namely complete planktonic foraminiferal faunal counts and stable isotope analysis of planktonic foraminifera. The faunal assemblages have been used to reconstruct sea surface temperature (SST) across the transition both using the Modern Analogue Technique (MAT) and the relative *Neogloboquadrina pachyderma* abundance to reconstruct SST in the Southern Ocean/South Atlantic. We suggest here, based on our record from T5, that the magnitude of the millennial scale event in the South Atlantic during MIS 12 and corresponding cold event in the North Atlantic has no impact on the amplitude of the termination when records from T5 are compared to the records from T2 and T1.

Also, with reference to G-IG transitions chapter 3 assesses the interplay between deep ocean circulation and high latitude climate change across Termination 2 (T2) in the North Atlantic. Using ODP Core 1063 from Bermuda Rise, we show that the relative timing of events across this termination determines the large and rapid deglacial CO_2 change across Termination 2.

Chapter 4 will focus on Marine Isotope Stage (MIS) 11 at ODP Site 983. MISs were first identified by Shackleton, (1967) referring to the $\delta^{18}O$ record being dominated by the effect of changes in the oxygen isotopic composition of the global ocean, now referred to as MIS 1, 2, 3 etc. for example. We will assess changes in temperature at the core location over this interval by using paired Mg/Ca-$\delta^{18}O$ analysis on a species of planktonic foraminifera, *Globorotalia inflata*. This chapter compares the relationship between the two hemispheres across MIS 11 (ODP Site 983 and ODP Site 1089). Using the data from this chapter, in connection with the data from chapter 2, we suggest that T5 is an 'extreme' termination in terms of the magnitude of the millennial scale events when we compare it to the following glacial terminations (T2 and T1).

Finally, chapter 5 synthesises all the work from the previous chapters and draws conclusions based on all the new data produced in this thesis. Furthermore, we make suggestions for future work and additional questions to be asked following the interpretation of the dataset sets presented here.

2 TERMINATION 5 (T5); AN 'EXTREME' TERMINATION?

2.1 INTRODUCTION

Ice cores from Greenland (Stuiver and Grootes, 2000) and sediment records from the North Atlantic (Shackleton et al., 2000) suggest that during the last glacial and deglacial periods the northern hemisphere was subjected to abrupt fluctuations in temperature. These abrupt fluctuations are recorded as Dansgaard-Oeschger (D-O) events in the ice core records (Stuiver and Grootes, 2000). In contrast to these D-O events in the north, the associated temperature fluctuations in the south, over Antarctica, were more gradual in nature and approximately out of phase with the north (Blunier and Brook, 2001). Further work has found a direct link between the extent of warming in Antarctica and the duration of the stadial conditions in the north (EPICA Community Members, 2006); it is this contrasting temperature relationship between the hemispheres that led to the notion of the bipolar seesaw (Stocker and Johnsen, 2003), whereby changes in the strength of the AMOC specifically alters the distribution of heat between the hemispheres (Crowley, 1992; Broecker, 1998).

The bipolar seesaw can explain the asynchronous nature of the climate signals seen in the northern and southern hemispheres (see **Error! Reference source not found.**) (Stocker and Johnsen, 2003). This asynchronicity can be explained by variability in the Atlantic Meridional Overturning Circulation (AMOC) (McManus et al., 2004) (see section in introductory chapter for explanation of AMOC). Presently, the AMOC continually moves warm waters from the South Atlantic to the North Atlantic where the warmer waters cool, become more dense and sink to form North Atlantic Deep Water (NADW) (Dickson and Brown, 1994). The warm waters in the South Atlantic are primarily derived from the Indian Ocean but also warm waters from the Antarctic Circumpolar Current (ACC) and South Atlantic itself (Stramma and England, 1999).

However, the modern day transport of warmer waters northwards and deep-water formation in the North Atlantic has not always been the case. A slowing down of AMOC perhaps as a result of cold, buoyant freshwater input to the North Atlantic results in a weaker surface water current in the Atlantic and a slow down of deep-water formation in the North Atlantic. This slowdown of AMOC results in an increase in temperature in the South Atlantic as the warmer waters are 'held' there, unable to move northwards due to a reduction in NADW formation. Conversely, the North Atlantic

cools as the slowdown of the AMOC stops warmer waters moving northwards. This asynchronicity explains the opposing natures of the signals observed when comparing the North and South Atlantic on millennial timescales (Figure 1.3).

2.1.1 MOTIVATION FOR THIS STUDY

The focus of this study is to reconstruct surface ocean conditions in the South Atlantic in order to assess the response of the South Atlantic to millennial scale climate events during termination 2 and 5. This has already been studied previously for Termination (T) 1 at core location TN057-21 (41.1°S, 7.8°W in 4981m water depth) (Barker et al., 2009) and our study extends the understanding of the dynamics of the bipolar seesaw during the earlier Terminations, 2 and 5. We study T2 as it is the next logical termination to study following T1, and T5 to assess the findings of Barker et al., (2009). These terminations were also chosen as they have contrasting insolation patterns. T5 has a similar insolation configuration to T1 allowing for direct comparison between the two studies whereas T2 has a different insolation configuration. Previously Bard and Rickaby, (2009) have highlighted that Marine Isotope Stage (MIS) 12 is a very cold glacial period and the following interglacial (MIS 11) is longer than the earlier interglacials studied here (MIS 5 and the Holocene). As such, T5 shows much larger fluctuations in temperature in the North Atlantic than the preceding terminations and appears rather anomalous in comparison.

To investigate changes in surface ocean temperatures Barker et al. (2009) used a combination of planktonic foraminiferal assemblage counts and planktonic foraminifera Mg/Ca paleothermometry. Here we use the same methods to generate planktonic foraminiferal assemblage counts and use the full assemblages to assess the extent of instantaneous temperature changes in the South Atlantic during this Termination by generating a sea surface temperature record using Modern Analog Technique (MAT) analysis. Following the findings of the work by Barker et al., (2009) we hypothesise that the temperature record from ODP Site 1089 in the South Atlantic is the southern hemisphere counterpart to the abrupt millennial scale events in the northern hemisphere (recorded as D-O events during T1), providing evidence for the instantaneous bipolar seesaw during the earlier T5.

2.2 OCEANOGRAPHIC SETTING OF THE CORE LOCATION

ODP Site 1089 (40°56.2′S, 9°53.6′E) is located in the southern Cape Basin off the Southwestern tip of Africa, just north of the Agulhas Ridge (Figure 2. and Figure 2.). ODP Site 1089 is located on a sediment drift and benefits from high sedimentation rates, averaging approximately 15cm/kyr during the Pleistocene (Shipboard Scientific Party, 1999). The sediment core was recovered at a water depth of 4620m. The high sedimentation rates allow high-resolution climate records to be produced from this core location in the South Atlantic. ODP Site 1089 is located at the northern margin of the modern Subtropical Front (Figure 2.). The core is therefore a sensitive recorder of changes in the position of the fronts, this makes it ideal for studying the inverse of these D-O events, the South Atlantic component of the bipolar seesaw (e.g. Barker et al., 2009).

In the modern ocean ODP Site 1089 is bathed in Circumpolar Deep Water (CDW), which fills the Cape Basin from the south (Figure 2.). CDW can be found near the continental shelf break around most of Antarctica (Dinniman et al., 2012) and is derived from a mixture of the deep waters from all the world's oceans (Orsi et al., 1995, 1999). The water mass is characterised by temperatures between 0-2°C and a salinity greater than 34.6 (Dinniman et al., 2012). CDW is divided into upper and lower Circumpolar Deep Water (UCDW and LCDW respectively); distinguishable by low oxygen content and high nutrient concentrations (UCDW) (Sievers and Nowlin, 1984) and higher salinity (LCDW) (Orsi et al., 1995), it is the LCDW that bathes the core site at depth.

In between LCDW and UCDW lies North Atlantic Deep Water (NADW) that flows southwards from the North Atlantic. At the latitude of ODP 1089 it occupies the ocean between approximately 2250-3750m (see Figure 2.). NADW is characterised by temperatures ranging between 1.5-4.0°C and salinities between 34.8-35.0 (Emery, 2001). In the modern ocean, NADW forms in the North Atlantic where the warm surface waters of the North Atlantic Current cool and become denser where they then sink, combining with Labrador Sea Water (LSW) and the overflows from the Greenland-Scotland ridge (Dickson and Brown, 1994). The resulting NADW represents a mixture of deep waters formed in the Nordic Seas and the Labrador Sea (Dickson and Brown, 1994); NADW then travels southwards in the Atlantic at depth only slightly shoaling as it meets the denser LCDW that fills the deepest part of the

South Atlantic (in the modern ocean). Antarctic intermediate water (AAIW) travels northwards from the south occupying depths between 500-1000m; above the UCDW tongue, Subantarctic surface water (SASW) occupies the surface waters (down to 500m) in the modern ocean (Shipboard Scientific Party, 1999).

As well as different temperature and salinity characteristics, NADW and CDW have very different nutrient contents; the northern sourced NADW is low in preformed nutrients and has a high $\delta^{13}C$ of dissolved inorganic carbon (DIC) (>0.8‰ (Kroopnick, 1985; Oppo and Curry, 2012)) compared to the southern sourced CDW which is higher in preformed nutrients and is characterized by low $\delta^{13}C$ DIC (<0.7‰ (Kroopnick, 1985; Oppo and Curry, 2012). Antarctic Bottom Water (AABW) is found south of the core location in the modern ocean and has even lower $\delta^{13}C$ DIC values (typically <0.5‰ (Kroopnick, 1985; Oppo and Curry, 2012)).

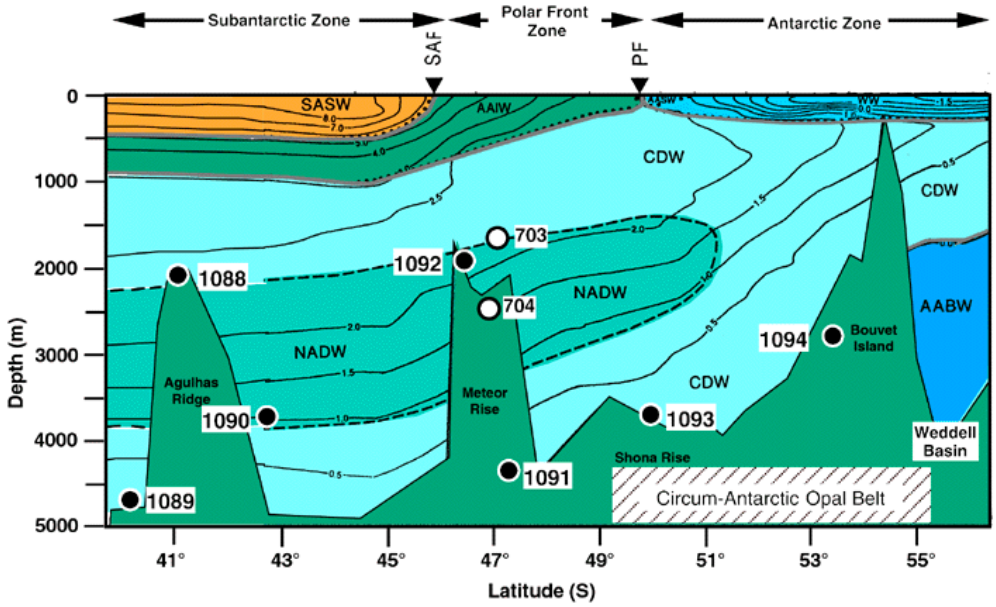

Figure 2.8. Leg 177 sites relative to the vertical distribution of potential temperature on a north-south transect from the Agulhas Ridge to Bouvet Island in the southeast Atlantic Ocean. NADW = North Atlantic Deep Water; CDW = Circumpolar Deep Water; AABW = Antarctic Bottom Water; AAIW = Antarctic Intermediate Water; SASW = Subantarctic Surface Water; SAF = Subantarctic Front; and PF = Polar Front (Shipboard Scientific Party, 1999).

Figure 2. shows the modern surface oceanographic setting of the Atlantic sector of the (northern part of the) Southern Ocean and the position of ODP Site 1089 with respect to

the thermal fronts. The fronts separate different water masses from north to south, the Subtropical Front (Subtropical Surface Water converging with Subantarctic Surface Water) (Sabine et al., 2004); the Subantarctic Front (Subantarctic Surface Water converging with Antarctic Intermediate Water) (Sabine et al., 2004); and the Polar Front (Antarctic waters converging with Subantarctic Surface Water (Lutjeharms and Valentine, 1984)). The fronts are characterized by steep temperature gradients; in the present day ocean there are large temperature differences between the STF and SAF (14.2°C north of the SFT (Lutjeharms and Valentine, 1984) to 8.4°C south of the STF (Lutjeharms, 1981)) (note the temperatures are annual averages); and the close proximity of ODP Site 1089 to the STF makes this core excellent to monitor changes in the position of this front through time.

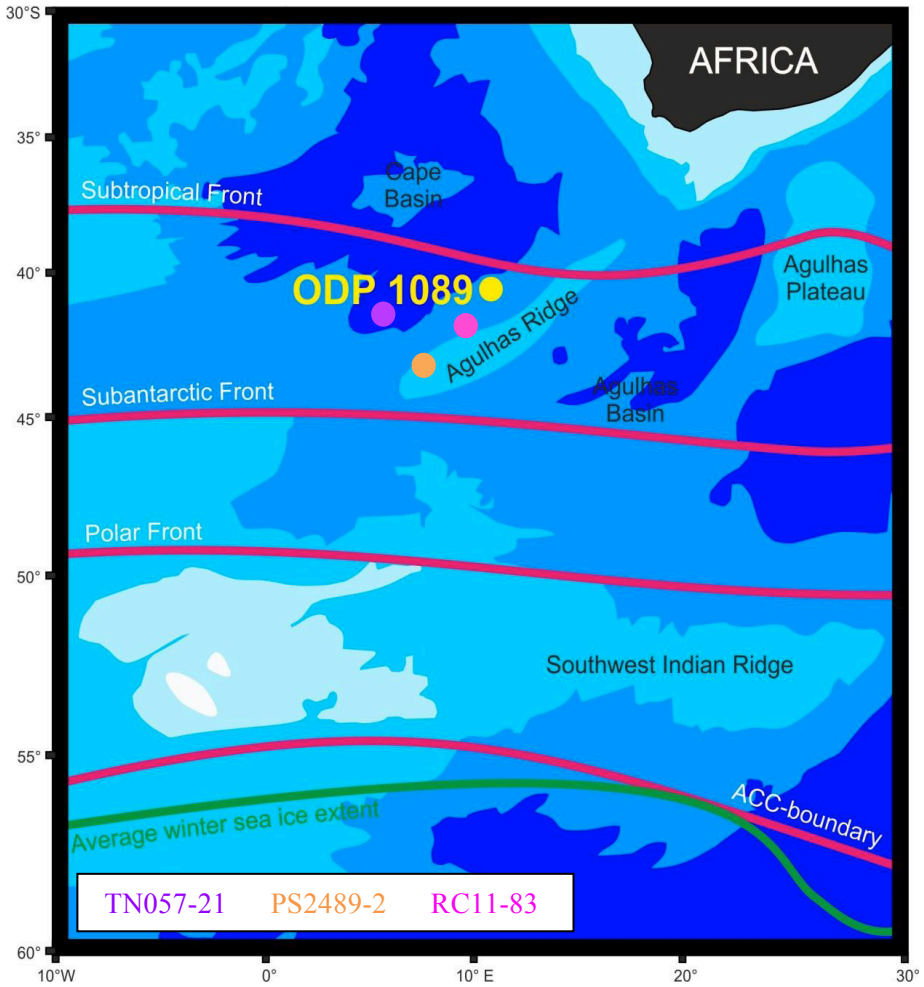

Figure 2.9. ODP Site 1089 (40°56.2'S, 9°53.6'E); located on the northern flank of the Agulhas Ridge, just south of the Subtropical Front. South of the Subtropical Front lies the Subantarctic and Polar Front. Antarctica (to the south of the map) is enclosed by the Antarctic Circumpolar Current (ACC), which controls the extent of

the winter sea ice (green). Increasing bathymetry indicated by the gradational blue (light to dark) Adapted from (Hodell et al., 2003a). Core locations used later in this chapter for comparison are shown here; the orange circle indicates the location of core PS2489-2 (42.9°S, 8.97°E); the purple circle indicates the location of core TN057-21 (41.1°S, 8.8°E) and; the pink circle indicates the location of core RC11-83 (41.6°S, 9.72°E).

2.3 MATERIALS AND METHODOLOGY

2.3.1 FORAMINIFERAL ANALYSIS

The samples required for the analysis of ODP Site 1089 across Terminations 2 and 5 were obtained from the ODP repository in Bremen, Germany. The data across Termination 2 were collected by Joanna Langhelt, a former MSc student at Swansea University under the supervision of Prof S. Barker. For both terminations the wet sediment was disaggregated by adding deionised (DI) water to it and placing it on a rotating wheel for 12-16 hours. It was then washed over a 63μm sieve using a fine water spray; the coarse fraction (>63μm) was then dried off in the oven at 40°C for approximately 36 hours. The fine fraction (<63μm) was allowed to settle and then the water was syphoned off, and allowed to dry in the oven (40°C) for approximately one week until the sediment was completely dry. Both fractions were weighed using an Ohaus Pioneer PA413C balance.

In line with samples used in the Brown University Foraminiferal database (Prell et al., 1999) sub-samples across Termination 5 were obtained by sieving (>150μm) the coarse fraction for each sample and further divided using a binary splitter in order to obtain approximately 300 whole foraminifera shells that were subsequently counted. This number of whole shells was counted to ensure that smaller sub-sample is an accurate representation of the whole sample and encompasses a larger enough diversity of species following the methods of CLIMAP Members (1984) and Pflaumann et al., (1996). We followed the taxonomy of Parker (1962); Figure 2.9 shows drawings of the main foraminifera identified in the samples (taken from Parker, (1962)).

For Termination 2; Joanna Langhelt generated records of abundance of the warm planktonic foraminifera species, *Globigerinoides ruber* and the polar species, *Neogloboquadrina pachyderma* (note in this study *N.pachyderma* refers to the left

coiling species, we use *Neogloboquadrina incompta* to replace the previously used *N. pachyderma* (dextral)); these counts were made following the same sieving and splitting methods as mentioned above. In addition to the two species of planktonic foraminifera, whole shells/g and % fragmentation counts were made.

Planktonic foraminiferal $^{18}O/^{16}O$ and $^{13}C/^{12}C$ ratios (T2) ($\delta^{18}O$ and $\delta^{13}C$ respectively, expressed in ‰ Vienna Pee-Dee Belemnite, VPDB) across T2 were measured at Bloomsbury Environmental Isotope Facility (BEIF) at University College London on a ThermoFinnigan Delta PLUS mass spectrometer. Twenty planktonic foraminifera, *Globigerinoides bulloides* specimens were handpicked from core ODP 1089 from a narrow size range to minimise size effects on isotopic ratios (250-315µm). The samples were rinsed in methanol and dried overnight in a 70°C oven. Precision of all internal and external standards was ±0.03‰ for $\delta^{13}C$ and ±0.08‰ for $\delta^{18}O$ (based on the standard deviation of repeat measurements of the international standard NBS-19).

The % fragmentation of planktonic foraminifera is used as a proxy for carbonate dissolution (Berger, 1968, 1970; Le and Shackleton, 1992; Le and Thunell, 1996). Shells that have been subjected to dissolution have thinner shells and break more easily and thus the more a sample has been affected by dissolution, the larger the percentage of fragmentation will be. For this study a fragment is defined as a piece of foraminiferal shell that is less than 50% intact.

The total number of whole shells/gram in a sample can be used as a proxy for productivity (Barker et al., 2010; Barker and Diz, 2014) in the water column as the abundance of foraminifera is an indicator of the availability of food (as well as other prevailing conditions in the water column) in the water column. As well as providing a proxy for food productivity, the number of whole shells in a sample is also an indicator of preservation of the sample as the larger the number of whole shells, the greater the preservation of that sample.

2.3.1.1 PLANKTONIC FORAMINIFERA AS ENVIRONMENTAL INDICATORS/PROXIES

Planktonic foraminifera are free-floating surface dwelling single-celled microorganisms with a global distribution. These protozoa form elaborate calcite shells (tests) that allow visual differentiation between (morpho)species. Following death, the shells sink to the

seafloor and are preserved in the sediment. Sediment traps (Tolderlund and Bé, 1971; Chapman, 2010), plankton tows (Bé and Tolderlund, 1971) and modern (core-top) sediment assemblages (Prell et al., 1999) of planktonic foraminifera reveal a very distinct geographical pattern in the modern ocean as shown in ***Figure 2.8***. The study of planktonic foraminiferal ecology and distribution highlights the preference that species display for certain environmental conditions and the relative maximum abundance of particular species correlates with ecologic optima (e.g. Bé and Tolderlund, 1971). Foraminiferal distribution in the modern ocean shows a latitudinal pattern suggesting temperature is the most important control on their distribution (Murray 1897). Although temperature is the most important control on their distribution there are also other parameters that influence their distribution such as, surface salinity, pycnocline phosphate concentrations, the seasonal range in nitrate concentrations, water depth, and chlorophyll concentrations (e.g. Morey et al., 2005).

It is for these reasons that planktonic foraminiferal assemblage counts have been recognised and long since used as surface-water property tracers; given a particular assemblage and the known distribution of species in the modern ocean, it is possible to use the combined assemblage of each individual species to determine the past (near) sea surface temperature (e.g. Bradshaw, 1957; Parker, 1960; Berger, 1969; CLIMAP Members, 1984; Pflaumann et al., 1996; Kucera et al., 2005; MARGO Members, 2005). There are different approaches that can be used to reconstruct sea surface temperature (SST) using the foraminiferal assemblage; for example Modern Analog Technique (MAT) (Hutson, 1980; Overpeck et al., 1985; Prell et al., 1999), SIMMAX (an acronym for a MAT using a similarity index) (Pflaumann et al., 1996) and weighted-average partial least squares (WA-PLS) analysis (Braak and Juggins, 1993). In this study we apply the MAT analysis to reconstruction SSTs over Termination 5 in the South Atlantic (ODP Site 1089).

The use of planktonic foraminifera assemblages to infer past environmental change requires that the sedimentary assemblage be unaltered by post-depositional processes. Dissolution could potentially affect the fossil assemblage (Le and Shackleton, 1992; Le and Thunell, 1996), and sedimentary records thus need to be carefully screened for dissolution for accurate/sensible paleoclimate reconstructions.

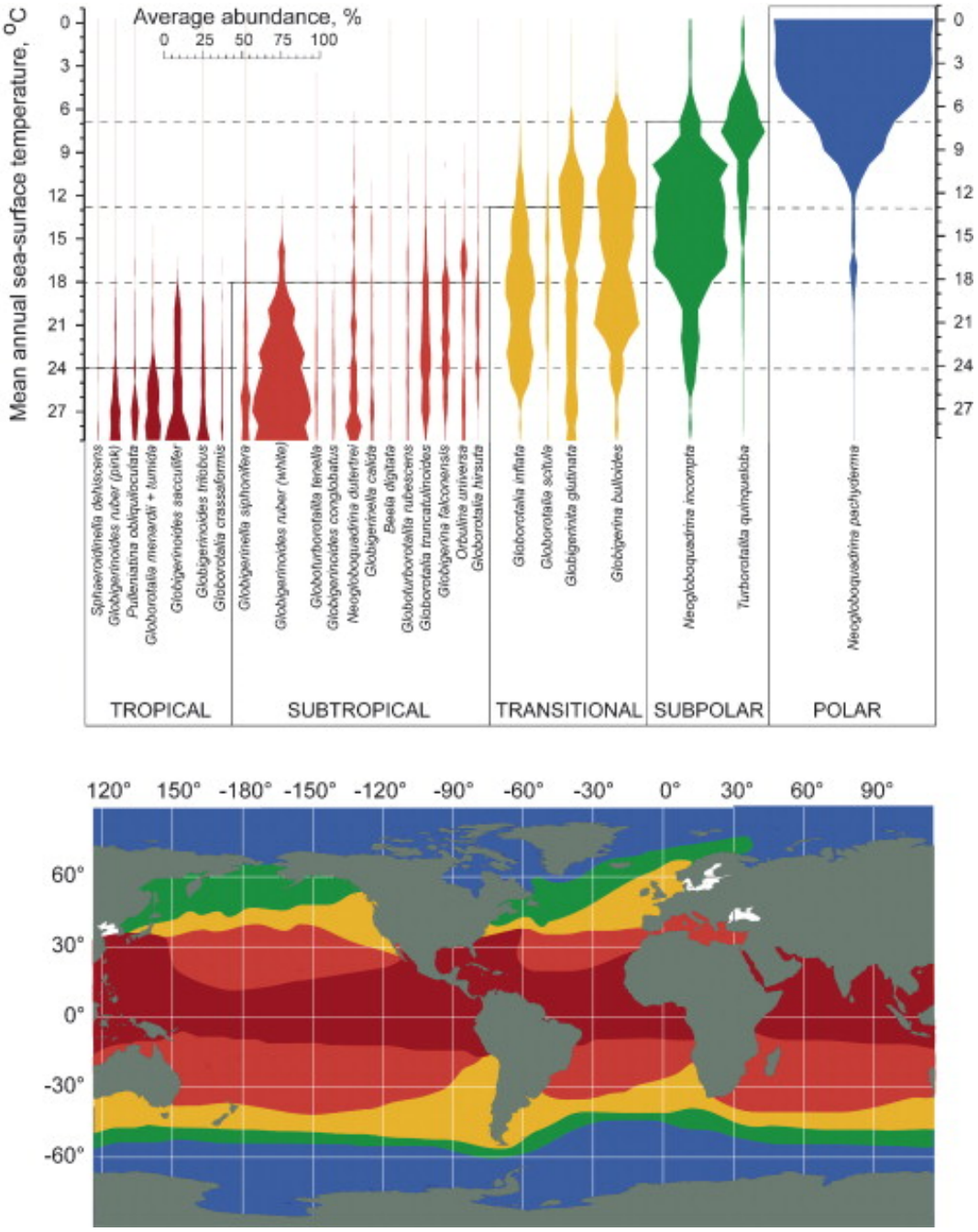

Figure 2.8. Planktonic foraminiferal provinces in the modern ocean. The distribution of the provinces (Bé and Hutson, 1977; Vincent and Berger, 1981) follows the gradients of the sea surface temperature; reflecting the correlation between sea surface temperature and the distribution of planktonic foraminiferal species (Kucera et al., 2005).

2.3.1.2 ENVIRONMENTAL PREFERENCES OF INDICATOR SPECIES

Neogloboquadrina pachyderma and *Turborotalita quinqueloba* inhabit primarily polar and to a lesser extent subpolar regions (Hemleben et al., 1989); *Neogloboquadrina incompta* prefers slightly less cold, subpolar regions where it thrives (Hemleben et al., 1989). *Globorotalia inflata* and *Globigerinoides bulloides* tolerate a wide range of temperatures (Hemleben et al., 1989) and as such inhabit a wide range of latitudes making them nearly ubiquitous throughout the core. *G. inflata* and *G. bulloides* are transitional to subpolar species (Hemleben et al., 1989). *Globigerinoides ruber* thrives in warmer, sub-tropical/tropical conditions (Hemleben et al., 1989). *Orbulina universa* is widely distributed from the tropics to the subpolar regions whereas *Globorotalia crassaformi*s, *Globorotalia hirsuta* and *Globorotalia truncatulinoides* are temperate to subtropical species (Hemleben et al., 1989).

In order to get a clear representation of changes in the assemblage species that have similar temperature tolerances can be grouped together (Vautravers et al., 2004; Vautravers and Shackleton, 2006; Barker and Diz, 2014). Here the groupings of planktonic foraminifera were chosen based on a recent paper from Barker and Diz (2014). Together, these groups account on average for 90 % of the total assemblage (Figure 2.16).

- **Warm species**; *Globigerinoides ruber*; *Orbulina universa*; *Globorotalia truncatulinoides* (d); and *Globorotalia hirsuta* (total (sinistral + dextral))
- **Transitional species**; *Globorotalia inflata* and *Globigerinoides bulloides*
- **Sub-polar species**; *Neogloboquadrina incompta*
- **Polar species**; *Neogloboquadrina pachyderma* and *Turborotalita quinqueloba*

Primarily these groups were defined based on their ecological preferences, notably temperature (see ***Figure 2.8***). Importantly both the warm and polar species groups contain species that are, according to Berger (1970), both susceptible to dissolution; *G. ruber* (warm), *G. bulloides* (transitional) and *T. quinqueloba* (polar) and those that are more robust; *G. truncatulinoides* (d) (warm), *G. inflata* (transitional) and *N. pachyderma* (polar) (see Table 2.3). Similar trends in the relative proportions of species

with differing susceptibilities within these groups, give us confidence that dissolution is not the primary signal in our records and that changes in the original assemblage have been preserved (see later sections).

Additionally, the following species were counted but not included in the species groupings; *Globorotalia truncatulinoides* (s), *Globorotalia crassaformi*s (sinistral (s)), *Globorotalia crassaformi*s (dextral (d)) and *Pulleniatina obliquiloculata*.

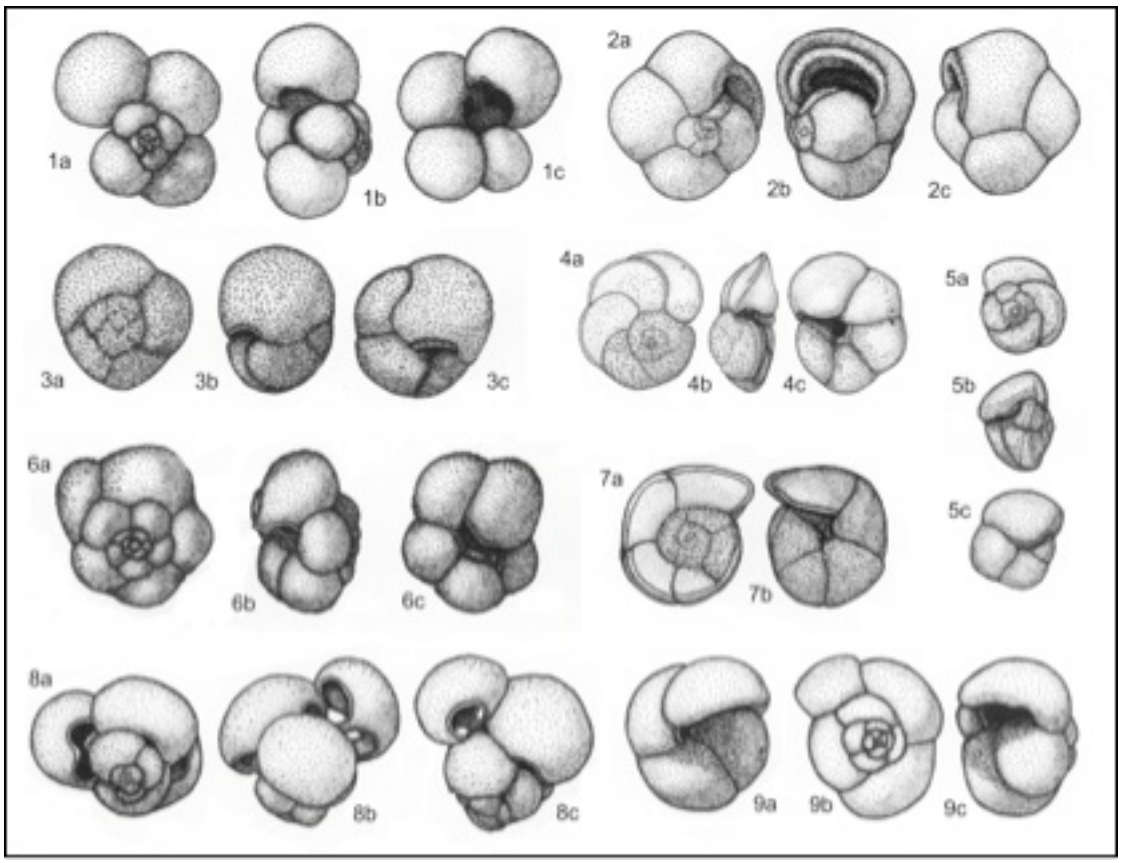

Figure 2.9. Images adapted from Parker, 1962 to show taxonomy followed for planktonic foraminiferal assemblage counts. (1) Globigerina bulloides; (2) Pulleniatina obliquiloculata; (3) Neogloboquadrina pachyderma; (4) Globorotalia hirsuta; (5) Globorotalia crassaformis; (6) Turborotalita quinqueloba; (7) Globorotalia truncatulinoides; (8) Globigerinoides ruber; and (9) Globorotalia inflata.

2.3.2 CALCIUM CARBONATE ANALYSIS

The sedimentary calcium carbonate content (% $CaCO_3$) was measured to align the records from this study (for both Termination 2 and 5) to that of previously published

records on the same core site using a different splice (Hodell et al., 2003a, 2003b) to allow comparison of the records. Carbonate content was determined by CO_2 coulometry using a UIC.inc CM5130 Acidification Module connected to a UIC.inc CM5014 CO_2 Coulometer

Approximately 1 cm^3 of bulk sediment was dried at 40°C degrees and ground to ensure homogenisation using agate pestle and mortar and aliquots of approximately 30mg were used for analysis. A Standard (100% $CaCO_3$) and a blank were run every 10 samples.

2.4 RESULTS

2.4.1 SEA SURFACE TEMPERATURE ESTIMATES

Two methods were used to estimate past sea surface temperatures (SSTs) based on planktonic foraminifera assemblages. First, SSTs were estimated from the full assemblage using the Modern Analogue Technique (MAT) (Hutson, 1980; Overpeck et al., 1985; Prell et al., 1999). For comparison SSTs were also inferred from the relative abundance of *N. pachyderma* only (Govin et al., 2009) based on analogous work from a nearby core location (Vázquez Riveiros et al., 2010, 2013).

2.4.2 MODERN ANALOGUE TECHNIQUE SST RECONSTRUCTION

The Modern Analogue Technique (MAT) quantifies temperature changes in planktonic foraminiferal assemblages within marine sediment cores by comparing the assemblage composition to modern oceanographic conditions. The method uses a measure of dissimilarity to compare each of the samples from the core (using the full planktonic faunal assemblage) to a database of core top assemblages. This study runs the MAT analysis (Hutson, 1980; Overpeck et al., 1985; Prell et al., 1999) using The Brown University Foraminiferal Database as a reference (Prell et al., 1999). Here we run MAT analysis using the squared chord distance (a signal to noise measure) as a measure of dissimilarity. The analysis compares each of the down-core faunal assemblages to the Brown University Foraminiferal Database (Prell et al., 1999); with the output averaging the 10 closest analogues to the sample. This analysis was carried out using the program *Analog* run in Terminal on Mac OS X. The error of each temperature estimate is based on the standard deviation of the 10 closest analogues.

2.4.3 % NEOGLOBOQUADRINA PACHYDERMA SST RECONSTRUCTION

The relative abundance of the planktonic foraminifer *N. pachyderma* has been used as a sea surface temperature (SST) indicator in polar regions (Bond et al., 1993; Barker et al., 2009; Govin et al., 2009; Vázquez Riveiros et al., 2010; Govin et al., 2012; Vázquez Riveiros et al., 2013) as it is a species that thrives in cold waters (Bé and Tolderlund, 1971; Govin et al., 2009). Since *N. pachyderma* dominates the assemblages at low temperatures and is (virtually) absent above 12°C (Niebler and Gersonde, 1998; Govin et al., 2009), its relative abundance can only be used as a quantitative paleotemperature indicator between 0-12°C (Govin et al., 2009). Quantitative summer SST estimates were obtained from the relative abundances of *N. pachyderma* using a previously established calibration based on data from 245 core tops in the Southern Ocean (sSST = -0.087 x %NPS +11.339) (Kucera et al., 2005; Govin et al., 2009). Because of the constraints described above, this method only yields reliable results between 3 to 11°C, the uncertainty of the SST estimates is ± 1.7°C (Govin et al., 2009).

2.5 NEW SPLICE FROM ODP SITE 1089

Previously, planktonic and benthic foraminifera stable isotope and preservation counts (% fragmentation) data from ODP Site 1089 (from the 'original' splice) were published by Hodell et al., (2002, 2003a). The data presented here however have been generated from samples from different holes at ODP Site 1089 for both Termination 2 (Table 2.1) and 5 (Table 2.2).

Table 2.1. Sample sections used in both the original splice and the 'new' splice from ODP 1089 for Termination 2.

ODP 1089 Original Splice (T2)	**ODP 1089 Splice used in this study (T2)**
Hole D, Core 3, Section 5 (0-149cm)	Hole C, Core 3, Section 1 (98-151cm)
Hole D, Core 3, Section 6 (0-149cm)	Hole C, Core 3, Section 2 (1-150cm)
Hole B, Core 3, Section 1 (120-149cm)	Hole C, Core 3, Section 3 (0-39cm)
Hole B, Core 3, Section 2 (0-80cm)	Hole A, Core 3, Section 2 (61-116cm)

Table 2.2. Sample sections used in both the original splice and the 'new' splice from ODP 1089 for Termination 5.

ODP 1089 Original Splice (T5)	**ODP 1089 Splice used in this study (T5)**
Hole C, Core 7 Section 1 (80-147cm)	Hole D, Core 7, Section 6 (6-149cm)
Hole C, Core 7, Section 2 (0-147cm)	Hold D, Core 7, Section 7 (0-27cm)
Hole C, Core 7, Section 3 (0-147cm)	Hole B, Core 7, Section 1 (3-150cm)
Hole C, Core 7, Section 4 (0-147cm	Hold B, Core 7, Section 2 (0-149cm)
Hole C, Core 7, Section 5 (0-147cm)	Hole D, Core 8, Section 2 (25-150cm)
Hole C, Core 7, Section 6 (0-77cm)	Hold D, Core 8, Section 3 (1-150cm)
Hole B, Core 7, Section 3 (100-147cm)	Hold D, Core 8, Section 4 (1-149cm)
Hole B, Core 7, Section 4 (0-147cm)	Hold D, Core 8, Section 5 (0-105cm)
Hole B, Core 7, Section 5 (0-52cm)	
Hole C, Core 8, Section 1 (100-147cm)	
Hole C, Core 8, Section 2 (0-147cm)	

In order to compare the new and previously published data, the two splices were placed on a common depth scale, from Hodell et al., (2002, 2003a) by aligning their $CaCO_3$ content records (T2; Figure 2.10 and T5; Figure 2.11).

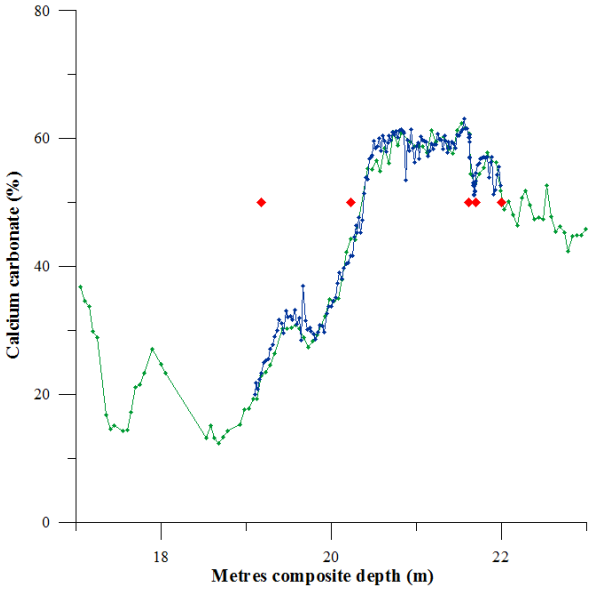

Figure 2.10. T2; Percent carbonate records from this study (blue) and from the original splice from ODP 1089 (Hodell et al., 2003a) (green). The red diamonds indicate the tie points used to align the percent carbonate records.

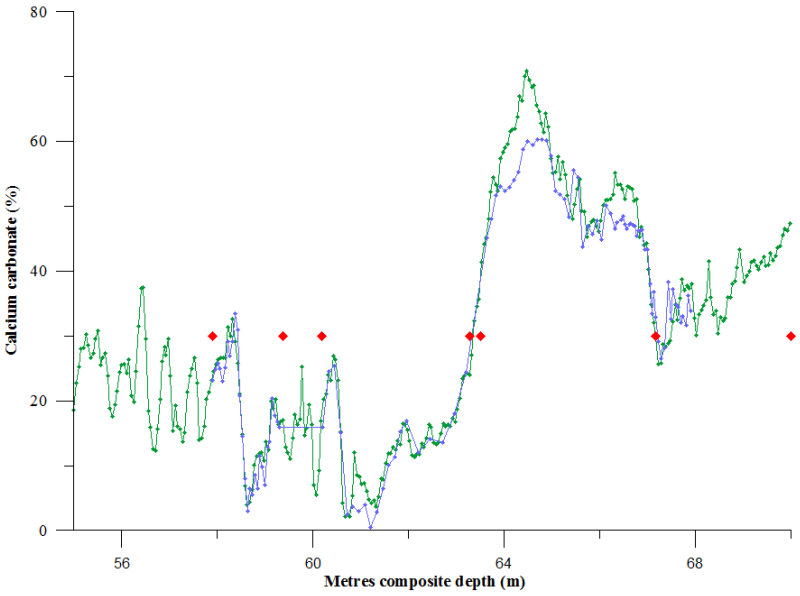

Figure 2.11. T5; Percent carbonate records from this study (blue) and from the original splice from ODP 1089 (Hodell et al., 2003a) (green). The red diamonds indicate the tie points used to align the percent carbonate records.

2.6 AGE MODEL

A low-resolution benthic foraminifera $\delta^{18}O$ record from ODP 1089 is included in the global benthic foraminifera stable oxygen isotope stack (Lisiecki and Raymo, 2005). However, for both Terminations 2 and 5, the record of 1089 is not perfectly aligned with the global stack (T2; Figure 2.12 (panel a) and T5;

Figure 2.13 (panel a)) and we use a higher resolution benthic foraminifera $\delta^{18}O$ record (Hodell et al., 2003a) to improve the alignment (T2; Figure 2.12 (panel b) and T5;

Figure 2.13 (panel b)). Although the adjustments to the original age model (Lisiecki and Raymo, 2005) are within the 4 kyr chronological error of the global stack, we believe that the updated age model allows for more precise comparison with other records. The average sedimentation rates are 15.6cm/kyr for T2 and 16.0cm/kyr for T5.

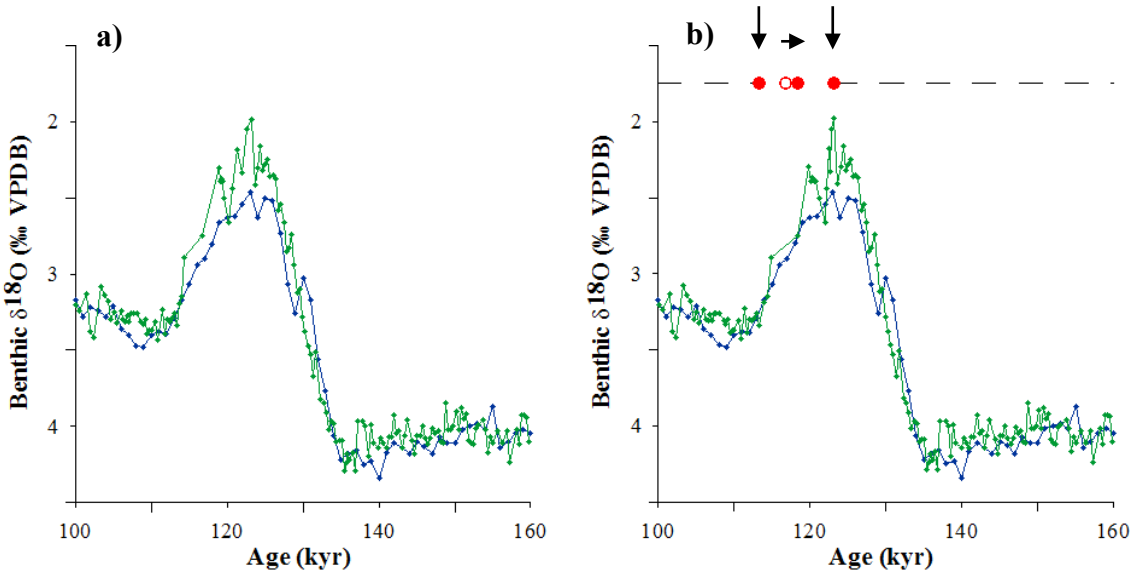

Figure 2.12. T2; panel (a) plot of benthic $\delta^{18}O$ showing room for improvement of the age model; the LR04 stack (blue) (Lisiecki and Raymo, 2005) and from Hodell et al., (2003a). Panel (b) age model plot; showing the benthic $\delta^{18}O$ record (Cibicidoides sp.) from Hodell et al., (2003a) (green) compared to the tuning target for T2, the benthic LR04 stack (Lisiecki and Raymo, 2005) (blue). The tie points are shown as red circles; outside of both of the vertical arrows the age model was fixed and unchanged from Hodell's original age model (Hodell et al., 2003b), however the open circle represents the original tie point for 18.83m and our improved tie point indicated by the horizontal arrow and closed circle.

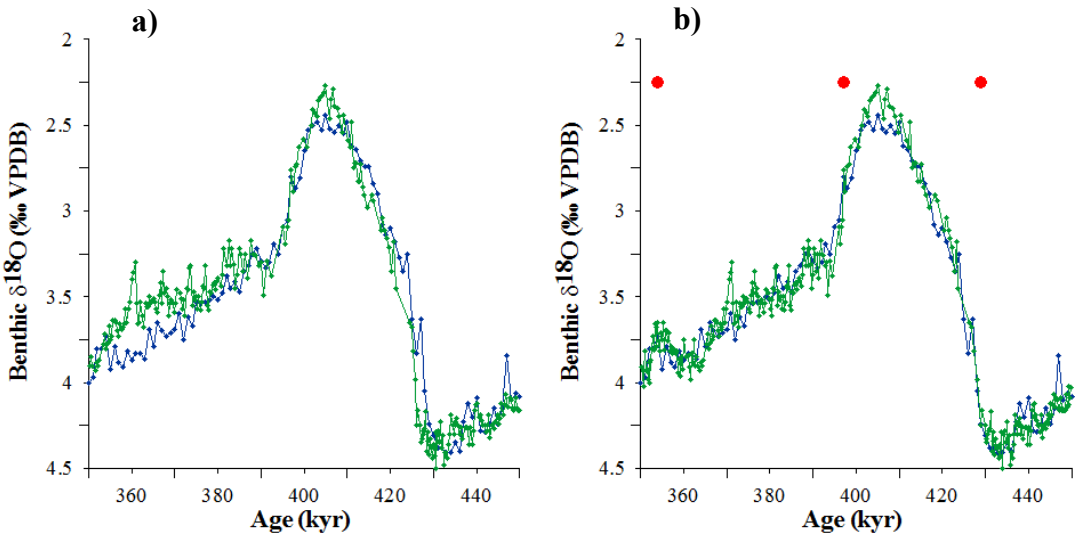

Figure 2.13. T5; panel (a) plot of benthic $\delta^{18}O$ (T5) showing room for improvement of the age model; the LR04 stack (blue) (Lisiecki and Raymo, 2005) and from Hodell et al., (2003a) (green). Panel (b) age model plot; showing the benthic $\delta^{18}O$ record (Cibicidoides sp.) from Hodell et al., (2003a) (green) compared to the tuning target for T5, the benthic LR04 stack (Lisiecki and Raymo, 2005) (blue). The tie points are shown as red circles.

The absolute error of the age model is determined by a combination of tuning error and age uncertainty in the tuning target, which for the LR04 stack is 4 kyr (Lisiecki and Raymo, 2005). We can also calculate the error of our tuning by using the resolution of both the tuning target (1 kyr) and the resolution of our record. As a coarse estimate we calculate the error propagation of our age model (for both T2 and T5) relative to LR04. This is calculated by the square root of the resolution of the tuning target (LR04) squared plus the average resolution of our record squared. The average resolution for both Terminations 2 and 5 is 124 years and 206 years respectively, i.e. for T2; the error = $\sqrt{(1000^2 + 124^2)}$. The average error of our age model based on this calculation is 1008 yr for T2 and 1021 yr for T5. Given the resolution of the tuning target is 1 kyr, by definition our tuning error can not be less than 1 kyr; a way to decrease the error would be to tune to a higher resolution tuning target, potentially allowing for an age model with smaller errors.

2.7 EVALUATION OF FORAMINIFERAL ASEMBLAGES/DISSOLUTION

The distribution of calcium carbonate ($CaCO_3$) with depth in the oceans shows a characteristic shape; sediments down to the mid-depths are rich in $CaCO_3$ (the water

column is supersaturated with respect to $CaCO_3$) and those from the abyssal depths are barren in $CaCO_3$ (undersaturated with respect to $CaCO_3$) (Murray and Renard, 1891; Berger, 1968, 1970; Broecker, 2003). In between these two depths (variable depending on local conditions) is a transition zone between the two extremes of $CaCO_3$ preservation, defined as the lysocline. The lysocline describes the transition zone between the start of dissolution and the '$CaCO_3$ compensation depth' (Archer, 1991), which is itself defined as the depth at which $CaCO_3$ content is reduced to <10% (Berger, 1970).

Not only is the preservation state of a particular foraminiferal shell (comprised of $CaCO_3$) in the sediments a function of depth (i.e. a function of pressure) and the CO_3^{2-} (carbonate ion) concentration of the bottom waters; it is also a function of the preservation potential of calcium carbonate organisms that are produced in the surface ocean (e.g. planktonic foraminifera as well as coccolithophores). Each foraminiferal species varies in its susceptibility to dissolution; controlled by the thickness of their shells. Typically the thin-shelled forms tend to be much less resistant than thick-shelled ones (Arrhenius, 1953; Berger, 1967). Foraminiferal dissolution susceptibility is also dependent on wall structure and porosity; the spinose forms have been recorded to be more susceptible to dissolution than the non-spinose forms (Phleger et al., 1953; Berger, 1967, 1970). Finally, their susceptibility is also dependent on the organic matter content in the skeletons; species with high organic matter have been found to be less resistant to dissolution (Berger, 1970). In order to establish the extent of dissolution in a given sample Berger (1970) ranked the 22 most common species of planktonic foraminifera in order of their susceptibility to dissolution (see Table 2.3).

Table 2.3. The ranking of 22 common planktonic Foraminifera in terms of their average susceptibility to dissolution; 1 is the most susceptible and 22 is the most robust (Berger, 1970). The species in bold are those used in this study. Note that Turborotalita quinqueloba used to be called Globigerina quinqueloba and Neogloboquadrina pachyderma used to be called Globigerina pachyderma and that in Berger's (1970) paper Globigerina pachyderma refers to both coiling varieties, hence why N. incompta does not appear in this ranking.

Ranking in terms of their susceptibility to dissolution

1	***Globigerinoides ruber***	12	***Globorotalia hirsuta***
2	***Orbulina universa***	13	***Globorotalia truncatulinoides***
3	*Globigerinella siphonifera*	14	***Globorotalia inflata***
4	*Globigerina rubescens*	15	*Globorotalia cultrata*
5	*Globigerinoides sacculifer*	16	*Globoquadrina dutertrei*
6	*Globigerinoides tenellus*	17	***Neogloboquadrina pachyderma***
7	*Globigerinoides conglobatus*	18	*Pulleniatina obliquiloculata*
8	***Globigerina bulloides***	19	*Globorotalia crassaformis*
9	***Turborotalita quinqueloba***	20	*Sphaeroidinella dehiscens*
10	*Globigerinita glutinata*	21	*Globorotalia tumida*
11	*Candeina nitida*	22	*Turborotalita humilis*

As suggested above, an individual foraminiferal shell that we observe in the sedimentary record may have been altered by dissolution; both as it travels through the water column and once it reaches the seafloor (due to exposure to (corrosive) bottom waters and to increased fragmentation from compaction of the overlying sediments after burial (Le and Shackleton, 1992; Le and Thunell, 1996)). We therefore need to assess the sedimentary assemblage for the effects of dissolution. The effects of dissolution as a result of exposure to (corrosive) bottom waters is likely to be greater than the effects of dissolution in the water column mainly because foraminifera take up to a month to sink to the seafloor (Berger and Piper, 1972), yet they are likely to spend decades if not centuries exposed at the seafloor.

The effects of dissolution to a sample typically results in fewer whole shells/g and a reduced diversity of species as the most susceptible species are dissolved. The reduction in diversity affects the assemblage unequally across the species; typically making the assemblage appear colder as the more susceptible, warm species (*G. ruber* and *O. universa* for example), preferentially dissolve first (see Table 2.3 (Berger, 1970)).

ODP Site 1089 is located at a water depth of 4620m and dissolution is therefore likely to have affected the foraminiferal assemblages. To evaluate the extent to which dissolution affected the record we use the same criteria as established by Barker and Diz (2014) in nearby core TN057-21. Recent work by Vautravers et al., (in preparation, 2014) and Barker and Diz (2014) evidences that samples with a low species diversity (<6) are generally associated with lowest concentration of whole shells, suggesting the most intense dissolution. This is also the case in our record from ODP Site 1089 for T5 (Figure 2.14). When we plot the complete record for species diversity vs. whole shells/g (Figure 2.14) we see a positive correlation between the two preservation indices. However, when we consider only the samples where the diversity is greater than 6 species (black symbols only) the correlation disappears, suggesting that we are able to use diversity as an indicator of preservation.

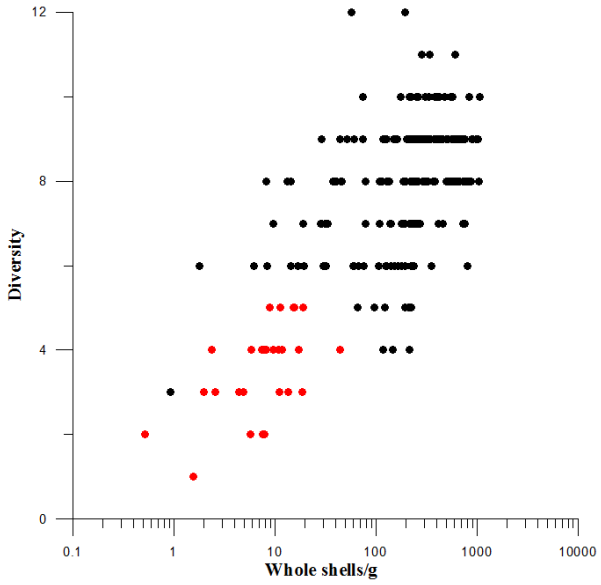

Figure 2.14. Diversity and whole shells/g on a log scale for each sample from ODP Site 1089, Termination 5. Note the positive correlation when we consider all samples (black and red symbols); but the lack of any correlation when we remove samples with a species diversity of less than 6 (black symbols only). We are therefore able to use species diversity and whole shells/g as preservation indicators.

On the other hand, a low species diversity does not necessarily mean that the sample is highly dissolved, rather it could be a sample dominated by just a couple of different species, for example the modern polar ocean is typically only inhabited by *N. pachyderma*, and/or *T. quinqueloba* (Bé and Hutson, 1977; Vincent and Berger, 1981).

If, however we observe low species diversity, few whole shells/g and the dominant species is resistant to dissolution this sample could be affected by dissolution (Figure 2.15). Dissolution is more likely to have affected the assemblage if species with similar ecological preferences, but different preservation potential do not co-occur. Accordingly, Barker and Diz (2014) argued that samples with low diversity, more *G. inflata* than *G. bulloides* and/or <50 whole shells/g could be affected by dissolution. Thus, samples that meet the following criteria are likely to be heavily influenced by dissolution and were rejected from further analyses:

- % *G. inflata* > % *G. bulloides*; and
- Species diversity < 6; and/or
- Total number of whole shells/gram < 50

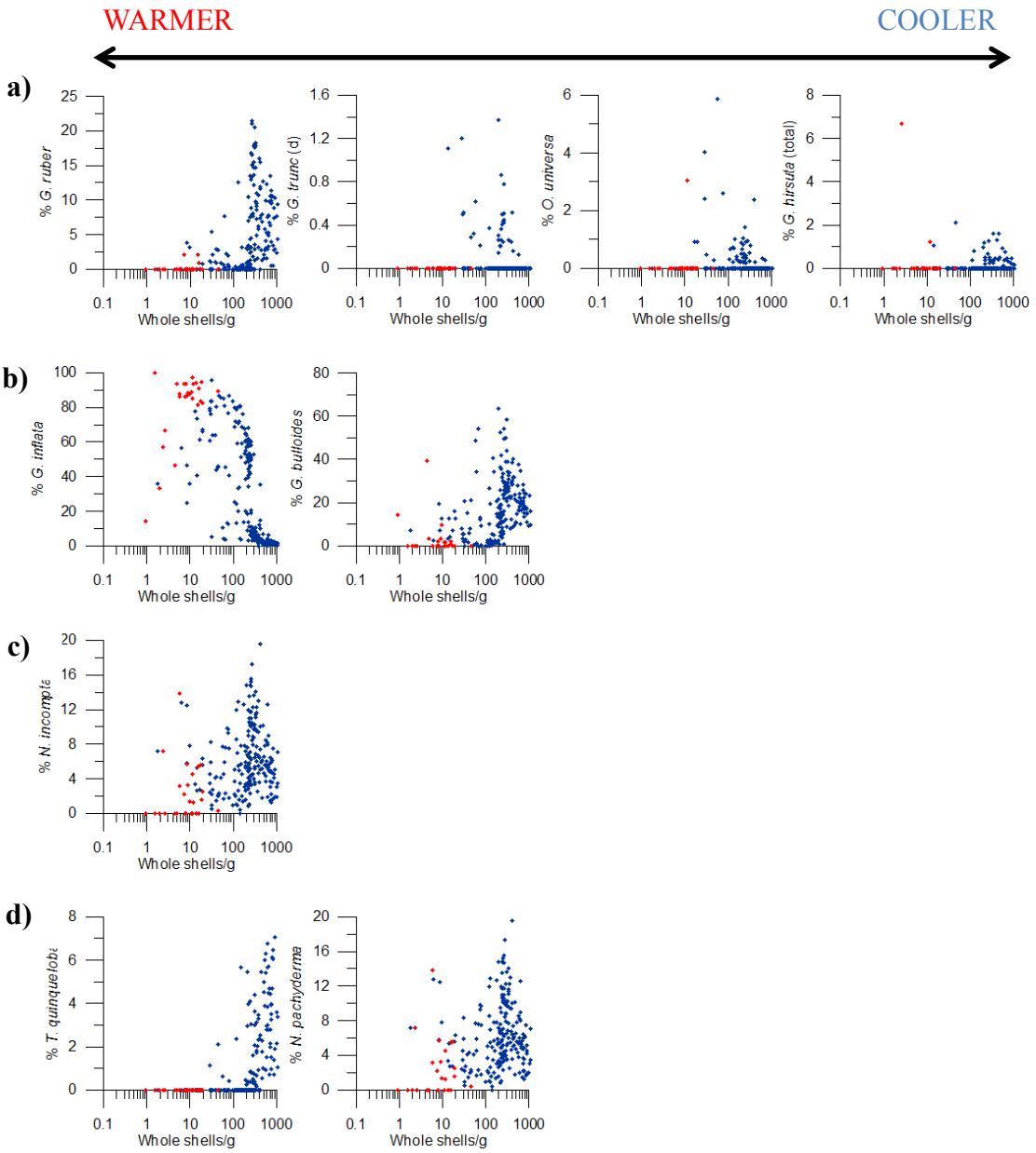

Figure 2.15. The relationship between the number of whole shells/gram and each species counted in the planktonic foraminiferal faunal assemblage counts. Group a) is the warm species group (L-R; G. ruber, O. universa, G. truncatulinoides (d) and G. hirsuta (total)). Group b) is the transitional species group (L-R; G. inflata and G. bulloides). Group c) is the sub-polar group (N. incompta). Group d) is the polar species group (L-R; N. pachyderma and T. quinqueloba). The species within the groups are ordered according to their temperature preference from warmer to cooler species from left to right.

Figure 2.16 shows the down core distribution of the foraminiferal species. The majority of the rejected samples (18 out of 28) fall between 403-410 kyr; during this period the

number of whole shells/g is at its lowest (approximately 0). Outside of this interval of dissolution (Figure 2.16; where the abundances are shown as a solid line, i.e. outside of the 403-410 kyr interval) we have confidence in the data; in particular the timing of the onset of the 'warm' species peak. Prior to, and during the early onset of the increase in warm species (approximately 441 kyr) *G. bulloides* and *T. quinqueloba* (ranked 8/22 and 9/22 respectively for susceptibility (Berger, 1970)) are also preserved in the assemblage. As all these species are susceptible to dissolution (and have very different environmental preferences) their simultaneous presence suggests that the onset of the large *G. ruber* peak is a true signal rather than an alteration of the assemblage by dissolution. Also during this interval, the proportion of *G. bulloides* (ranked 8/22 for susceptibility (Berger, 1970)) is greater than the proportion of *G. inflata* (ranked 14/22 (Berger, 1970)) suggesting that the record is not heavily influenced by dissolution. Furthermore during this interval of very high *G. ruber* percentages, species diversity is also relatively high (approximately 10 different species in the assemblage), again suggesting that the assemblage has not been altered by dissolution, preserving a diverse range of different species. At approximately 427 kyr the proportion of both *G. ruber* and *G. bulloides* decreases at the same time we record an increase in the percentage of *G. inflata* (from about 5 to 60% of the assemblage). As the abundance of any given species is dependent upon the presence/absence of all other species this simultaneous change is not a surprise. We suggest that dissolution is altering the record from this point forward as the reduction in the abundance of two susceptible species to dissolution (*G. ruber* and *G. bulloides*) is replaced by the presence of a more robust species (*G. inflata*). As discussed in the previous paragraph we are able to confidently constrain the onset of the warming by the presence of *G. ruber*. However as the presence of large abundances of *G. inflata* indicates dissolution the end of the warm period is harder to constrain.

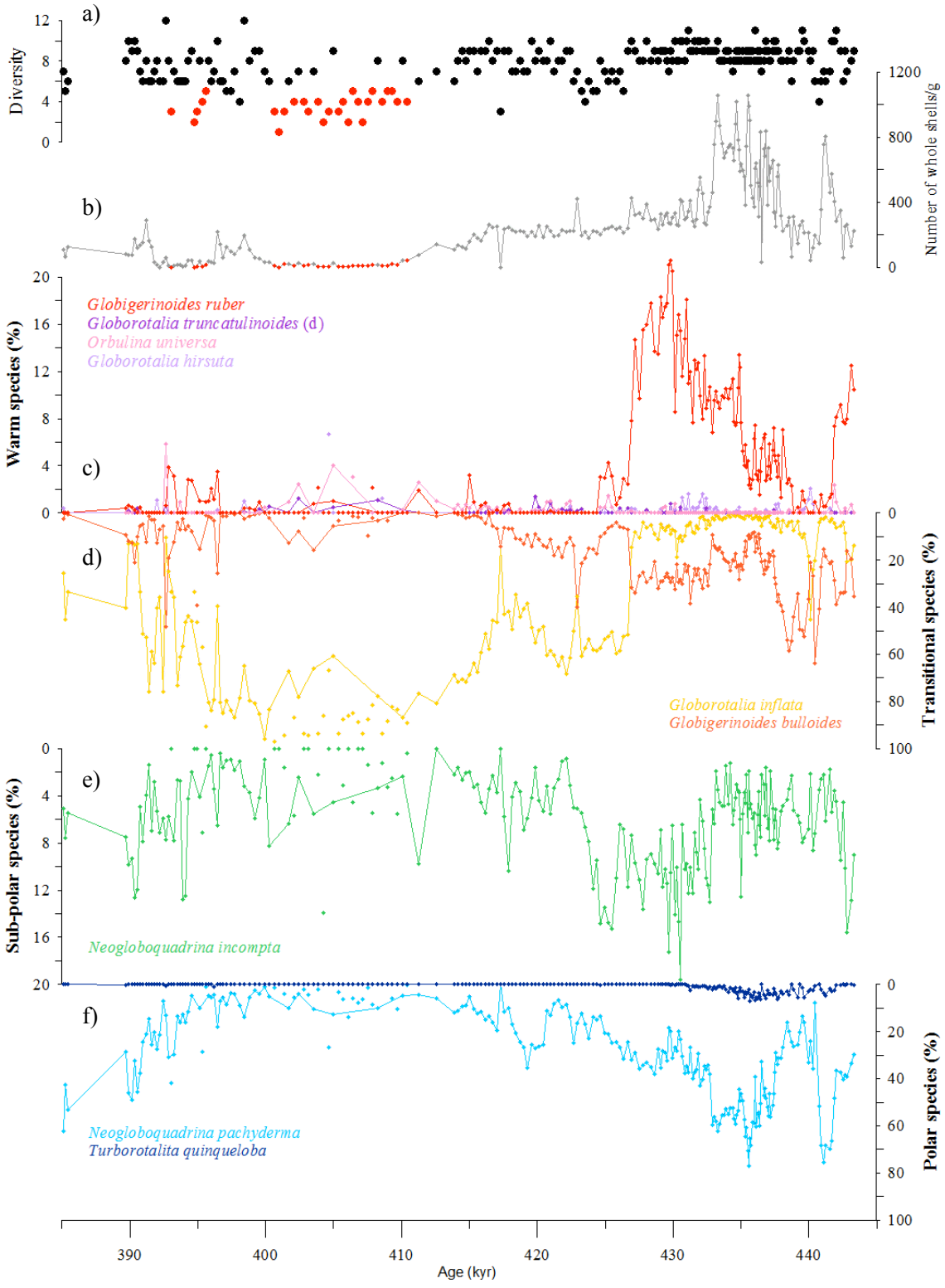

Figure 2.16. Evaluation of dissolution on the planktonic assemblages across T5; the species are divided in to their groups; warm (c), transitional (d), sub-polar (e) and polar species (f). The individuals species are plotted – top to bottom; red: G. ruber; purple: G. truncatulinoides; pink: O. universa; purple: G. hirsuta; yellow: G. inflata; orange: G. bulloides; green: N. incompta; dark blue: T. quinqueloba; and light blue:

N. pachyderma (s). Plot (a) shows the number of whole shells/g, samples with less than 50 whole shells/g highlighted in red; and plot (b) shows the species diversity, samples with species diversity <6 highlighted in red.

The work carried out by Joanna Langhelt (T2; ODP Site 1089) does not allow for a similar analysis of the potential alteration of the record by dissolution as only two species of foraminifera were counted (Figure 2.16). However, as we have the same species counts for both T5 and T1 we are able to make inferences in the magnitude of events across all three terminations. In the first part of the record from approximately 138-128 kyr the concentration of whole shells varies between 1000-5000 per gram and the fragmentation is low (typically varying between 10-30%). Based on our three rejection criteria for dissolution (see section on Evaluation of foraminferal assemblages/dissolution) none of the samples from this interval would be rejected. Of the 150 samples that were counted; only two of them have less than 100 whole shells/g and none of them have less than 50 whole shells/g (Figure 2.). Given that the whole shells/g record does not fall below our threshold value of 50 whole shells/g and the % fragmentation record is never greater than 75% fragmented we are confident that this record has not been heavily altered by dissolution. Furthermore, 75% fragmentation does not mean that 75% of the shells have broken as each individual foraminifera breaks into more than one fragment (Le and Shackleton, 1992). Using the fragmentation calculation from Le and Shackleton (1992) who suggest that an individual foraminifera breaks in to 8 pieces, we record a lower percentage of fragmentation (maximum 27%). We note, however, that there is an increase in fragmentation and decrease in the number of whole shells from 128kyr onwards. Although the number of whole shells does not fall below our threshold value (<50 whole shells/g) it is likely based on our findings from T5, that the assemblage is dominated by *G. inflata* (a species that is more resistant to dissolution). That said, the transition from MIS 6 to MIS 5 appears to be unaffected by dissolution.

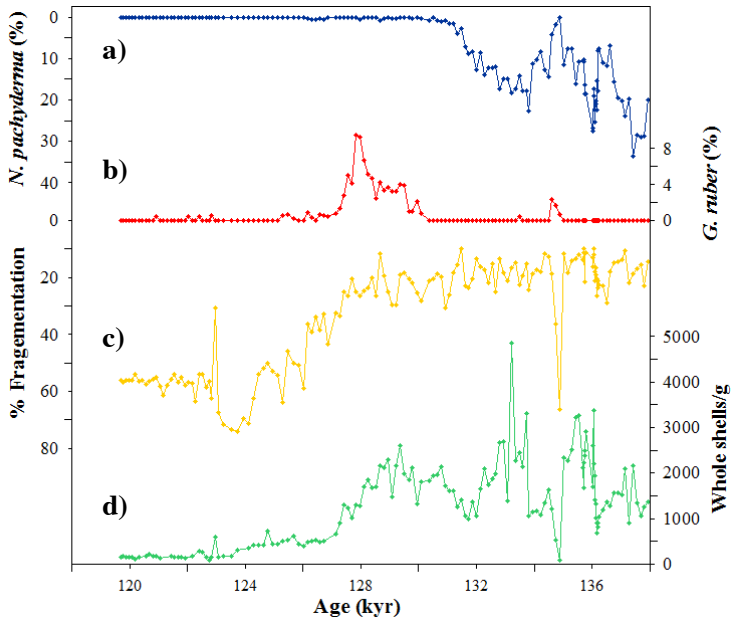

Figure 2.19. T2 faunal assemblages and preservation indices; a) N. pachyderma (%); b) G. ruber (%); c) % fragmentation; and d) whole shells/g. Data generated by J. Langhelt and analysed here.

2.8 EVALUATION OF SST ESTIMATES

The summer SST (SSST) reconstruction using MAT analysis (Figure 2.17) highlights the structure of the deglacial interval for MIS 12 to MIS 11. The temperature reconstruction ranges between 6-23°C. The modern annual sea surface temperatures recorded in the top 10m at this core location range between 10.5-15.2°C (Locarnini et al., 2013).

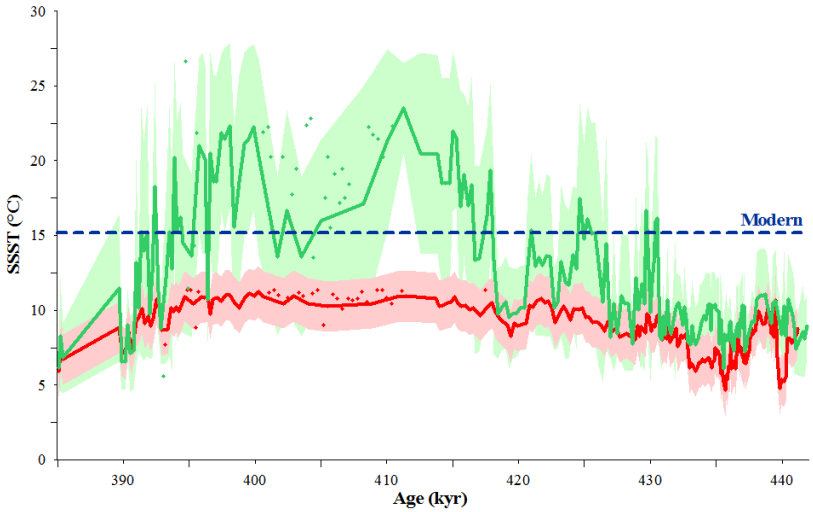

Figure 2.17. Summer SST reconstructions made using the MAT analysis run using the program Analog (Hutson, 1980; Overpeck et al., 1985; Prell et al., 1999) shown in

green. Reconstructions based on core-top analogues from the ocean, the individual points highlight the samples that have been removed due to dissolution (see preceding section). The corresponding coloured envelopes highlight ± 1 standard deviation from each sample. SST reconstruction based on the relative abundance of N. pachyderma (Govin et al., 2009) shown in red, again the individual points highlight the samples that have been removed due to dissolution. The red envelope highlights the error of ± 1.7°C (Govin et al., 2009). The dashed blue line indicates the modern SSST of 15.2°C in the South Atlantic (Locarnini et al., 2013).

Although the peak interglacial values from the reconstruction are higher than the modern temperature range recorded at ODP Site 1089, these higher temperature occur mostly during the interval of greatest dissolution (see sections above) and as such are dominated by the presence of *G. inflata* and are likely to be overestimated. For the most part, the SST reconstruction provides realistic temperatures compared to modern day conditions.

The SST reconstruction method based on using the relative abundance of *N. pachyderma* yields lower SSTs on average for the interval when compared to the MAT analysis (above) (Figure 2.17), likely the result of recording annual mean SST as apposed to SSST; the temperature ranges are 6-20°C and 4-11°C respectively. Although the minimum temperatures are similar for both reconstructions the maximum temperatures from the % *N. pachyderma* SST reconstruction are lower than the modern summer SST at the core location (approximately 15°C (Locarnini et al., 2013). The SST estimates based on the MAT analysis method uses all the information we have available regarding the planktonic foraminiferal assemblages and as such produces more reliable SST reconstruction (albeit not without the potential to over-estimate temperatures (Vázquez Riveiros et al., 2010, 2013)) when compared to only using one indicator species.

2.9 SST AND FAUNAL ASSEMBLAGE ANALYSIS AND RESULTS

Comparison of the three terminations (T1, T2 and T5) in the South Atlantic is discussed in the following section; this results section shall focus on the SST reconstruction and the corresponding changes in the foraminiferal faunal assemblage.

The SST reconstruction (Figure 2.18) based on the faunal assemblage suggests a long-term change in the temperature record. A change from cold glacial conditions during the early part of Marine Isotope Stage (MIS) 12 (approximately 442-431 kyr) is recorded, followed by a deglacial interval (426.9 - 434.50 kyr). The deglacial interval is accompanied by a *G. ruber* peak (Figure 2.18). Following this interglacial conditions and associated higher temperatures are recorded during MIS 11 (approximately 427 kyr onwards). At the onset of MIS 11 (424kyr (Lisiecki and Raymo, 2005)) we record the coexistence of *N. pachyderma* and *G. ruber* in a several samples. After the deglacial event we record an assemblage that is mainly dominated by *G. inflata*. From approximately 394kyr onwards we record an increase in *N. pachyderma*.

The SST values range from 6.1°C to 23.5°C across the interval (Figure 2.18); representing the glacial-interglacial amplitude across Termination 5 at ODP Site 1089. Within the glacial-interglacial variability we also observe large millennial scale oscillations in our record; notably across the extreme glacial conditions of MIS 12 and transition to MIS 11 and at the end of our record (towards the end of MIS 11) where we see a return to lower temperatures (and an increase in *N. pachyderma*) (Figure 2.18).

One of the most interesting features of our record is the very large *G. ruber* peak that occurs early in termination (starting before the benthic $\delta^{18}O$ decrease) between 426.9 and 434.50 kyr) (we shall refer to this interval as the 'deglacial' event). During this interval the *G. ruber* abundance peaks at just over 21% and at the same time there is the coexistence of both *G. ruber* and *N. pachyderma* in the same samples. Despite this very large peak in *G. ruber* during the deglacial transition from MIS 12 to MIS 11 the corresponding SST reconstruction (MAT analysis) is relatively low (the average SST for the interval is 10.1°C), likely as a result of the simultaneous presence of *N. pachyd*erma. As well as the deglacial interval (peak *G. ruber* abundance) there is a short maximum of similar temperature maximum (approximately 17°C) during the peak interglacial interval (410.1 – 417.6 kyr) of MIS 11 when there is a near absence of *G. ruber*. The SST reconstruction must be getting its 'warm' signal from another species during the interglacial interval and/or the SST reconstruction is colder due to the presence of *N. pachyderma* during the deglacial interval.

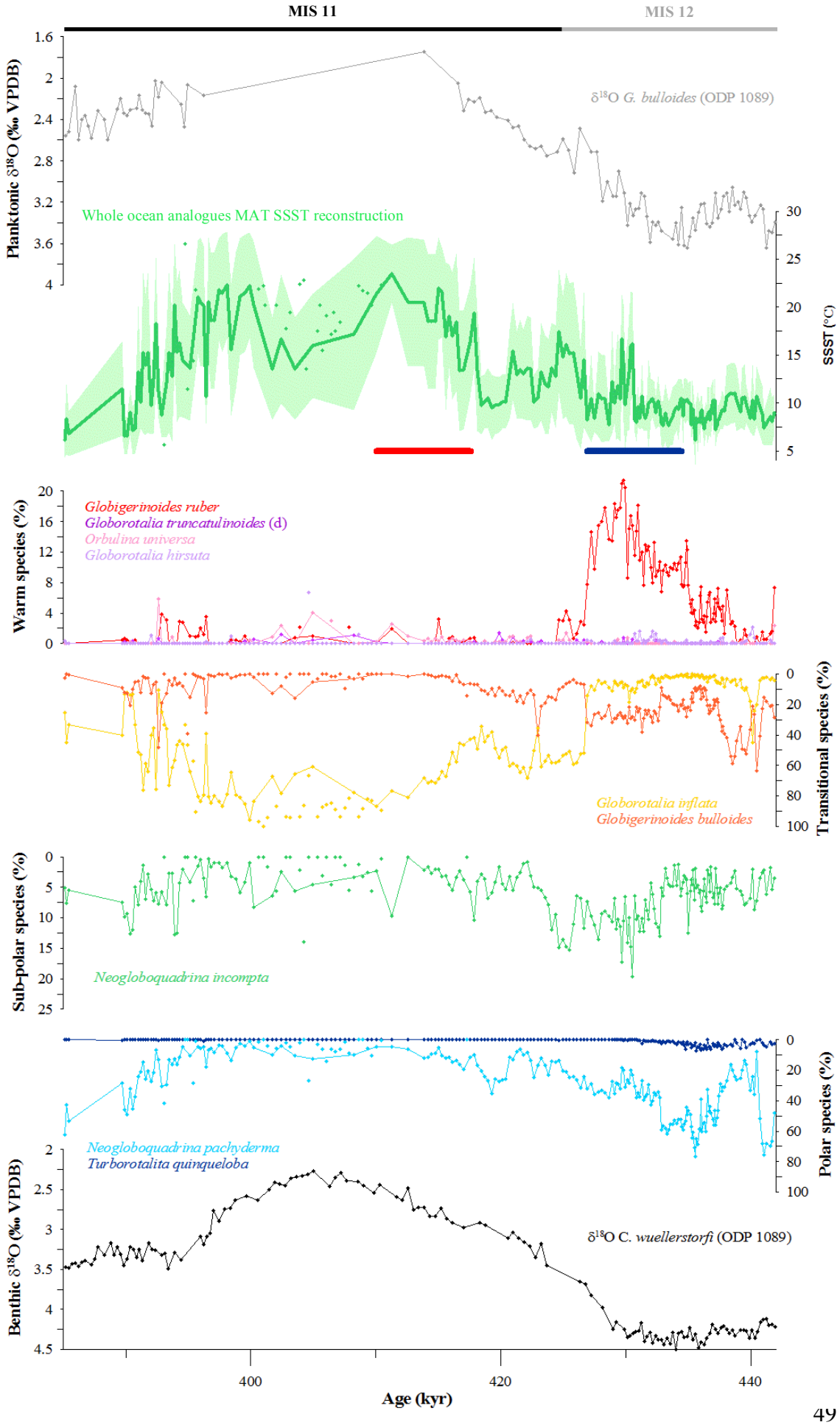
MIS 11
MIS 12
Planktonic δ18O (‰ VPDB)
δ18O G. bulloides (ODP 1089)
Whole ocean analogues MAT SSST reconstruction
SSST (°C)
Warm species (%)
Globigerinoides ruber
Globorotalia truncatulinoides (d)
Orbulina universa
Globorotalia hirsuta
Transitional species (%)
Globorotalia inflata
Globigerinoides bulloides
Sub-polar species (%)
Neogloboquadrina incompta
Polar species (%)
Neogloboquadrina pachyderma
Turborotalita quinqueloba
Benthic δ18O (‰ VPDB)
δ18O C. wuellerstorfi (ODP 1089)
Age (kyr)

Figure 2.18. Individual planktonic foraminiferal records compared to the SST reconstructions from MAT analysis (green). The thick red and blue lines indicate the intervals used in the closest analog analysis, interglacial and deglacial intervals respectively. The grey plot is the planktonic $\delta^{18}O$ of G. bulloides from ODP Site 1089 (Hodell et al., 2003b). The species are divided in to their groups: warm, transitional, sub-polar and polar species. The individual species are plotted – top to bottom; red: G. ruber; purple: G. truncatulinoides; pink: O. universa; purple: G. hirsuta; yellow: G. inflata; orange: G. bulloides; green: N. incompta; dark blue: T. quinqueloba; and light blue: N. pachyderma (s). Benthic $\delta^{18}O$ of C. wuellerstorfi from ODP Site 1089 (Hodell et al., 2003b) is shown in black.

During the deglacial event (426.9 - 434.50 kyr) we record the simultaneous presence of both *G. ruber* (tropical to sub-tropical species) and *N. pachyderma* (subpolar to polar species) (Hemleben et al., 1989). The coexistence of both these species is unusual and we suggest that there are two possibilities for this; 1) extreme seasonality within a particular year; in the modern ocean *G. ruber* and *N. pachyderma* coexist only in areas of upwelling in the Arabian Sea (Ivanova et al., 1999), off of Java (Mohtadi et al., 2009) and in the North Pacific (Kuroyanagi et al., 2002; Mohiuddin et al., 2005). Given the distance of ODP Site 1089 from an upwelling area and the modern day seasonal SST range of 4.7°C this is unlikely; and 2) inter-annual shifts in the front systems. The record is sampled (on average) at approximately 200-year intervals (integrating approximately 125 years in a single sample) and as such *N. pachyderma* and *G. ruber* could have existed within the same decade or century and would still be integrated in the same sample.

We suggest that the coexistence of these two species with very different environmental preferences suggests a very dynamic frontal system at this core location in the South Atlantic which results in shifts in the Subtropical Front to the north and south of ODP Site 1089 over sub-millennial time scales. Based on the information provided by the analogs used to produce the SST reconstruction we take this analysis further; we compared the location of the average analog (average of the 10 closest analogs) for each of the samples within these two different intervals (*G. ruber* deglacial event; 426.9 - 434.50 kyr and the interglacial interval of MIS 11; 410.1 – 417.6 kyr). The results of

this comparison provide us with a crude proxy of where similar conditions are present in the modern ocean and as such where similar assemblages can be found today.

The results of this analysis (Figure 2.19) show that there is a clear difference in the location of the samples in the modern ocean with a near similar assemblage during the two intervals; firstly, the interglacial interval peak shows that the nearest analogs cluster in the Indian Ocean (perhaps suggesting an influence of Indian Ocean Waters (Peeters et al., 2004)). Secondly, during the deglacial period (*G. ruber* peak) between MIS 12 and MIS 11 (426.9 – 434.5 kyr), the analogs are clustered in the equatorial Atlantic but with spread across the whole of the Atlantic. This suggests that during the interglacial interval warm surface waters coming in from the Indian Ocean influenced the surface waters above ODP Site 1089. Conversely, during the deglacial interval (where we record high abundance of *G. ruber*), we record assemblages much more Atlantic-like in composition; suggesting that there is a southward contraction of the thermal fronts in the South Atlantic/Southern Ocean region resulting in warmer assemblages being bought here from the subtropical Atlantic.

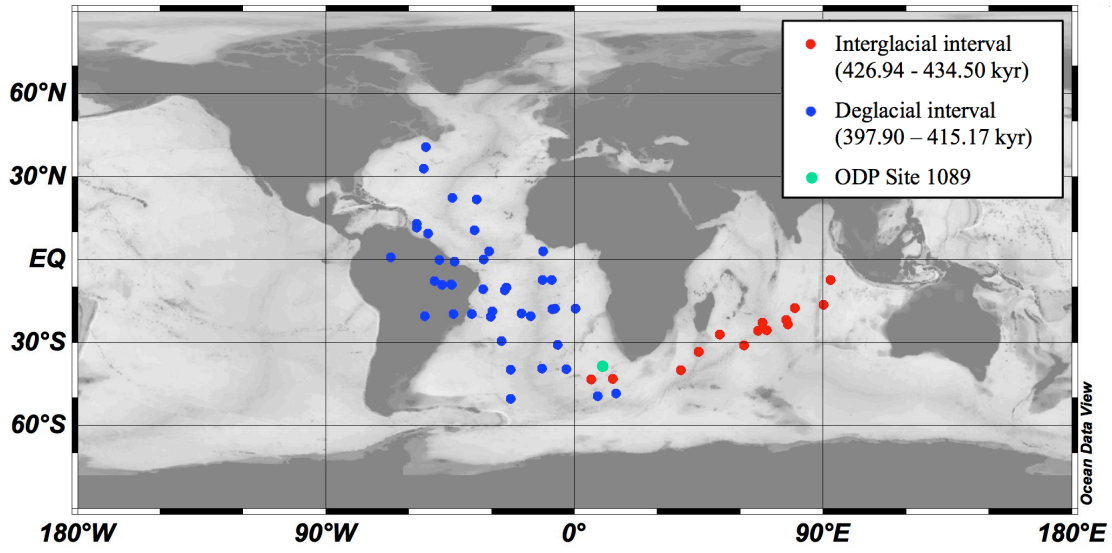

Figure 2.19. Average position of the 10 closest analogs in the Whole Ocean used for SST reconstruction (MAT analysis). The colours denote the interval from which the samples were taken; deglacial interval (426.9 - 434.50 kyr) (blue); peak interglacial of MIS 11 (410.1 – 417.6 kyr) (red). The green circle indicates the location of ODP Site 1089.

2.9.1 CONFIRMING ALIGNMENT OF SOUTH ATLANTIC CORES ACROSS TERMINATION 1

In order to be able to compare the new data from ODP Site 1089 with nearby core locations in the South Atlantic we confirmed the alignment of three cores from the South Atlantic. The cores that were aligned to each other are; ODP Site 1089 (Hodell et al., 2002, 2003a, 2003b), Site RC11-83 (41.6°S, 9.7°E, 4718 m water depth) (Charles et al., 1996) and TN057-21 (41.1°S, 7.8°E, 4981 m water depth) (Ninnemann et al., 1999; Sachs and Anderson, 2005; Barker et al., 2009, 2010; Barker and Diz, 2014). Previously (Barker and Diz, 2014) aligned these records using $CaCO_3$ content; placing the records from ODP Site 1089 (Hodell et al., 2002, 2003a, 2003b) and Site RC11-83 (Charles et al., 1996) on a common depth scale from TN057-21. We have plotted these records on the radiocarbon-based age model for TN057-21 (Barker et al., 2009) and compared the records from the three cores (Figure 2.20). The benthic $\delta^{13}C$ records from all three of these cores (TN057-21, RC11-83 and ODP Site 1089) have previously been interpreted (at least in part) to reflect variations in water mass mixing between northern and southern sources of deep water within the Atlantic basin. There is an offset in the benthic $\delta^{18}O$ between the three cores (on average < 0.5‰) likely the result of different water depths of the cores given the close proximity of their locations; TN057-21 is located the deepest of the three cores and has the largest benthic $\delta^{18}O$ values. However, we are able to confidently align the records according to their $CaCO_3$ content allowing us to use the timing of changes in the records further back in time (T5).

Agreement of the planktonic $\delta^{18}O$ records from both TN057-21 (Barker et al., 2009) and ODP Site 1089 (Hodell et al., 2003b) suggest that the core locations are close enough to have been influenced by similar (if not the same) local salinity and temperature changes across this interval. As all the benthic $\delta^{13}C$ (TN057-21 (Ninnemann et al., 1999); RC11-83 (Charles et al., 1996); ODP Site 1089 (Hodell et al., 2003b) and planktonic $\delta^{18}O$ records align well with each other providing us with evidence that these cores are in close enough proximity to each other to allow us to use them interchangeably with each other.

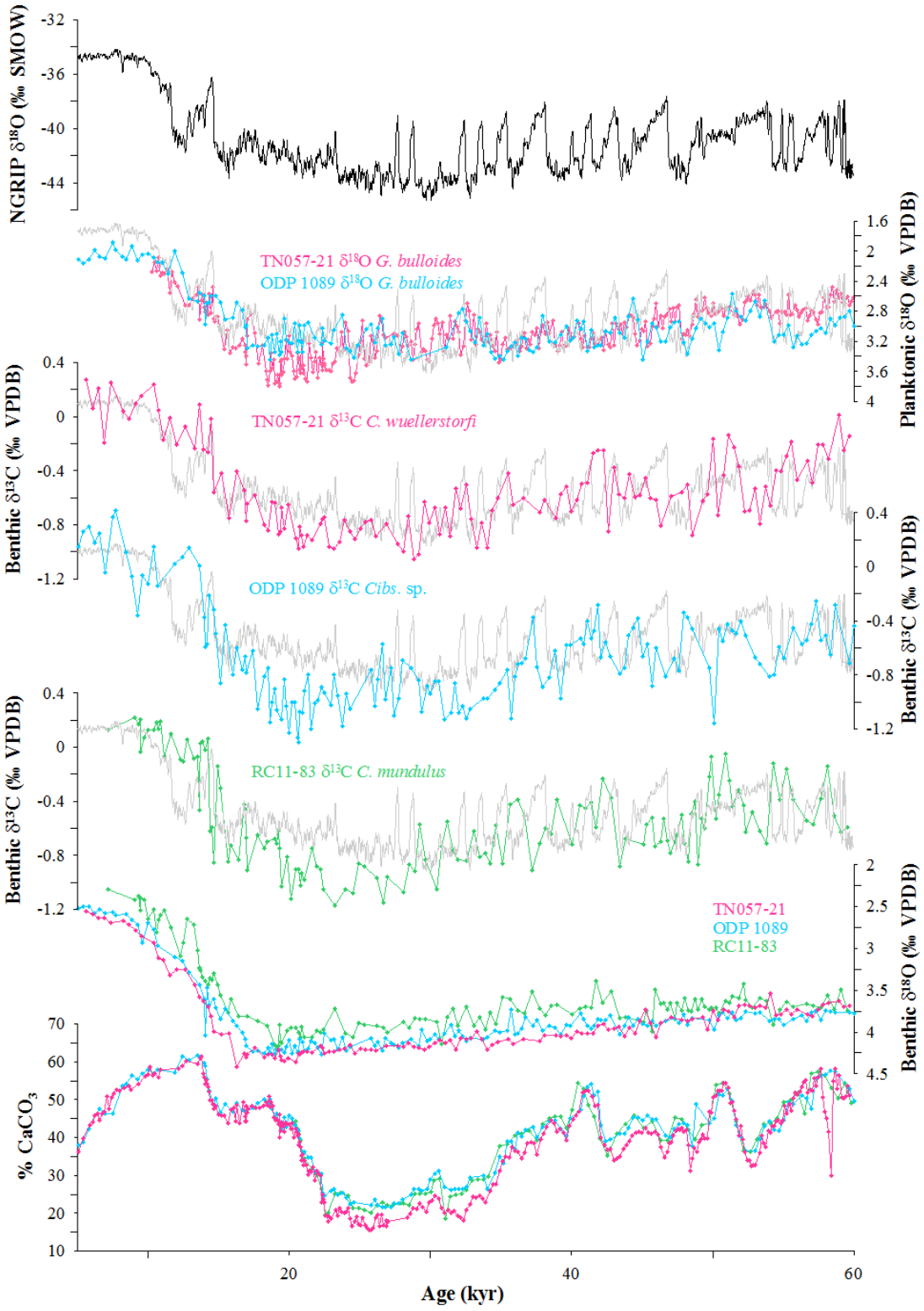

Figure 2.20. Comparison of records from the South Atlantic; TN057-21, ODP 1089 and RC11-83 across T1. The records were placed on a common depth scale (TN057-21), by tuning their $CaCO_3$ records together by Barker and Diz (2014 - see supplementary material) and we have assigned ages to the record using the radiocarbon age model from Barker et al., (2009). NGRIP record (black) for

reference (NGRIP Members, 2004); planktonic $\delta^{18}O$ records from TN057-21 (Barker et al., 2009) and ODP Site 1089 (Hodell et al., 2003b); benthic $\delta^{13}C$ and $\delta^{18}O$ from TN057-21 (Ninnemann et al., 1999); RC11-83 (Charles et al., 1996) and ODP Site 1089 (Hodell et al., 2003b); the % CaCO3 records from TN057-21 (Sachs and Anderson, 2005); RC11-83 (Charles et al., 1996) and ODP Site 1089 (Hodell et al., 2003b).

2.9.2 SST RECONSTRUCTIONS FROM THE SOUTH ATLANTIC (T5)

In this section we compare two proxies for SST reconstruction from ODP Site 1089, MAT analysis (this study) and a radiolarian-based reconstruction (Cortese et al., 2007); and two proxies from core PS2489-2, MAT analysis (Becquey and Gersonde, 2002) and an alkenone-based reconstruction (Martínez-Garcia et al., 2010). The comparisons of the SST reconstructions from the South Atlantic are shown in Figure 2.21.

Both the SSST records produced from MAT analysis across T5 at ODP Site 1089 (green) and site PS2489-2 (orange) show a similar overall pattern (Figure 2.21). They show colder temperatures during MIS 12 (approximately 6°C and 4°C respectively) with a transition to interglacial conditions by MIS 11 (approximately 22°C and 19°C respectively); the records are offset from each other by approximately 3-4°C throughout the record, to be expected given that ODP Site 1089 is further north than site PS2489-2 and the modern day offset in SST is approximately 3°C between the two sites (Locarnini et al., 2013). It should be noted that the authors of the SSST reconstruction from PS2489-2 (Becquey and Gersonde, 2002) suggest an over-estimation of the temperatures during MIS 11 and thus it is likely that the temperatures during this interval produced in this study likely overestimate the interglacial temperatures too. Following MIS 11, both records show the beginning of a cooling in temperature towards glacial values again (Figure 2.21). The duration of the warm interval (early MIS 11) is shorter at site PS2489-2 than at ODP Site 1089; we hypothesise this is a result of the close proximity of site PS2489-2 to the Polar Front surrounding the Antarctic. During this interglacial period, the record from ODP Site 1089 shows a slight decrease in temperature by about 4°C; we suggest that this cooling is an artefact of dissolution of the record. This decrease in temperature occurs during the period of greatest dissolution in the record and as such, the cooling is a result of a bias of these remaining samples that have potentially been slightly impacted by dissolution, which

would result in the warm, less resistant species partially being dissolved, leaving a slightly colder assemblage and a decrease in the SSTs during this interval.

Although we do not record an increase in the SSST reconstruction in line with our increase in *G. ruber,* likely the result of the simultaneous presence of *N. pachyderma*, the alkenone SST reconstruction from PS2489-2 (Martínez-Garcia et al., 2010) does indicate a warming at the same time as our inferred peak warming event (*G. ruber* peak) at ODP Site 1089 (430 kyr) (Figure 2.21).

When compared to subsequent terminations, the MAT SST reconstructions from PS2489-2 (Becquey and Gersonde, 2002) and from this study (ODP Site 1089) appear to overestimate the temperatures during MIS 11 (19°C for MIS 11; compared to 12°C for MIS 5 and the Holocene; (this study; MIS 11 and Becquey and Gersonde, (2002); MIS 5 and Holocene) (Figure 2.21). During MIS 11 the assemblage is dominated by *G. inflata* which thrives in temperatures between approximately 15-18°C). As previously mentioned, the dominance of *G. inflata* in an assemblage is indicative of dissolution and as such the overestimation of temperatures during this interval is likely the result of dissolution of the assemblage.

Although the SSST reconstruction produced during this study appears to overestimate temperatures during MIS 11, we suggest that this is the result of dissolution (and hence dominance of *G. inflata* in the assemblage). Furthermore, when comparing the temperatures during the rest of the record, there is good agreement with the annual range of temperatures at the core location. We reconstruct temperatures well below the modern SSST during MIS 12 and following the transition to interglacial conditions, the SSST reconstruction suggests that the temperatures during MIS 11 are near to, if not slightly warmer than, modern day SSST. We suggest that the presence of the *G. ruber* peak at the onset of the transition from MIS 12 to MIS 11 indicates at least intermittently warm conditions in the South Atlantic.

2.9.3 SYNTHESIS OF PLANKTIC RECORDS ACROSS TERMINATIONS 1, 2 AND 5 AT ODP SITE 1089

Comparison of records for Terminations 1, 2 and 5 in the South Atlantic/South Ocean (T1; core site TN057-21 and T2/T5; core site ODP 1089) shows similarities and

differences in both magnitude and timing of key events across terminations (Figure 2.23). The first and most notable difference is in the magnitude and duration of the warm event during the terminations; during T5 we record up to 22% warm species, during T2 10% (note this is only *G. ruber* as the full assemblage was not counted) and T1 reaches just 7%. For T5 this increase is predominately controlled by an increase in the abundance of the most dissolution susceptible warm species, *G. ruber*. Conversely during T1 the peak is dominated by *O. universa* (Figure 2.23). Not only is the magnitude of the warm species (*G. ruber*) peak much larger in T5 compared to T1 and T2, but the duration of the peak is also much larger; lasting approximately 6 kyr in total compared to 3.5 kyr for T2 and 3 kyr for T1. We should note that as we are less able to constrain the end of the warm period due to the potential dissolution control at the end of the warm peak. The duration of this warm peak during T5 (and indeed T2 and to a lesser extent T1 also) could be longer than the *G. ruber* record suggests (Figure 2.23). Based on the large difference we record between T1 and T5 in the abundance of warm species it is likely that the deglaciation transition between MIS 12 and MIS 11 (T5) was more dynamic than the transition from MIS 2 to the Holocene (T1) and from MIS 6 to MIS 5 (T2) as there is the coexistence of both *G. ruber* and *N. pachyderma* within the same samples across this interval.

When we consider the other fauna in the assemblage there are notable differences here too; firstly T5 again, has a much larger change in magnitude of polar species (specifically *N. pachyderma*) across the transition from MIS 12 to MIS 11 from nearly 80% to <10% in 12 kyr. The very cold interval of MIS 12 has previously been identified by Bard and Rickaby, (2009) for example. Terminations 1 and 2 reach a maximum of 40% and 35% respectively for *N. pachyderma*. The lower abundance of *N. pachyderma* during T1 suggests that MIS 2 was a less extreme cold interval than MIS 12, indeed the assemblage from MIS 2 is warmer than that of MIS 12. During T1 *T. quinqueloba* reaches abundances of 30% which when combined with *N. pachyderma* is closer to the magnitude of change we observe in polar species across T5, albeit of a different faunal composition. That said, given that the proportion of polar species is slightly lower during T1 at the onset of the termination and the abundance of warm species reaches a larger magnitude during T5, the change recorded across the termination is much larger for T5 than it is for T1. T2 also records smaller abundances of *N. pachyderma* (35%) when compared to T5. Without the full assemblage we are

unable to assess the full magnitude of the change in both polar (and warm) species across this interval. However, when comparing the magnitude of events using just *G. ruber* and *N. pachyderma* we can say that the magnitude of both the cold glacial interval (proportion of *N.pachyderma*) and warming peak (proportion of *G. ruber*) during the transition to the interglacial that T5 is much larger than both T2 and T1.

Not only do we record differences in the magnitude and duration of events across these three terminations there are also significant differences in the timing of the changes with respect to benthic $\delta^{18}O$. Terminations 1 and 5 appear to be more closely aligned in terms of timing; both terminations record the peak in warm species early in the termination, just as the benthic $\delta^{18}O$ begins to decrease, however, the equivalent peak in *G. ruber* during T2 occurs much later in the termination just before the peak in the benthic $\delta^{18}O$. The duration of the warm species peak in T5 is much longer than for T1 and T2, the onset of the warming in the surface waters to occur approximately 5-6 kyr before the onset of the termination as defined by the decrease in benthic $\delta^{18}O$ from Lisiecki and Raymo (2005). We also record differences in the timing of the *G. bulloides* $\delta^{18}O$ and warm species peak; again, the timing of events across T1 and T5 are more similar. We record the peak in warm species to occur just as we see a decrease in the planktonic $\delta^{18}O$. Although both records are recording surface water conditions, the planktonic $\delta^{18}O$ record from *G. bulloides* only tells us about the surface ocean conditions when *G. bulloides* is present whereas the assemblage records a longer-term average of what is going on in the surface ocean which is measured relative to all other species in the assemblage too.

The composition of the assemblage also varies between the terminations and tells us something about the conditions in the surface waters; Terminations 1 and 2 generally record either a presence of polar species with an absence of warm species or vice versa. T5 however, records the simultaneous presence of both *G. ruber* and *N. pachyderma* in the same interval (indeed in the same samples). This coexistence of these two species that have differing environmental preferences suggests that during T5 the surface waters in the South Atlantic were much more dynamic.

We suggest that on millennial timescales the mechanism for invoking these dynamic conditions in the South Atlantic across all terminations is likely a change in the dominance of water masses in the surface ocean. More specifically changes in the

latitudinal position of the frontal systems in the South Atlantic result in very different water masses dominating the surface ocean over ODP Site 1089 over very short periods of time. We suggest (in line with previous studies (e.g. Barker et al., 2009)) that a reduction in the northward heat transport (reduction in the strength of the AMOC) results in a contraction of the frontal system in the South Atlantic and is an expression of the (instantaneous) bipolar seesaw.

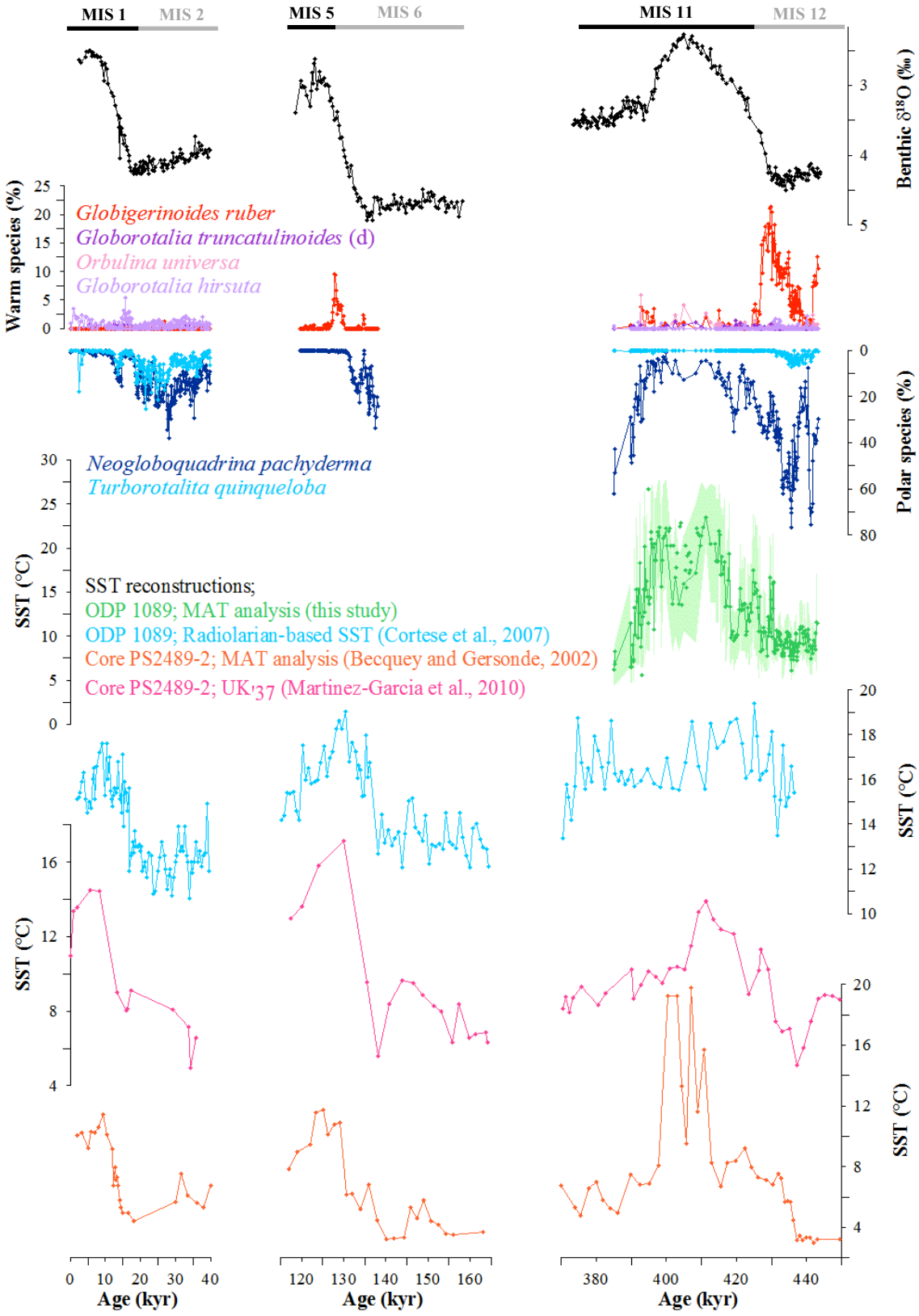

Figure 2.21. Regional South Atlantic comparison (ODP Site 1089 and site PS2489-2) for all terminations (T1, T2 and T5). SST reconstructions produced by Cortese et al., (2007) (light blue); Becquey and Gersonde (2002) (orange); Martinez-Garcia et al.,

(2010) (pink); and MAT analysis for T5 (this study) (green); the error window of ± 1 standard deviation is shown in light green. The faunal records are shown across the terminations; G. ruber (red); G. truncatulinoides (d) (dark purple); O. universa (pink); G. hirsuta (light purple); N. pachyderma (dark blue); and T. quinqueloba (light blue). All records from T1 are from TN057-21 (Barker and Diz, 2014); and ODP 1089 for T2 and T5 (this study). Benthic $\delta^{18}O$ is shown for reference (Hodell et al., 2003b; Barker and Diz, 2014).

2.10 NORTH AND SOUTH ATLANTIC EXPRESSION OF THE BIPOLAR SEESAW; IS T5 EXTREME?

In order to assess the variability of the bipolar seesaw in the Atlantic during T5 we compare cores from the North and South Atlantic (ODP Sites 983 in the North Atlantic and ODP 1089 in the South Atlantic). We compare the percentages of *N. pachyderma* and the concentration of coarse ice-rafted debris (IRD) from the North Atlantic, which indicates freshwater input through ice melting.

Here we suggest that the extreme warm event (*G. ruber* peak) during T5 and the extreme cold event (as indicated by the large IRD event) in the North Atlantic (Figure 2.22) are probably an expression of a weakened AMOC; Figure 2.23 shows that this *G. ruber* peak (red) (and associated warm SST (green)) at ODP Site 1089 coincides with the intense cold conditions in the North Atlantic at ODP Site 983 (shown by the large abundances of both *N. pachyderma* and IRD grains/g). We suggest that the 'extreme' nature of both of these events during late MIS 12 is not a coincidence, and is instead, the most northerly and southerly (latitudinally extreme) expression of the instantaneous bipolar seesaw as has been previously recorded for T1 (Barker et al., 2009). These apparent 'extreme' results from T5 are further corroborated when we look at the same records from the later terminations. Although, the abundance of *N. pachyderma* at ODP Site 983 in the North Atlantic is similar during each respective glacial interval (90-100% of the assemblage), the IRD record suggests that the Heinrich stadial event of MIS 12 in the North Atlantic is colder (larger numbers of IRD grains/g) than either MIS 6 (T2) or MIS 2 (T1). Comparison of these cold conditions in the North Atlantic with the faunal record in the South Atlantic further highlights the 'extreme' nature of Termination 5, recording much larger peaks in IRD grains/g in the north and *G. ruber* in the south.

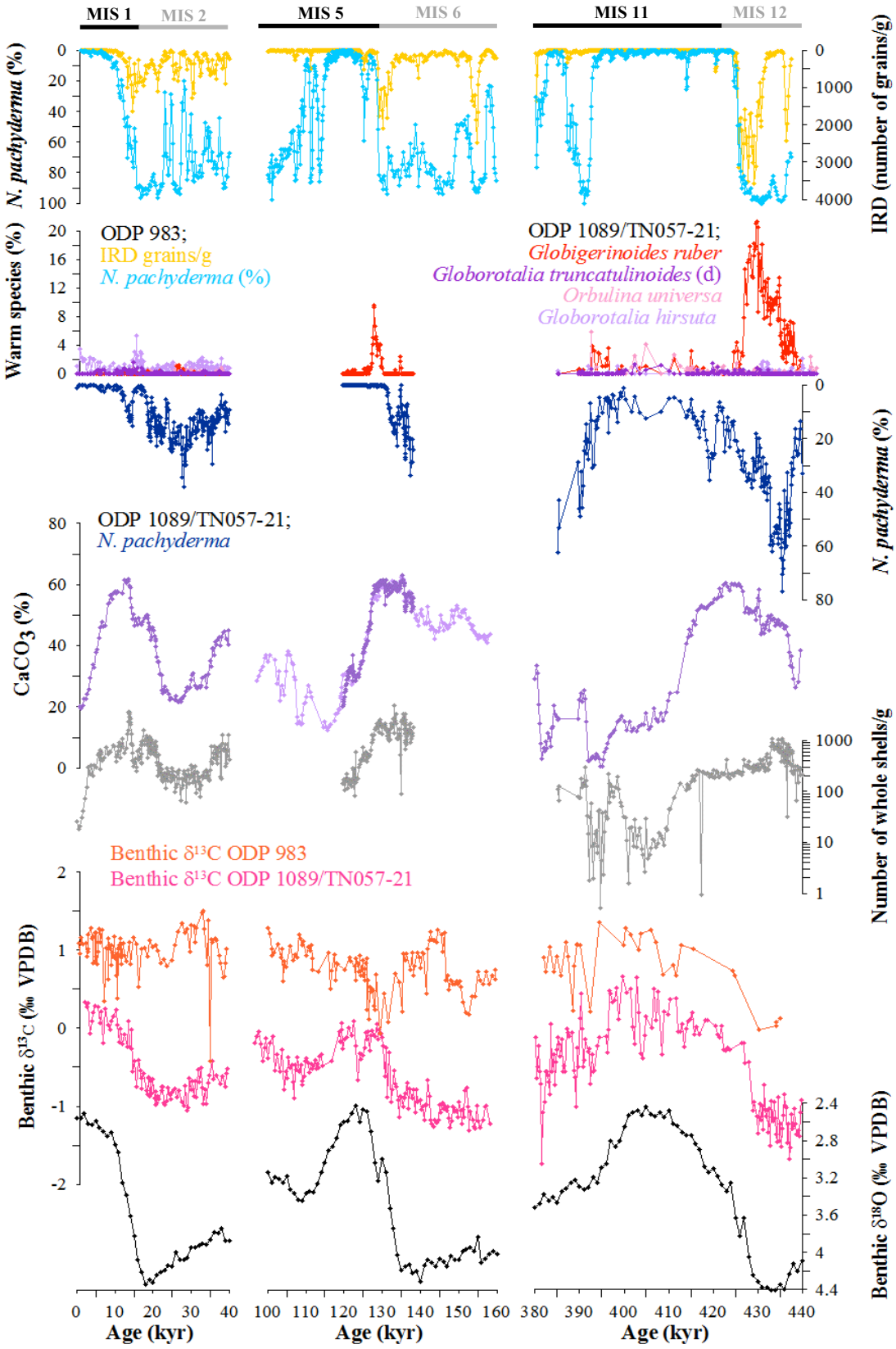

Figure 2.22. North and South Atlantic comparison across T1, T2 and T5. ODP Sites 983 (North Atlantic). % N. pachyderma and IRD grains/g; (Barker et al., 2015)); blue and yellow respectively. ODP Site 1089/TN057-21 in the South Atlantic.

Planktonic foraminiferal faunal records from this study across T5 and T2 and data from Barker et al., (2009) and Barker and Diz (2014) across T1. The purple plot indicates the %$CaCO_3$ across the three terminations; for all terminations from Hodell et al., (2003a). CaCO3 data from T2 and T5 are from this study (dark purple) and from Hodell et al., 2003a (light purple). The records of whole shells/g are from Barker and Diz (2014) for T1 and from this study for both T2 and T5. Benthic $\delta^{13}C$ records for the North Atlantic (ODP 983) from Raymo et al., (2004) and for the South Atlantic for T1 from Ninneman et al., (1999) and for T2 and T5 from Hodell et al., (2003a). The black plot at the bottom is the benthic $\delta^{18}O$ LR04 stack for reference (Lisiecki and Raymo, 2005).

2.11 DEEP WATER/PRESERVATION PROXIES

2.11.1 BENTHIC $\delta^{13}C$

Benthic $\delta^{13}C$ has been used to infer changes in mixing between deep waters of southern versus northern sources in the Atlantic Ocean (Oppo and Fairbanks, 1987; Curry et al., 1988; Charles and Fairbanks, 1992; Charles et al., 1996; Ninnemann et al., 1999; Shackleton et al., 2000; Piotrowski et al., 2005) and can be used to trace the origin of water masses and infer changes in the geometry of the AMOC over time (e.g. Duplessy et al., 1988; Shackleton et al., 2000). As primary producers take up nutrients and carbon in the surface water they preferentially remove ^{12}C resulting in the surface waters being enriched in ^{13}C; when they remineralise at depth, this adds carbon with low $^{13}C/^{12}C$ to depth. The $\delta^{13}C$ distribution has been found to reflect mixing between NADW and AABW in the Atlantic (e.g. Oppo and Fairbanks, 1987; Curry et al., 1988; Shackleton et al., 2000). We interpret the $\delta^{13}C$ proxy at our core location based on the mixing of these end members; a) NADW with low preformed nutrients and high $\delta^{13}C$ (Kroopnick, 1985); and b) AABW with high preformed nutrients due to inefficiency of the biological pump (Kroopnick, 1985) (the rapid cycling of surface waters back to the deep). These northern- and southern-sourced water masses therefore have very different nutrient and $\delta^{13}C$ values and due to the short residence time of waters in the deep Atlantic.

The benthic $\delta^{13}C$ values from ODP Sites 983 and 1089 are offset from each other as expected given the different locations of these cores. ODP site 983 has an overall more positive benthic $\delta^{13}C$ value by approximately 1-1.5‰ interpreted as a greater influence of NADW than at ODP Site 1089. Both records reveal the longer-term trend of increasing benthic $\delta^{13}C$ values across the termination as they record the switch from more southern to northern sourced waters as the AMOC resumes. This occurs following a slowdown during the glacial interval (akin to the slowdown in AMOC recorded during HS1 (T1) (McManus et al., 2004). The resumption of AMOC results in NADW formation in the North Atlantic, filling the deep abyssal of both the North and South Atlantic with lighter benthic $\delta^{13}C$ values.

The timing of the benthic $\delta^{13}C$ changes in the South Atlantic cores across Terminations 1, 2 and 5 varies considerably; overall we observe the G-IG change in the dominance of more depleted $\delta^{13}C$ waters (AABW) during the preceding glacial interval; with waters with a higher $\delta^{13}C$ value (NADW) dominating during the interglacial period, i.e. an change in the geometry of the AMOC from the glacial interval to the interglacial interval (McManus et al., 2004; Barker et al., 2010; Sarnthein, 2011). The timing of this change in the dominance of the water masses in the abyssal Atlantic at ODP Site 1089 varies between the terminations; the onset of the rise in benthic $\delta^{13}C$ occurs approximately in line with the onset of the decrease in $\delta^{18}O$, however, the peak in benthic $\delta^{13}C$ occurs much sooner in T2 when compared to T1 and T5, suggesting that the switch from glacial to interglacial conditions during T2 occurred much quicker than for T1 or T5.

Over millennial timescales most of the rapid benthic $\delta^{13}C$ increase (increased NADW to the South Atlantic) correspond with increase in planktonic $\delta^{18}O$ (colder conditions in the South Atlantic) (Figure 2.22 and Figure 2.23), in agreement with other authors (Ninnemann et al., 1999) suggesting more NADW present in the South Atlantic (ODP Site 1089) when overturning circulation is strong and warm conditions prevail in the north and cooling is occurring in the south. The longer-term variability is different to this however, we typically record low benthic $\delta^{13}C$ (influence of southern source bottom waters) when cold conditions prevail over the South Atlantic (high planktonic $\delta^{18}O$ values) – this is indeed the relationship we observe during Termination 1 and 5. During Termination 2, however, we record a distinct exception to this general relationship over

millennial time scales; during a rapid increase in benthic $\delta^{13}C$ rather than recording an increase in planktonic $\delta^{18}O$, we actually record a decrease; the 'in phase' relationship between the North and South (inferred from the benthic $\delta^{13}C$) has also previously been identified (Ninnemann et al., 1999) and a nearby core location (RC11-83) but lacks any firm understanding of the mechanism.

2.11.2 PRESERVATION

The preservation of sediments can be used as an indicator of the origin of water masses in the deep Atlantic based on observations from Barker and Diz (2014) and suggested previously based on evidence from benthic foraminiferal $\delta^{13}C$ (Charles et al., 1996; Ninnemann et al., 1999). Barker and Diz (2014) suggest that the preservation indices (notably whole shells/g) are a function of the corrosivity of the deep water mass and use this argument in the development of the age model. They suggest that as northern-sourced deep water (NADW) is much less corrosive than its southern counterpart (AABW) when they record heavily dissolved samples in the South Atlantic they are recording an AABW signal. This is interpreted as a weakened and/or shoaled overturning circulation and a 'negative' phase of the bipolar seesaw. Conversely when there is less dissolution NADW is bathing the deep abyssal and the overturning circulation is strengthened and the bipolar seesaw is in a 'positive' state. Note that use of the term 'positive' bipolar seesaw refers to warm conditions in the northern hemisphere and deep water formation in the North Atlantic and a 'negative' bipolar seesaw refers to a slowing of AMOC resulting in warmer conditions in the south and cooler in the north with a shoaling of NADW to form Glacial North Atlantic Intermediate Water (GNAIW) and AABW bathing the deep south Atlantic. We use this interpretation of the preservation record from T1 to look at Terminations 2 and 5 and check our findings of deep-water changes in the South Atlantic.

As with the surface records, there are significant differences in the magnitude of changes in the preservation indices across the terminations. The record of whole shells/g across Terminations 2 and 5 show similar amplitude in variability, with maximum numbers of whole shells/g reaching approximately 800 and 1000 respectively with minimum values of approximately 10 shells; whereas T1 shows much better preservation on average, with the number of whole shells/g ranging between approximately 100-3000. Sediments that are deeper in the core (i.e. at a larger metres

below sea floor (mbsf)) are likely to be compacted by overlying sediments and as such could have larger number of fragments; this reasoning could explain why T1 has a larger number of whole shells/g than both T2 and T5.

In addition to the large magnitude of this change there are differences in the timing of events relative to the peak abundance of warm species, notably the peak in preservation (whole shells/g). For T1 the warm species peak occurs before the peak in preservation (by 1.5 kyr); for T2 the two peaks occur at approximately the same time; and for T5 the peak in preservation occurs before the peak in warm species (by 8.4 kyr), however we need to remember that as discussed above proxies for preservation are not straight forward and have complications in interpretation. The authors of the data from T1 (Barker et al., 2010) suggest that during T1 the warm planktonic foraminiferal species suggest intervals of enhanced preservation follow periods of weakened AMOC (cold in the north and warm in the south). If we use the preservation record as an indicator of bottom water changes then during T5 as *G. ruber* abundance starts to increase we record an associated increase in preservation (increase in whole shells/g) but by the time *G. ruber* peaks in the South Atlantic we see a slight reduction in the preservation of the record (decrease in numbers of whole shells/g) suggesting an influence of more corrosive southern-sourced bottom waters in the South Atlantic and a reduction in NADW formation at this time. These findings are comparable to the results from T1 (Barker et al., 2009; Barker and Diz, 2014) where the authors attribute the reduction in the number of whole shells/g during the warm species peak to an increase in the influence of more southerly sourced deep waters in the South Atlantic.

Additionally, the timing of events compared to the % $CaCO_3$ record varies between the terminations (T1, T2 and T5); the peak in % $CaCO_3$ occurs following the warm species peak for T5, whereas the reverse is true for T2; the % $CaCO_3$ peak occurs prior to the warm species peak. The percentage of $CaCO_3$ recorded is a function of productivity of the surface oceans and its preservation at depth; typically in the deep Atlantic $CaCO_3$ records show high carbonate concentrations (i.e. enhanced preservation) during glacial and low carbonate concentrations (i.e. enhanced dissolution) during interglacials (Hodell et al., 2003b). The previously studied records from T1 at TN057-21 noted a relationship between variations in % $CaCO_3$ and the AMOC (Barker et al., 2009). Our results from T5 corroborate these suggestions as we also observe transient reductions in

the % $CaCO_3$ record during events across T5. These events are associated with very cold conditions in the North Atlantic (see chapter 3) and associated warming in the South Atlantic, recorded as an abrupt decrease in GLT_syn (Barker et al., 2011). This warming in the South Atlantic is due to a reduction in the AMOC preventing NADW from reaching the abyssal Atlantic and as such ODP Site 1089 briefly (despite high background $CaCO_3$ levels) becomes bathed in poorly-ventilated, southern-sourced, AABW increasing dissolution in the South Atlantic.

We conclude here that as the warm species peak coincides with a reduction in preservation (whole shells/g and % $CaCO_3$) that the changes in the surface and deep ocean are as a result of changes in the Atlantic Meridional Overturning Circulation and the response that we record in the South Atlantic, when compared to sites from the North Atlantic, is an expression of the bipolar seesaw.

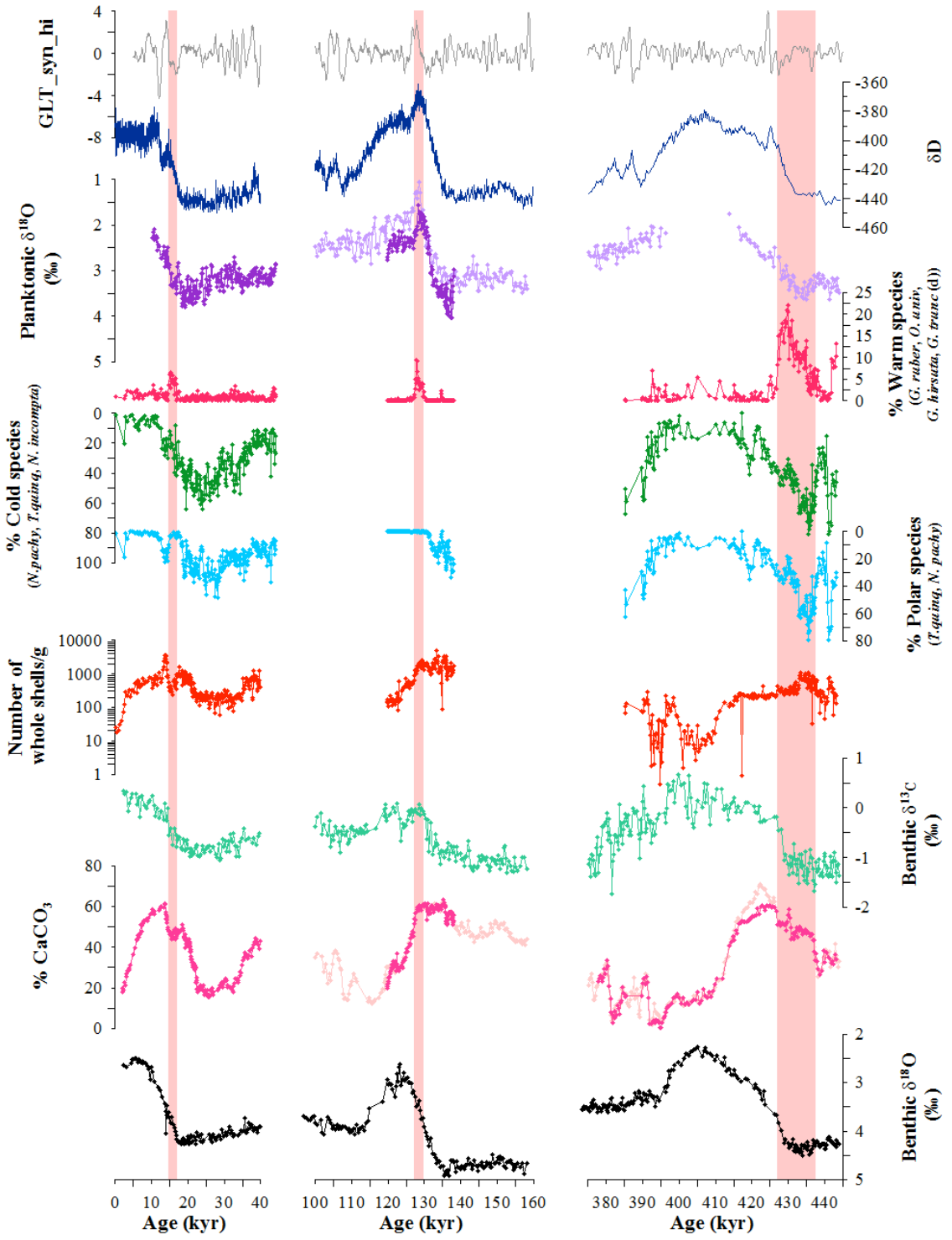

Figure 2.23. Synthesis of records from Terminations 1, 2 and 5. From top to bottom; GLT_syn (black) (Barker et al., 2011); EDC δD record (dark blue) (Jouzel et al., 2007); planktonic $\delta^{18}O$ (‰) for T1 (dark purple) from (Barker et al., 2009) for T2 (dark purple) (this study) and for T2 and T5 (light purple) (Hodell et al., 2003b) (note that all the planktonic records were recorded on G. bulloides); % warm species (pink) for T1 (Barker et al., 2009) and T5 (this study) species included (G. ruber, O.

universa, G. truncatulinoides (d) and G. hirsuta) but for T2 (this study) this only includes G. ruber; % cold species (green) (N. pachyderma, N. incompta and T. quinqueloba) (note that we do not have a cold species record for T2 (this study); % polar species (light blue) for T1 (Barker et al., 2009) and T5 (this study) (N. pachyderma and T. quinqueloba) but for T2 (this study) this only includes N. pachyderma; whole shells/g (red) for T1 (Barker et al., 2009) and for T2 and T5 (this study); benthic $\delta^{13}C$ (light green) for T1 (Ninnemann et al., 1999) and for T2 and T5 (Hodell et al., 2003b); % $CaCO_3$ (pink) for T1 (Sachs and Anderson, 2005) and for T2 and T5 (this study); % $CaCO_3$ (light pink) for T2 and T5 (Hodell et al., 2003b); the benthic $\delta^{18}O$ (black) for T1 (Ninnemann et al., 1999) and for T2 and T5 (Hodell et al., 2003b).

2.12 ALTERNATIVE AGE MODEL FOR ODP SITE 1089 (T5)

In this section we consider an alternative age model that was produced by tuning the planktonic faunal records to a prediction of South Atlantic/Southern Ocean temperature variability (Figure 2.24). We have developed this age model based on our interpretation above, that the millennial-scale faunal changes we observe in our record across T5 are related to the bipolar seesaw. We are able to use this understanding to develop an age model based on tuning the planktonic record to a prediction of South Atlantic/South Ocean temperature changes. This prediction was calculated by subtracting the GL_T_syn_hi record (a predication of Greenland climate variability minus the orbital timescale variability) (Barker et al., 2011) from Antarctic temperature (Jouzel et al., 2007). This provides us with the southern hemisphere counterpart to the abrupt millennial scale events in the North Atlantic, i.e. the South Atlantic/Southern Ocean prediction is the southern hemisphere component of the bipolar seesaw, excluding the heat reservoir of the Southern Ocean.

The records were aligned using the faunal records from ODP Site 1089; namely the 'warm' (*G. ruber*, *G. hirsuta*, *O. universa* and *G. truncatulinoides* (d)) and 'cold' (*N. pachyderma*, *N. incompta* and *T. quinqueloba*) with the prediction of South Atlantic climate variability record and previously published records from ODP 1089. In total five tuning points were chosen based on aligning the transition in the faunal records with the equivalent transitions in the South Atlantic/Southern Ocean prediction (Figure

2.24). The warm species were tuned to the negative of GLT_syn_hi (the prediction of the South Atlantic (Barker et al., 2011)).

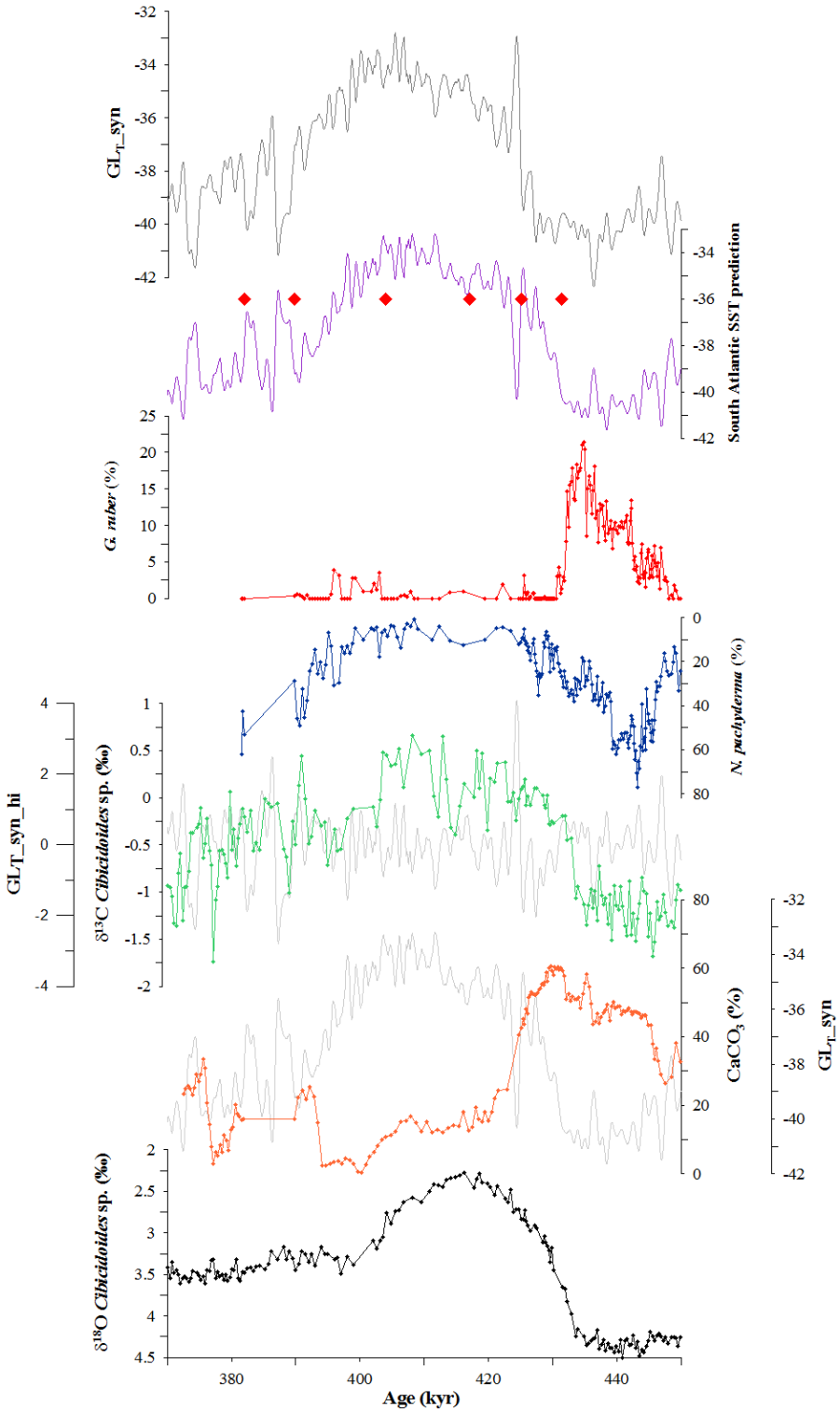

Figure 2.24. Alternative age model for ODP Site 1089. GLT_syn shown in (black) (Barker et al., 2011); the South Atlantic/Southern Ocean prediction (purple) with the tie points shown as re diamonds, % G. ruber (red) (this study) and % N. pachyderma

(blue) (this study); $\delta_{13}C$ Cibicidoides sp. (green) (Hodell et al., 2003b) with GLT_syn_hi shown in grey behind (Barker et al., 2011); % $CaCO_3$ record (orange) (this study) with GLT_syn (a prediction of Greenland temperature variability) shown in grey behind (Barker et al., 2011). $\delta^{18}O$ Cibicidoides sp. (black) (Hodell et al., 2003b) is shown at the bottom for reference.

Comparison of the synthetic prediction of Greenland temperature variability, GL_T_syn record (Barker et al., 2011), with the benthic $\delta^{13}C$ from ODP Site 1089 (Hodell et al., 2003a) following the alignment suggests that as Greenland warms (i.e. a reduction in $\delta^{18}O$, there is overturning circulation in the Atlantic and deep water formation in the North Atlantic (NADW). The NADW (low in preformed nutrients) produced in the North Atlantic sinks to depth and as such bathes the deep abyssal in the Atlantic. This water mass, depleted in ^{12}C has a high $\delta^{13}C$ value and varies in sync with the prediction of Greenland temperature.

The $CaCO_3$ record has been compared with the GL_T_syn record (Barker et al., 2011), a synthetic reconstruction of Greenland temperature variability ((Barker et al., 2011)). The % $CaCO_3$ record reflects whole ocean alkalinity (see results section above) but with the localised changes recorded too; specifically we record jumps in % $CaCO_3$ that coincide with the larger amplitude transitions in the prediction of Greenland temperature variability (notably at 436.29kyr and 432.16kyr). These rapid changes in $CaCO_3$, appears as 'bite' that marks have been taken out of the record during the inferred warm interval (*G. ruber* peak). These 'bite' marks in ODP Site 1089 can also be seen in other records from the South Atlantic (TN057-21) during more recent HS events of T1 (Barker et al., 2009). The reason for transient reduction in $CaCO_3$ during HS/HS-like events is due to the slowdown of AMOC due to very cold conditions prevailing in the North Atlantic (as such associated with warming in the South Atlantic/Southern Ocean). The reduction of deep-water formation in the North Atlantic and associated slowdown of AMOC results in southern-sourced waters bathing the Atlantic abyss. These nutrient-rich and poorly ventilated southern-sourced waters result in increased dissolution during these cold northern hemisphere events and thus the amount of $CaCO_3$ preserved in the record decreases as some of it is dissolves. The resumption of the AMOC aligned with warming in the North Atlantic (following a HS event) results in an increase in the $CaCO_3$ record as northern-sourced deep-water

formation resumes and well ventilated NADW bathes the abyssal allowing for the preservation of $CaCO_3$ in the South Atlantic/Southern Ocean at ODP Site 1089.

2.13 CONCLUSION

In conclusion we suggest based on our findings that there was a major seesaw event across T5. Comparison of cold conditions in the North Atlantic (*N. pachyderma* abundance and IRD grains/g records from ODP 983 (Barker et al., 2015)) with the faunal record in the South Atlantic further highlights the 'extreme' nature of Termination 5. Compared to Terminations 1 and 2, Termination 5 records much larger peaks in IRD grains/g in the north and *G. ruber* in the south and we suggest that the seesaw event across this interval is far greater than it was for either T2 or T1.

Our records here suggest that despite the extreme cold conditions and large ice-rafting event in the North Atlantic and associated warming conditions in the South Atlantic during MIS 12 there is little, if any, impact of the magnitude on the termination. As previously highlighted T5 is a prolonged termination and records a much slower transition from glacial to interglacial conditions in both the benthic $\delta^{18}O$ values as well as the atmospheric gases. From this we suggest that it does not appear to matter how much the bipolar seesaw is forced ('extreme' conditions in both the north and south hemispheres) there is no impact on the magnitude of the termination. Apparently, it does not matter how warm the South Atlantic gets the ice core records from Antarctica do not record similar 'extreme' temperatures (Figure 2.23). It appears that the heat reservoir of the Southern Ocean is able to absorb these very large magnitude changes in SST in the South Atlantic.

3 LATE RECOVERY OF THE AMOC EXPLAINS LARGER AMPLITUDE OF CO_2 CHANGE ACROSS THE PENULTIMATE DEGLACIATION

3.1 INTRODUCTION

The G-IG cycles of the Late Pleistocene document large variations in deglacial atmospheric CO_2. These large G-IG variations in CO_2 can not simply be explained simply by variations in the incoming solation ration (Milankovitch cycles (Milankovitch, 1941) (see chapter 1). Rather, the G-IG variability is the result of the net consequence of several competing millennial scale mechanisms (e.g. Archer et al., 2000; Köhler et al., 2005; Brovkin et al., 2007). The rise in atmospheric CO_2 across T1 occurred in several phases (Figure 3.25) that could reflect numerous distinct (although possibly related) processes (Monnin et al., 2001). During the earliest phase of T1, ~18-14.5ka (variously labelled the Mystery Interval (Denton et al., 2006) or Heinrich Stadial, HS1 (Barker et al., 2009)) CO_2 rose by ~40 ppmv. Proxy reconstructions suggest that the dominance and export of North Atlantic Deep Water (NADW; which today penetrates the North Atlantic to abyssal depths as part of the Atlantic Meridional Overturning Circulation, AMOC) was significantly reduced in favour of southern-sourced deep waters during HS1 (McManus et al., 2004; Barker et al., 2010; Roberts et al., 2010). At the same time, and possibly as a direct consequence of a weakened or shallower AMOC, reduced vertical stratification within the Southern Ocean (Anderson et al., 2009; Skinner et al., 2010) (possibly in combination with decreased delivery of Fe-bearing dust (Gaspari et al., 2006)) is thought to have led to the release of CO_2 from the deep ocean. A similar set of processes is thought to have operated during the Younger Dryas, Y-D (McManus et al., 2004; Anderson et al., 2009; Roberts et al., 2010; Skinner et al., 2010) when CO_2 rose by a further ~30 ppmv.

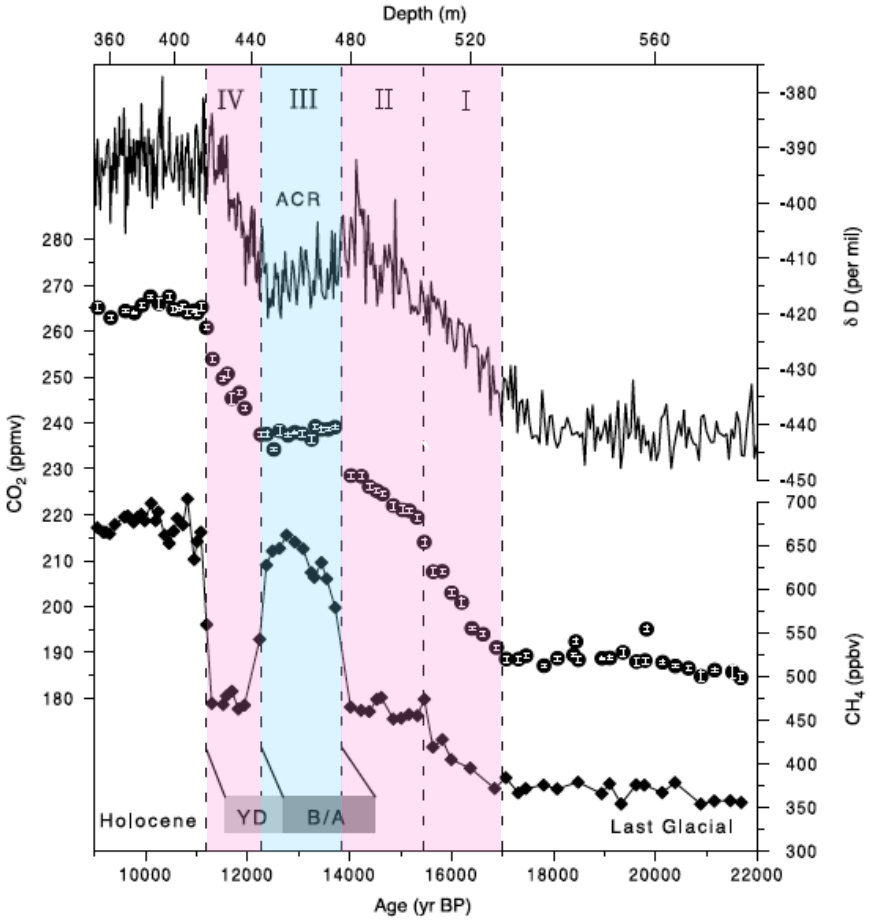

Figure 3.25. From Monnin et al., (2001). The solid curve indicates the Dome C δD in the ice as a proxy for local temperature (Jouzel et al., 2007). Solid circles represent CO_2 data from Dome C (mean of six samples; error bars, 1s of the mean). Diamonds show methane data from Dome C (the 1s uncertainty is 10 ppbv). The time scale used for the gas-ice age is from work by Schwander et al., (2001) (the depth at the top of the figure is only valid for the CO_2 and methane records). In the CO_2 and methane records, four intervals (I through IV) can be distinguished during the transition. The δD record is highly correlated with the CO_2 record, with the exception that the increased rates during intervals I and II are not significantly different in the deuterium record. The YD and the B/A events recorded in Greenland ice cores are indicated by shaded bars according to the GRIP time scale. Comparisons of the methane record with that of GRIP demonstrate that the YD corresponds to interval IV and the B/A event corresponds to interval III (Monnin et al., 2001).

In contrast to HS1 and the Y-D, ocean circulation during the Bølling-Allerød (B-A, an interval of northern hemisphere warmth which occurred between HS1 and the Y-D) was more akin to modern conditions (McManus et al., 2004; Roberts et al., 2010). In fact modelling studies and proxy evidence from the deep South Atlantic/Southern Ocean suggest that the strength and depth of the AMOC during the B-A could have exceeded the modern range (Knorr and Lohmann, 2007; Liu et al., 2009; Barker et al., 2010; Skinner et al., 2010). Similar changes from a shallow (or weak) to deep AMOC during Marine Isotope Stage (MIS) 3 (Shackleton et al., 2000; Barker et al., 2010) were paralleled by transitions from increasing to decreasing CO_2 (Ahn and Brook, 2008) and yet following an initial rise of CO_2 of ~10ppmv at ~14.6ka (which could reflect permafrost thawing and flooding of continental shelves, (Köhler et al., 2014)) CO_2 remained roughly constant during the B-A (Figure 3.25 and Figure 3.40). Modelling studies suggest that even allowing for a decrease in solubility due to higher surface ocean temperatures (that may be expected as a consequence of an enhanced AMOC, (Menviel et al., 2008; Schmittner and Galbraith, 2008)), an increase in the proportion of northern- versus southern-sourced deep waters would lead to lower atmospheric CO_2 due to a corresponding decrease in the global net inventory of preformed nutrients within the deep sea (Ito and Follows, 2005; Marinov et al., 2008; Schmittner and Galbraith, 2008; Sigman et al., 2010) so why was there no change in CO_2 across the B-A?

The answer to this question most probably lies in the complex sequence of events associated with deglaciation. By their nature, the CO_2 records recovered from ice cores integrate the various mechanisms that ultimately contribute to the observed signal, obscuring our ability to deconvolve the individual processes involved. The lack of a perceptible change in CO_2 during the B-A could then reflect the coincidence of two (or more) mechanisms with opposing influences on CO_2. For example the tendency for a strengthened AMOC to draw down CO_2 (Schmittner and Galbraith, 2008) could have been countered by outgassing of CO_2 as a result of reduced sea ice cover and continued deep ocean ventilation within the Southern Ocean during the B-A (Skinner et al., 2013). It follows that if T1 had not been interrupted by resumption of the AMOC at ~14.6 ka then the net change in CO_2 would have been larger. We suggest that this could have been the case during T2.

The penultimate deglaciation, T2 (from about 136-129kya) occurred under quite different climatic and orbital context to the much-studied last deglaciation. T2 was characterised by a larger eccentricity and a different phasing between precession and obliquity (Berger, 1978; Berger and Loutre, 1991) (Figure 3.). Furthermore the structure of the response of the global climate system is very different when comparing T1 with T2. As described above, we record an interruption to the deglacial rise in atmospheric CO_2 during the B-A, whereas in T2 Heinrich Stadial 11 (an prominent North Atlantic cold episode (Oppo et al., 2006; Martrat et al., 2014) that occurred between 135±1 and 130±2 kyr (Marino et al., 2015)) isn't interrupted until the end of the termination.

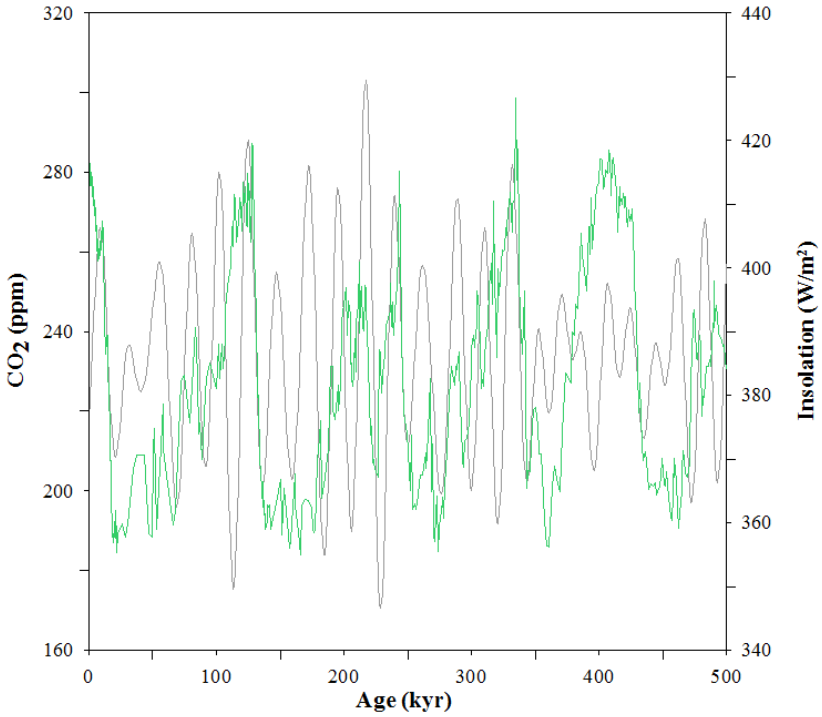

Figure 3.29. CO_2 (Lourantou et al., 2010) and insolation (Berger, 1978; Laskar et al., 2004) over the last 5 terminations. The records show that variability in insolation alone is not sufficient enough to drive G-IG terminations.

Records from North Atlantic marine sediments (McManus et al., 1999), Chinese speleothems (Cheng et al., 2009) and Antarctic ice cores (Loulergue et al., 2008; Barker et al., 2011) suggest that the rise in CO_2 across Termination 2 (Figure 3.25 and Figure 3.40) was associated with a prolonged interval of weakened AMOC and that resumption to a warm mode of circulation did not occur until the onset of MIS 5. However, to date there has been no corroboration from direct proxies of ocean circulation. Recently

published records of authigenic Nd isotopes and sedimentary Pa/Th ratios from ODP core 1063 from the North Atlantic (Böhm et al., 2015) support the notion of a deepening of NADW during early MIS 5, but a lack of precise age control makes it difficult to know how this change corresponded to changes in atmospheric CO_2. Here we present a record of Nd isotopes measured on fish debris using well established analytical methods (Staudigel et al., 1985; Grandjean et al., 1987; Martin and Haley, 2000) from the same core (ODP Site 1063) which we pair with high resolution records of planktonic and benthic foraminiferal $\delta^{18}O$, foraminiferal fragmentation and abundance counts made on the same material, that allow us to place much tighter constraints on the timing of events.

In this chapter we show that the ~20ppmv overshoot in CO_2 at the end of Termination 2 (T2) ~129ka was associated with an abrupt (≤300±60yr) deepening of Atlantic Meridional Overturning Circulation (AMOC). Specifically we employ Nd isotopes to highlight the dominant role of deep-water formation in the NW Atlantic during the earliest phase of the last interglacial period. We conclude that, with respect to the last deglaciation, the late resumption and deepening of AMOC associated with T2 was responsible for the larger amplitude of observed CO_2 change across this termination.

3.2 MATERIALS AND METHODOLOGY

3.2.1 STUDY LOCATION AND OCEANOGRAHPIC SETTING

ODP Site 1063 is located on the Bermuda Rise at 33.69°N, 57.62°W at a water depth of 4584m (Figure 3.26). The location of ODP Site 1063 is ideally positioned in the mixing zone between North Atlantic Deep Water (NADW) and Antarctic Bottom Water (AABW) and as such high resolution records from ODP 1063 (average sedimentation rates of ~17cm/kyr) and other nearby locations have recorded past changes in water mass mixing and circulation dynamics (Keigwin and Jones, 1994; Adkins et al., 1997; Böhm et al., 2015). The core location in the modern ocean is bathed in NADW and has a Nd isotopic composition (expressed as εNd, the deviation of the measured $^{143}Nd/^{144}Nd$ ratio from the chondritic uniform reservoir (CHUR) (in parts per 10,000, CHUR = 0.512638; Jacobsen and Wasserburg, 1980) of ~ -12.7 (Figure 3.32), reflecting the

exported mixture of deep waters formed in the eastern and western North Atlantic (NADW) and those emanating from the Southern Ocean (Lambelet et al., submitted).

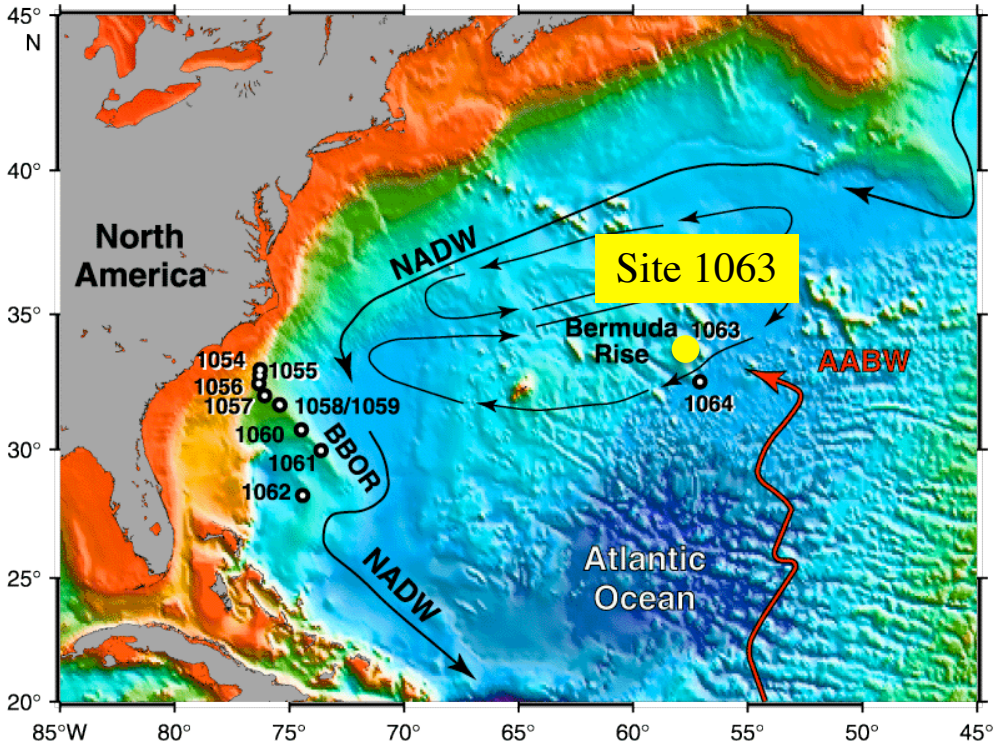

Figure 3.26 Study location of ODP Site 1063, Bermuda Rise. Located in the western North Atlantic Ocean at 33.69°N, 57.62°W in a water depth of 4.584 km. Figure adapted from Keigwin and Acton, 2001.

3.3 PROXY RECORDS FROM ODP SITE 1063

3.3.1 SEDIMENT PROCESSING

The samples required for the analysis of ODP Site 1063 across T2 were obtained from the ODP repository in Bremen, Germany. The wet sediment was disaggregated by adding deionised (DI) water to it and placing it on a rotating wheel for 12-16 hours. It was then washed over a 63µm sieve using a fine water spray; the coarse fraction (>63µm) was then dried off in the oven at 40°C for approximately 36 hours. The fine fraction (<63µm) was allowed to settle and then the water was syphoned off, and allowed to dry in the oven (40°C) for approximately one week until the sediment was completely dry. Both fractions were weighed using an Ohaus Pioneer PA413C balance.

3.3.2 CALCIUM CARBONATE ANALYSIS

The sedimentary calcium carbonate content (% $CaCO_3$) was measured to align the records from this study (for both Termination 2 and 5) to that of previously published records on the same core site using a different splice (Hodell et al., 2003a, 2003b). Carbonate content was determined by CO_2 coulometry using a UIC.inc CM5130 Acidification Module connected to a UIC.inc CM5014 CO_2 Coulometer. Approximately 1 cm^3 of bulk sediment was dried at 40°C degrees and ground to ensure homogenisation using an agate pestle and mortar and aliquots of approximately 30mg were used for analysis. A standard (100% $CaCO_3$) and a blank were run every 10 samples. See appendix for full operating instructions.

3.3.3 FORAMINIFERAL ASSEMBLAGE ANALYSIS

Planktonic foraminifera are free-floating surface dwelling single-celled microorganisms with a global distribution. These protozoa form elaborate calcite shells (tests) that allow to visually differentiate between (morpho)species. Following death, the shells sink to the seafloor and are preserved in the sediment. Sediment traps (Tolderlund and Bé, 1971; Chapman, 2010), plankton tows (Bé and Tolderlund, 1971) and modern (core-top) sediment assemblages (Prell et al., 1999) of planktonic foraminifera reveal a very distinct geographical pattern in the modern ocean as shown in Figure 3.27 The study of planktonic foraminiferal ecology and distribution highlights the preference that species display for certain environmental conditions and the relative maximum abundance of particular species correlates with ecologic optima (e.g. Bé and Tolderlund, 1971). Foraminiferal distribution in the modern ocean shows a latitudinal pattern suggesting temperature is the most important control on their distribution (Murray 1897). However, there are also other parameters that influence their distribution such as, surface salinity, pycnocline phosphate concentrations, the seasonal range in nitrate concentrations, water depth, and chlorophyll concentrations but temperature is the most important influence on their distribution (e.g. Morey et al., 2005).

It is for these reasons that planktonic foraminiferal assemblage counts have been recognised and long since used as surface-water property tracers; given a particular assemblage and the known distribution of species in the modern ocean, it is possible to use the proportions of each individual species to determine the past (near) sea surface

temperature (e.g. Bradshaw, 1957; Parker, 1960; Berger, 1969; CLIMAP Members, 1984; Pflaumann et al., 1996; Kucera et al., 2005; MARGO Members, 2005).

The use of planktonic foraminifera assemblages to infer past environmental change requires that the sedimentary assemblage be unaltered by post-depositional processes. Dissolution could potentially affect the fossil assemblage (Le and Shackleton, 1992; Le and Thunell, 1996), and sedimentary records thus need to be carefully screened for dissolution for accurate/sensible paleoclimate reconstructions.

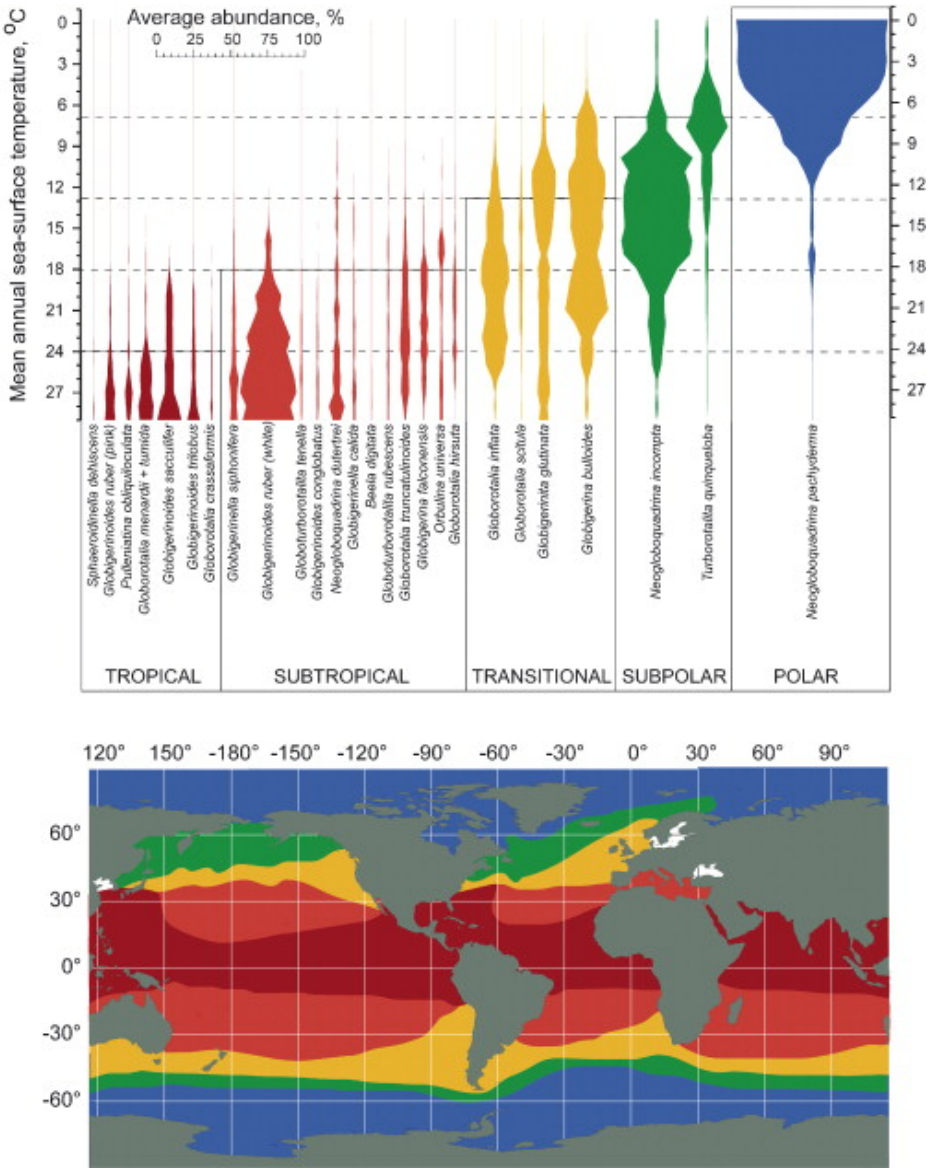

Figure 3.27. Planktonic foraminiferal provinces in the modern ocean. The distribution of the provinces (Bé and Hutson, 1977; Vincent and Berger, 1981) follows the gradients of the sea surface temperature; reflecting the correlation

between sea surface temperature and the distribution of planktonic foraminiferal species (Kucera et al., 2005).

Sub-samples across Termination 2 were obtained by sieving (>150μm) the coarse fraction for each sample and further divided using a binary splitter in order to obtain approximately 300 whole foraminifera shells that were subsequently counted. This number of whole shells was counted to ensure that the assemblage obtained is representative of the whole sample, following the methods of CLIMAP Members (1984) and Pflaumann et al., (1996). The following entities were counted in each sample following the taxonomy of Parker (1962): *Neogloboquadrina pachyderma, Neogloboquadrina incompta, Globigerinoides inflata,* 'other' planktonic foraminiferal species (see chapter 2 for descriptions of their habitat preferences). The number of fragments and whole shells (including species not included above), the number of pieces of fish debris, and the number of pieces of IRD were also counted in each sample and the combined data is summarised in Figure 3.28 below.

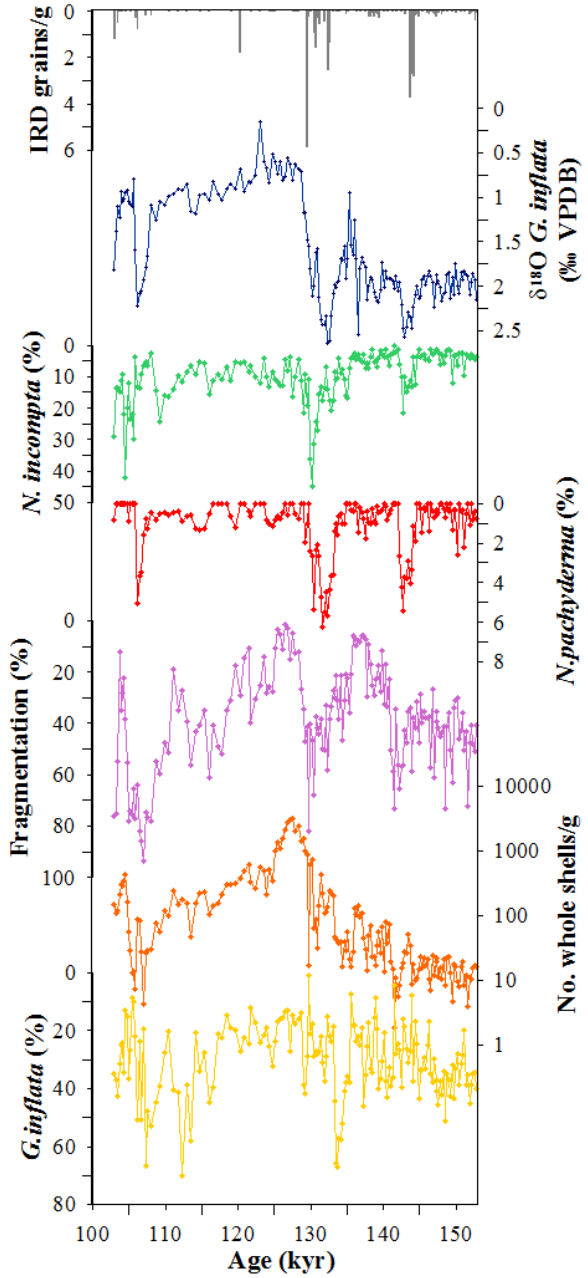

Figure 3.28 A surface ocean synthesis plot of the faunal assemblage data and the planktonic stable $\delta^{18}O$ record. The following plots are shown; number of IRD grains/g (grey); stable $\delta^{18}O$ of G. inflata (dark blue); percentage of Neogloboquadrina incompta (green); percentage of Neogloboquadrina pachyderma (sinistral) (red); the percentage of fragmentation (purple); and total number of whole shells/gram in each sample (orange) and; the percentage of Globorotalia inflata (yellow).

The % fragmentation of planktonic foraminifera is used as a proxy for carbonate dissolution (Berger, 1968, 1970; Le and Shackleton, 1992; Le and Thunell, 1996). The

susceptibility of a particular species to dissolution controls the susceptibility of an assemblage to fragmentation initially. Shells that have been subjected to dissolution have thinner shells and break more easily and thus the more a sample has been affected by dissolution, the larger the percentage of fragmentation will be. For this study a fragment is defined as a piece of foraminiferal shell that is less than 50% intact. The total number of whole shells/gram in a sample is a proxy for preservation of the sample as the larger the number of whole shells, the greater the preservation of that sample.

3.4 INTRODUCTION TO STABLE ISOTOPES

It has long been established that the fractionation of stable oxygen isotopes ($\delta^{18}O$) between calcium carbonate and the surrounding water it was formed in, is sensitive to temperature changes and $\delta^{18}O_{sw}$ (Urey, 1947; Epstein and Mayeda, 1953). Subsequent work used the $\delta^{18}O$ values of planktonic foraminifera as a paleothermometer noting that changes in the $\delta^{18}O$ of seawater (variations in both continental ice volume and local salinity changes) also have an effect on the $\delta^{18}O$ value recorded in the foraminiferal test (e.g. Emiliani, (1955) and Shackleton (1967). Oxygen isotope measurements in foraminifera ($\delta^{18}O$) have provided a wealth of information about past climate change (e.g. Emiliani, 1955, 1972; Shackleton, 1967, 1987).

Benthic $\delta^{13}C$ has been used to infer changes in mixing between deep waters of southern versus northern sources in the Atlantic Ocean (Oppo and Fairbanks, 1987; Curry et al., 1988; Charles and Fairbanks, 1992; Charles et al., 1996; Ninnemann et al., 1999; Shackleton et al., 2000) and can be used to trace the origin of water masses and infer changes in the geometry of the AMOC over time (e.g. Duplessy et al., 1988; Shackleton et al., 2000). Primary producers take up nutrients and carbon in the surface waters, where they preferentially remove ^{12}C, resulting in the surface waters being enriched in ^{13}C; when they remineralise at depth, this adds carbon with low $^{13}C/^{12}C$ ratio to depth. The proxy is based on the mixing of the end members; a) NADW with low preformed nutrients and high $\delta^{13}C$ (Kroopnick, 1985); and b) AABW with high preformed nutrients due to inefficiency of the biological pump (Kroopnick, 1985) (the rapid cycling of surface waters back to the deep). These northern- and southern-sourced water masses therefore have very different nutrient and $\delta^{13}C$ values and due to the relatively short residence time (approximately 100 years (Broecker, 1979)) of waters in the deep Atlantic, the $\delta^{13}C$ distribution has been found to reflect mixing between these

two water masses (NADW and AABW) (e.g. Oppo and Fairbanks, 1987; Curry et al., 1988; Shackleton et al., 2000).

3.4.1 TEST RUN TO DETERMINE CLEANING METHODOLOGY FOR $\delta^{18}O$ AND $\delta^{13}C$ ANALYSIS (ULTRASONIFICATION VS. NON-ULTRASONIFICATION)

An initial test to determine if the samples needed to be ultrasonicated to remove any sediment infill within the shells or not was carried out prior to running the rest of the samples (samples depths are shown in the appendix). This test was carried out to establish whether or not there was any benefit to individually cleaning each sample before analysis on the mass spectrometer. Four samples were used for the analysis – these samples were chosen because they all have a large number of *G. inflata* individuals in them but differing numbers of whole shells/g (i.e. size of sample). Two of the samples (samples HB, C4, S5; 48-50cm and HB, C4, S5; 52-54cm) have very large coarse fraction weights and conversely, the other two have very low coarse fraction weights (samples HB, C4, S5; 108-110cm and HB, C4, S5; 112-114cm). From each sample 10 individual foraminifera were handpicked from the >150µm size fraction and split in to two vials. To one of the vials 18.2Ω DI water was added and the sample was then ultrasonicated for 3 seconds prior to being analysed and the other one was not. The locations of the samples chosen for the initial test analysis are shown on Figure 3.29 below, indicated by the red diamonds.

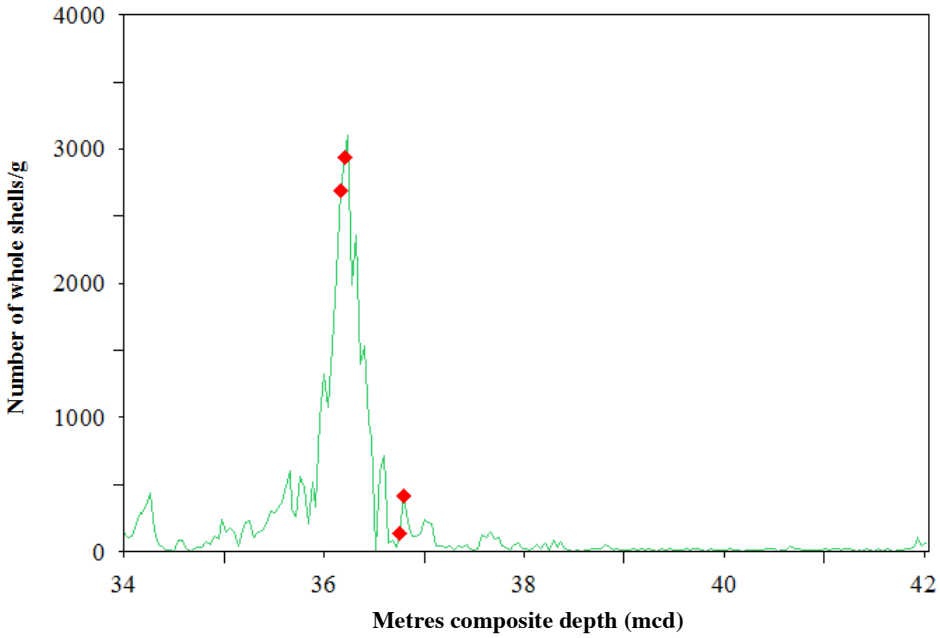

Figure 3.29. A plot to show the samples (red diamonds) used for the initial test samples to establish the cleaning procedures for stable isotope analysis for ODP Site 1063. The samples were chosen to straddle the termination and also to see the effect of the cleaning procedure on differing numbers of whole shells/g in the sample. The green record shows the total number of whole shells/g in each sample.

3.4.2 RESULTS OF TEST RUN FOR PLANKTONIC STABLE ISOTOPE ANALYSIS

The results of this initial test show that when comparing the ultrasonicated and non-ultrasonicated samples that all bar one $\delta^{13}C$ result (sample 1) were within error of each other (Figure 3.30). Precision of all internal and external standards was ±0.03‰ for $\delta^{13}C$ and ±0.08‰ for $\delta^{18}O$ (based on the standard deviation of repeat measurements of the international standard NBS-19). Note that one of the samples did not acidify properly (likely a result of the foraminifera not being at the very bottom of the test tube). The differences in $\delta^{18}O$ between the two vials are 0.042‰, 0.051‰ and 0.17‰ and differences in the $\delta^{13}C$ of the same three samples are 0.102‰, 0.12‰ and 0.038‰ (see appendix for relative variation of results). These differences are not systematically offset from each other depending on the cleaning method used and are within the error of each other. As such it was concluded that ultrasonicfication of the samples would not be included in the protocol for the cleaning method for the rest of the record. Instead, any sediment infill/debris in the samples would be removed by hand under a microscope to ensure the samples are as clean as possible for analysis. In addition, this test confirmed the importance of the individual foraminifera being placed at the bottom of the vial for analysis to ensure complete acidification of the sample.

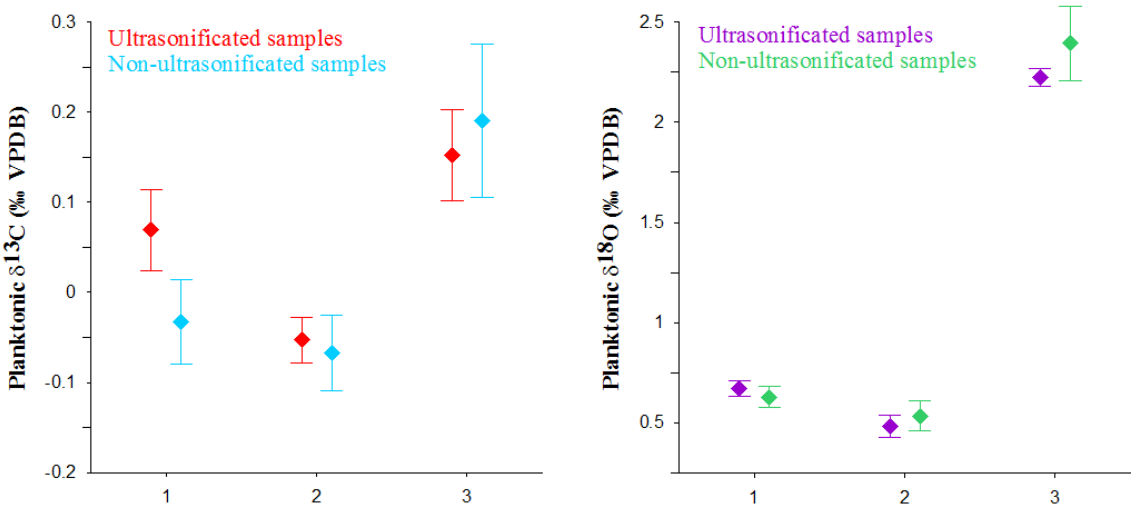

Figure 3.30 Results of the test to determine the cleaning methods used for the stable isotope analysis. Panel a) planktonic $\delta^{13}C$ of G. inflata results and panel b) planktonic $\delta^{18}O$ of G. inflata.

3.4.3 PLANKTONIC STABLE ISOTOPE ANALYSIS

A minimum of 200 µg is targeted for stable isotope analysis for the Thermo Delta V Advantage with Gasbench 2 mass spectrometer based on previous analytical experimentation on the machine at Cardiff University by Dr. Sandra Nederbragt. As such, a target of 30 *G. inflata* individuals (see appendix on how the numbers required were determined) were handpicked from the 300-355µm size fraction for analysis. The numbers of individual specimens varies throughout the core and as such between 5-30 individual specimens (the exact number recorded is shown in the appendix) were picked from each of the samples at 4 cm resolution and weighed using the Mettler Toledo XP6 balance.

The mass spectrometer holds 48 samples plus 16 standards at a time. The standards used during this analysis are *Carrara*, *Estremoz* and *Atlantis*. The *Carrara* standard was used to correct for the weight of each of the samples. The other standards are used to monitor the slightly non-linear response of the mass spectrometer, i.e. to ensure that changes in the $\delta^{18}O/\delta^{13}C$ record are not a function of changing sample size. The *Atlantis* standard is very enriched in $\delta^{18}O$ and the *Estremoz* is very depleted in $\delta^{18}O$. Thus by running these standards we are able to test (and correct if required) if the mass spectrometer behaves linearly for all carbonates regardless of the isotopic composition.

The individual weights and standards required for each run matrix are shown in the appendix.

The stable isotope measurements were carried out on a Thermo Delta V Advantage with Gasbench 2 at Cardiff University with technical support from Dr. Sandra Nederbragt. The spectrometer was calibrated through the international standards mentioned above and all isotopic results are reported as a ‰ deviation from the Vienna Pee Dee Belemnite scale (‰ VPDB). External reproducibility of carbonate standards was better than 0.07‰ and 0.06‰ for $\delta^{18}O$ and $\delta^{13}C$ respectively when the records produced in this thesis were run.

3.4.4 BENTHIC STABLE ISOTOPE ANALYSIS

The analysis of the benthic isotopes from ODP Site 1063 was carried out by Mrs Lindsey Owen and Dr. Sandra Nederbragt at Cardiff University. The benthic record was produced in order to provide some context for the bottom waters at ODP Site 1063 and to be able to get a better idea of the timing of the changes in the deep waters from different sources bathing the site and also to enable analysis of the timing of changes between the surface and the deep at the site. The foraminifera were handpicked from the >150μm size fraction for analysis.

The target species for the record was *Cibicidoides wuellerstorfi, Oridorsalis umbonatus* and *Melonis pompilioides*. Where there were two or more different species in a given sample they were all analysed to calculate the offset between the three species. The offsets were calculated by taking the average of the difference between the species in every sample and normalised to *Cibicidoides wuellerstorfi*. The raw data and offset calculations are shown in the appendix.

Figure 3.31 below shows the three original datasets on which the offset calculations were based. We also calculated compiled benthic $\delta^{18}O$ and $\delta^{13}C$ records across the study interval. This was done in order of preference of each of the species; if *Cibicidoides wuellerstorfi* was present in a sample, this species was used as a first preference, then *Oridorsalis umbonatus,* and *Melonis pompilioides* was used only if the other two species were not present. The compiled benthic records for stable oxygen ($\delta^{18}O$) and stable carbon ($\delta^{13}C$) isotopes is presented below in Figure 3.31.

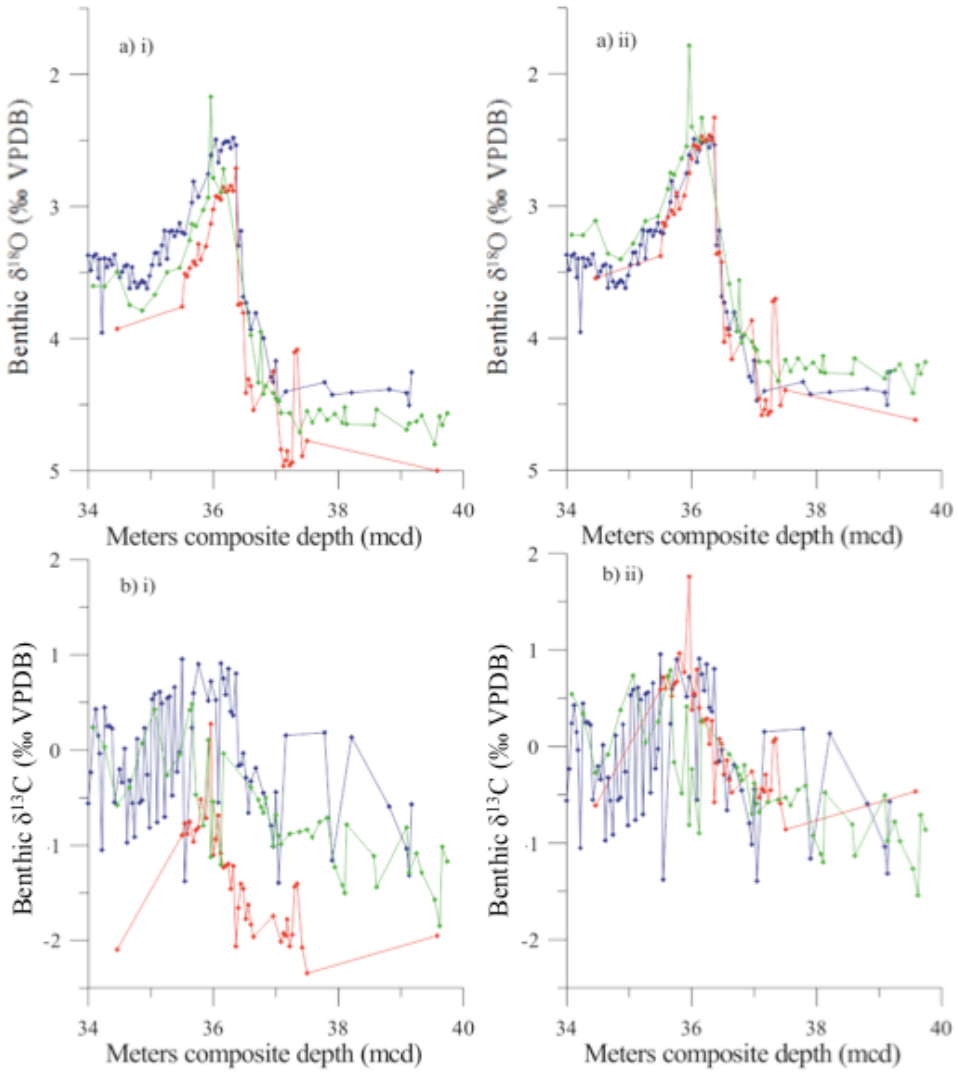

Figure 3.31. Diagrams showing the benthic stable isotopes produced from ODP Site 1063. The different colours indicate the different species used for the compilation: Cibicidoides wuellerstorfi (blue), Oridorsalis umbonatus (red), and Melonis pompilioides (green). Plot a) i) shows the 'raw' data for the benthic stable oxygen ($\delta^{18}O$) isotopes, plot b) i) shows the 'raw data for the benthic stable carbon ($\delta^{13}C$) isotopes and plots a) ii) and b) ii) show the same plots but with the average offset of each of the species to Cibicidoides wuellerstorfi applied to the Oridorsalis umbonatus and Melonis pompilioides plots for $\delta^{18}O$ isotopes and $\delta^{13}C$ isotopes respectively.

3.5 THEORY OF NEODYMIUM ISOTOPES

Neodymium isotope ratios were measured on fossilised fish teeth and debris/bones from deep-water core ODP Site 1063 covering the MIS 6/5 transitions to reconstruct past seawater Nd isotopic compositions (e.g. Martin and Haley, 2000). The $^{143}Nd/^{144}Nd$ ratio of seawater, typically expressed as ε_{Nd}, has been successfully used to trace water masses within the Atlantic Ocean (e.g. Piotrowski et al., 2005; Roberts et al., 2010), with more negative values indicating unradiogenic waters associated with North Atlantic Deep Water (NADW) (Piepgras and Wasserburg, 1987; ε_{Nd} = -13.5), whereas less negative, radiogenic ε_{Nd} values are associated with Southern Soured Water (SSW) (Jeandel, 1993; ε_{Nd} = -7 to -9). It follows that incursion of nutrient-rich, corrosive SSW to the core sites would result in higher % fragmentation, low $\delta^{13}C$, and higher ε_{Nd} values, whereas a dominance of nutrient-depleted (high $\delta^{13}C$), relatively uncorrosive NADW allows better preservation, lower % fragmentation and lower ε_{Nd} values.

Deep water records of εNd across the last deglaciation (Termination 1, T1) have provided valuable information about water mass mixing that has improved our understanding of the ocean dynamics (e.g. Piotrowski et al., 2004; Gutjahr et al., 2008; Roberts et al., 2010; Crocket et al., 2014; Piotrowski et al., 2012; Skinner et al., 2013; Böhm et al., 2015). However, considering all these records, questions still remain whether the Nd isotopic composition of northern and southern sourced water masses stay constant on glacial-interglacial timescales, and processes such as boundary exchange have to be taken into account as well (Lacan and Jeandel, 2005; Wilson et al., 2013a).

Here we present a high-resolution record of ε_{Nd} derived from fish debris from ODP site 1063 across Termination 2. The different external and internal forcing (e.g. insolation versus freshwater) applicable to T2 make this a useful comparator for studies focused on T1. We find large (up to 4 εNd units) fluctuations across T2 that can be related to high latitude climate changes as recorded by ice cores and other high-resolution climate archives. We also identify periods of extremely negative Nd isotopic compositions (i.e. values as low as -15.6; see also Böhm et al., (2015) that require explanations beyond the simple mixing of northern and southern derived water masses as encountered in the modern ocean. Our results may therefore carry important implications for understanding North Atlantic deep-water formation processes during critical climate transitions.

3.5.1 NEODYMIUM ISOTOPE SYSTEMATICS

Radiogenic ^{143}Nd is produced by the alpha decay of ^{147}Sm over billions of years. Samarium is more compatible than Nd in the mantle, and the two processes combine to produce distinct Nd isotopic composition (i.e. $^{143}Nd/^{144}Nd$ ratio) on the continents dependent on age and lithology (e.g. Goldstein and Hemming, 2003). In the case of the North Atlantic, the Labrador Sea is surrounded by old continental crust, resulting in very negative run-off from weathering and erosion to the surface ocean. In contrast, the Nordic Seas are characterised by more radiogenic values due to the influence of young volcanic areas such as Iceland (Figure 3.32; see Jeandel et al., (2007), for a global bedrock compilation). It is hence continental inputs from the geographical area surrounding sites of deep-water formation that set the surface ocean isotopic composition.

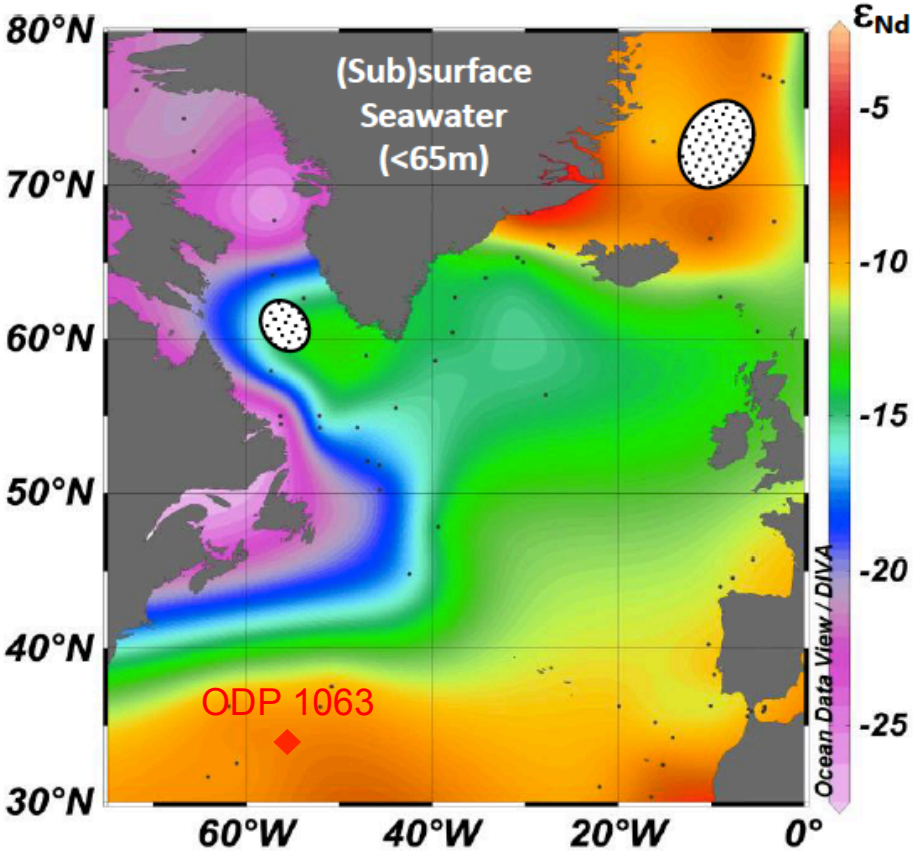

Figure 3.32. Map of modern near-surface seawater Nd isotopic composition, based on a compilation of data by (Lacan et al., 2012) with additional data from Stichel et al., (2015) and Lambelet et al., (submitted) using stations where the topmost measurement was in the uppermost 65m of the water column. One exception was

made in the Labrador Sea, where a measurement from 100m depth was included. For the Baffin Bay area north of the shallow sill separating it from the Labrador Sea, data from the entire water column were integrated. ODP Site 1063 indicated by the red diamond. Sites of deep-water formation indicated by the white areas with black dots. Figure created using Ocean Data View (Schlitzer, 2009), http://odvawi.de, 2014.

3.5.2 NEODYMIUM SIGNAL IN THE MODERN OCEANS

The power of Nd isotopes as a water mass tracer, away from the continental input sources, is illustrated using the northern part of GEOTRACES transect GA02 along the western North Atlantic (Figure 3.33). Modern NADW is mainly composed of a delicate balance of waters sinking in the Nordic Sea (i.e. overflows, which ultimately form lower-NADW) and winter time convection in the Labrador Sea (producing upper-NADW) (e.g. Dickson and Brown, 1994) (see Figure 3.32). Hence surface water Nd isotopic compositions in these areas are important to the composition of NADW exported from the subpolar gyre. Figure 3.33 denotes modern Labrador Sea water in blue/purple with very negative Nd isotopic compositions (ε_{Nd} ~ -14). This water mass travels southwards from the Labrador Sea and is confined to water depth above ~2000 metres. ODP Site 1063 is located on the Bermuda Rise at 33.69°N, 57.62°W at a water depth of 4584m. It is important to note that in the modern LSW does not reach the depth of ODP Site 1063, which instead is bathed in lower-NADW with an ε_{Nd} value about -12.7 at the location (Lambelet et al., submitted) in the modern ocean.

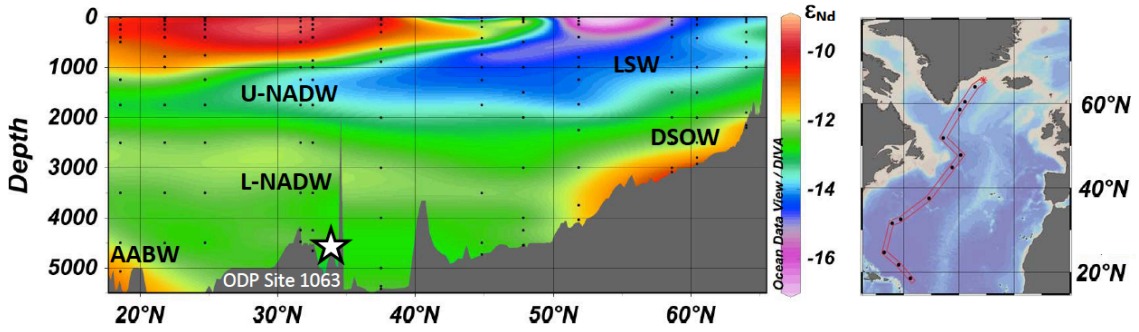

Figure 3.33. Station map and seawater Nd isotopic compositions from GEOTRACES cruise GA02 (Lambelet et al., submitted) highlighting that in the modern ocean only upper NADW carries a very negative εNd fingerprint, derived from subduction of waters in the Labrador Sea (NW Atlantic Ocean). Overflow waters from the NE Atlantic Ocean, which form the precursor water masses for lower NADW, carry a

more radiogenic (higher εNd) fingerprint. Figure created using Ocean Data View (Schlitzer, 2009), http://odvawi.de, 2014.

3.5.3 NEODYMIUM METHODOLOGY

Neodymium isotope analyses were carried out on targeted samples following the production of the planktonic $\delta^{18}O$ record (*Globigerinoides inflata)*. The criteria for sample selection were to target the extremes of the planktonic $\delta^{18}O$ record as well as important transitions. Figure 3.34 shows the selected samples for neodymium analysis based on the planktonic $\delta^{18}O$ record.

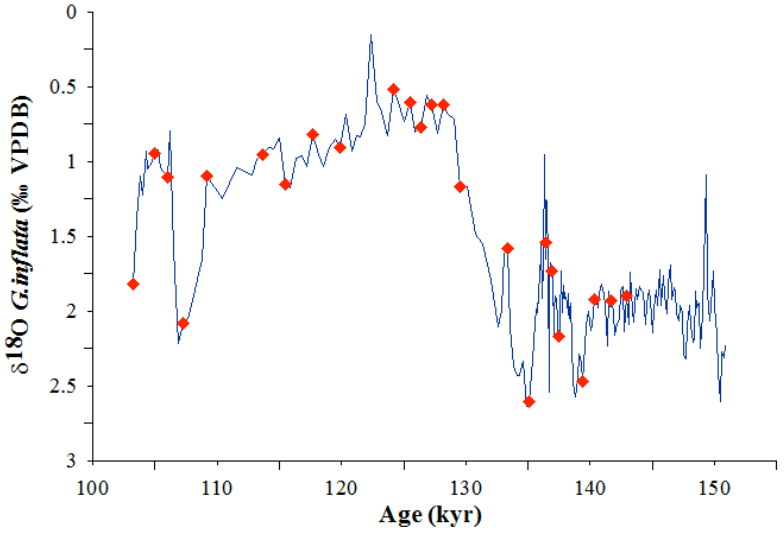

Figure 3.34. The targeted samples for Nd isotope analysis (red diamonds) based on the planktonic $\delta^{18}O$ record from G. inflata (blue).

Neodymium was isolated from 200-400µg of fish teeth and/or debris, cleaned via multiple ultrasonication steps with de-ionized water (ultrapure Milli-Q water, 18.2MΩ water) and methanol. Samples were dissolved in 2M HCl and the rare earth element (REE) fraction was separated from the sample matrix using Eichrom TRUspec™ resin. Subsequently, Nd was separated from the remaining REE using Eichrom LNspec™ resin, following standard procedures (following Pin and Zalduegui, 1997). The majority of the neodymium isotope analysis (16 samples) were performed in static mode on a Nu Plasma multi-collector inductively coupled plasma mass spectrometer (MC-ICP-MS) with additional samples (12 samples) being analysed on a Thermo Scientific Triton thermal ionization mass spectrometer (TIMS) at Imperial College London. Instrumental

mass bias was corrected for using an exponential law and a $^{146}Nd/^{144}Nd$ ratio of 0.7219, measured $^{143}Nd/^{144}Nd$ ratios of the JNdi standard yielded ratios of 0.512133 ± 0.000013 (2SD, n=8) and 0.512056 ± 0.000015 (2SD, n=27) during two separate sessions on the Nu Plasma. Measurements on the TIMS were carried out as Nd oxides (NdO+) following the method outlined by Crocket et al., (2014) yielding JNdi $^{143}Nd/^{144}Nd$ ratios of 0.512101 ± 0.000007 (2 SD; n= 5). Accuracy was achieved by correcting all sample results from both machines to the published $^{143}Nd/^{144}Nd$ JNdi ratio of 0.512115 ±0.000007 (Tanaka et al., 2000). Processing of the USGS BCR-2 basalt reference material yielded a $^{143}Nd/^{144}Nd$ value of 0.512625±16 (2 s SE) on the Nu Plasma and 0.512631±5 and 0.512644±4 on the TIMS , which compares well to the published value of 0.512638±15 (2s SD, n= 10) (Weis et al., 2006). Analysis of a fossil bone composite standard (using published preparation techniques (Scher and Delaney, 2010) yielded $^{143}Nd/^{144}Nd$ of 0.512364±20 and 0.512368±23 (2 s SE), in agreement with the average published value of 0.512349±21, (Scher and Delaney, 2010). Comparability between both machines was furthermore demonstrated by excellent agreement of results for four samples (see Appendix 11, chapter 7), where replicate sample runs were performed and an average value was taken for the figures. Procedural blanks were consistently below 10pg Nd.

3.5.4 SAMPLE COMPOSITION

There were various different types of fish teeth/debris found throughout the core and indeed within the same sample. All fish teeth and debris were picked from each of the identified samples to be analysed and the composition of each of the samples was noted (the details can be found in the appendix). Some samples in parts of the core were too small for analysis and thus some samples were combined (see appendix for details). Figure 3. and Figure 3.35 show a few examples of the different types of fish teeth/debris that were analysed in the core.

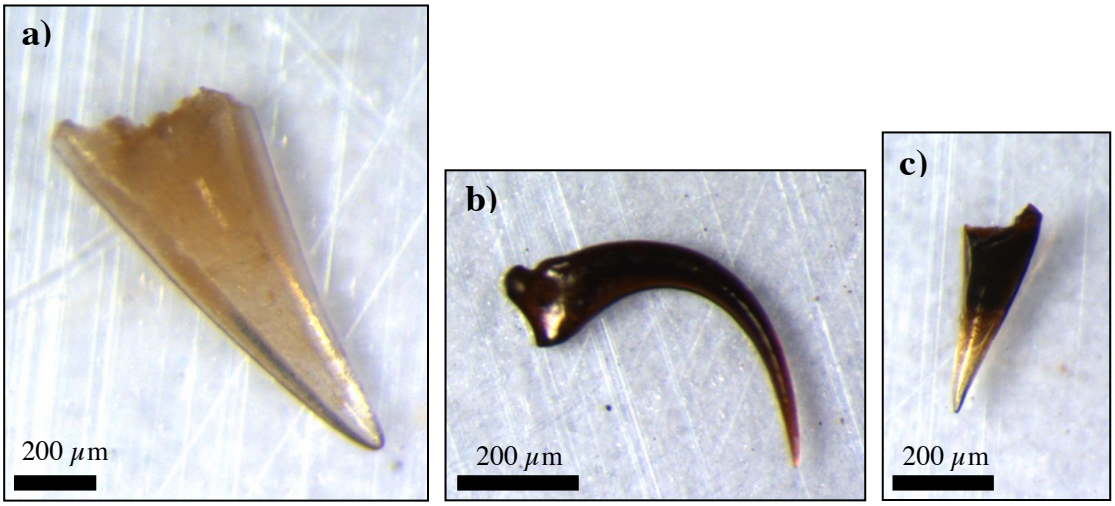

Figure 3.39. A few examples of fish teeth that were found in the core; specimen a) HB, C4, S4; 96-98cm – 35.14mcd; b) HB, C4, S4; 60-62cm – 34.78mcd; and c) HC, C5, S3; 89-91cm – 38.85mcd.

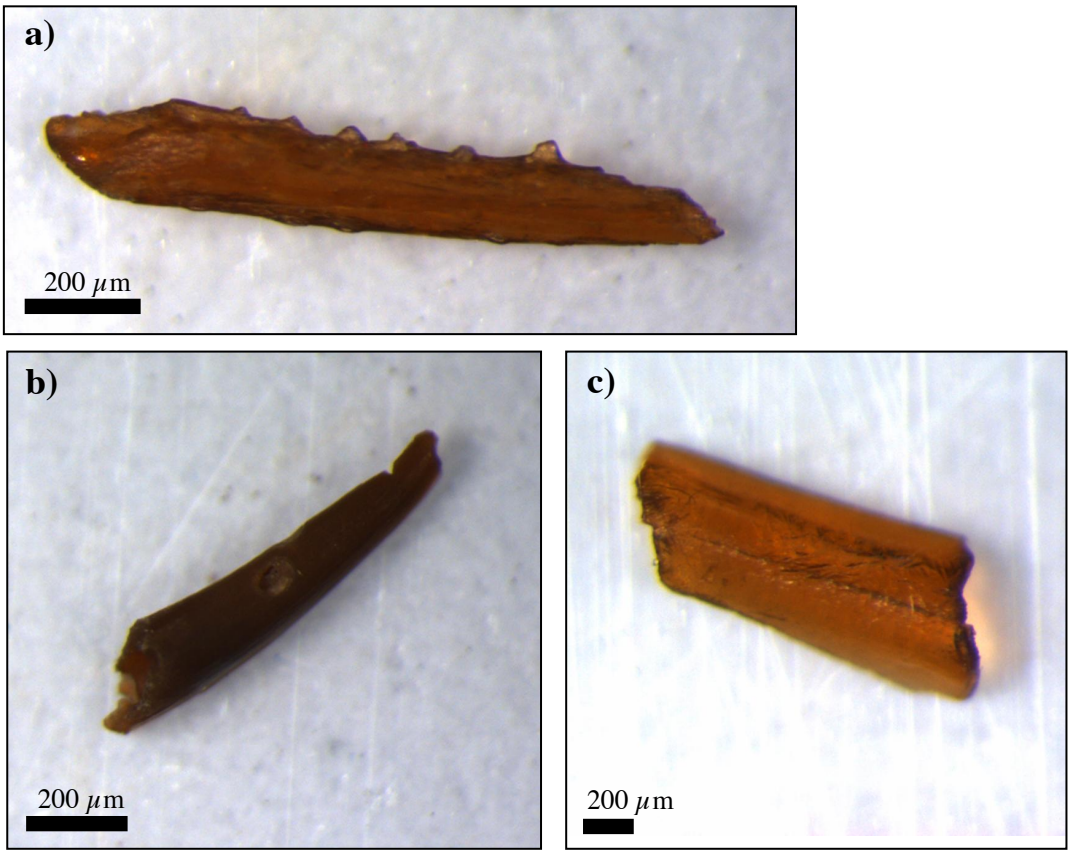

Figure 3.35. A few examples of fish debris that were found in the core; specimen a) HB, C4, S5; 48-50cm – 36.16mcd; b) HB, C4, S5; 112-114cm – 36.80mcd; and c) HB, C4, S5; 52-54cm – 36.20mcd.

Fish teeth and debris acquire their Nd concentrations during an early diagenetic reaction at the sediment/water interface (e.g. Staudigel et al., 1985). As such, the fossil material records the Nd isotopic composition of the overlying bottom water (Wright et al., 1984; Martin and Haley, 2000). Once buried the Nd isotopic signal in fish teeth has been shown to resist alteration during burial (Martin and Haley, 2000), thus providing a way to reconstruct the bottom-water compositions through time. Both fish teeth and debris have been found to uptake the ε_{Nd} signal in the same way and produce the same isotopic compositions (Thomas et al., 2003). Here we therefore combine both fish teeth and debris in a single sample.

3.6 AGE MODEL

Since we wish to compare our records directly with those from ice cores we need to refine earlier versions of the age model for ODP site 1063 across T2 that were based on orbital and palaeomagnetic approaches (Gruetzner et al., 2002; Channell et al., 2012). In a recent study Thornalley et al., (2013) derived an age model for the same core across the MIS 5a/4 boundary by tuning between a high resolution record of planktic $\delta^{18}O$ (measured on *G. inflata*) and the Greenland ice core temperature record (Figure 3.36). Abrupt shifts in planktic $\delta^{18}O$ (including for *G. inflata*) in the Northwest Atlantic are thought to have been synchronous to the shifts in Greenland ice core $\delta^{18}O$ across Termination 1 and throughout MIS 3 (Keigwin, 1996; McManus et al., 2004). Although planktic $\delta^{18}O$ from the subtropical Northwest Atlantic during D-O events likely contains both temperature and salinity signals, the 'raw' planktic $\delta^{18}O$ appears in-phase with Greenland climate, at least on multi-centennial and longer timescales (Schmidt et al., 2006). Because the Greenland record does not encompass Termination 2 we instead use the synthetic record of Greenland variability, GL$_T$_syn (the millennial-scale component of which, GL$_T$_syn_hi, provides a proxy for anomalous northward heat transport associated with abrupt changes in the AMOC (Barker et al., 2011)) as a tuning target. The record of atmospheric CH_4 from EDC (Loulergue et al., 2008) provides additional constraints because sharp increases in CH_4 are consistently aligned (within ~60yr) with rapid shifts in Greenland temperature during the last 120kyr (Baumgartner et al., 2014). We place our interval of interest within a longer-term temporal context using a slightly lower resolution record of planktic $\delta^{18}O$ (made on *G. ruber*) (Channell et al., 2012)

before making refinements using our new high-resolution $\delta^{18}O$ record (Figure 3.36). Also shown in Figure 3.36 is the proxy record for $\%CaCO_3$ in the same core (Gruetzner et al., 2002), which shows good correspondence between carbonate preservation and warm intervals over the last glacial cycle, in line with the interpretation of (Keigwin and Jones, 1994). Based on this we add an additional 2 tie points beyond 200kya, although these do not affect our interval of interest. Absolute uncertainty in our age model will derive from the precision of alignment between the records and the absolute uncertainty of the ice core age model (in this case AICC2012 (Bazin et al., 2013; Veres et al., 2013)) but since we are interested in the relative timing of events with respect to the ice core record we can exclude the latter of these components. Furthermore, if our alignment approach (which assumes synchronicity between surface ocean temperature variability and northern climate, as reflected by CH_4 and GL_T_syn) is correct then we can assess the relative timing of deep ocean changes with respect to those in the ice core record by comparing between the surface and deep water responses within our core. In the case of the implied resumption of deep overturning circulation following HS11, we note that the -0.75‰ shift in benthic $\delta^{18}O$ occurs across the same interval (i.e. from one sample to the next) as the final warming implied by planktic $\delta^{18}O$ at the end of the HS11, which we tie to the abrupt rise in CH_4 ~129ka (Figure 3.36). The tie point at this time implies a sedimentation rate change from 16.7 to 11.1cm/kyr and given a sampling frequency of 4cm we estimate that the surface and deep responses were synchronous to within 300±60yr. Since the abrupt rise in CO_2 ~129ka (actually taking place between 128.8 and 128.5ka (Bereiter et al., 2015)) was aligned with the rise in CH_4 (128.9 to 128.5ka) to within 100yr we estimate that the recovery of deep overturning circulation within the North Atlantic was synchronous with the abrupt rise in CO_2 to within 400yr.

Table 3.4 Sample sections used in both the original splice from work by Channell et al., (2012) and the 'new' splice from ODP Site 1063 for Termination 2.

ODP 1063 Original Splice (T2)	**ODP 1063 Splice used in this study (T2)**
Hole C, Core 4, Section 4 (148-150cm)	Hole B, Core 4, Section 3 (132-150cm)
Hole C, Core 4, Section 5 (0-149cm)	Hole B, Core 4, Section 4 (0-150cm)

Hole A, Core 4, Section 5 (50-62cm)	Hole B, Core 4, Section 5 (0-150cm)
Hole A, Core 4, Section 4 (70-132cm)	Hole B, Core 4, Section 6 (0-94cm)
Hole A, Core 4, Section 5 (0-142cm)	Hole C, Core 5, Section 3 (17-151cm)
Hole A, Core 4, Section 6 (0-142cm)	Hole C, Core 5, Section 4 (0-146cm)
Hole A, Core 4, Section 7 (0-52cm)	Hole B, Core 5, Section 1 (109-151cm)
Hole C, Core 5, Section 2 (0-132cm)	Hole B, Core 5, Section 2 (0-70cm)
Hole C, Core 5, Section 3 (0-62cm)	

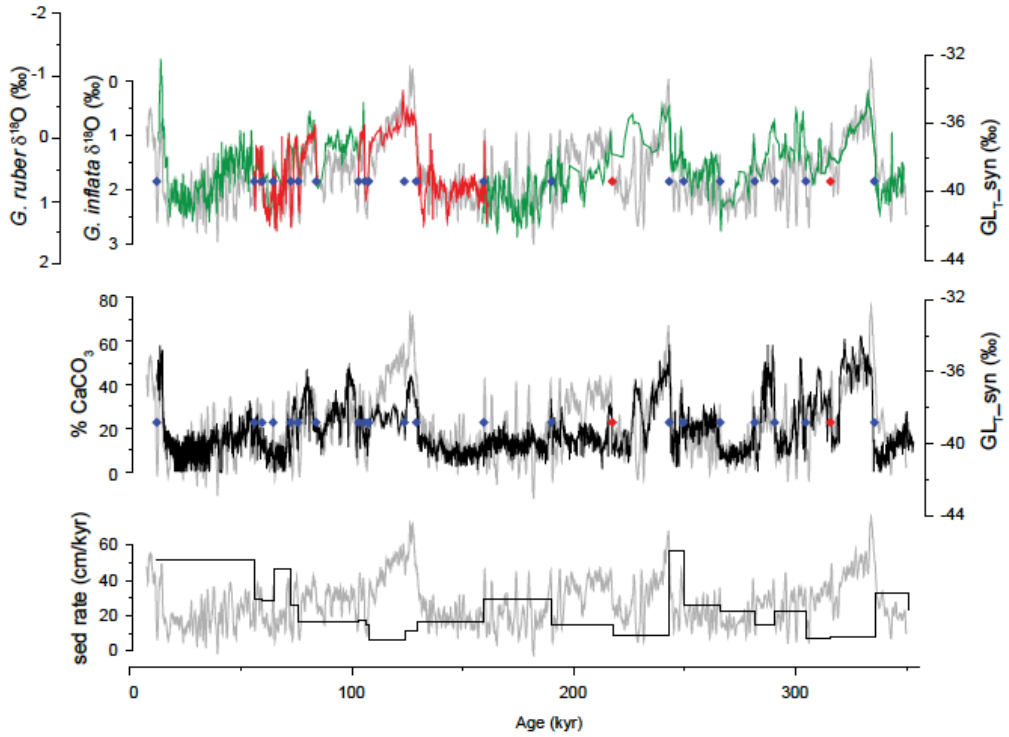

Figure 3.36. Age model used in this study. Tuning target is the synthetic record of Greenland climate variability (Barker et al., 2011) (in grey) on the AICC2012 age model (Bazin et al., 2013; Veres et al., 2013), supplemented by the record of atmospheric CH_4 (Loulergue et al., 2008) across the interval of interest. Upper green curve is the record of planktic $\delta^{18}O$ measured on G. ruber (Channell et al., 2012). Red curves are $\delta^{18}O$ of G. inflata as published by Thornalley et al., (2013) across MIS 5/4 and as part of this study across T2. Black curve is the proxy record for $\%CaCO_3$ (Gruetzner et al., 2002) showing better carbonate preservation during warmer intervals. Blue diamonds in upper panels are tuning points between planktic $\delta^{18}O$ and

GLT_syn. Red diamonds are additional points between %CaCO3 and GLT_syn. Lower curve is sedimentation rate implied by our age model.

3.7 RESULTS

Our new record (Figure 3.37) indicates that the water mass bathing the site during HS6 had a very radiogenic Nd isotopic composition (ε_{Nd} = -10.1) approaching the composition of modern Antarctic Bottom Water (AABW) (εNd of ~ -9 (Piepgras and Wasserburg, 1982; Stichel et al., 2015)) in the Atlantic sector of the Southern Ocean. The preservation proxies suggest that the water mass bathing the site was corrosive (high % fragmentation ~ 40-80% and low whole shells/g, ~10-50 shells/g) with a high preformed nutrient content (low benthic $\delta^{13}C$), indicating a weakened/shoaled AMOC. The most negative εNd values are observed during MIS 5e ((ε_{Nd} = -15.6, and coincide with the peak in the number of whole shells/g (>3000 shells/g) and minimum fragmentation (<1.5%), suggesting that a well-ventilated, possible northern sourced water mass dominated the deep North Atlantic during MIS 5e. A three epsilon unit shift in the Nd isotopic composition from less negative to more negative values at the end of T2 is in line with the abrupt surface warming recorded by planktic $\delta^{18}O$ along with the disappearance of ice rafted debris (IRD grains/gram) and *Neogloboquadrina pachyderma* (%NPS) in the North Atlantic (resumption of strong and deep AMOC bringing warm surface waters to the North Atlantic). Combined, these records provide evidence for a shift from southern to northern-sourced deep waters at the end of T2, as also suggested recently by (Böhm et al., 2015). According to our age model, this shift occurred in line with a sharp rise in atmospheric CH_4 at the beginning of MIS 5e. Comparing this shift during T2 with T1, we suggest that a similar sequence of events (and thus a similar switch in the dominance of water masses in the deep North Atlantic) was observed during the transition from HS1 to the B-A (McManus et al., 2004; Roberts et al., 2010), with the notable difference of less radiogenic absolute Nd isotopic compositions during the B-A.

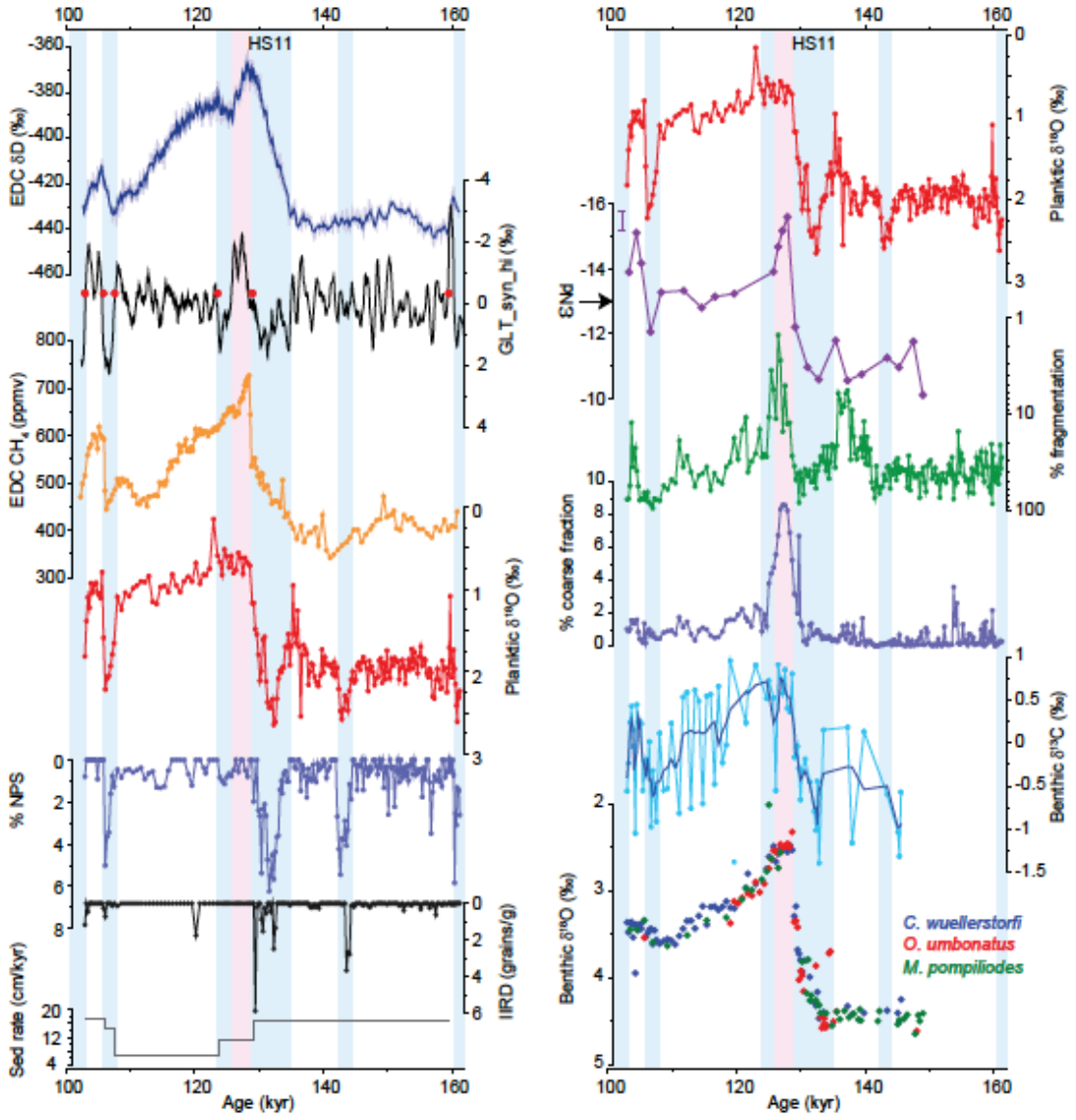

Figure 3.37. Surface and deep records from ODP Site 1063. Panel A (from top to bottom) Antarctic ice core temperature proxy, EDC (EPICA Dome C) δD (Jouzel et al., 2007); GLT_syn_hi, a proxy for northward heat transport associated with the AMOC (derived from EDC δD) (Barker et al., 2011); atmospheric CH_4 from EDC (Loulergue et al., 2008); (all other records are from ODP Site 1063) planktonic $\delta^{18}O$ measured on Globorotalia inflata; %NPS (% Neogloboquadrina pachyderma out of total planktic foraminifera); number of IRD (Ice Rafted Debris) grains/g; implied sedimentation rate. Filled red circles are tuning points between ODP Site 1063 planktic $\delta^{18}O$ and CH_4/ GLT_syn_hi. Panel B (from top to bottom); planktonic $\delta^{18}O$; seawater ε_{Nd} (arrow is modern value at ODP Site 1063, error bar is max representative uncertainty); % foraminiferal fragmentation; % coarse (>63mm) fraction; benthic $\delta^{18}O$ (Cibicidoides wuellerstorfi, Melonis pompilioides (-0.15;

Methods) and Oridorsalis umbonatus (-0.38)). Blue vertical boxes are cold intervals; pink box is our inferred overshoot of the AMOC.

Figure 3.38 places our ε_{Nd} record into context and compares it with other published and unpublished records (Roberts et al., 2010 and Thornalley et al, unpublished respectively) across the last 160 kyr. The absolute values of the three records align well with each other (ranging between ~ -10 to -16) suggesting that the ε_{Nd} signal is preserved consistently in both fish teeth/debris (this study, Thornalley et al., unpublished, Roberts et al., 2010) as well as uncleaned foraminifera (Roberts et al., 2010).

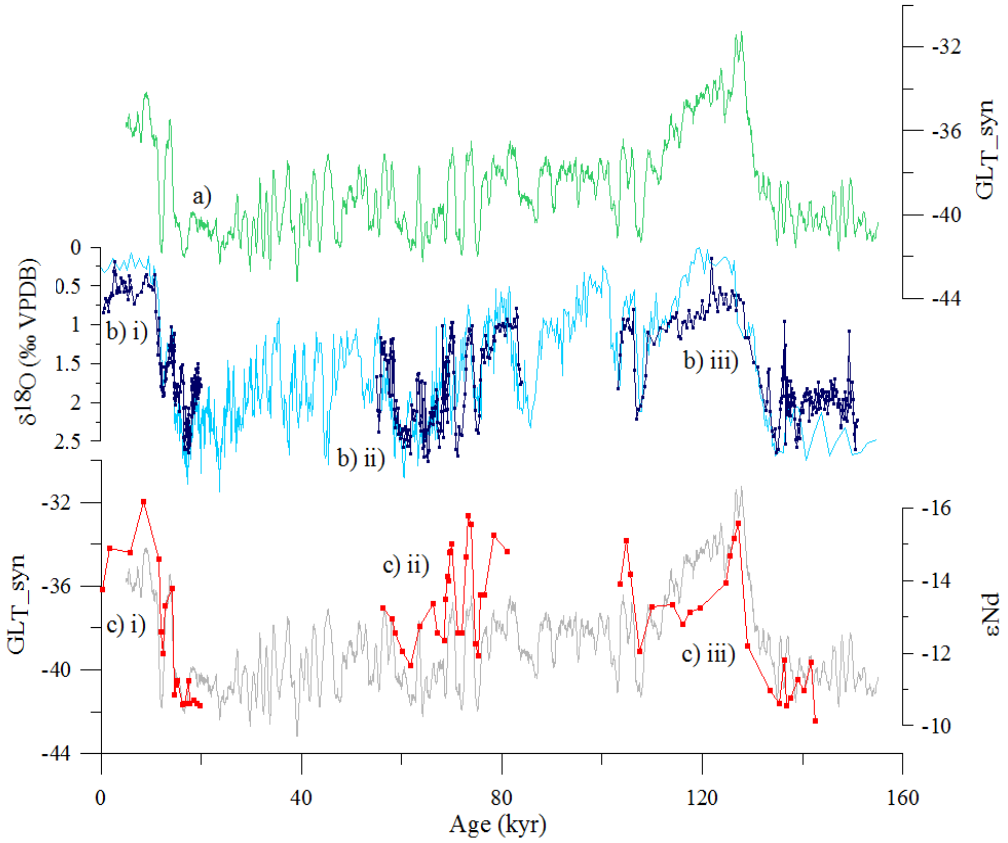

Figure 3.38. Comparison of εNd results with other proxy records and with published and unpublished data from ODP Site 1063. a) GL_T_syn on EDC3 (Barker et al., 2011); b) light blue plot, $\delta^{18}O$ G.bulloides from Site MD95-2042 (Shackleton et al., 2000), dark blue plot $\delta^{18}O$ G.inflata from ODP Site 1063, i) data from Roberts et al., 2010; ii) Thornalley et al., unpublished and iii) this study; c) grey plot shows GL_T_syn on EDC3 (Barker et al., 2011) red plot shows the εNd values of i) Roberts et al., 2010

from fish debris and uncleaned foraminifera; ii) Thornalley et al., unpublished from fish teeth and debris and iii) this study from fish teeth and debris.

3.8 DISCUSSION

The shift towards higher benthic $\delta^{13}C$ and better preservation (Figure 3.37) at the onset of MIS 5e suggests the arrival of better-ventilated deep waters to the North Atlantic. This observation is consistent with the presence of northern sourced deep waters at the core location, suggesting a deepening (or strengthening) of NADW. Very negative seawater Nd isotopic compositions, however, require a different density structure from that of the modern North Atlantic. Wintertime convection in the modern Labrador Sea produces relatively warm and fresh Labrador Sea Water, which only penetrates to ~ 2000m (UNADW; Figure 3.33). Today ODP Site 1063 is bathed within LNADW, with a minor influence from the much colder and fresher AABW (Figure 3.32 and Figure 3.33). The very negative values we observe during early MIS 5e can only be derived from surface waters in and around the Labrador Sea (Figure 3.32) as the deep waters derived from the Nordic Seas and from southerly sources have much more positive values. Therefore we must conclude that as the AMOC recovered after HS11 it was the result of a drastic deepening of Labrador Sea Water. Results from a recent Coupled General Circulation Model experiment (Gong et al., 2013) suggest that convection in the South Labrador Sea could reach depths of 3000-4000m during an abrupt deepening (our inferred 'overshoot') of the AMOC following a period of weakened AMOC. We use the term 'overshoot' to refer to the heightened mode of the AMOC following the abrupt deglaciation of a termination. The AMOC resumes and 'overshoots' following a reduced state of overturning during the preceding glacial period. The overshoot occurs as AMOC turns back on with more vigour, resulting in a deepening of AMOC and a greater penetration of NADW in to the Atlantic abyss. Following the overshoot, AMOC reduces again to resume a more typical overturning state.

Our new record of benthic foraminiferal $\delta^{18}O$ (Figure 3.37 and Figure 3.40) provides evidence for the timing and rapidity of the change in ocean circulation at the onset of MIS 5e (Figure 3.37). The record reveals a very large (~0.75‰) and abrupt decrease in $\delta^{18}O$ at the same time as we observe surface-ocean warming ~129kyr. The transition

takes place in less than 300±60yr (occurring between two samples) and so cannot be explained by a decrease in continental ice volume. More likely it reflects a change in the relative dominance of water masses with very different Temperature/Salinity (TS) characteristics within the abyssal North Atlantic. The observed shift in benthic $\delta^{18}O$ can be projected into TS space by assuming some knowledge of deep water $\delta^{18}O$:salinity relationships in the past. The projected shift encompasses the entire range of modern AABW to LNADW (Figure 3.39). In fact the implied change is larger than the modern offset between AABW and bottom waters at our site, meaning that if an equivalent to modern AABW were present at the site of ODP 1063 during HS11 then its replacement by a water mass more similar to modern UNADW could explain the observed change in benthic foraminiferal $\delta^{18}O$.

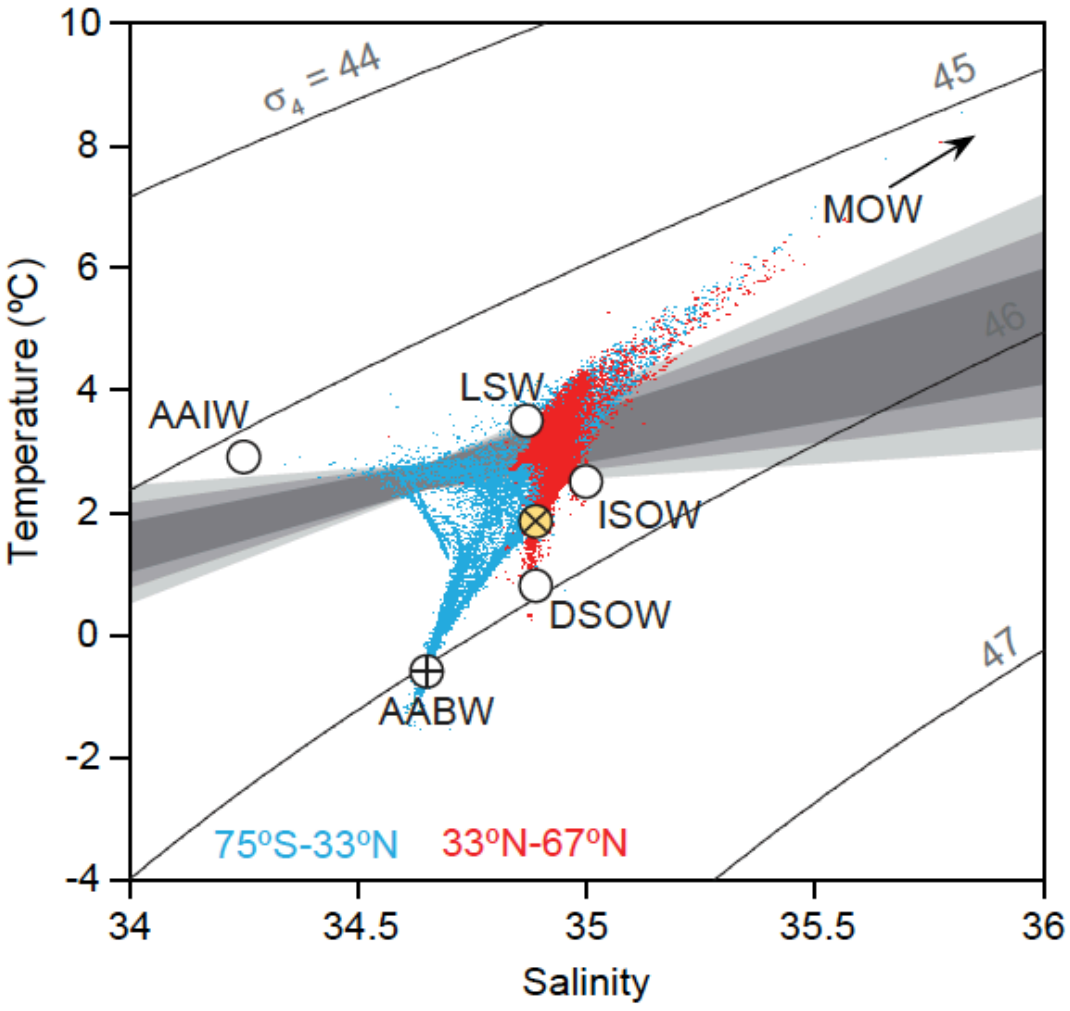

Figure 3.39. Temperature/Salinity plot showing the modern distribution of waters >1500m in the open Atlantic Ocean (0 to 80°W) (Key et al., 2004). Yellow circle is

bottom water at ODP Site 1063, white circles are end-members. The grey envelope represents the range of solutions attained with a 0.75‰ decrease in benthic $\delta^{18}O$ starting from the AABW end member, calculated using a temperature sensitivity ranging from 0.22 to 0.25‰ per ºC and $\delta^{18}O$:salinity = 0.42 with an uncertainty of ±0.3 (light grey region), ±0.2 (mid grey) and ±0.1 (dark grey). AAIW =Antarctic Intermediate Water; AABW = Antarctic Bottom Water; LSW = Labrador Sea Water; DSOW = Denmark Straight Overflow Water; ISOW = Iceland Scotland Overflow Water; MOW = Mediterranean Overflow Water.

As eluded to, the main differences in the records when comparing T1 with T2 is that in T1 there is an interruption half way through the termination that is recorded as a plateau of CO_2 change, during the Bølling-Allerød, B-A (Figure 3.40). We do not record a similar interruption to the deglacial CO_2 record during HS11 (T2), instead this is postponed until the end of the termination whereby an 'overshoot' is recorded as the resumption in the ocean circulation is observed (MIS Stage 5e). We suggest here that MIS Stage 5e is T2's equivalent of the B-A recording an 'overshoot' in AMOC as the overturning circulation resumes with increased vigour, resulting in a greater penetration of NADW in to the deep Atlantic.

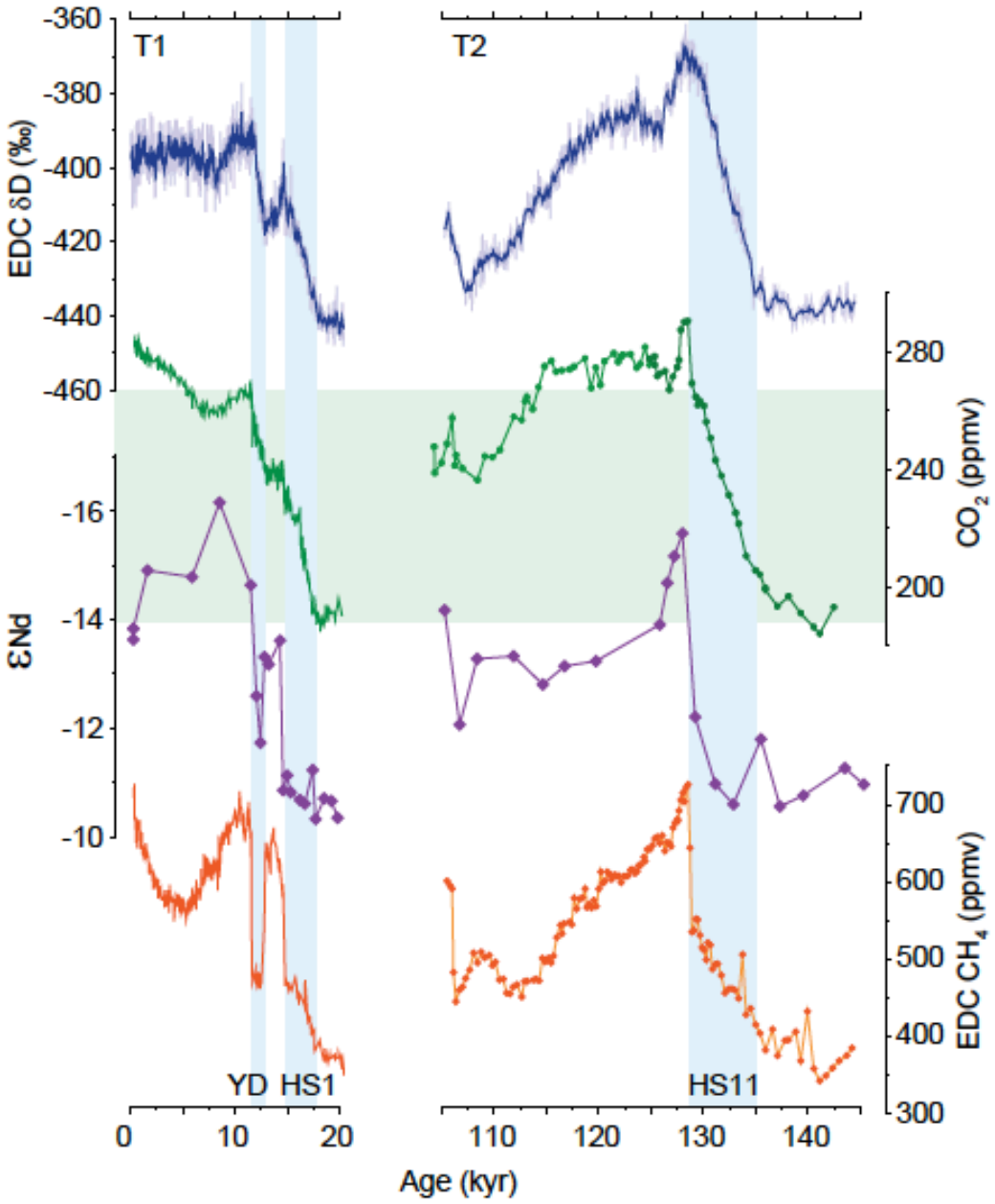

Figure 3.40. Evolution of CO_2 across the last two terminations. Records of (from top to bottom) Antarctic temperature (δD proxy) (Jouzel et al., 2007), atmospheric CO_2 (Lourantou et al., 2010; Marcott et al., 2014; Bereiter et al., 2015), seawater ε_{Nd} ((Roberts et al., 2010) and this study) and atmospheric CH_4 (Loulergue et al., 2008). Blue boxes are intervals of weakened and / or shallow AMOC; Green box encompasses the deglacial change in CO_2 across T1. YD = Younger Dryas, HS1 and HS11 are Heinrich stadials.

3.9 CONCLUSION

When compared to T2, the apparent lack of response of CO_2 during the B-A, following HS1, should perhaps be considered as anomalous, probably reflecting a complex combination of mechanisms with opposing influences on CO_2. For example the tendency for a strengthened AMOC to draw down CO_2 (Schmittner and Galbraith, 2008) could have been countered by continued outgassing of CO_2 as a result of reduced sea ice cover and sustained deep ocean ventilation within the Southern Ocean during the B-A (Skinner et al., 2013). The continuous rise in CO_2 throughout T2 was associated with cold conditions across the North Atlantic and a corresponding reduction in the AMOC and thus the influence of northern –sourced deep waters to the North Atlantic, analogous to the rise in CO_2 during HS1. However, unlike the last deglaciation, Termination 2 was not interrupted by a resumption of the AMOC. By the end of HS11 atmospheric CO_2 had already reached similar levels as attained by the end of Termination 1 (Figure 3.40). Following the subsequent resumption and overshoot of the AMOC early in MIS 5e we then record a reduction in CO_2 reaching values more like those of the Holocene as ocean circulation recovered to more modern-like conditions by ~124yr (Hodell et al., 2009) (Figure 3.40). We therefore suggest that the larger net change in CO_2 across T2 (as compared with T1) was a direct consequence of the timing of abrupt AMOC resumption with respect to other deglacial changes.

Furthermore, we suggest the extreme negative εNd values down to -15.6 in the record require a different origin/mixture of water than is bathing ODP Site 1063 today. The Labrador Sea is an obvious candidate for generating such negative values. Our results show a persistent coupling of changes in the deep ocean chemistry (ε_{Nd}) in the North Atlantic and high latitude climate change. Secondly we suggest that the late recovery of the AMOC during T2 (in particular the absence of a 'B-A-like' interruption) may explain the larger amplitude of deglacial CO_2 rise associated with the penultimate deglaciation.

4 VERY RAPID ATTAINMENT OF INTERGLACIAL CONDITIONS AT THE ONSET OF MIS 11

4.1 INTRODUCTION

In terms of orbital forcing (Berger, 1978; Berger and Loutre, 1991) and the degree of climate variability, Marine Isotope Stage (MIS) 11 (428–360 kyr) is the closest past analogue we have to the Holocene (Loutre and Berger, 2003), and as such the closest analogue we have when making predictions about the future state of our climate system. The orbital parameters during the early part of this isotope stage were very similar to those that prevail at the present day, with low eccentricity, high obliquity and low precessional amplitude (Berger and Loutre, 1991; Loutre and Berger, 2003). It is important, therefore to produce records from climatically sensitive areas (i.e. North Atlantic) to aid our understanding of this possible analogue for future climate change.

In the modern the North Atlantic Ocean (ODP Site 983) is influenced by the warm, saline surface waters of the Irminger Current, specifically the location of the Polar Front (PF) (Figure 4.41). The PF separates the North cyclonic (warm, saline waters) and Arctic anticyclonic (cold, fresh waters) circulation systems (Bashirova et al., 2014)). The Irminger Current flows northwestward towards Greenland after splitting from the North Atlantic Current (NAC) which subsequently flows across the Iceland-Scotland Ridge and in to the Nordic Seas. The NAC is a major contributor to the surface limb of the Atlantic Meridional Overturning Circulation (AMOC), flowing northeastwards across the North Atlantic into the Nordic Seas (Worthington, 1970; Østerhus et al., 2005). The AMOC redistributes heat, salt, carbon and nutrients in the Atlantic Ocean. The surface current flux in northwards and the returning deep-water flux is southwards in the Atlantic. The warm NAC plays an important role in maintaining a mild climate in northwest Europe (Rahmstorf, 2002), and as such any interglacial variability in the position of the Polar Front and resulting changes to the currents in the North Atlantic (notably the Irminger Current) would have important impacts on the climate of northwest Europe.

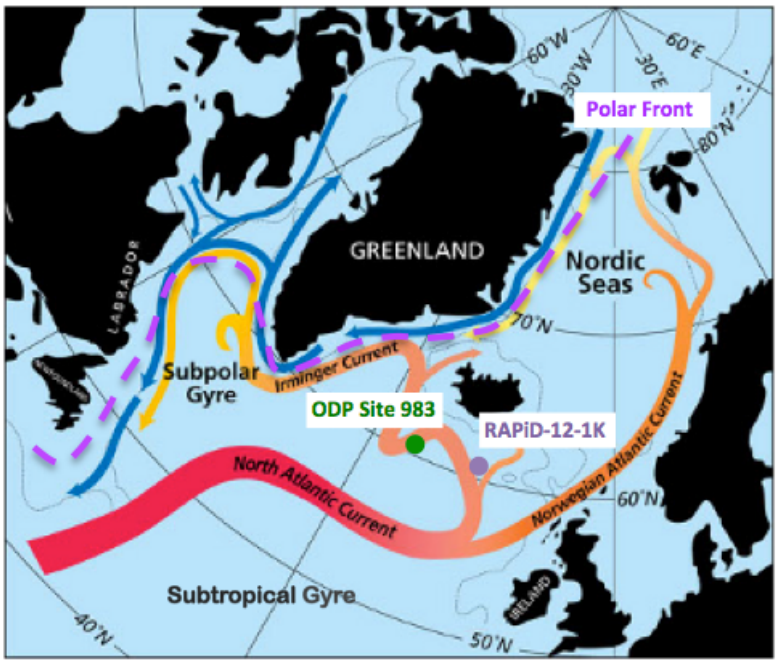

Figure 4.41 A map of the North Atlantic showing the core location of ODP Site 983; 60.408°N, 23.648°W, located in 1984m water depth and RAPiD-12-1K; 62.05°N, 17.49°N, located in 1938m water depth. The map also shows the locations of the Subpolar and Subtropical gyres as well as the North Atlantic Current and Irminger Current and the Polar Front. Figure adapted from Jack Cook graphics from Woods Hole Oceanographic Institution, Oceanus magazine.

During the Last Glacial Maximum the PF was positioned south of its modern location (Bashirova et al., 2014), reflecting a reduction in the heat transport to the Nordic Seas; (Barker et al., 2015) and producing an east-west orientated PF. The changing position of the North Atlantic Polar Front corresponds with changes the location of deep-water formation such that the southward movement of the front during the Last Glacial Maximum resulted in a southward shift in the locus of deep-water formation (MARGO Members, 2009; Sarnthein et al., 1994). Similar changes are also thought to have been associated with shifts from stadial to interstadial conditions and are important on glacial-interglacial timescales (Boyle and Keigwin, 1982; Shackleton et al., 1983; Duplessy and Shackleton, 1985; Oppo and Fairbanks, 1987; Duplessy et al., 1988), important because large scale changes in ocean circulation (notably changes in AMOC) contribute to changes in atmospheric CO_2 and the magnitude of G-IG changes.

This chapter seeks to understand the interglacial conditions of MIS 11 in the North Atlantic and provides comparison with the same interval in the South Atlantic. In addition, we compare the interglacial conditions of MIS 11 with the current interglacial of the Holocene. Primarily this chapter focuses on millennial scale changes during MIS 11 and looks at changes in the stratification of the water column during this interval. Additionally, this chapter compares the magnitude of changes across the two interglacial intervals (MIS 11 and the Holocene). Comparison of our data from MIS 11 with previously published data (see data from Chapter 2) we conclude that T5 is an extreme termination in the context of T2 and T1.

4.2 OCEANOGRAPHIC SETTING OF THE CORE LOCATION

ODP Site 983 (60.41°N, 23.65°W, 1984m water depth) was drilled in 1995 as part of Ocean Drilling Program Leg 162 (Figure 4.41) and lies south of the Arctic Front. ODP Site 983 is located on the rapidly accumulating Bjorn-Gardar sediment drift, south of Iceland. Seasonal SSTs range between 7.6-11.8°C (Figure 4.47) with an annual mean of ~9°C (Locarnini et al., 2013).

As mentioned above ODP Site 983 is located on the rapidly accumulating Bjorn-Gardar Drift, just to the south of Iceland. Today the site is under the influence of the warm surface Irminger Current as it turns northwards after splitting from the North Atlantic Current (NAC), which itself transports ~7.5Sv (1Sv = 10^6 m^3 s^{-1}) of warm (~8.5ºC) water into the Nordic Seas via the Iceland-Scotland Ridge and Fareo-Shetland Channel (Worthington, 1970; Østerhus et al., 2005). The inflow of warm Atlantic surface waters to the Nordic Seas and their subsequent cooling, convection and outflow as cold dense overflows, therefore represent an essential component of the modern Atlantic Meridional Overturning Circulation (AMOC) (Dickson and Brown, 1994).

4.3 METHODOLOGICAL BACKGROUND

4.3.1 INTRODUCTION TO STABLE ISOTOPE ANALYSIS

The distribution of temperature and salinity, both of the sea surface and the bottom waters is controlled by changes in ocean circulation, an indicator of the state of the

climate system. It has long been established that the fractionation of stable oxygen isotopes ($\delta^{18}O$) between calcium carbonate and the surrounding water it was formed in, is sensitive to temperature changes and $\delta^{18}O_{sw}$ ($\delta^{18}O$ of seawater) (Urey, 1947; Epstein and Mayeda, 1953) (see Equation 4.1 below). Subsequent work used the $\delta^{18}O$ values of planktonic foraminifera as a paleothermometer noting that changes in the $\delta^{18}O$ of seawater which records variations in both continental ice volume and local salinity changes are recorded in the $\delta^{18}O$ value in the foraminiferal test (e.g. Emiliani, 1955 and Shackleton 1967). Oxygen isotope measurements in foraminifera ($\delta^{18}O$) have provided a wealth of information about Cenozoic climate change (e.g. Emiliani, 1955, 1972; Shackleton, 1967, 1987). However, the dependence of $\delta^{18}O$ of foraminiferal calcite on both temperature and $\delta^{18}O_{sw}$ complicates their interpretation and requires independent proxies for temperature reconstruction.

Equation 4.1. Paleotemperature equation originally based on work by Shackleton, (1974) and Kim and O'Neil et al., (1997) and reformulated by Bemis et al., (1998).

$$T\,(°C) = 16.1 - 4.64\,(\delta^{18}O_c - \delta^{18}O_{sw}) + 0.09\,(\delta^{18}O_c - \delta^{18}O_{sw})$$

Note that the conversion from VPDB to VSMOW used in this study is $\delta^{18}O_{sw} = \delta^{18}O_w - 0.27‰$ (Hut, 1987).

4.3.2 INTRODUCTION TO Mg/Ca

Mg and Ca have a long residence time in seawater (22×10^6 and 1.4×10^6 years respectively (Brown et al., 1995)) and therefore changes recorded in the foraminiferal calcite on the glacial-interglacial time-scales studied here reflect changes in the substitution of Mg^{2+} in to the test rather than long-term changes in the Mg or Ca in the water column. The substitution of Mg^{2+} for Ca^{2+} into foraminiferal $CaCO_3$ is dependent on the temperature of the ambient seawater during growth such that foraminiferal Mg/Ca ratios increase with increasing temperature (e.g. Nürnberg et al., 1996; Lea et al., 1999, 2000; Lear et al., 2000; Rosenthal et al., 2000; Elderfield et al., 2002). Thermodynamic calculations for pure mineral phases predict an exponential temperature dependence on Mg uptake into calcite of approximately 3% increase in Mg/Ca per °C (Rosenthal et al., 1997), consistent with inorganic calcite precipitation (Oomori et al., 1987; Burton and Walter, 1991); however, it should be remembered

that biologically mediated processes, such as foraminifera shell growth, are rarely at equilibrium with the water it is precipitated in (de Nooijer et al., 2014). Mg/Ca in foraminiferal calcite is normally between 1-2 orders of magnitude less than predicted for inorganic precipitation (Oomori et al., 1987; Lea et al., 1999; Rosenthal and Linsley, 2006), emphasising the influence of biological processes and highlighting the need for species-specific calibrations..

In order to use the Mg/Ca paleothermometer it needs to be calibrated. Different calibration approaches have been used to determine the temperature dependence of Mg uptake into planktonic foraminiferal tests; (i) culture-based (e.g. Lea et al., 1999; Nürnberg et al., 1996); (ii) sediment traps (e.g. Anand et al., 2003); and (iii) core tops (e.g. Elderfield and Ganssen, 2000; Cléroux et al., 2008; Farmer et al., 2010; Groeneveld and Chiessi, 2011). The results from these experiments conclude there is an exponential dependence of temperature on the Mg/Ca in foraminiferal calcite such that Mg/Ca = B exp (AT) (T is the calcification temperature (in °C) and A and B are constants dependent on species). Constant A is the temperature sensitive component, e.g. Elderfield and Ganssen, (2000) quote A as 0.49, indicating approximately a 10% change in Mg/Ca ratio per °C.

Paired $\delta^{18}O$ and Mg/Ca analysis of foraminiferal shells provides a way to adjust for the temperature-dependency of $\delta^{18}O$ and isolate the $\delta^{18}O$ of ambient seawater ($\delta^{18}O_{sw}$) (Mashiotta et al., 1999; Elderfield and Ganssen, 2000; Lea et al., 2002). After removal of the ice volume effect the $\delta^{18}O_{sw}$ signal can be used to reconstruct salinity and hydrographic changes as $\delta^{18}O_{sw}$ and salinity are related linearly (both are closely affected by evaporation and precipitation). However, care must be taken when reconstructing salinity from $\delta^{18}O_{sw}$ as additional fractionation of the oxygen isotopes in the atmosphere (due to fractionation during evaporation (Craig and Gordon, 1965)) and during sea ice formation for example (O'Neil, 1968) affect the $\delta^{18}O_{sw}$ and salinity differently and as such $\delta^{18}O$ to salinity ($\delta^{18}O$-S) relationships are only regionally-coherent. Furthermore the $\delta^{18}O$-S relationship varies on seasonal, annual and inter-annual timescales. Thus the $\delta^{18}O$-S relationship varies in both time and space (LeGrande and Schmidt, 2006).

4.3.3 GLOBOROTALIA INFLATA ECOLOGY AND Mg/Ca PALEOTHERMOMETRY

The planktonic foraminifer *Globorotalia inflata* is a deep-dwelling species that inhabits transitional to subpolar oceanic regions (e.g. Bé and Hutson, 1977; Hemleben et al., 1989; Niebler and Gersonde, 1998). During its ontogenetic cycle, *G. inflata* migrates deeper in the water column, typically between 100-200m but as deep as 400m (Hemleben et al., 1989) providing great potential of recording past thermocline conditions (Cléroux et al., 2007; Chiessi et al., 2008) and subsurface temperatures.

G. inflata may form an outer calcite crust as it migrates to greater depths in the water column (Groeneveld and Chiessi, 2011; Haarmann et al., 2011). This continued calcification at depth means that *G. inflata* Mg/Ca (and $\delta^{18}O$) integrates temperature over a wide depth range. Indeed, the presence of a crust lowers the mean shell Mg/Ca (Groeneveld and Chiessi, 2011). Therefore, to obtain a meaningful temperature signal, encrusted and non-encrusted shells should not be mixed for analysis (Thornalley et al., 2009; Groeneveld and Chiessi, 2011; Haarmann et al., 2011).

Published Mg/Ca temperature calibrations for *G. inflata* from the Atlantic Ocean show significant differences (Figure 4.42). The six calibrations considered in this study (Elderfield and Ganssen, 2000; Anand et al., 2003; Cléroux et al., 2007; Thornalley et al., 2009; Farmer et al., 2010; Groeneveld and Chiessi, 2011) can be divided broadly in to two groups with different temperature sensitivities. The calibrations from Anand et al., (2003), Cléroux et al., (2007), and Farmer et al., (2010) suggest a higher sensitivity of Mg/Ca to temperature than the calibrations from Elderfield and Ganssen (2000), Thornalley et al., (2009) and Groeneveld and Chiessi (2011) as the values for constant A is higher in the former studies. The pre-exponential constant being either set or calculated to be 0.1 (Elderfield and Ganssen, 2000; Thornalley et al., 2009) or close to it (0.076 (Groeneveld and Chiessi, 2011)) follows the comprehensive multi-species calibrations results from Elderfield and Ganssen (2000) in which it was suggested that this relationship was common in the calibration equations of all the foraminiferal species. The higher value of constant A and lower pre-exponential constant used in studies by Anand et al., (2003), Cléroux et al., (2007) and Farmer et al., (2010) results in higher sensitivities of Mg/Ca to temperature and temperatures that appear too high to be correct for this study (Figure 4.42, Figure 4.46 and Figure 4.47).

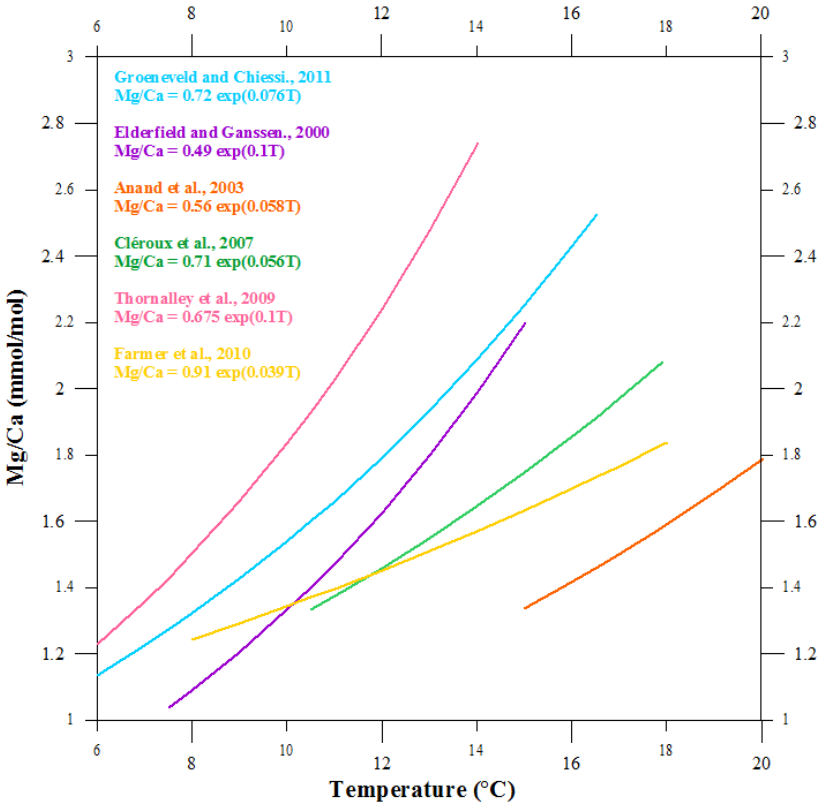

Figure 4.42. Comparison of G.inflata Mg/Ca temperature calibration curves from different studies from the Atlantic.

4.4 MATERIALS AND METHODOLOGY

Typically 30 individuals of *G. inflata* (300-355µm) were analysed for each sample for paired Mg/Ca stable isotope analysis. However as the abundance of *G. inflata* is not consistent throughout the core the total number of foraminifera analysed for analysis dropped to less than 5 individuals for 18 out of the 187 samples (see appendix for exact numbers of individuals in each sample used for paired Mg/Ca-$\delta^{18}O$ analysis). The samples were weighed, crushed, homogensied and split; approximately ¼ of the sample was used for the stable isotope analysis and the remaining ¾ was used in the Mg/Ca analysis. Analysis of the same species (and indeed the same sample) minimised the potential effects of different depth habitats and seasonality of different species on the temperature reconstruction.

4.4.1 STABLE ISOTOPE ANALYSIS

The stable isotope measurements were carried out on the Thermo Finnigan MAT 252 isotope ratio mass spectrometer coupled to a Kiel II carbonate preparation device at Cardiff University. The mass spectrometer was calibrated through the international

standard NBS-19 and all isotopic results are reported as a ‰ deviation from the Vienna Pee Dee Belemnite scale (‰ VPDB). External reproducibility of carbonate standards was better than 0.08‰ and 0.06‰ for $\delta^{18}O$ and $\delta^{13}C$.

Visual analysis of the record suggested that the $\delta^{18}O_c$ values of *G. inflata* in four samples at the bottom of the record (50.33-50.39 mcd) appeared to be too light when compared to the rest of the core. We crossed checked these samples with the $\delta^{13}C$ values and they too appeared to be too light compared to the rest of the record. We suggest that the numbers of *G. inflata* analysed in these four samples was too low ranging from 3 to 8 individuals, compared to the 30 individuals typically being analysed for the rest of the core. As such, these samples have been removed from the dataset herein.

4.4.2 Mg/Ca ANALYSIS

The presence of organic material and silicates within the foraminifera tests (Barker et al., 2003) increases the magnesium content and alters the ratio of Mg/Ca. Post-depositional diagenesis and Fe-Mn coatings (Boyle, 1983) can also alter the Mg/Ca ratio. To try to minimise the influence of these post-depositional processes and the contamination of silicates, the cleaning process that is carried out prior to the analysis aims to remove silicate phases (silicate removal stage) and organic matter (oxidation stage) following the methods of Barker et al., (2003). The same protocol was followed by the Mg/Ca temperature calibration studies mentioned in this chapter (Anand et al., 2003; Cléroux et al., 2007; Thornalley et al., 2009; Farmer et al., 2010; Groeneveld and Chiessi, 2011).

The first stage of the Mg/Ca cleaning protocol is the clay removal step; including multiple rinses with DI water and methanol with ultrasonication intervals in between rinses to get rid of any sediment attached to the test. This was followed by the oxidation step to remove organic matter by oxidation using alkali (NaOH 0.01M) buffered 1% H_2O_2. Following this, the samples were removed from the centrifuge tube to a slide with a cavity and under a microscope any remaining coarse-grained silicate particles and/or discoloured foraminiferal calcite fragments were removed using a single lash brush before replacing into new clean centrifuge tubes. The dilute acid-leach step was carried out next, using 0.002M HNO_3. This step aims to remove any potential contaminants that may have adsorbed to the shell surface during the

cleaning process (Boyle and Keigwin, 1985). Finally, the samples were dissolved in 120µl of 0.065M HNO_3 and centrifuged to remove any remaining silicate grains. Samples were transferred in to clean vials before each step involving acid and to ensure that the acid used was completely removed an additional step involving an extra two water rinses was also added. Two procedural blanks were inserted in each cleaning batch (24 samples) and were carried through all of the cleaning steps and analysed to test for any potential contamination during the cleaning process. The detailed instructions of each of the stages used in the Mg/Ca cleaning are outlined in the appendix.

Trace metal measurements were carried out using a Thermo Element XR High Resolution Inductively Coupled Plasma Mass Spectrometer (HR-ICPMS) at Cardiff University. The samples were first run for Ca concentration to enable matrix matching of the standard with the foraminiferal samples in order to calculate the elemental ratios. Three consistency standards that are made up at Cardiff University (CS1 - Consistency Standard 1; MCS - Multi-element Calibration Standard; and CS2 - Consistency Standard 2) were run at the beginning and end of every run for long-term precision calculations. During the time that the samples presented in this thesis were run on the HR-ICPMS the long-term precision for Mg/Ca measurements was better than ± 1%.

4.4.2.1 A STUDY OF POTENTIAL BIASES IN THE Mg/Ca SIGNAL FROM SILICATES

A test was carried out to establish if the samples required the additional (coarse) silicate removal stage prior to the dilute acid leach step (see protocol in the previous section). I hypothesised that as the aperture of *G. inflata* is much smaller that that of other planktonic foraminifera commonly used for Mg/Ca analysis (e.g. *G. bulloides* and *N. pachyderma),* silicates would be less likely to enter the foraminiferal chambers, and thus that the silicate removal stage might be redundant. This test was carried out on three different samples from the interglacial period MIS 11, (Hole A, Core 5, Section 5); approximately 50 individual translucent *G. inflata* specimens were picked from the 300-355µm size fraction, (the exact numbers of shells and the sample divisions and depths of each sample are shown in the appendix). Each sample was crushed, homogenised and split into 6 equal aliquots; 3 of them were ‘dirty’ samples

and then other 3 were 'clean' samples. The difference between the two protocols is that the although both sets of samples were taken through the clay removal step, the 'clean' samples involved an additional step which included removing any remaining the silicates by hand using a single lash brush under the microscope.

4.4.2.2 A STUDY OF POTENTIAL BIASES IN THE Mg/Ca SIGNAL OF *G. INFLATA*

A second test was carried out to establish the potential differences that may arise from measuring opaque vs. translucent forms of *G. inflata*. Differentiation between the different wall types has previously been associated with encrustation of the shells at depth (i.e. at colder temperatures) (Groeneveld and Chiessi, 2011) and as such have lower Mg/Ca values (thus can bias the temperature signal towards colder temperatures) than the non-encrusted specimens. This test was carried out on samples from the interglacial period of MIS Stage 11, (Hole A, Core 5, Section 5); approximately 50 three-chambered translucent *G. inflata* and 50 three-chambered opaque *G. inflata* specimens were picked from the 300-355μm size fraction, (the exact numbers of *G. inflata* and the sample divisions and depths of each sample are shown in the appendix). Each sample was crushed, homogenised and split in to 5 equal samples (10 aliquots for each sample – 5 translucent and 5 opaque) and then all were taken through the same stages of the cleaning protocol.

4.4.2.3 RESULTS OF THE CLEANING TEST (COARSE SILICATE REMOVAL STAGE VS. NON-COARSE SILICATE REMOVAL STAGE)

Overall we record a reduction in the influence of contaminants when we include the coarse silicate removal stage in our experiments (Figure 4.43). On average we record a reduction in the mean Mg/Ca (from 2.07 to 2.01mmol/mol), Fe/Mg (from 0.14 to 0.11mol/mol), Fe/Ca values (from 294.6 to 220.2μmol/mol) (reduction of 2.9%, 21.4% and 25.2% respectively) when we include the silicate removal stage. In all of the samples we also recorded a reduction in the range of Fe/Ca values (from 127.8 to 48.9μmol/mol – 61.7% reduction), Mn/Ca (from 86.67 to 54.33μmol/mol – 37.3% reduction), Fe/Mg (from 0.07 to 0.03mol/mol – 57.1% reduction), Mn/Mg (from 0.05 to 0.02mol/mol – 60% reduction) and in 2 of the 3 Mg/Ca values (from 0.28 to 0.13mmol/mol – 53.6% reduction)

The Mg/Ca results from sample 1 show no difference in the average of the repeat measurements and as such we conclude that whilst it is not always necessary to remove all the silicates from the sample, it does reduce the spread of the data. The same is true when we compare the Fe/Ca and Fe/Mg data (Figure 4.43b, e); we record an overall reduction in the spread of the data when we include the silicate removal stage. All the Fe/Ca and Fe/Mg data that included the silicate removal stage show lower values and a reduction in the range of values (Table 4.5). However, although there is a clear effect of the cleaning on the Fe/Ca and Fe/Mg results, there does not always appear to be any corresponding reduction in the Mg/Ca values, suggesting that high Fe values are not always associated with high Mg/Ca values.

The Al/Ca results require some more consideration as the results are not straightforward; Al is difficult to measure in HR-ICPMS. It appears from the results (Figure 4.43) that some Al was introduced during the silicate removal stage of sample 1 (Figure 4.43d) as the average value for the cleaned sample is over six times larger than for the supposed dirty sample and the spread of data for the repeat aliquots of the same sample (sample 1) was much greater than for the dirty samples. Despite this large increase in the Al content in the cleaned sample 1, there is no positive correlation between the Al/Ca and Mg/Ca ratios, suggesting that Al/Ca is probably not a good indicator of silicate contamination in our samples.

The Mn/Ca values on average show a reduction in the spread of data when the coarse silicate removal stage is included (dirty samples average range is 86.67μmol/mol whereas for clean samples it is 54.33 μmol/mol). Overall, the Mn/Ca values are high in each of the samples however, similar Mn/Ca values have been recorded in nearby core sites during the Holocene (RAPiD-12-1K, RAPiD-15-4P and RAPiD-17-5P) Thornalley, (2008)). To identify a cause for the high Mn/Ca values in the record the behaviour of manganese in North Atlantic sediments must be considered and is revisited in the next section.

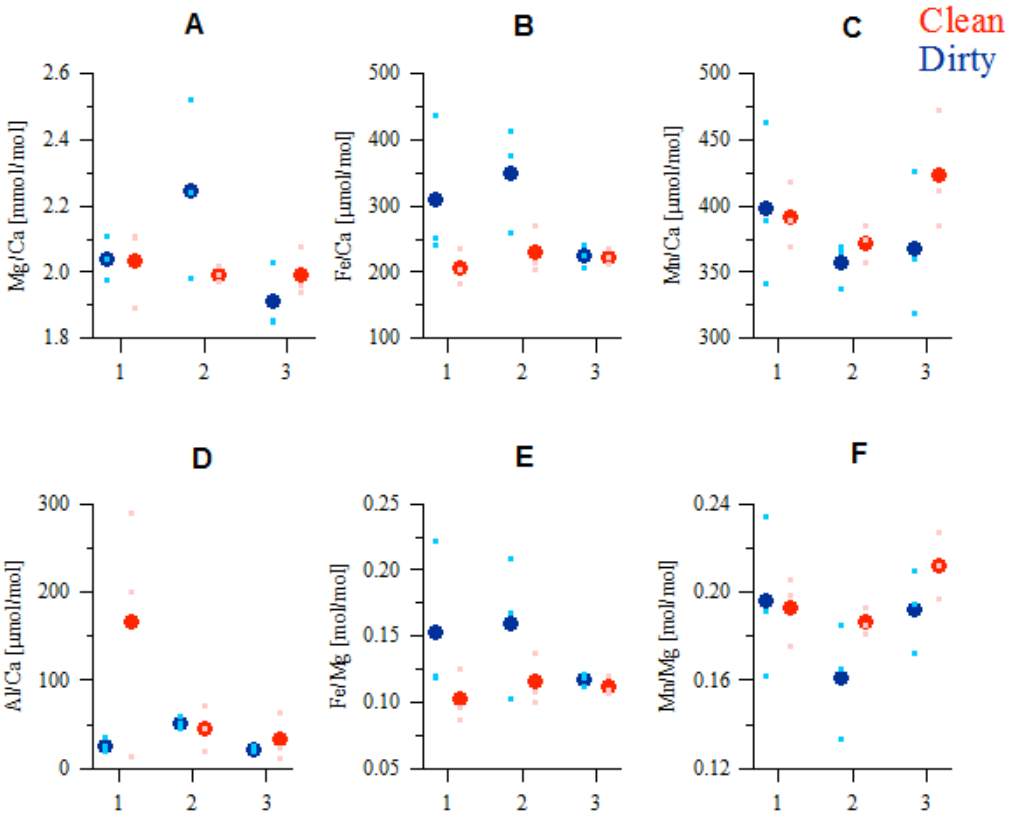

Figure 4.43 Results of a cleaning test to establish the effects of including (clean (red)) or excluding (dirty (blue)) the coarse silicate removal stage during the Mg/Ca cleaning protocol. The silicate removal stage involves removing all silicates with a single eyelash under a microscope between the removal of organic matter and dilute acid leach stages of the protocol.

Table 4.5 Summary of results from experiment to test whether or not the coarse silicate removal stage is necessary in the Mg/Ca cleaning protocol.

		Mg/Ca [mmol/mol]		Fe/Ca [µmol/mol]		Mn/Ca [µmol/mol]	
		mean	**range**	**mean**	**range**	**mean**	**range**
Silicate removal stage excluded	1	2.04	0.13	310.15	197.11	398	121
	2	2.25	0.54	349.32	152.04	357	32
	3	1.91	0.18	224.19	34.22	368	107

Silicate removal stage included	1	2.04	0.22	207.49	54.55	392	48
	2	1.99	0.05	229.51	68.39	372	28
	3	1.99	0.13	223.64	23.77	423	87
		Al/Ca [µmol/mol]		**Fe/Mg [mol/mol]**		**Mn/Mg [mol/mol]**	
		mean	**range**	**mean**	**range**	**mean**	**range**
Silicate removal stage excluded	1	26	14	0.15	0.10	0.19	0.07
	2	52	14	0.16	0.11	0.16	0.05
	3	22	6	0.12	0.01	0.19	0.04
Silicate removal stage included	1	167	275	0.10	0.03	0.20	0.03
	2	45	52	0.12	0.04	0.19	0.01
	3	33	53	0.11	0.01	0.21	0.03

4.4.2.4 RESULTS FOR DIFFERENT WALL APPEARANCES OF *G. INFLATA* (TRANSLUCENT VS. OPAQUE)

Lower Mg/Ca values were recorded in the opaque tests when compared to the translucent tests; the averages are 1.79 mmol/mol and 2.03 mmol/mol respectively Figure 4.44. We also record a smaller spread in the Mg/Ca values in the translucent tests compared to the opaque ones (average of 0.56 mmol/mol range for the opaque tests and an average of 0.21 mmol/mol for the translucent ones); the spread of the data is 62.5% smaller in the translucent tests. All the samples (excluding the Fe/Ca and Fe/Mg ratios from sample 2) record a smaller spread in the data in the translucent tests when compared to the opaque ones. The increase spread in the data of the opaque tests suggests that the population and/or the individuals are more heterogeneous in their trace element composition and are recording a wider range of environments and/or are altered by diagenesis when they reach the sediment. The average Mn/Ca values from the opaque shells are significantly higher (673µmol/mol)

than in the translucent shells (368μmol/mol). Overall, the Mn/Ca values are high in both samples (albeit similar to Mn/Ca values recorded in nearby core sites during the Holocene (RAPiD-12-1K, RAPiD-15-4P and RAPiD-17-5P) Thornalley, (2008)) but are particularly elevated in the opaque shells. To identify a cause for the high Mn/Ca values in the record the behaviour of manganese in North Atlantic sediments must be considered.

Manganese in seawater is supplied by river runoff, fallout of atmospheric particles, injection of hydrothermal solutions, diffusion out of pelagic sediments and diffusion out of near-shore reducing environments (Bender et al., 1977). Manganese is redox sensitive and under oxic conditions, exists as Mn(IV), in the form of manganese oxides(s). A high manganese oxide flux to the sediment is expected south of Iceland from terrestrial run-off (Thornalley, 2008). As manganese is also added to seawater from hydrothermal input, the Mid-Atlantic Ridge hydrothermal plume is likely to add additional manganese that is then advected at shallow depths by the NAC to ODP Site 983 (Thornalley, 2008).

In order to assess the influence of manganese oxides at our core location we need to consider the depth of oxygenated sediments in the North Atlantic at our core location. Oxygenated sediments can be found at least 2m below the sediment water interface in areas of low sedimentation rates (typically less than 4cm/kyr (Wilson et al., 1985)). Across MIS 11 at ODP Site 983 we record high sedimentation rates (17.7cm/kyr), these high sedimentation rates, coupled with high organic carbon fluxes to the sea floor, limits the depth of oxic sediments as the pore water oxygen is exhausted by the oxidation of organic carbon. This results in a shoaling of the depth of oxic sediments and as such reducing conditions occur closer to the surface in areas of higher sedimentation. Once buried (as a result of continued sedimentation and sediments that once resided in the oxic zone being found in the sub-oxic/anoxic zone) the manganese oxides (possibly advected to the core location from the hydrothermal input from the Mid-Atlantic Ridge) are reduced and mobilised to Mn(II) (Thomson et al., 1986) (see Figure 4.). The Mn(II) can then precipitate onto foraminiferal tests, possibly as rhodochrosite ($MnCO_3$) or kutnahorite ($Mn,Ca(CO_3)_2$) (Boyle, 1983; Thomson et al., 1986).

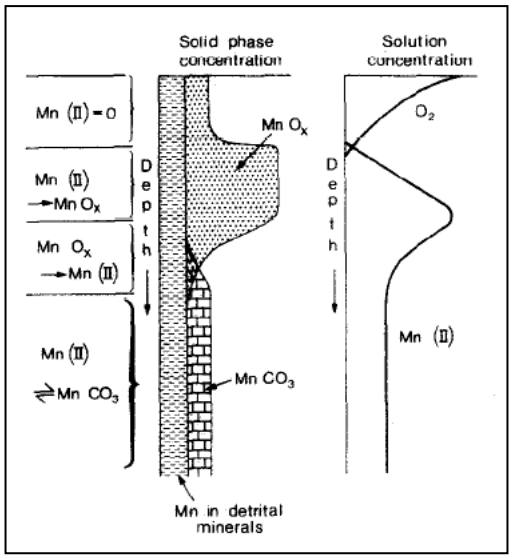

Figure 4.49. From Thomson et al., (1986). A representation of the steady-state behaviour of Mn in a carbonate sediment. The top layer is the oxic layer where no Mn(II) is in solution. The second layer has Mn(II) diffusing upwards from its base, without uptake, to precipitate as Mn oxyhydroxide at its top against the downward oxygen flux from bottom water. The third layer has oxyhydroxide reduction occurring throughout, but most intensely at the top. It is assumed that oxyhydroxide reduction and $MnCO_3$ formation are both completed in this layer. The deepest layer has Mn(II) in its pore waters.

The High Mn/Ca ratios are not incorporated into the shells during calcification as the Mn/Ca ratios found in seawater are extremely low (Hatta et al., 2015) compared to the values found in foraminiferal calcite (10-100mmol/mol (Boyle, 1983)). High Mn/Ca ratios at ODP site 983 during MIS 11 occur well below the typical depth of oxic sediments in the North Atlantic (Wilson et al., 1985; Thomson et al., 1986) and therefore are not caused by the presence of Fe-Mn oxides. Although it is possible that the oxides could have been produced higher in the sediment column and subsequently buried, based on foraminiferal Mn/Ca studies from the Panama Basin (Pena et al., 2005) and nearby core location in the North Atlantic (Thornalley, 2008) the most likely phase in which Mn is present is manganese carbonate. In conclusion, the high Mn values in our record from the North Atlantic can be explained by the high sedimentation rates and mobilisation of Mn and subsequent precipitation onto the foraminiferal shell.

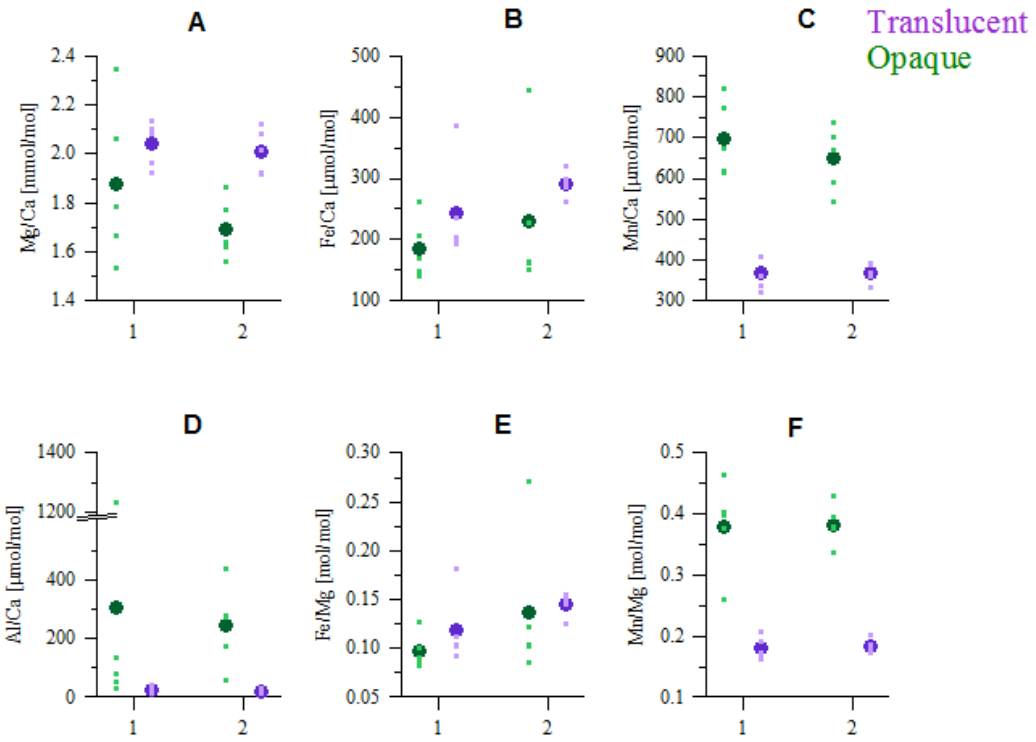

Figure 4.44. Results of a test to establish the effects of different wall encrustations; translucent (purple) and opaque (green) tests were picked from the same samples to establish if the different wall types produce different Mg/Ca results.

Table 4.6 Summary of results from experiment to test whether or not the different appearance of the shell walls (translucent vs. opaque) alters the trace element composition of G. inflata.

		Mg/Ca [mmol/mol]		Fe/Ca [µmol/mol]		Mn/Ca [µmol/mol]	
		mean	range	mean	range	mean	range
Opaque	1	1.88	0.82	184.59	123.12	698	208
	2	1.69	0.30	229.81	291.78	648	194
Translucent	1	2.04	0.21	242.73	194.00	367	87
	2	2.01	0.21	291.30	58.51	368	58

		Al/Ca [µmol/mol]		Fe/Mg [mol/mol]		Mn/Mg [mol/mol]	
		mean	**range**	**mean**	**range**	**mean**	**range**
Opaque	1	304	1200	0.10	0.05	0.38	0.20
	2	245	383	0.14	0.18	0.39	0.09
Translucent	1	23	29	0.12	0.09	0.18	0.05
	2	20	16	0.15	0.02	0.18	0.03

4.4.3 CONCLUSION OF EXPERIMENTS TO TEST THE CLEANING PROTOCOL AND ENCRUSTATION VARIABILITY

The conclusions from these experiments are that the full cleaning protocol should be carried out on all samples in order to reduce the error associated with not removing the silicates (i.e. to reduce the spread of the data). We also recommend that only one type of shell is consistently picked (we used only translucent shells due to the smaller spread of the repeat aliquots when compared to the opaque shells) and analysed for Mg/Ca analysis. Furthermore, our results suggest that the presence of Mn (due to a diagenetic coating) does not influence the Mg/Ca record and as such, the presence of Mn at our core location is not necessarily indicative of contamination.

4.5 ANALYSIS OF CONTAMINATION OF SAMPLES

Ensuring that the record of Mg/Ca values has not be contaminated post deposition is critical as any potential contamination can have a large effect on the concentration of trace metals in a sample and our subsequent analysis and interpretation of them. Aluminium (Al^{3+}), manganese (Mn^{2+}) and iron (Fe^{3+}) were measured as indicators of possible silicate and clay mineral contamination and Fe-Mn oxide coatings (Boyle, 1983; Barker et al., 2003; Pena et al., 2005).

Mg/Ca values in ODP Site 983 vary between ~1.3-2.5mmol/mol (Figure 4.45). We record the highest Mg/Ca values during the early part of MIS 11 (~50.40-48.00m depth); overall across this interval we record a very slight decrease in the Mg/Ca

values. Following this early interval during late MIS 11 we record a faster decrease in Mg/Ca values from ~2.25-1.3mmol/mol in just over 1.5m (48.00-46.50m). The Mg/Ca values then increase rapidly again to a peak at about 45.40m before decreasing again overall (interrupted by an abrupt decrease in Mg/Ca values between 45.25-45.10m) to the end of the record.

The Fe/Ca record varies between ~100-400µmol/mol with larger variability and on average higher values during the first part of MIS 11 (~48.11-50.33m). Following this interval we record a decrease in the average Fe/Ca values and a decrease in the amplitude of the variability (values vary between 150-250µmol/mol) from ~48.00m to the end of the record.

The Fe/Mg record (Figure 4.45) varies between ~0.08-0.18mol/mol, as with the Fe/Ca record, the Fe/Mg values record higher values on average and greater variability during the earliest part of the record (~48.20-50.40m). During the second part of the record (~48.20m onwards) the values range between ~0.08-0.12mol/mol and shows much smaller amplitude changes. The first part of the record shows a slight decrease in Fe/Mg values that then flattens out from ~48.00m to the end of the record. The record of Fe/Mg displays similar trends to the Fe/Ca record, such that there is greater variability and larger amplitude changes during the first part of the record during MIS 11.

The Mn/Ca record (Figure 4.45) varies between ~200-700µmol/mol (peaking at 900µmol/mol on two occasions during the record at 48.49m and 48.27m). Overall we record a decrease in the Mn/Ca record until approximately 47.00m followed by a slight increase to the end of the record (44.79m). As with the Fe/Ca and Fe/Mg records, the Mn/Ca record also records greater variability and a slight decrease in values during the first half of the record (approximately 48.00-50.33m) before flattening out (or slightly increasing in the case of Mn/Ca) during the second part of the record. For the most part, high Mn/Ca values are not associated with high Mg/Ca values (Figure 4.45) although there are similarities in the general trend. Although generally high, similar Mn/Ca values have been recorded in nearby core sites during the Holocene (RAPiD-12-1K, RAPiD-15-4P and RAPiD-17-5P) Thornalley, (2008)). The Mn/Mg record varies between ~0.10-0.50mol/mol (average value 0.23mol/mol)

(Figure 4.45). The record shows a slight decrease in values until approximately 47.40m, followed by a slight increase until the end of the record.

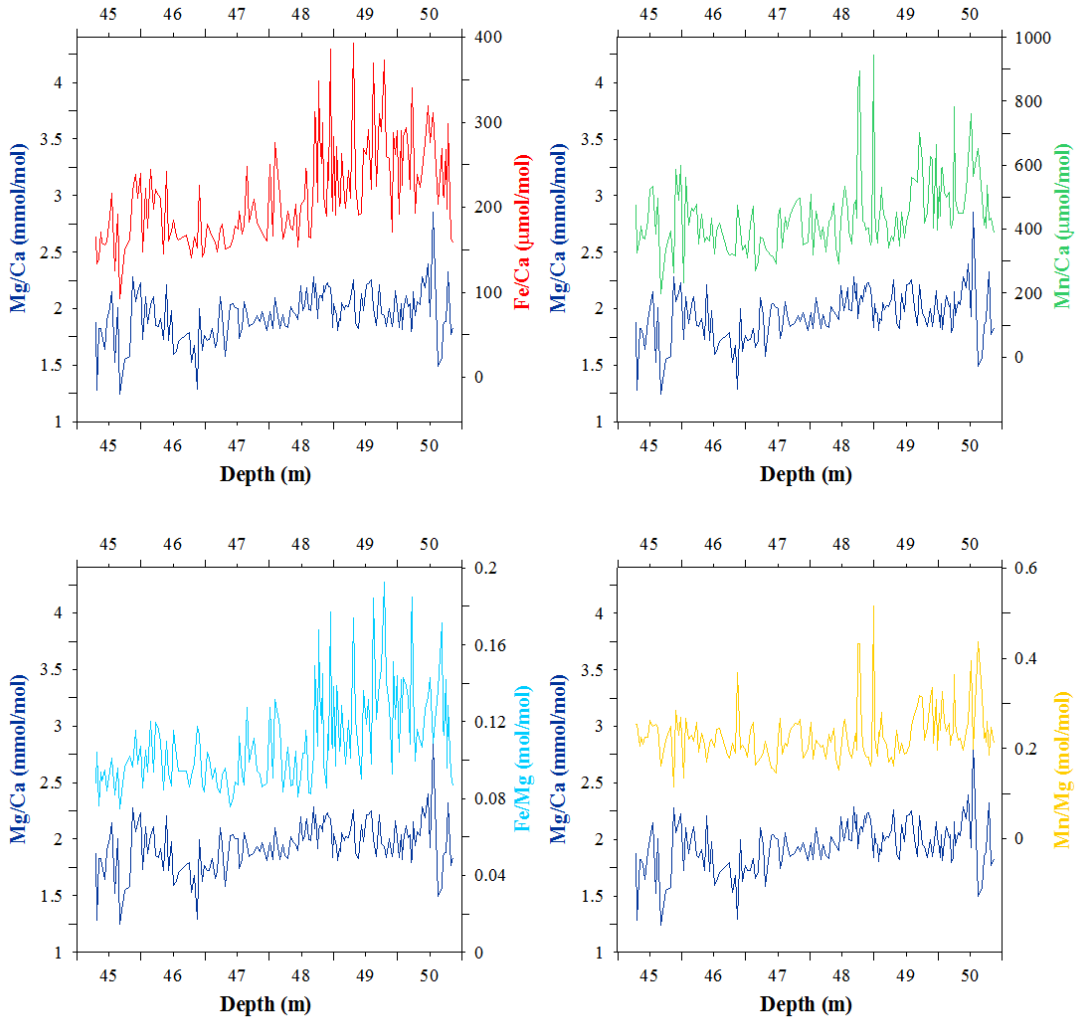

Figure 4.45. Comparison of trace elements down core; Mg/Ca (dark blue); Fe/Ca (red); Mn/Ca (green); Fe/Mg (light blue); and Mn/Mg (yellow).

Following the initial visual screening of the raw data (a total of 21 samples were rejected) we further corrected the Mg/Ca record for contamination from iron based sources on the Fe/Ca results (Figure 4.45). We calculated the excess Fe/Ca in the Mg/Ca following the work from Lea et al., (2005) whereby we correct for the presence of iron by dividing the Fe/Ca ratio by 1.13 and subtracting this from the Mg/Ca record. The average correction is 0.192mmol/mol and the maximum correction is 0.348mmol/mol (9.81% and 17.0% respectively). Based on the results from the initial experiments we showed that although there is a clear effect of

individually removing the silicate grains during the protocol on the Fe/Ca and Fe/Mg results there does not always appear to be any corresponding reduction in the Mg/Ca values. This suggests that high Fe values are not always associated with high Mg/Ca values and as such the Fe/Ca correction we apply here may well be over-correcting the Mg/Ca record.

As mentioned, Mn values at this core location, and other nearby cores in the North Atlantic (Thornalley, 2008) appear to be high (see previous section for explanation). However, we conclude from our experiments (sections A Study of Potential Biases in the MG/CA Signal from Silicates and A Study of Potential Biases in The MG/CA Signal of *G. inflata*) that the high Mn values do not seem to influence the Mg/Ca and as such, we do not correct the Mg/Ca record for Mn.

The range of temperatures calculated from the Mg/Ca values (corrected for Fe coatings) based on the different calibrations for *G. inflata* (Elderfield and Ganssen, 2000; Anand et al., 2003; Cléroux et al., 2007; Thornalley et al., 2009; Farmer et al., 2010; Groeneveld and Chiessi, 2011) are shown in Figure 4.46. For our results in this study we use the calibration from Thornalley et al., (2009) to convert our Mg/Ca values to temperature where Temperature = ln (Mg/Ca x (1/0.675)) x (1/0.1).

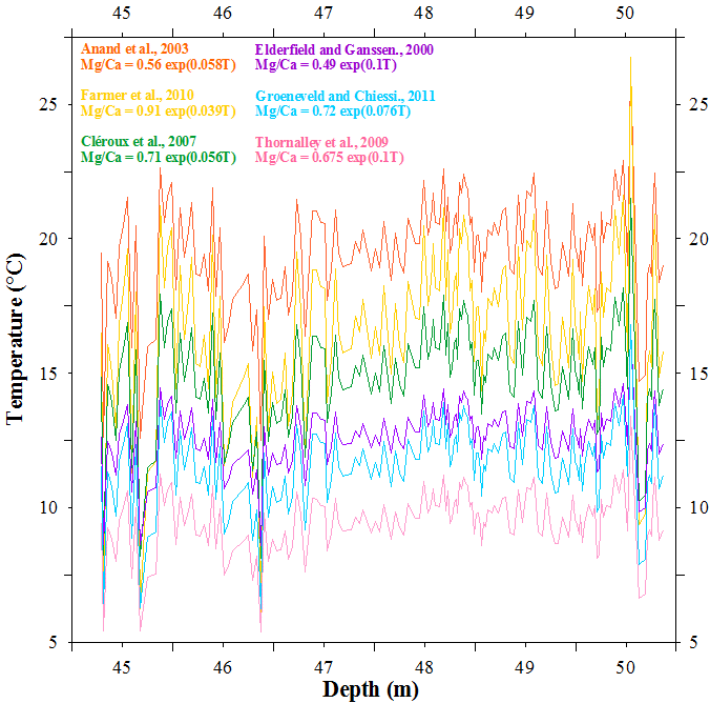

Figure 4.46 Comparison of G. inflata Mg/Ca temperature calibration curves from different studies (Elderfield and Ganssen, 2000; Anand et al., 2003; Cléroux et al., 2007; Thornalley et al., 2009; Farmer et al., 2010; Groeneveld and Chiessi, 2011).

We use this calibration as it yields temperatures closest to the modern day conditions in the North Atlantic. *G. inflata* typically live in the uppermost 200m which is a temperature range of 7.7-12.6°C in the modern ocean (Levitus et al., 2013) (Figure 4.47 and Figure 4.48).

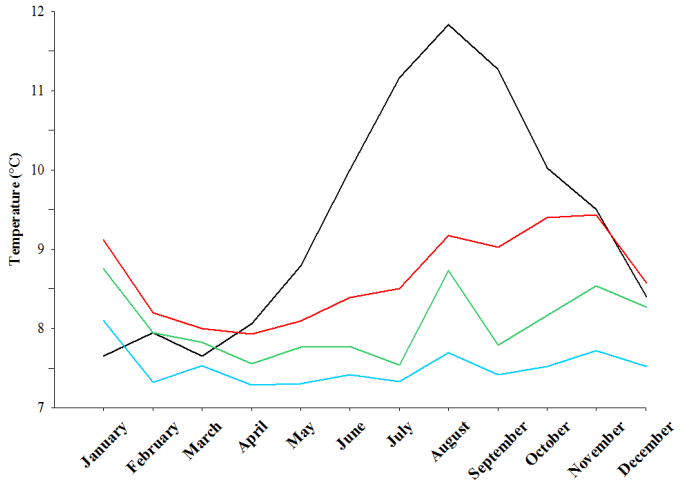

Figure 4.47. Seasonal temperature variability at ODP Site 983 (specifically 60.5°N, 23.5°W) at different water depths; 0m (black); 100m (red); 300m (green); and 500m (blue) (Levitus et al., 2013).

We show the temperature correction between the original Mg/Ca and the Fe/Ca corrected record (Figure 4.48c). The largest correction occurs during the early part of the record (early MIS 11) between 50.39m and 48.19m where the average temperature correction is 1.2°C. During the second part of the record between 48.17m and 44.79m the average temperature correction is lower, 0.9°C on average. The largest correction across the whole record is 1.9°C.

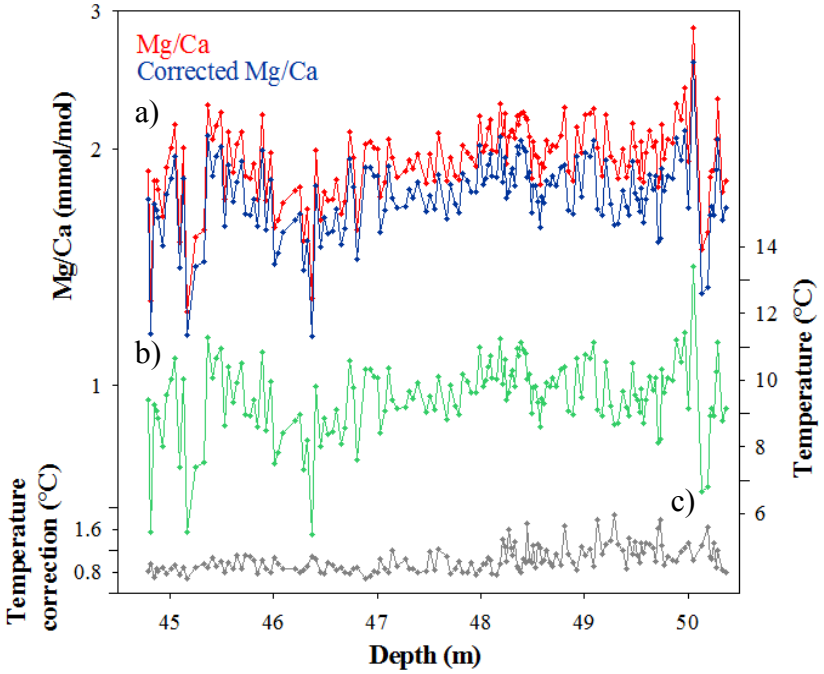

Figure 4.48. Original and corrected Mg/Ca record (red and blue respectively) with the temperature conversion of the corrected record shown in green. The plot at the bottom shows the temperature correction when comparing the original and corrected Mg/Ca record.

4.6 AGE MODEL

Several age models have been produced for ODP Site 983 (e.g. Channell et al., 1997; Hyun et al., 1999; Lisiecki and Raymo, 2005; Barker et al., 2015). Here we used the most recently published age model for ODP Site 983 from Barker et al. (2015). This age model was developed based on the assumption that abrupt warming events in the records from this study at ODP Site 983 which also align with the disappearance of IRD are synchronous with warming across the wider North Atlantic region and the authors align these with warming transitions in the synthetic prediction of Greenland temperature (GL_T_syn) (Barker et al., 2011) (Barker et al., 2015).

4.7 RESULTS

We record $\delta^{18}O_c$ (*G. inflata*) values between ~1.6-2.6‰ across MIS 11 (Figure 4.49). The data show a broad peak (minimum values) between approximately 407-413kyr with a faster decrease in values during the first half of the record compared to the second. In order to obtain an ice-free estimate of $\delta^{18}O_c$ we corrected for the effect of ice volume. To do this we subtract the mean ocean $\delta^{18}O_{sw}$ (Waelbroeck et al., 2002) from our $\delta^{18}O_c$ (*G. inflata*) record (Figure 4.49).

The temperature record produced here (Figure 4.49b) shows some millennial scale variability within the interglacial interval, with an overall temperature range between 5.4-13.4°C. Following a prolonged period (~426kyr-409kyr) when there is relatively little variation in the temperatures (between approximately 9-10.5°C), we record a broad cooling in the record beginning at ~405kyr before returning to interglacial temperatures by ~400kyr (3.3°C change in temperature of three-point running mean). Following this broad cooling a more abrupt cooling occurs between 397.69kyr and 395.83kyr (3.1°C decrease in temperature of three-point running mean) before an increase in the interglacial temperatures at 395.83kyr followed by an onset of a gradual decrease in temperatures towards the end of MIS 11.

The calculated record of $\delta^{18}O_{sw}$ varies between -0.6 and 1‰ across MIS 11. Much like the temperature record, the $\delta^{18}O_{sw}$ record shows a broad increase in values, which indicates an increase in salinity from the beginning of MIS 11 to approximately 412kyr. Following this there is a broad decrease in $\delta^{18}O_{sw}$. There is an abrupt decrease in $\delta^{18}O_{sw}$ from ~0.75 to -0.4‰ followed by a return to values near to 0.7‰ again by the end of MIS 11.

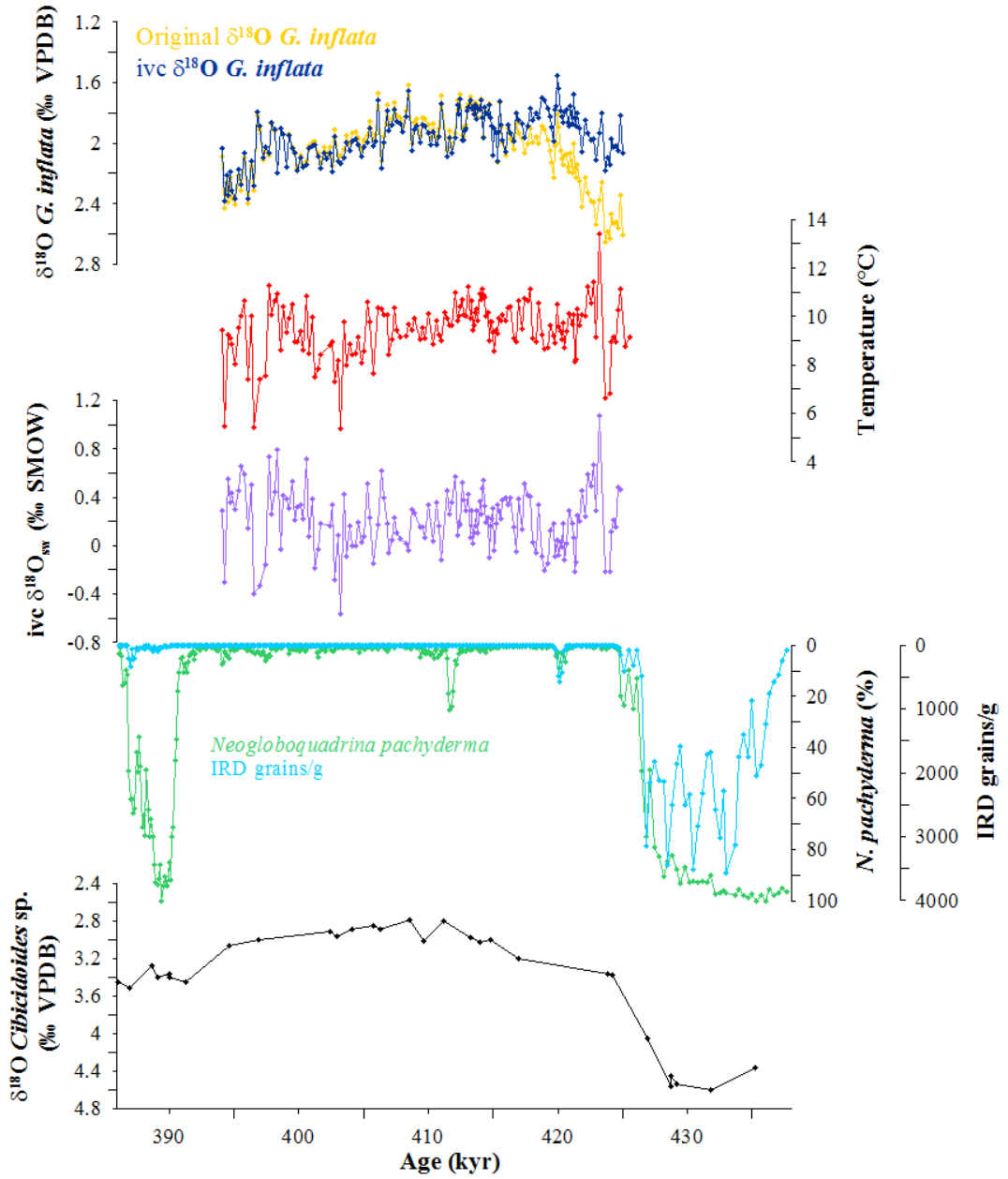

Figure 4.49 Records from the North Atlantic, ODP Site 983, across MIS 11. a) original $\delta^{18}O$ G. inflata record (blue) and ivc $\delta^{18}O$ G. inflata (yellow) (this study); b) temperature reconstruction (red) (this study); c) ice volume corrected $\delta^{18}O_{sw}$ (purple) (this study using Waelbroeck et al., (2002)); d) N. pachyderma (%) (green) and IRD grains/g (blue) (Barker et al., 2015); and e) benthic $\delta^{18}O$ Cibicidoides sp. (Raymo et al., 2004).

4.8 DISCUSSION

4.8.1 THE MIS 11 INTERGLACIAL IN THE NORTH ATLANTIC (ODP SITE 983)

On two occasions during the interglacial interval of MIS 11 (420kyr and 414kyr) there are short, abrupt increases in the abundance of *N. pachyderma* from near 0% to 9.0% and 25.5% respectively (Figure 4.51). According to the calibration of Govin et al., (2009) a 10% increase in *N. pachyderma* equates to a decrease in temperature of ~0.8°C. Accordingly, these two intervals could represent a 0.8°C and 2.2°C decrease in summer SST, respectively. From the glacial of MIS 12 to the interglacial interval of MIS 11 the abundance of *N. pachyderma* varies between 100% and 0% in the surface waters (Barker et al., 2015). Based on a calibration of 245 core tops this range in abundance of *N. pachyderma*, indicates a temperature change from 2.6°C to 11.3°C (Govin et al., 2009) across T5. However, as covered comprehensively in chapter 2, the use of *N. pachyderma* as a proxy for temperature should be used with caution. 100% abundance of *N. pachyderma* gives a temperature of 2.6°C however, the proxy effectively becomes saturated at 100% and thus doesn't record any additional cooling. The same is true when temperatures rise above 11.3°C, the abundance of *N. pachyderma* declines to 0% and thus if temperatures were to rise above 11.3°C this proxy would again, be unable to record such a change.

The *G. inflata* Mg/Ca temperature record provides us with a quantitative record across MIS 11, however we should note that it only records temperatures when *G. inflata* is present in the water column and then only at the depths that it inhabits (up to 400m (Hemleben et al., 1989)). The relative abundance of *N. pachyderma* however, is recording the presence of all the species relative to each other and thus is also dependent upon all the other species present in the assemblage providing us with an integrated long-term temperature indicator. The lack of response in the record of temperature change (paired Mg/Ca-$\delta^{18}O$ analysis) indicates that *G. inflata* showed very little response during MIS 11, despite two apparent cooling intervals identified by the record of % *N. pachyderma* (Barker et al., 2015). We suggest a couple of possible explanations for this; 1) the cooling intervals at 420kyr and 414kyr are only recorded in the surface ocean. *N. pachyderma* lives in the uppermost 100m (Hemleben et al., 1989) whereas *G. inflata* can be found up to 400m deep in the water

column (Hemleben et al., 1989). 2) Alternatively, *G. inflata* might have moved vertically in the water column in order to buffer any temperature changes in the surface ocean. The *G. inflata* temperature therefore, although quantitative, does not provide us with an integrated temperature and simply allows us to interpret temperature changes associated with *G. inflata*. The record is also influenced by seasonality, such that as *G. inflata* typically exists during the months of September, October and November our record reflects temperature changes during these months only. Furthermore, the intermittent presence of *G. inflata* and variations in the abundance of the species are possible limitations in interpreting the dataset.

4.8.2 THERMOCLINE CHANGES

Here we see that the trend in $\delta^{18}O$ of both species co-varied from the beginning of our $\delta^{18}O$ *G. inflata* record (425kyr) until approximately 410kyr where the two records become decoupled from each other (Figure 4.50). Both records show an increase in $\delta^{18}O$ from 410kyr onwards, but the $\delta^{18}O$ *G. inflata* increases to 2.4‰ whereas over the same period up until 394.2kyr the $\delta^{18}O$ *G. bulloides* increases to just 1.77‰. There are two possibilities for the decoupling of these records; 1) the different species are recording the different temperatures associated with different depth habitats (*G. inflata* typically inhabits the thermocline whereas *G. bulloides* lives higher in the water column (Hemleben et al., 1989)) or 2) the difference in $\delta^{18}O$ values of the two species is recording the seasonal temperature variability. The species both occur during the autumn months (September, October and November) but *G. bulloides* also occurs during late spring (April, May and June) too (Tolderlund and Bé, 1971). As such the species are recording slightly different seasons and the difference between the two records could be a record of the extent of seasonality. We suggest that the former argument is more likely given that the species have different depth habitats and broadly similar seasonal variability. Therefore, we suggest that the water column in the North Atlantic prior to approximately 410kyr was well mixed and both species were recording similar temperatures/salinities at this location in the North Atlantic. Following 410kyr there is an increase in the difference between the $\delta^{18}O$ of the two species suggesting that there was increased stratification in the water column during the second part of MIS 11.

Similar comparisons for the Holocene have been made at a nearby core location (RAPiD-12-1K – 62.05°N, 17.49°N (Thornalley et al., 2009)) where the authors suggest that stratification results from changes in the strength of the Subpolar gyre (see below).

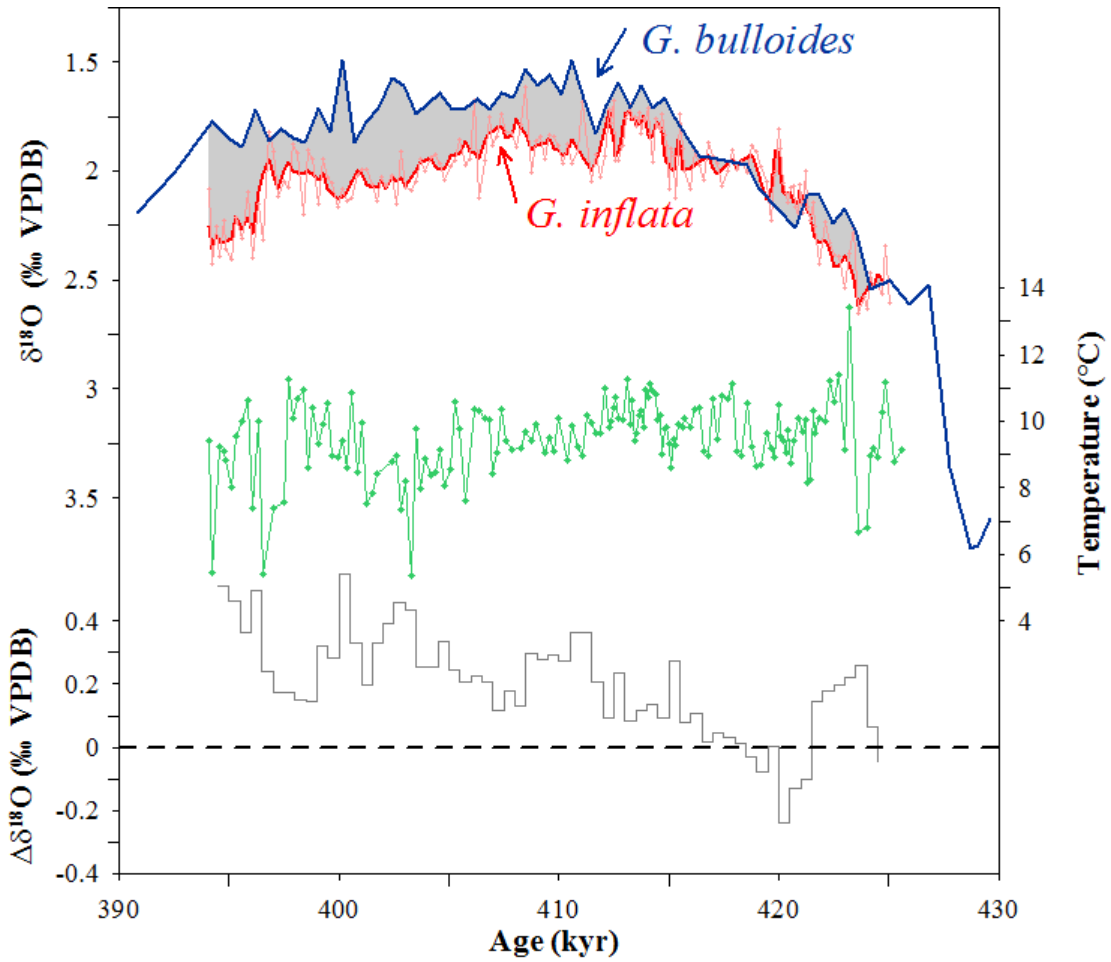

Figure 4.50 Records of $\delta^{18}O$ of G. inflata (red) (this study) and $\delta^{18}O$ G. bulloides (blue) (Channell et al., 1997) from ODP Site 983. The records show a well-mixed water column from 425kyr to approximately 410kyr, but stratification between the surface waters and the thermocline from 410kyr onwards. Temperature from G. inflata Mg/Ca at ODP Site 983 shown in green (this study) and the difference between the $\delta^{18}O$ records of G. inflata (this study) and G. bulloides (Channell et al., 1997) shown in grey. This was calculated by interpolating the G. bulloides record (Channell et al., 1997) to the same resolution as the dataset from this study and subtracting this from the G. inflata record (this study).

As mentioned, Thornalley et al. (2009) record a similar decoupling of *G. bulloides* and *G. inflata* at a nearby core location (RAPiD-12-1K) during the Holocene. The

authors attribute the decoupling to changes in the proportion of water being drawn from either the cold, fresh Subpolar gyre (SPG) or the warm, saline Subtropical gyre (STG), which has been shown to depend strongly on the dynamics of the SPG (Cubasch et al., 2001). Strong SPG circulation results in a more East-West oriented SPG and thus contributes more water to the Atlantic inflow into the Nordic Seas, making it fresher and increasing stratification between *G. bulloides* and *G. inflata*. Conversely, weak SPG circulation results in a more North-South oriented SPG, which contributes less water to the Atlantic inflow making it saltier (Thornalley et al., 2009), decreasing stratification between *G. bulloides* and *G. inflata*. The strength of the SPG circulation depends on local wind stress and/or local air-sea buoyancy forcing (Häkkinen and Rhines, 2004). The implications of these findings during the Holocene to our record from MIS 11 are such that we also record inferred changes in the strength of the SPG circulation. These changes occur on a millennial timescale during MIS 11, suggesting oscillations in the strength of circulation in the surface waters. Thornalley et al., (2009) demonstrate 1,500 year cyclicity in the strength of the SPG circulation during the Holocene, our record presented here does not demonstrate any cyclicity. Variability in the strength of the SPG circulation is important when considering the role of millennial scale events in G-IG cycles. Climate fluctuations during the Holocene have been linked with changes in North Atlantic Ocean circualtion (Bianchi and McCave, 1999; Bond et al., 2001). Variations the strength of the SPG, result in changes in the temperature and salinity of the North Atlantic and thus impact upon the region of deep water formation in the North Atlantic, an important component in G-IG cyclicity (Thornalley et al., 2009). Thornalley et al., (2009) demonstrate that the inflow to the North Atlantic becomes more saline during enhanced freshwater flux to the subpolar North Atlantic. As such, the increased stratification during the latter part of our record presented here from MIS 11 suggests an increase in the freshwater water flux results in a decrease in the strength of AMOC on millennial time scales, perhaps providing a millennial scale negative feedback mechanism to G-IG variability.

4.8.3 NORTH ATLANTIC TEMPERATURE CHANGES ACROSS MIS 11 AND THE HOLOCENE

Marine isotope stage 11 is thought to be the closest analogue we have to the Holocene (Loutre and Berger, 2003) and as such it is important to understand, characterise and

compare our records to those from the present interglacial. Here we compare records from a nearby core location (RAPiD-12-1K; 62.05°N 17.49°W) (Thornalley, 2008). The orbital parameters during the early part of this isotope stage were very similar to those prevailing today (Figure 4.51), with low eccentricity, high obliquity and low precessional amplitude (Berger and Loutre, 1991; Loutre and Berger, 2003).

Comparison of the temperature record from the Holocene (RAPiD-12-1K) and MIS 11 across (ODP Site 983) (note that both records were produced using the same Mg/Ca temperature calibration (Thornalley et al., 2009)) show that the temperatures recorded during MIS 11 are slightly higher than during the Holocene and range between 5.4-13.4°C and 6.0-11.2°C respectively (Figure 4.50). The atmospheric CO_2 records (Bazin et al., 2013) and temperature records (Thornalley et al., 2009 (Holocene) and this study (MIS 11)) of the two intervals show very different patterns across the termination (Figure 4.51); the transition between the glacial and interglacial interval of T5 is much longer and drawn out than the equivalent transition across T1. The peak CO_2 values of the two terminations are very similar (approximately 280ppm) and as expected the peak CO_2 values align with the end of the transition from 100-0% *N. pachyderma*, i.e. the onset of MIS 11 and the Holocene.

There is a broad decrease in temperature across MIS 11 (Figure 4.51) whereby the lowest temperatures are recorded during the interval of greatest stratification (~ 405-395kyr). Given our interpretation above, that a increased in stratification is a result of a enhanced SPG circulation, we can say that this broad decrease in temperature is associated with a broad increase in the strength of the SPG during the latter part of MIS 11, freshening the North Atlantic as more water is contributed to the Nordic Seas via the SPG.

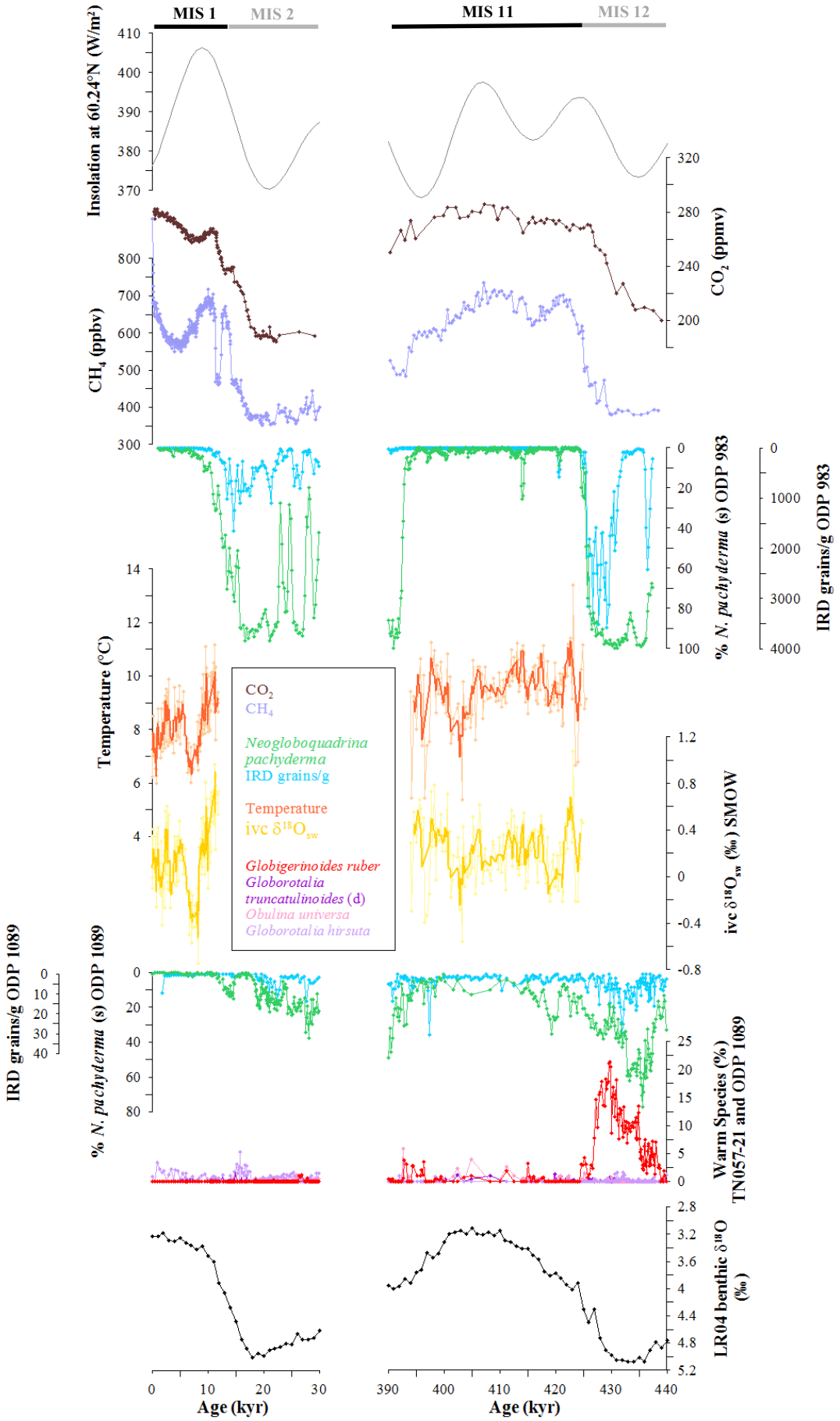
MIS 1
MIS 2
MIS 11
MIS 12
Insolation at 60.24°N (W/m²)
CH4 (ppbv)
CO2 (ppmv)
% N. pachyderma (s) ODP 983
IRD grains/g ODP 983
Temperature (°C)
CO2
CH4
Neogloboquadrina pachyderma
IRD grains/g
Temperature
ivc δ18Osw
Globigerinoides ruber
Globorotalia truncatulinoides (d)
Obulina universa
Globorotalia hirsuta
ivc δ18Osw (‰) SMOW
IRD grains/g ODP 1089
% N. pachyderma (s) ODP 1089
Warm Species (%) TN057-21 and ODP 1089
LR04 benthic δ18O (‰)
Age (kyr)
Age (kyr)

Figure 4.51 a) insolation at 60.24°N (Laskar et al., 2004) (created in Analyseries (Paillard et al., 1996)); b) CO_2 record (Lüthi et al., 2008); c) CH_4 record (Loulergue et al., 2008); d) N. pachyderma (%) (green) and IRD grains/g (blue) counts from ODP Site 983 (Barker et al., 2015); e) temperature reconstruction based on Mg/Ca analysis for the Holocene (core RAPiD-12-1K, (Thornalley et al., 2009)) and for MIS 11 (this study); f) ice volume corrected $\delta^{18}O_{sw}$ for the Holocene (Thornalley et al., 2009) and for MIS 11 (this study); g) N. pachyderma (%) (green) and IRD grains/g (blue) counts from TN057-21 (Barker et al., 2009) for T1\Holocene and from ODP Site 1089 (this study) for T5; h) warm species faunal counts from ODP Site 1089 (this study, chapter 2) – Globigerinoides ruber (red), Globorotalia truncatulinoides (dark purple), Orbulina universa (pink), Globorotalia hirsuta (light purple); i) the LR04 benthic stack (black) (Lisiecki and Raymo, 2005) is shown at the bottom for reference.

4.8.4 TIMINGS OF PEAK INTERGLACIAL CONDITIONS RELATIVE TO CHANGES IN BENTHIC $\delta^{18}O$

Concerning the transition from MIS 12 to MIS 11 (i.e. the Termination) both the percent *N. pachyderma* and IRD records (Barker et al., 2015) (Figure 4.51) consistently record this transition to occur very rapidly (>80% *N. pachyderma* to near 0% in under 4kyr). This is contrary to the benthic $\delta^{18}O$ record, which suggests that it takes approximately 31kyr from the beginning of deglacial warming and sea level rise to peak interglacial conditions (Figure 4.51). Furthermore comparison of the relative timing of peak interglacial conditions in MIS 11/Holocene to the benthic $\delta^{18}O$ shows that peak temperatures during MIS 11 (as indicated by the abrupt decrease in % *N. pachyderma* record) are reached before the minimum in benthic $\delta^{18}O$ by approximately 20kyr. The decrease in % *N. pachyderma* across T1 is less abrupt than the equivalent decrease during T5 and occurs as the benthic $\delta^{18}O$ is decreasing, approximately 10kyr after the initial onset of the termination (Figure 4.51).

In order to quantitatively compare the relative rate of change between the last 5 transitions between glacial to interglacial conditions the first derivative of the rate of change of CO_2 (Lüthi et al., 2008), benthic $\delta^{18}O$ (Lisiecki and Raymo, 2005), δD (Jouzel et al., 2007) and sea level (Grant et al., 2014) was calculated (figure 4.52). These calculations show that T5 has the slowest rate of change of any of the last 5

terminations, such that the transition from MIS 12 to MIS 11 is the most prolonged perhaps reflecting a larger magnitude of change between the glacial conditions of MIS 12 to the interglacial of MIS 11.

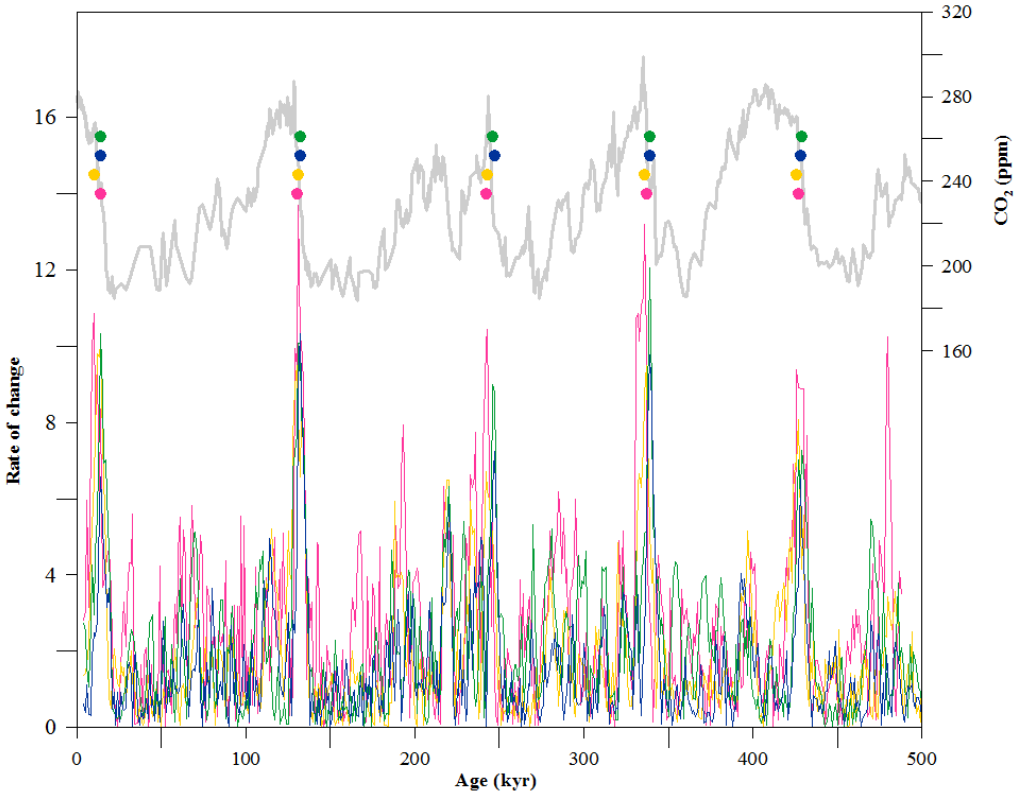

Figure 4.58. Timing of peak rate of change (first derivative) when comparing benthic $\delta^{18}O$ (‰/kyr) (yellow), δD (‰/kyr) (green), CO_2 (ppm/kyr) (blue) and sea level (m/kyr) (pink); (Lisiecki and Raymo, 2005; Jouzel et al., 2007; Lüthi et al., 2008; Grant et al., 2014). The coloured circles highlight the timing of each of the parameters (i.e. without units).

4.8.5 EXTREME NATURE OF TERMINATION 5

The next logical step following comparison of records from the North Atlantic across both T5 and T1 is to move to the South Atlantic to analyse any possible relationships between the two hemispheres and the expression of the bipolar seesaw. Here we compare the relevant records from ODP Site 983 in the North to ODP Site 1089 (see

chapter 2 for full datasets). The record of the abundance of warm species from the South Atlantic suggests that there was an extreme warming at the onset of the T5 in the South Atlantic (*G. ruber* peaks at 21% of the assemblage); following this extreme warm interval in the South Atlantic, in the North Atlantic (ODP Site 983) we see an abrupt reduction in the abundance of *N. pachyderma* (Barker et al., 2015), from >80% to <5%, in the North Atlantic approximately 425kyr (Figure 4.51).

The same records for T1 show the same general trend, however, they show less extreme variability in each of the proxies; *G. ruber* peak at little over 1% and the reduction in *N.pachyderma* from >80% to <5% occurs over a much longer period (the transition between MIS 12 and MIS 11 occurs in less than 5kyr, whereas it takes over 8kyr for the transition from MIS 2 and the Holocene). As such, we suggest that the 'extreme' warming in the South Atlantic and corresponding 'extreme' ice rafting event in the North Atlantic associated with T5 (MIS 2 had a much smaller IRD event, >1600 grains/g compared to >3500 grains/g during MIS 12) somehow resulted in the near instantaneous shift from glacial to interglacial conditions in the surface waters of the North Atlantic. This is evidenced by the early expression of warm interglacial conditions as indicated by the near complete absence of *N. pachyderma* and the high temperatures from the Mg/Ca analysis.

Although interglacial conditions in the surface waters of the North Atlantic (at ODP Site 983) are reached quickly after the onset of MIS 11, the story in the deep ocean is very different (as alluded to in the results section of this chapter). The transition from MIS 12 to MIS 11 in the deep ocean occurs over a much longer time interval and as such, full interglacial conditions are not reached until approximately 410kyr likely the result of incorporation of ice volume in the benthic $\delta^{18}O$ value obtained.

We suggest that the extreme conditions during Termination 5 (i.e. a massive ice rafting event in the North Atlantic and very warm conditions in the South Atlantic) reflected a particularly weakened/shoaled AMOC that may have been caused ultimately by the extreme glacial conditions of MIS 12 (Lisiecki and Raymo, 2005; Bard and Rickaby, 2009). The extreme conditions of MIS 12 mean that although the interglacial temperatures of the surface waters in the North Atlantic were reached early during MIS 11, it took much longer for global climate to recover from the very cold conditions of MIS 12.

4.9 CONCLUSIONS

In conclusion we suggest that the interglacial conditions of MIS 11 are reached very rapidly following the transition from MIS 12 in the North Atlantic. This is particularly interesting when we consider that the benthic $\delta^{18}O$ records from ODP Site 983 (Channell et al., 1997) as well as the atmospheric gases (Loulergue et al., 2008; Lüthi et al., 2008) that suggest that the transition from MIS 12 to 11 is rather slow.

Secondly, the relative timing of the transition (as indicated by a sharp decrease in the abundance of *N. pachyderma*) compared to the onset of the termination (as defined by the decrease in the benthic $\delta^{18}O$ record) is different when we compare T1 and T5. Peak interglacial conditions (at least at our site) are reached much earlier during T5 relative to the benthic $\delta^{18}O$ record than they are for T1. During T1, the interglacial conditions are not reached until nearly the end of the decrease in benthic $\delta^{18}O$ (~7.1kyr), approximately 10kyr after the initial onset of the termination. Comparatively for T5, the peak interglacial conditions are reached by 424kyr, less than 7kyr after the initial decrease in benthic $\delta^{18}O$.

Comparison of the *G. inflata* $\delta^{18}O$ record from this study with previously published *G. bulloides* $\delta^{18}O$ (Channell et al., 1997) highlight the differences in stratification of the water column at ODP Site 983 during the interglacial of MIS 11. We show that during the early part of the interglacial the water column is well mixed perhaps as the result of the resumption of the overturning circulation and formation of deep-water in the North Atlantic. In the latter part of the interglacial we record a decoupling of the two records, such that the *G. bulloides* records lighter $\delta^{18}O$ values when compared to *G. inflata*, suggesting increased stratification of the water column. These observations have been linked to variability in the strength of the SPG during the Holocene (Thornalley et al., 2009), we too suggest that there were millennial scale oscillations of the currents in the North Atlantic during the interglacial of MIS 11 such that variations in the strength of the SPG, resulted in changes in the temperature and salinity of the North Atlantic such that the North Atlantic became more saline during enhanced freshwater flux to the subpolar North Atlantic. As such, the increased stratification during the latter part of the record presented here from MIS 11 suggests an increase in the freshwater water flux results in a decrease in the strength of AMOC on millennial time scales, perhaps providing a millennial scale negative

feedback mechanism to G-IG variability. In turn, the variability impacts upon the region of deep water formation in the North Atlantic (Thornalley et al., 2009), an important component in G-IG cyclicity.

In conclusion, we suggest that T5 is an 'extreme' example of a termination. The IRD record covering the last 440kyr from ODP Site 983 (Barker et al., 2015) shows that the ice-rafting event at the onset of the transition from MIS 12 to MIS 11 is the second largest event of the last 440kyr (>3500 IRD grains/g) and is over two times larger than the equivalent ice rafting event of T1 (>1600 IRD grains/g). Further evidence that T5 is a more extreme event that T1 is apparent when we consider the faunal records from the South Atlantic (TN057-21; T1 and ODP Site 1089; T5). Here, as discussed comprehensively in chapter 2, we record a large peak (>21%) in the abundance of warm species (notably *G. ruber*) prior to the onset of the decrease in benthic $\delta^{18}O$ (i.e. the end of MIS 12). Whereas the equivalent peak in warm species in T1 occurs comparatively later in the termination and is notably smaller in magnitude (<10% warm species) (Barker et al., 2009).

We suggest that the large differences in sea surface conditions during T5 between the two hemispheres results in the rapid transmission of the oceanic signal and peak interglacial conditions (MIS 11) being reached more quickly for T5 than T1, however, the 'extreme' conditions recorded in both hemispheres appear to have little impact (if any) on the magnitude of deglacial CO_2 change across Termination 5.

5 SYNTHESIS AND CONCLUSIONS

In the introduction to this thesis, the idea that glacial-interglacial cyclicity cannot be explained by orbital forcing alone and that internal feedbacks are required to amplify the orbital forcing was outlined. With this overarching statement in mind, this thesis seeks to better understand the role of millennial scale events in driving G-IG climate variability; notably the relationship between the magnitude of millennial scale events and the magnitude of G-IG climate variability. This section briefly outlines the main findings of each of the chapters in the context of the questions outlined in the introduction;

Are all terminations equal? Does each termination respond the same way to being orbitally forced? Are their any feedback mechanisms contributing to G-IG climate variability?

Are abrupt changes in ocean circulation a persistent feature of terminations? If so, do they matter and how? Do we observe the same changes in ocean circulation patterns across each of the terminations?

Are the relationships between ocean circulation, CO_2 and glacial terminations consistent between different terminations? And ask such are we able to unravel the complexities of the relationships and interactions of them?

5.1 SUMMARY OF CHAPTERS

5.1.1 TERMINATION 5 (T5); AN 'EXTREME' TERMINATION?

Chapter 2 specifically looks at a core location in the South Atlantic and compares the faunal assemblage data collected for this core location (ODP Site 1089) across terminations 2 and 5 with another nearby core (TN057-21 (Barker et al., 2009, 2010). The percentage abundance of all planktonic foraminifera in both the samples from T1 (Barker and Diz, 2014) and T5 (this study) were counted (note only *G. ruber* and *N. pachyderma* were counted for the T2). Interpretation of the results presented here suggest that, when compared to T1 and T2, the magnitude of the warm event recorded in the surface ocean of the South Atlantic during Termination 5 is unprecedented in

magnitude. However, despite this very large peak in the abundance of the planktonic warm species during MIS 12, it appears that this millennial scale event does not impact upon the magnitude of the G-IG cycle itself, suggesting that perhaps it is not the magnitude of the millennial scale event that influences the magnitude of the glacial termination.

5.1.2 LATE RECOVERY OF THE AMOC EXPLAINS LARGERS AMPLITUDE OF CO_2 CHANGE ACROSS THE PEMULTIMATE DEGLACIATION

This chapter uses neodymium isotopes to understand the complexities of the changes in the strength, and the resulting influence of changes in the strength on the amplitude of deglacial CO_2 changes across T2. The amplitude of deglacial CO_2 variability of the two terminations (T1 and T2) is different; such that T2 records a CO_2 rise approximately 20ppmv greater than T1. With the use of stable oxygen and carbon isotopes as well as planktonic faunal counts and the use of neodymium isotopes we are able to access the role of millennial scale events in the North Atlantic (ODP Site 1063). We suggest that the reason for the difference in amplitude of deglacial CO_2 release across the two terminations is again not as a result of different amplitudes of millennial scale events but rather the relative timing of the changes during the transition from glacial to interglacial conditions.

We suggest, based on the data presented in chapter 3 that the reason for the larger amplitude of deglacial CO_2 rise across T2 is because the resumption of the AMOC occurs late in the termination. Conversely during T1 the B-A (resumption of the AMOC), the deglacial CO_2 rise plateaus suggesting that there is the possibility of competing millennial scale mechanisms seeking to oppose the rise in CO_2. We suggest that given that the CO_2 record returns to typical interglacial CO_2 values following the late resumption of AMOC at the end of T2, that again, it appears to be the timing of these millennial scale events during the terminations, rather than the magnitude of the faunal changes themselves that have the greatest impact upon the magnitude of G-IG itself.

5.1.3 VERY RAPID ATTAINMENT OF INTERGLACIAL CONDITIONS AT THE ONSET OF MIS11

This chapter quantifies the changes in temperature in the sea surface in the North Atlantic (ODP Site 1063) during MIS 11. We used paired δ^{18}O-Mg/Ca analysis on the planktonic foraminifera, *G. inflata* (up to 400m water depth (Hemleben et al., 1989)). The record covers MIS 11 and indicates that temperatures of approximately 8-11°C were reached near instantaneously following the transition from MIS 12 in the North Atlantic (approximately 424kyr). This is particularly interesting when we consider that the benthic δ^{18}O records from ODP Site 983 (Channell et al., 1997) as well as the atmospheric gases (Loulergue et al., 2008; Lüthi et al., 2008) that suggest that the transition from MIS 12 to 11 is rather slow.

Additionally, the relative timing of the transition compared to the onset of the termination (the decrease in the benthic δ^{18}O record) differs between terminations 1 and 5. At our core location during T5 the peak interglacial conditions are reached much earlier compared to the same change in T1 (7kyr compared to 10kyr respectively).

Furthermore, our records show differences in the stratification of the water column during MIS 11 by comparing the *G. inflata* δ^{18}O record from this study with previously published *G. bulloides* δ^{18}O (Channell et al., 1997). The records show that the water column was well mixed during the early part of MIS 11, likely the result of a strong overturning circulation following MIS 12, but that during the later stages of MIS 11 the records become decoupled from each other suggesting stratification between the uppermost 100m (as indicated by the *G. bulloides* δ^{18}O record (Hemleben et al., 1989) and approximately 200-400m (*G. inflata* δ^{18}O record (Hemleben et al., 1989)). These observations have been linked to variability in the strength of the SPG during the Holocene (Thornalley et al., 2009), we too suggest that there were millennial scale oscillations of the currents in the North Atlantic during the interglacial of MIS 11 such that variations in the strength of the SPG, resulted in changes in the temperature and salinity of the North Atlantic such that the North Atlantic became more saline during enhanced freshwater flux to the subpolar North Atlantic. As such, the increased stratification during the latter part of the record presented here from MIS 11 suggests an increase in the freshwater water flux results in a decrease in the strength of AMOC on millennial time scales, perhaps providing a millennial scale negative feedback mechanism to G-IG variability. In turn, the

variability impacts upon the region of deep water formation in the North Atlantic (Thornalley et al., 2009), an important component in G-IG cyclicity.

In conclusion, based on the data in this chapter (faunal records from the South Atlantic (TN057-21; T1 and ODP Site 1089; T5), we suggest that T5 is an 'extreme' example of a termination. During T5, as discussed comprehensively in chapter 2, we record a large peak (>21%) in the abundance of warm species (notably *G. ruber*) prior to the onset of the decrease in benthic $\delta^{18}O$ (i.e. the end of MIS 12). Whereas the equivalent peak in warm species in T1 occurs comparatively later in the termination and is notably smaller in magnitude (<10% warm species) (Barker et al., 2009). We suggest that the large difference in sea surface conditions during T5 between the two hemispheres results in the rapid transmission of the oceanic signal (via the AMOC) and peak interglacial conditions (MIS 11) being reached more quickly for T5 than T1. Despite the 'extreme' termination recorded in both hemispheres during T5, there appears to be little impact (if any) on the magnitude of deglacial CO_2 change across the termination, suggesting that the magnitude of millennial scale events does not impact upon the magnitude of the termination.

5.2 LIMITATIONS OF THE INTERPRETATIONS OF THE PROXY RESULTS

As with using any proxy methods there are limitations and assumptions that have to be made in order to make interpretations based on the results. In this section these limitations are outlined and the potential affect of the assumptions on some of the conclusions of this work.

The distribution of neodymium in the deep oceans is influenced by the inputs from continental weathering, mass advection as well as boundary exchange between particulate and dissolved fractions (Wilson et al., 2013b). In this thesis we interpret changes in the ε_{Nd} value to be as a result of changes in either continental weathering rates and/or location of origin. However, this approach is limited by uncertainties in the process of boundary exchange. In order to constrain the boundary exchange conditions further and increase our confidence in interpretation these results we need to gain a better understand the chemical mechanisms involved in the exchange of Nd isotopes with particles. At present the understanding of boundary exchange is poorly understood as it is so variable with time and space. Here we assume that there is

little/no effect of boundary exchange on our ε_{Nd} results and such we interpret any changes in the neodymium isotope values to primarily represent changes in the mixing of different water masses. Additionally, changes in the end-member neodymium values through time could influence the interpretation of the $\varepsilon_{Nd.}$ During our interpretations we assume that there is no change in the end-member composition with time as we are unable to constrain any potential changes, this is a sound assumption to make given that the changes that we record across Termination 2 in the North Atlantic occur over such short timescales that the near instantaneous change in ε_{Nd} value is most likely to be as a result of changes in the water mass in the bottom waters at the core location. That said, it should be noted that the inability to constrain the end-members and the process of boundary exchange are caveats to using neodymium isotopes as a proxy.

In addition to the caveats highlighted in the neodymium isotopic interpretation above there are similar caveats in the use of the Mg/Ca proxy notably in the correction for contaminants on the surface of, in this case, the foraminifera. Firstly, we have assumed here that all of the shells have been contaminated by the same amount as we use a 'blanket approach' to correcting for contamination. In the first instance it would have been a good idea to include the reductive cleaning step in the Mg/Ca analysis as this would have minimised the potential contamination from any oxide coating on the shell.

5.3 LIMITATIONS OF THE PALEOCEANOGRAPHIC RESULTS

One of the major limitations to making inferences of the timing of events when comparing different datasets and/or different locations is that the age modelling approach is sound and stands alone. We can be confident that when we are comparing the relative timing of changes in the surface and deep waters at the same core location and there is no offset between the two however, caution should be taken when making inferences on the timing of events when comparing different core locations and/or different proxies recorded on different parts of the core material. Here, we are careful to focus on the magnitude of events when we are unable to compare records from the same core as this reduces potential issues with making statements about the timing of changes but instead the relative magnitude of the same events. In the absence of being able to generate an absolute age model, we have used

the best approach possible on a case-by-case basis (see individual chapters for the detail) based on the timings of the major transitions across the terminations. However, the absolute ages stated should be used with caution as the age modelling approach is done by assigning ages to depths in the cores based on features from proxy results. Regardless of possible changes that could be made to the age modelling approach, there is little impact of any changes to the conclusions of this work; it is the sequence of millennial scale events that impacts upon of the magnitude of glacial-interglacial changes rather than the absolute timing of the changes.

5.4 SYNTHESIS

In terms of the contribution of millennial time-scale mechanisms to glacial terminations, the most important finding of the work in this thesis is the apparent lack of relationship between the extent millennial scale events in the Atlantic and the magnitude of glacial terminations. This finding is demonstrated by the fact that despite the large magnitude of the *G. ruber* warm event in the South Atlantic at the end of MIS 12 (T5; chapter 2) there appears to be little impact on the magnitude of the termination itself; when compared to the following terminations (T2 and T1).

What does appear to be important in determining the extent of deglacial CO_2 rise across a G-IG cycle however, is the differences in timing of the millennial scale events across the termination. The results of the neodymium analysis across Termination 2 (T2) (chapter 3), show that it is the sequence of events of the termination that is an important factor in determining the extent of CO_2 release across the G-IG transition rather than the magnitude of change; more specifically the interplay between different mechanisms seeking to increase/decrease atmospheric CO_2. When compared to T2, the apparent lack of response of CO_2 during the B-A, following HS1, should perhaps be considered as anomalous, probably reflecting a complex combination of mechanisms with opposing influences on CO_2 (see introduction). Unlike the last deglaciation, Termination 2 was not interrupted by a resumption of the AMOC (the B-A during T1). Instead, T2 records continual deglacial CO_2 rise across the transition from MIS 12 to MIS 11, whereby an 'overshoot' is subsequently recorded. This overshoot occurs due to the late resumption of AMOC and is recorded as a further quick rise in CO_2. Importantly,

following the late resumption of the AMOC early in MIS 5e we subsequently record a reduction in CO_2 reaching values more like those of the Holocene as ocean circulation recovered to more modern-like conditions by ~124yr (Hodell et al., 2009) (See figure 3.19 in chapter 3). We therefore suggest that the larger net change in CO_2 across T2 (as compared with T1) was a direct consequence of the timing of abrupt AMOC (late) resumption with respect to other deglacial changes.

Furthermore, we suggest the extreme negative ε_{Nd} values down to -15.6 in the record require a different origin/mixture of water than is currently bathing ODP Site 1063 today. We suggest here that the Labrador Sea is an obvious source of water with such a signature. These results show a persistent coupling of changes in the deep ocean chemistry (ε_{Nd}) in the North Atlantic and high latitude climate change and we suggest that the late recovery of the AMOC during T2 (in particular the absence of a 'B-A-like' interruption) may explain the larger amplitude of deglacial CO_2 rise associated with the penultimate deglaciation.

These results answer the question '*are the relationships between ocean circulation, CO_2 and glacial terminations consistent between different terminations?'* indicating that in fact the relationship between ocean circulation and CO_2 release across the different terminations considered here (T1, T2) is not consistent and shows that variability in the sequence of millennial scale events plays a crucial role in determining the extent of deglacial CO_2 rise.

Our results from the South Atlantic for each of the terminations studied here (T1, T2 and T5) show differences in the timings of planktonic faunal changes relative to changes in the benthic $\delta^{18}O$ record (crude proxy for ice volume). These records (Figure 2.20, chapter 2) suggest that the relationship between changes in the surface conditions of the South Atlantic do not occur at the same time across all of the terminations studied here. According to the planktonic foraminiferal faunal records, peak interglacial conditions are reached much earlier during T5 relative to the benthic $\delta^{18}O$ record than they are for T1. During T1, interglacial conditions are not reached until nearly the end of the decrease in benthic $\delta^{18}O$ (~7.1kyr, approximately 10kyr after the initial onset of the termination. Comparatively for T5, the peak interglacial conditions are reached by 424.5kya, less than 7kyr after the initial decrease in benthic $\delta^{18}O$. This suggests that in fact *not all terminations are equal* and that although the

overall G-IG variability of benthic $\delta^{18}O$ appears to be consistent in the amplitude of changes across the last five glacial terminations, there are differences in the relative timing and rate of change of events hidden within the overall G-IG trend.

Secondly we record a near instantaneous response of warming in the surface ocean of the North Atlantic (chapter 4) following the transition to interglacial conditions during MIS 11. Despite the apparent abrupt transition to interglacial conditions in the surface ocean, the deep ocean shows a prolonged transition form MIS 12 to MIS 11. As such the abrupt millennial scale warming in the North Atlantic does not appear to have had an impact on the extent of deglacial CO_2 release. This suggests perhaps that the instantaneous response in the North Atlantic is more a response to local climate features rather than a response to changes in the bipolar seesaw, accounting for the apparent lack of influence of this abrupt change to the magnitude of G-IG variability.

During T2 there is a difference in the extent of deglacial CO_2 rise, compared to T1 there is a much larger increase (approximately 20ppm) in deglacial CO_2 rise across the transition from MIS 6 to MIS 5. However, we suggest that this is not a result of differing magnitudes of millennial scale events, but rather a result of the differences in timings of these events with respect to each other across the transition. We suggest that it is the late recovery of AMOC at the onset of MIS 5e that is the cause for the larger deglacial CO_2 release (as a result of T2 not being interrupted by a 'B-A like' event similar to T1).

What appears to be true is that the changes in ocean circulation are abrupt in comparison to the benthic $\delta^{18}O$ changes, occur during each of the terminations studied and appear to be a persistent feature of G-IG climate variability.

The findings of this work suggest that no two glacial terminations are the same and that it is a complex sequence of events that result in amplification of a modest forcing resulting in a glacial termination. We suggest that rather than the magnitude of millennial scale events being important in determining the amplitude of G-IG variability, it is instead the timing and sequence of ocean circulation changes in determining the amplitude of these climatically important events.

5.5 CONCLUSIONS

In conclusion, using the results from the work presented here we find that the magnitude of millennial scale events is not important in determining the extent of a glacial termination. Instead, it is the timing of millennial scale events within a given termination that determines the magnitude of CO_2 released and the amplitude of G-IG variability. This conclusion is based on the following findings that the 'extreme' conditions recorded during T5 (specifically across MIS 12) are anomalous and that the extent of warming in the South Atlantic during MIS 12 is unprecedented when compared to the following G-IG cycles. Despite this, there is no evidence to suggest that this 'extreme' event has any impact on the magnitude of the G-IG variability recorded. We suggest that T5 is an extreme termination in the South Atlantic because of the large ice-rafting event in the North Atlantic during MIS 12 suggesting that the seesaw is very active during this interval. The ice rafting event in the North Atlantic causes the near cessation of AMOC slowing down the movement of warm surface warms from the South Atlantic northwards, allowing the South Atlantic time to warm up to temperatures favourable for *G. ruber* to survive in. *So why does the extreme event as recorded by the presence of large abundances of G. ruber not appear to matter in terms of the magnitude of deglacial CO_2 rise across T5?* We suggest that this is perhaps the result of the heat reservoir of the Southern Ocean absorbing the large warming event in the South Atlantic, the heat reservoir is so large that it does not propagate as far as the Antarctic ice core records (e.g. CO_2, δD) and thus is not recorded. The thermal bipolar seesaw mechanism (Stocker and Johnsen, 2003) calls upon the Southern Ocean to act as a heat reservoir, but it appears from our results that despite the unprecedented increase in temperature in the South Atlantic during MIS 12, it does not matter how much you increase temperatures in the South Atlantic, still no change is recorded in the Antarctic records. This would suggest that it does not matter how warm the South Atlantic gets, and thus how much the seesaw is forced, the magnitude of G-IG variability remains the same. Such that the magnitude of millennial scale variability appears to have no impact on the magnitude of the glacial-interglacial climate variability. This suggests that because variability is recorded in the climate records between the different terminations that it is the timing of millennial scale events that influence the magnitude of G-IG variability.

The records from ODP 1063 across MIS 6/5 (T2) suggest that the late resumption of AMOC at the early onset of MIS 5 may have resulted in higher atmospheric CO_2 levels during the penultimate interglacial of MIS 5 when compared to the Holocene interglacial interval. We suggest that it is the sequence of events during T1 that cause a stalling of deglacial CO_2 rise during the B-A and that the CO_2 rise plateaus due to competing mechanisms occurring releasing and absorbing CO_2 simultaneously. For example the tendency for a strengthened AMOC to draw down CO_2 (Schmittner and Galbraith, 2008) could have been countered by continued outgassing of CO_2 as a result of reduced sea ice cover and sustained deep ocean ventilation within the Southern Ocean during the B-A (Skinner et al., 2013). We suggest that this was not the case during T2 and instead, due to the late recovery of the AMOC, we record an overshoot of AMOC and an associated radical departure from modern oceanographics in the North Atlantic. We suggest from the results of the neodymium isotope analysis that the extreme negative εNd values down to -15.8 in the record require a different origin/mixture of water than is bathing ODP Site 1063 today. The Labrador Sea is an obvious candidate for generating such negative values. Our results show a persistent coupling of changes in the deep ocean chemistry (ε_{Nd}) in the North Atlantic and high latitude climate change.

Chapter 4 concludes that the interglacial conditions of MIS 11 are reached very rapidly following the transition from MIS 12 in the North Atlantic. This is particularly interesting when we consider that the benthic $\delta^{18}O$ records from ODP Site 983 (Channell et al., 1997) as well as the atmospheric gases (Loulergue et al., 2008; Lüthi et al., 2008) suggest that the transition from MIS 12 to 11 is prolonged and that that the transition from MIS 12 to 11 is expressed very differently in the surface and deep-ocean. The differences in stratification during the early and latter stages of interglacial of MIS 11 show that during the early part of the interglacial the water column is well mixed perhaps as the result of the resumption of the overturning circulation and formation of deep-water in the North Atlantic. In the latter part of the interglacial the decoupling of the two records (*G. bulloides* record lighter $\delta^{18}O$ values when compared to *G. inflata*) suggests increased stratification of the water column. We conclude, inline with the observations from (Thornalley et al., 2009) that the variability in stratification during MIS 11 is a result of millennial scale oscillations in the strength of the Subpolar Gyre (SPG) (Thornalley et al., 2009). We suggest that

there was increased stratification during the latter part of MIS 11, suggesting an increase in the freshwater water flux results in a decrease in the strength of AMOC on millennial time scales, providing perhaps a millennial scale negative feedback mechanism to G-IG variability. In turn, the variability impacts upon the region of deep water formation in the North Atlantic, an important component in G-IG cyclicity.

Based on the work presented here we conclude that not all terminations are equal, both in terms of the magnitude of glacial-interglacial variability and the contribution of the millennial scale events to the termination. Furthermore, we suggest that the relationships between ocean circulation, CO_2 and glacial terminations is not consistent between the terminations studied here (T1, T2 and T5) but that (abrupt) changes in ocean circulation, notably the bipolar seesaw, is indeed a persistent feature of glacial terminations albeit that the resulting expression of the bipolar seesaw appears not to influence the magnitude of glacial-interglacial variability.

5.6 FUTURE WORK

5.6.1 METHODOLOGICAL FUTURE WORK

There are two potential areas for future development in terms of the methods used in this thesis. Firstly, we need to better understand the implications of the differences in the *G. inflata* test wall coatings in the North Atlantic that has been highlighted in this research as well as others (Moffa Sánchez, 2012). We identify unexpected and unexplained differences in the two types of test appearance displayed by *G. inflata* in the North Atlantic. The opaque test appearance have previously been attributed to a crust that forms as a result of changes in the depth habitat of the species during its life cycle (Groeneveld and Chiessi, 2011). The research presented here suggests this link is unlikely as the foraminifera with the opaque wall structure are consistently lighter than the translucent ones, implying that rather than an encrustation the white appearance of the tests is likely the result of something else. This has much wider implications for the research field of paleoclimate and requires further investigation to enable us to better understand and account for the differences in wall structure of *G. inflata*.

Secondly, dissolution of the foraminiferal assemblages is another area of research that requires additional study. This thesis highlights the questions *'how well are we able to account for the effects of dissolution?'* and *'are we able to quantify the extent of dissolution of a particular sample?'* The research here highlights the need for better assessment of dissolution and the subsequent correction for it. The use of foraminiferal assemblages is crucial in enabling us to reconstruct changes in the water column over time. However, improvement in being able to quantify the extent of dissolution would provide us with greater confidence in the reliability of the datasets and the integrity of that particular field of research and allow us to quantitatively indicate the samples that have been most heavily influenced by dissolution. Previous work by Barker and Diz, (2014) and the work presented here is, at the moment, the best way to establish the extent of dissolution whereby species with similar environmental preferences but differing susceptibilities are compared to account for the extent of dissolution. However, if we were able to measure the weight of a selection of different species for example and compare that to the expected weight without any dissolution taking place, we would be better placed to make quantifiable decisions on a faunal assemblages based on the extent of dissolution.

5.6.2 THEORETICAL FUTURE WORK

The work presented in chapter 2 concludes that there was a major seesaw event across T5. However, T2 and T1 did not show the same 'extreme' conditions despite very similar orbital conditions at the onset of T1 and T5. In order to gain a more complete picture of the extent of the millennial scale oscillations across the last 5 terminations to ensure that the findings presented here are not just features of the terminations studied here, the same suite of proxies would need to be tested on T3 and T4 also. This would allow us to understand the sequence of millennial scale events across all of the last 5 terminations and enable us to make the best interpretations of this work in the context of all of the last 5 glacial terminations.

As mentioned above and discussed extensively in chapter 4, T5 is an 'extreme' example of a termination. Both the IRD record from ODP Site 983 (Barker et al., 2015) and the *G. ruber* abundance from the South Atlantic (TN057-21; T1 (Barker et al., 2009) and ODP Site 1089; T5 (this study)) show that when compared to T1 and

T2, T5 records much larger amplitude changes in both parameters. As such, this suggests that in the northern and southern hemispheres during the MIS 12/11 transition both the cold conditions in the North Atlantic and the warm conditions in the South Atlantic are unparalleled in extremity compared to the following terminations. The future work following these findings in chapter 4 would be to study the glacial-interglacial transitions for all of the last five terminations in depth. Full faunal assemblages and IRD counts as well as quantitative SST reconstructions from the surface and deep-ocean would aid our understanding of the complexities of glacial terminations and the relationship between the surface and deep-ocean and the role of millennial scale events in glacial terminations.

Additional future work would be to extend the neodymium analysis to earlier terminations and assess them in connection with the atmospheric CO_2 records to establish if the timing of the sequence of events across MIS 6/5 is unique or rather the halting of CO_2 during the B-A is anomalous. Further work needs to be carried out to assess the extent of CO_2 release/drawdown for each of the mechanisms that occur during terminations and then deconvolve the sequence of events to see if there is an impact on the magnitude of CO_2 release during the transition from glacial to interglacial conditions. I suggest that, based on the findings of this research, that it is the state and timing of changes in the overturning circulation that are the most important in determining the extent of G-IG climate change. This is further supported by the evidence that, based on the work from T5 and T2 presented here, the magnitude of the millennial scale events appears to have very little (if any) impact on the magnitude of G-IG climate variability.

An obvious line for future work following chapter 4 is to extend the sea surface temperature record in both directions to cover MIS 12 and as well as from MIS 11 to MIS 10. This would allow us to see if the transition in sea surface temperature is as abrupt at the *G. inflata* record suggests or if the near-thermocline waters are not recording the G-IG variability in the North Atlantic. This paired Mg/Ca-$\delta^{18}O$ record would need to be carried out using a different species to *G. inflata*, as they are not present continuously through this section. This work would build on the high-resolution data set produced from this core location in the North Atlantic (ODP Site

983) (Barker et al., 2015) and provide a quantitative record of temperature changes occurring in the water column over T5.

6 REFERENCES

Adkins, J.F., Boyle, E.A., Keigwin, L., and Cortijo, E. (1997). Variability of the North Atlantic thermohaline circulation during the last interglacial period. Nature *390*, 154–156.

Ahn, J., and Brook, E.J. (2008). Atmospheric CO2 and climate on millennial time scales during the last glacial period. Science *322*, 83–85.

Anand, P., Elderfield, H., and Conte, M.H. (2003). Calibration of Mg/Ca thermometry in planktonic foraminifera from a sediment trap time series. Paleoceanography *18*.

Anderson, R.F., Ali, S., Bradtmiller, L.I., Nielsen, S.H.H., Fleisher, M.Q., Anderson, B.E., and Burckle, L.H. (2009). Wind-driven upwelling in the Southern Ocean and the deglacial rise in atmospheric CO2. Science *323*, 1443–1448.

Archer, D. (1991). Modeling the calcite lysocline. J. Geophys. Res. *96*, 17037–17050.

Archer, D., Winguth, A., Lea, D., and Mahowald, N. (2000). What caused the glacial/interglacial atmospheric pCO2 cycles? Reviews of Geophysics *38*, 159–189.

Arrhenius, G. (1953). Sediment cores from the East Pacific. Swedish Deep-Sea Expedition Reports *75*, 115–118.

Bard, E., and Rickaby, R.E. (2009). Migration of the subtropical front as a modulator of glacial climate. Nature *460*, 380–383.

Bard, E., Rostek, F., Turon, J.-L., and Gendreau, S. (2000). Hydrological impact of Heinrich events in the subtropical northeast Atlantic. Science *289*, 1321–1324.

Barker, S., and Diz, P. (2014). Timing of the descent into the last ice age determined by the bipolar seesaw. Paleoceanography *29*, 489–507.

Barker, S., Greaves, M., and Elderfield, H. (2003). A study of cleaning procedures used for foraminiferal Mg/Ca paleothermometry. Geochemistry, Geophysics, Geosystems *4*.

Barker, S., Diz, P., Vautravers, M.J., Pike, J., Knorr, G., Hall, I.R., and Broecker, W.S. (2009). Interhemispheric Atlantic seesaw response during the last deglaciation. Nature *457*, 1097–1102.

Barker, S., Knorr, G., Vautravers, M.J., Diz, P., and Skinner, L.C. (2010). Extreme deepening of the Atlantic overturning circulation during deglaciation. Nature Geoscience *3*, 567–571.

Barker, S., Knorr, G., Edwards, R.L., Parrenin, F., Putnam, A.E., Skinner, L.C., Wolff, E., and Ziegler, M. (2011). 800,000 years of abrupt climate variability. Science *334*, 347–351.

Barker, S., Chen, J., Gong, X., Jonkers, L., Knorr, G., and Thornalley, D. (2015). Icebergs not the trigger for North Atlantic cold events. Nature *520*, 333–336.

Bashirova, L.D., Kandiano, E.S., Sivkov, V.V., and Bauch, H.A. (2014). Migrations of the North Atlantic Polar front during the last 300 ka: Evidence from planktic foraminiferal data. Oceanology *54*, 798–807.

Baumgartner, M., Kindler, P., Eicher, O., Floch, G., Schilt, A., Schwander, J., Spahni, R., Capron, E., Chappellaz, J., Leuenberger, M., et al. (2014). NGRIP CH4 concentration from 120 to 10 kyr before present and its relation to a δ15N temperature reconstruction from the same ice core. Climate of the Past *10*, 903–920.

Bazin, L., Landais, A., Lemieux-Dudon, B., Toyé Mahamadou Kele, H., Veres, D., Parrenin, F., Martinerie, P., Ritz, C., Capron, E., Lipenkov, V., et al. (2013). An optimized multi-proxy, multi-site Antarctic ice and gas orbital chronology (AICC2012): 120-800 ka. Climate of the Past *9*, 1715–1731.

Bé, A.W.H., and Tolderlund, D.S. (1971). Distribution and ecology of living planktonic foraminifera in surface waters of the Atlantic and Indian Oceans. The Micropaleontology of Oceans 105–149.

Bé, A.W., and Hutson, W.H. (1977). Ecology of planktonic foraminifera and biogeographic patterns of life and fossil assemblages in the Indian Ocean. Micropaleontology 369–414.

Becquey, S., and Gersonde, R. (2002). Past hydrographic and climatic changes in the Subantarctic Zone of the South Atlantic–The Pleistocene record from ODP Site 1090. Palaeogeography, Palaeoclimatology, Palaeoecology *182*, 221–239.

Bemis, E.B., Spero, H.J., Bijma, J., and Lea, D.W. (1998). Reevaluation of the oxygen isotopic composition of planktonic foraminifera: Experimental results and revised paleotemperature equations. Paleoceanography *13*, 150–160.

Bender, M.L., Klinkhammer, G.P., and Spencer, D.W. (1977). Manganese in seawater and the marine manganese balance. Deep Sea Research *24*, 799–812.

Bereiter, B., Eggleston, S., Schmitt, J., Nehrbass-Ahles, C., Stocker, T.F., Fischer, H., Kipfstuhl, S., and Chappellaz, J. (2015). Revision of the EPICA Dome C CO2 record from 800 to 600 kyr before present. Geophysical Research Letters *42*, 542–549.

Berger, A. (1978). Long-term variations of daily insolation and Quaternary climatic changes. Journal of the Atmospheric Sciences *35*, 2362–2367.

Berger, W.H. (1967). Foraminiferal ooze: solution at depths. Science *156*, 383–385.

Berger, W.H. (1968). Planktonic foraminifera: selective solution and paleoclimatic interpretation. In Deep Sea Research and Oceanographic Abstracts, (Elsevier), pp. 31–43.

Berger, W.H. (1969). Ecologic patterns of living planktonic foraminifera. In Deep Sea Research and Oceanographic Abstracts, (Elsevier), pp. 1–24.

Berger, W.H. (1970). Planktonic foraminifera: selective solution and the lysocline. Marine Geology *8*, 111–138.

Berger, A., and Loutre, M.-F. (1991). Insolation values for the climate of the last 10 million years. Quaternary Science Reviews *10*, 297–317.

Berger, W.H., and Piper, D.J. (1972). PLANKTONIC FORAMINIFERA: DIFFERENTIAL SETTLING, DISSOLUTION, AND REDEPOSITION1. Limnology and Oceanography *17*, 275–287.

Bianchi, G.G., and McCave, I.N. (1999). Holocene periodicity in North Atlantic climate and deep-ocean flow south of Iceland. Nature *397*, 515–517.

Blunier, T., and Brook, E.J. (2001). Timing of millennial-scale climate change in Antarctica and Greenland during the last glacial period. Science *291*, 109–112.

Böhm, E., Lippold, J., Gutjahr, M., Frank, M., Blaser, P., Antz, B., Fohlmeister, J., Frank, N., Andersen, M.B., and Deininger, M. (2015). Strong and deep Atlantic meridional overturning circulation during the last glacial cycle. Nature *517*, 73–76.

Bond, G., Broecker, W., Johnsen, S., McManus, J., Labeyrie, L., Jouzel, J., and Bonani, G. (1993). Correlations between climate records from North Atlantic sediments and Greenland ice. Nature 143–147.

Bond, G., Kromer, B., Beer, J., Muscheler, R., Evans, M.N., Showers, W., Hoffmann, S., Lotti-Bond, R., Hajdas, I., and Bonani, G. (2001). Persistent solar influence on North Atlantic climate during the Holocene. Science *294*, 2130–2136.

Boyle, E.A. (1983). Manganese carbonate overgrowths on foraminifera tests. Geochimica et Cosmochimica Acta *47*, 1815–1819.

Boyle, E.A., and Keigwin, L.D. (1982). Deep circulation of the North Atlantic over the last 200,000 years: Geochemical evidence. Science *218*, 784–787.

Boyle, E.A., and Keigwin, L.D. (1985). Comparison of Atlantic and Pacific paleochemical records for the last 215,000 years: Changes in deep ocean circulation and chemical inventories. Earth and Planetary Science Letters *76*, 135–150.

ter Braak, C.J., and Juggins, S. (1993). Weighted averaging partial least squares regression (WA-PLS): an improved method for reconstructing environmental variables from species assemblages. Hydrobiologia *269*, 485–502.

Bradshaw, J.S. (1957). Ecology of living planktonic foraminifera in the North and Equatorial Pacific Ocean.

Broecker, W.S. (1979). A revised estimate for the radiocarbon age of North Atlantic Deep Water. Journal of Geophysical Research: Oceans (1978–2012) *84*, 3218–3226.

Broecker, W.S. (1998). Paleocean circulation during the last deglaciation: a bipolar seesaw? Paleoceanography *13*, 119–121.

Broecker, W.S. (2003). The oceanic CaCO3 cycle. Treatise on Geochemistry *6*, 529–549.

Broecker, W.S., and Denton, G.H. (1989). The role of ocean-atmosphere reorganizations in glacial cycles. Geochimica et Cosmochimica Acta *53*, 2465–2501.

Broecker, W.S., and Donk, J. (1970). Insolation changes, ice volumes, and the O18 record in deep-sea cores. Reviews of Geophysics *8*, 169–198.

Broecker, W.S., Bond, G., Klas, M., Bonani, G., and Wolfli, W. (1990). A salt oscillator in the glacial Atlantic? 1. The concept. Paleoceanography *5*, 469–477.

Brovkin, V., Ganopolski, A., Archer, D., and Rahmstorf, S. (2007). Lowering of glacial atmospheric CO2 in response to changes in oceanic circulation and marine biogeochemistry. Paleoceanography *22*.

Brown, E., Colling, A., Park, D., Phillips, J., Rothery, D., and Wright, J. (1995). Seawater: its composition, properties and behaviour (Butterworth-Heinemann).

Burton, E.A., and Walter, L.M. (1991). The effects of P CO2 and temperature on magnesium incorporation in calcite in seawater and MgCl 2-CaCl 2 solutions. Geochimica et Cosmochimica Acta *55*, 777–785.

Channell, J.E.T., Hodell, D.A., and Lehman, B. (1997). Relative geomagnetic paleointensity and δ 18 O at ODP Site 983 (Gardar Drift, North Atlantic) since 350 ka. Earth and Planetary Science Letters *153*, 103–118.

Channell, J.E.T., Hodell, D.A., and Curtis, J.H. (2012). ODP Site 1063 (Bermuda Rise) revisited: oxygen isotopes, excursions and paleointensity in the Brunhes Chron. Geochemistry, Geophysics, Geosystems *13*.

Chapman, M.R. (2010). Seasonal production patterns of planktonic foraminifera in the NE Atlantic Ocean: Implications for paleotemperature and hydrographic reconstructions. Paleoceanography *25*.

Charles, C.D., and Fairbanks, R.G. (1992). Evidence from Southern Ocean sediments for the effect of North Atlantic deep-water flux on climate.

Charles, C.D., Lynch-Stieglitz, J., Ninnemann, U.S., and Fairbanks, R.G. (1996). Climate connections between the hemisphere revealed by deep sea sediment core/ice core correlations. Earth and Planetary Science Letters *142*, 19–27.

Cheng, H., Edwards, R.L., Broecker, W.S., Denton, G.H., Kong, X., Wang, Y., Zhang, R., and Wang, X. (2009). Ice age terminations. Science *326*, 248–252.

Chiessi, C.M., Mulitza, S., Paul, A., Pätzold, J., Groeneveld, J., and Wefer, G. (2008). South Atlantic interocean exchange as the trigger for the Bølling warm event. Geology *36*, 919–922.

Cléroux, C., Cortijo, E., Duplessy, J.-C., and Zahn, R. (2007). Deep-dwelling foraminifera as thermocline temperature recorders. Geochemistry, Geophysics, Geosystems *8*.

Cléroux, C., Cortijo, E., Anand, P., Labeyrie, L., Bassinot, F., Caillon, N., and Duplessy, J.-C. (2008). Mg/Ca and Sr/Ca ratios in planktonic foraminifera: Proxies for upper water column temperature reconstruction. Paleoceanography *23*.

CLIMAP Members (1984). The last interglacial ocean. Quaternary Research *21*, 123–224.

Cortese, G., Abelmann, A., and Gersonde, R. (2007). The last five glacial-interglacial transitions: A high-resolution 450,000-year record from the subantarctic Atlantic. Paleoceanography *22*.

Craig, H., and Gordon, L.I. (1965). Deuterium and oxygen 18 variations in the ocean and the marine atmosphere.

Crocket, K.C., Lambelet, M., van de Flierdt, T., Rehkämper, M., and Robinson, L.F. (2014). Measurement of fossil deep-sea coral Nd isotopic compositions and concentrations by TIMS as NdO+, with evaluation of cleaning protocols. Chemical Geology *374*, 128–140.

Crowley, T.J. (1992). North Atlantic deep water cools the Southern Hemisphere. Paleoceanography *7*, 489–497.

Cubasch, U., Meehl, G.A., Boer, G.J., Stouffer, R.J., Dix, M., Noda, A., Senior, C.A., Raper, S., and Yap, K.S. (2001). Climate change 2001: The scientific basis. Intergovernmental Panel on Climate Change (ed. Houghton, JT et Al.) 525–582.

Curry, W.B., and Oppo, D.W. (2005). Glacial water mass geometry and the distribution of δ13C of ΣCO2 in the western Atlantic Ocean. Paleoceanography *20*.

Curry, W.B., Duplessy, J.-C., Labeyrie, L.D., and Shackleton, N.J. (1988). Changes in the distribution of δ13C of deep water ΣCO2 between the last glaciation and the Holocene. Paleoceanography *3*, 317–341.

Denton, G.H., Broecker, W.S., and Alley, R.B. (2006). The mystery interval 17.5 to 14.5 kyrs ago. PAGES News *14*, 14–16.

Dickson, R.R., and Brown, J. (1994). The production of North Atlantic Deep Water: sources, rates, and pathways. Journal of Geophysical Research: Oceans (1978–2012) *99*, 12319–12341.

Dinniman, M.S., Klinck, J.M., and Hofmann, E.E. (2012). Sensitivity of Circumpolar Deep Water transport and ice shelf basal melt along the west Antarctic Peninsula to changes in the winds. Journal of Climate *25*, 4799–4816.

Duplessy, J.-C., and Shackleton, N.J. (1985). Response of global deep-water circulation to Earth's climatic change 135,000-107,000 years ago. Nature *316*, 500–507.

Duplessy, J.C., Shackleton, N.J., Fairbanks, R.G., Labeyrie, L., Oppo, D., and Kallel, N. (1988). Deepwater source variations during the last climatic cycle and their impact on the global deepwater circulation. Paleoceanography *3*, 343–360.

Elderfield, H., and Ganssen, G. (2000). Past temperature and δ18O of surface ocean waters inferred from foraminiferal Mg/Ca ratios. Nature *405*, 442–445.

Elderfield, H., Vautravers, M., and Cooper, M. (2002). The relationship between shell size and Mg/Ca, Sr/Ca, δ18O, and δ13C of species of planktonic foraminifera. Geochemistry, Geophysics, Geosystems *3*, 1–13.

Emery, W.J. (2001). Water types and water masses. Encyclopedia of Ocean Sciences *6*, 3179–3187.

Emiliani, C. (1955). Pleistocene temperatures. The Journal of Geology 538–578.

Emiliani, C. (1972). Quaternary paleotemperatures and the duration of the high-temperature intervals. Science *178*, 398–401.

EPICA Community Members (2006). One-to-one coupling of glacial climate variability in Greenland and Antarctica. Nature *444*, 195–198.

Epstein, S., and Mayeda, T. (1953). Variation of O 18 content of waters from natural sources. Geochimica et Cosmochimica Acta *4*, 213–224.

Farmer, E.J., Chapman, M.R., and Andrews, J.E. (2010). North Atlantic Globorotalia inflata coretop Mg/Ca calibrations and temperature reconstructions over Termination I. In IOP Conference Series: Earth and Environmental Science, (IOP Publishing), p. 012019.

Fofonoff, N.P. (1957). Some properties of sea water influencing the formation of Antarctic bottom water. Deep Sea Research (1953) *4*, 32–35.

Gaspari, V., Barbante, C., Cozzi, G., Cescon, P., Boutron, C.F., Gabrielli, P., Capodaglio, G., Ferrari, C., Petit, J.R., and Delmonte, B. (2006). Atmospheric iron fluxes over the last deglaciation: Climatic implications. Geophysical Research Letters *33*.

Goldstein, S.L., and Hemming, S.R. (2003). Long-lived isotopic tracers in oceanography, paleoceanography, and ice-sheet dynamics. Treatise on Geochemistry *6*, 453–489.

Gong, X., Knorr, G., Lohmann, G., and Zhang, X. (2013). Dependence of abrupt Atlantic meridional ocean circulation changes on climate background states. Geophysical Research Letters *40*, 3698–3704.

Govin, A., Michel, E., Labeyrie, L., Waelbroeck, C., Dewilde, F., and Jansen, E. (2009). Evidence for northward expansion of Antarctic Bottom Water mass in the Southern Ocean during the last glacial inception. Paleoceanography *24*.

Govin, A., Braconnot, P., Capron, E., Cortijo, E., Duplessy, J.-C., Jansen, E., Labeyrie, L., Landais, A., Marti, O., and Michel, E. (2012). Persistent influence of ice sheet melting on high northern latitude climate during the early Last Interglacial. Climate of the Past *8*, 483–507.

Grandjean, P., Cappetta, H., Michard, A., and Albarede, F. (1987). The Assessment of Ree Patterns and Nd-143-Nd-144 Ratios in Fish Remains. Earth and Planetary Science Letters *84*, 181–196.

Grant, K.M., Rohling, E.J., Ramsey, C.B., Cheng, H., Edwards, R.L., Florindo, F., Heslop, D., Marra, F., Roberts, A.P., Tamisiea, M.E., et al. (2014). Sea-level variability over five glacial cycles. Nature Communications *5*.

Groeneveld, J., and Chiessi, C.M. (2011). Mg/Ca of Globorotalia inflata as a recorder of permanent thermocline temperatures in the South Atlantic. Paleoceanography *26*.

Grootos, P.M., Stulvor, I.V.I., and Whltoi, J.W.C. (1993). Comparison of oxygen isotope records from the GISP2 and. Nature *366*.

Gruetzner, J., Giosan, L., Franz, S.O., Tiedemann, R., Cortijo, E., Chaisson, W.P., Flood, R.D., Hagen, S., Keigwin, L.D., Poli, S., et al. (2002). Astronomical age models for Pleistocene drift sediments from the western North Atlantic (ODP Sites 1055–1063). Marine Geology *189*, 5–23.

Gutjahr, M., Frank, M., Stirling, C.H., Keigwin, L.D., and Halliday, A.N. (2008). Tracing the Nd isotope evolution of North Atlantic deep and intermediate waters in the Western North Atlantic since the Last Glacial Maximum from Blake Ridge sediments. Earth and Planetary Science Letters *266*, 61–77.

Haarmann, T., Hathorne, E.C., Mohtadi, M., Groeneveld, J., Kölling, M., and Bickert, T. (2011). Mg/Ca ratios of single planktonic foraminifer shells and the potential to reconstruct the thermal seasonality of the water column. Paleoceanography *26*.

Häkkinen, S., and Rhines, P.B. (2004). Decline of subpolar North Atlantic circulation during the 1990s. Science *304*, 555–559.

Hansen, B., and Østerhus, S. (2000). North Atlantic–Nordic Seas exchanges. Progress in Oceanography *45*, 109–208.

Hatta, M., Measures, C.I., Wu, J., Roshan, S., Fitzsimmons, J.N., Sedwick, P., and Morton, P. (2015). An overview of dissolved Fe and Mn distributions during the 2010–2011 US GEOTRACES north Atlantic cruises: GEOTRACES GA03. Deep Sea Research Part II: Topical Studies in Oceanography *116*, 117–129.

Hays, J.D., Imbrie, J., Shackleton, N.J., and others (1976). Variations in the Earth's orbit: pacemaker of the ice ages. (American Association for the Advancement of Science),.

Hemleben, C., Spindler, M., and Erson, O.R. (1989). Modern planktonic foraminifera. Springer, Berlin.

Hodell, D.A., Gersonde, R., and Blum, P. (2002). Leg 177 synthesis: insights into Southern Ocean paleoceanography on tectonic to millennial timescales. In Proc. ODP, Sci. Results,.

Hodell, D.A., Venz, K.A., Charles, C.D., and Ninnemann, U.S. (2003a). Pleistocene vertical carbon isotope and carbonate gradients in the South Atlantic sector of the Southern Ocean. Geochemistry, Geophysics, Geosystems *4*, 1–19.

Hodell, D.A., Kanfoush, S.L., Venz, K.A., Charles, C.D., and Sierro, F.J. (2003b). The mid-brunhes transition in ODP sites 1089 and 1090 (Subantarctic South Atlantic). GEOPHYSICAL MONOGRAPH-AMERICAN GEOPHYSICAL UNION *137*, 113–130.

Hodell, D.A., Minth, E.K., Curtis, J.H., McCave, I.N., Hall, I.R., Channell, J.E., and Xuan, C. (2009). Surface and deep-water hydrography on Gardar Drift (Iceland Basin) during the last interglacial period. Earth and Planetary Science Letters *288*, 10–19.

Hut, G. (1987). Consultants' group meeting on stable isotope reference samples for geochemical and hydrological investigations.

Hutson, W.H. (1980). The Agulhas Current during the Late Pleistocene: Analysis of modern faunal analogs. Science *207*, 64–66.

Hyun, S., Ortiz, J.D., Raymo, M.E., and Taira, A. (1999). 14. LOW-FREQUENCY OSCILLATIONS IN SITE 983 SEDIMENTS: RELATIONSHIPS BETWEEN CARBONATE AND PRODUCTIVITY PROXIES1. In Proceedings of the Ocean Drilling Program: Scientific Results, (The Program), p. 197.

Imbrie, J., Berger, A., Boyle, E.A., Clemens, S.C., Duffy, A., Howard, W.R., Kukla, G., Kutzbach, J., Martinson, D.G., McIntyre, A., et al. (1993). On the structure and origin of major glaciation cycles 2. The 100,000-year cycle. Paleoceanography *8*, 699–735.

Ito, T., and Follows, M.J. (2005). Preformed phosphate, soft tissue pump and atmospheric CO2. Journal of Marine Research *63*, 813–839.

Ivanova, E.M., Conan, S.M.-H., Peeters, F.J., and Troelstra, S.R. (1999). Living Neogloboquadrina pachyderma sin and its distribution in the sediments from Oman and Somalia upwelling areas. Marine Micropaleontology *36*, 91–107.

Jacobs, S.S., Amos, A.F., and Bruchhausen, P.M. (1970). Ross Sea oceanography and Antarctic bottom water formation. In Deep Sea Research and Oceanographic Abstracts, (Elsevier), pp. 935–962.

Jacobsen, S.B., and Wasserburg, G.J. (1980). Sm-Nd isotopic evolution of chondrites. Earth and Planetary Science Letters *50*, 139–155.

Jeandel, C. (1993). Concentration and isotopic composition of Nd in the South Atlantic Ocean. Earth and Planetary Science Letters *117*, 581–591.

Jeandel, C., Arsouze, T., Lacan, F., Techine, P., and Dutay, J.-C. (2007). Isotopic Nd compositions and concentrations of the lithogenic inputs into the ocean: A compilation, with an emphasis on the margins. Chemical Geology *239*, 156–164.

Johnsen, S.J., Dansgaard, W., Clausen, H.B., and Langway, C.C. (1972). Oxygen isotope profiles through the Antarctic and Greenland ice sheets. Nature *235*, 429–434.

Jouzel, J., Masson-Delmotte, V., Cattani, O., Dreyfus, G., Falourd, S., Hoffmann, G., Minster, B., Nouet, J., Barnola, J.-M., and Chappellaz, J. (2007). Orbital and millennial Antarctic climate variability over the past 800,000 years. Science *317*, 793–796.

Keigwin, L.D. (1996). The little ice age and medieval warm period in the Sargasso Sea. Science *274*, 1504.

Keigwin, L.D., and Jones, G.A. (1994). Western North Atlantic evidence for millennial-scale changes in ocean circulation and climate. Journal of Geophysical Research: Oceans (1978–2012) *99*, 12397–12410.

Keigwin, L.D., Curry, W.B., Lehman, S.J., and Johnsen, S. (1994). The role of the deep ocean in North Atlantic climate change between 70 and 130 kyr ago. Nature *371*, 323–326.

Key, R.M., Kozyr, A., Sabine, C.L., Lee, K., Wanninkhof, R., Bullister, J.L., Feely, R.A., Millero, F.J., Mordy, C., and Peng, T.-H. (2004). A global ocean carbon climatology: Results from Global Data Analysis Project (GLODAP). Global Biogeochemical Cycles *18*.

Kim, S.-T., and O'Neil, J.R. (1997). Equilibrium and nonequilibrium oxygen isotope effects in synthetic carbonates. Geochimica et Cosmochimica Acta *61*, 3461–3475.

Knorr, G., and Lohmann, G. (2007). Rapid transitions in the Atlantic thermohaline circulation triggered by global warming and meltwater during the last deglaciation. Geochemistry, Geophysics, Geosystems *8*.

Köhler, P., Fischer, H., Munhoven, G., and Zeebe, R.E. (2005). Quantitative interpretation of atmospheric carbon records over the last glacial termination. Global Biogeochemical Cycles *19*.

Köhler, P., Knorr, G., and Bard, E. (2014). Permafrost thawing as a possible source of abrupt carbon release at the onset of the Bølling/Allerød. Nature Communications *5*.

Kroopnick, P.M. (1985). The distribution of 13 C of ΣCO 2 in the world oceans. Deep Sea Research Part A. Oceanographic Research Papers *32*, 57–84.

Kucera, M., Weinelt, M., Kiefer, T., Pflaumann, U., Hayes, A., Weinelt, M., Chen, M.-T., Mix, A.C., Barrows, T.T., and Cortijo, E. (2005). Reconstruction of sea-surface temperatures from assemblages of planktonic foraminifera: multi-technique approach based on geographically constrained calibration data sets and its application to glacial Atlantic and Pacific Oceans. Quaternary Science Reviews *24*, 951–998.

Kuroyanagi, A., Kawahata, H., Nishi, H., and Honda, M.C. (2002). Seasonal changes in planktonic foraminifera in the northwestern North Pacific Ocean: sediment trap experiments from subarctic and subtropical gyres. Deep Sea Research Part II: Topical Studies in Oceanography *49*, 5627–5645.

Lacan, F., and Jeandel, C. (2005). Neodymium isotopes as a new tool for quantifying exchange fluxes at the continent–ocean interface. Earth and Planetary Science Letters *232*, 245–257.

Lacan, F., Tachikawa, K., and Jeandel, C. (2012). Neodymium isotopic composition of the oceans: A compilation of seawater data. Chemical Geology *300*, 177–184.

Lamy, F., Kaiser, J., Arz, H.W., Hebbeln, D., Ninnemann, U., Timm, O., Timmermann, A., and Toggweiler, J.R. (2007). Modulation of the bipolar seesaw in the Southeast Pacific during Termination 1. Earth and Planetary Science Letters *259*, 400–413.

Laskar, J., Robutel, P., Joutel, F., Gastineau, M., Correia, A.C.M., and Levrard, B. (2004). A long-term numerical solution for the insolation quantities of the Earth. Astronomy & Astrophysics *428*, 261–285.

Le, J., and Shackleton, N.J. (1992). Carbonate dissolution fluctuations in the western equatorial Pacific during the late Quaternary. Paleoceanography *7*, 21–42.

Le, J., and Thunell, R.C. (1996). Modelling planktic foraminiferal assemblage changes and application to sea surface temperature estimation in the western equatorial Pacific Ocean. Marine Micropaleontology *28*, 211–229.

Lea, D.W., Mashiotta, T.A., and Spero, H.J. (1999). Controls on magnesium and strontium uptake in planktonic foraminifera determined by live culturing. Geochimica et Cosmochimica Acta *63*, 2369–2379.

Lea, D.W., Pak, D.K., and Spero, H.J. (2000). Climate impact of late Quaternary equatorial Pacific sea surface temperature variations. Science *289*, 1719–1724.

Lea, D.W., Martin, P.A., Pak, D.K., and Spero, H.J. (2002). Reconstructing a 350ky history of sea level using planktonic Mg/Ca and oxygen isotope records from a Cocos Ridge core. Quaternary Science Reviews *21*, 283–293.

Lea, D.W., Pak, D.K., and Paradis, G. (2005). Influence of volcanic shards on foraminiferal Mg/Ca in a core from the Galápagos region. Geochemistry, Geophysics, Geosystems *6*.

Lear, C.H., Elderfield, H., and Wilson, P.A. (2000). Cenozoic deep-sea temperatures and global ice volumes from Mg/Ca in benthic foraminiferal calcite. Science *287*, 269–272.

LeGrande, A.N., and Schmidt, G.A. (2006). Global gridded data set of the oxygen isotopic composition in seawater. Geophysical Research Letters *33*.

Levitus, S., Antonov, J.I., Baranova, O.K., Boyer, T.P., Coleman, C.L., Garcia, H.E., Grodsky, A.I., Johnson, D.R., Locarnini, R.A., Mishonov, A.V., et al. (2013). The World Ocean Database. Data Science Journal *12*, WDS229–WDS234.

Lisiecki, L.E., and Raymo, M.E. (2005). A Pliocene-Pleistocene stack of 57 globally distributed benthic δ18O records. Paleoceanography *20*.

Liu, Z., Otto-Bliesner, B.L., He, F., Brady, E.C., Tomas, R., Clark, P.U., Carlson, A.E., Lynch-Stieglitz, J., Curry, W., Brook, E., et al. (2009). Transient simulation of last deglaciation with a new mechanism for Bølling-Allerød warming. Science *325*, 310–314.

Locarnini, R.A., Mishonov, A.V., Antonov, J.I., Boyer, T.P., Garcia, H.E., Baranova, O.K., Zweng, M.M., Paver, C.R., Reagan, J.R., Johnson, D.R., et al. (2013). World

Ocean Atlas 2013. Vol. 1: Temperature. A. Mishonov, Technical Ed. NOAA Atlas NESDIS *73*, 40.

Loulergue, L., Schilt, A., Spahni, R., Masson-Delmotte, V., Blunier, T., Lemieux, B., Barnola, J.-M., Raynaud, D., Stocker, T.F., and Chappellaz, J. (2008). Orbital and millennial-scale features of atmospheric CH4 over the past 800,000 years. Nature *453*, 383–386.

Lourantou, A., Chappellaz, J., Barnola, J.-M., Masson-Delmotte, V., and Raynaud, D. (2010). Changes in atmospheric CO 2 and its carbon isotopic ratio during the penultimate deglaciation. Quaternary Science Reviews *29*, 1983–1992.

Loutre, M.F., and Berger, A. (2003). Marine Isotope Stage 11 as an analogue for the present interglacial. Global and Planetary Change *36*, 209–217.

Lüthi, D., Le Floch, M., Bereiter, B., Blunier, T., Barnola, J.-M., Siegenthaler, U., Raynaud, D., Jouzel, J., Fischer, H., and Kawamura, K. (2008). High-resolution carbon dioxide concentration record 650,000–800,000 years before present. Nature *453*, 379–382.

Lutjeharms, J.R.E. (1981). Spatial scales and intensities of circulation in the ocean areas adjacent to South Africa. Deep Sea Research Part A. Oceanographic Research Papers *28*, 1289–1302.

Lutjeharms, J.E., and Valentine, H.R. (1984). Southern Ocean thermal fronts south of Africa. Deep Sea Research Part A. Oceanographic Research Papers *31*, 1461–1475.

Marcott, S.A., Bauska, T.K., Buizert, C., Steig, E.J., Rosen, J.L., Cuffey, K.M., Fudge, T.J., Severinghaus, J.P., Ahn, J., Kalk, M.L., et al. (2014). Centennial-scale changes in the global carbon cycle during the last deglaciation. Nature *514*, 616–619.

MARGO Members (2005). Multiproxy approach for the reconstruction of the glacial ocean surface (MARGO). Quaternary Science Reviews *24*, 813–819.

MARGO Members (2009). Constraints on the magnitude and patterns of ocean cooling at the Last Glacial Maximum. Nature Geoscience *2*, 127–132.

Marino, G., Rohling, E.J., Rodríguez-Sanz, L., Grant, K.M., Heslop, D., Roberts, A.P., Stanford, J.D., and Yu, J. (2015). Bipolar seesaw control on last interglacial sea level. Nature *522*, 197–201.

Marinov, I., Follows, M., Gnanadesikan, A., Sarmiento, J.L., and Slater, R.D. (2008). How does ocean biology affect atmospheric pCO2? Theory and models. Journal of Geophysical Research: Oceans (1978–2012) *113*.

Martin, E.E., and Haley, B.A. (2000). Fossil fish teeth as proxies for seawater Sr and Nd isotopes. Geochimica et Cosmochimica Acta *64*, 835–847.

Martínez-Garcia, A., Rosell-Melé, A., McClymont, E.L., Gersonde, R., and Haug, G.H. (2010). Subpolar link to the emergence of the modern equatorial Pacific cold tongue. Science *328*, 1550–1553.

Martrat, B., Jimenez-Amat, P., Zahn, R., and Grimalt, J.O. (2014). Similarities and dissimilarities between the last two deglaciations and interglaciations in the North Atlantic region. Quaternary Science Reviews *99*, 122–134.

Mashiotta, T.A., Lea, D.W., and Spero, H.J. (1999). Glacial–interglacial changes in Subantarctic sea surface temperature and δ 18 O-water using foraminiferal Mg. Earth and Planetary Science Letters *170*, 417–432.

McCartney, M.S. (1992). Recirculating components to the deep boundary current of the northern North Atlantic. Progress in Oceanography *29*, 283–383.

McManus, J.F., Oppo, D.W., and Cullen, J.L. (1999). A 0.5-million-year record of millennial-scale climate variability in the North Atlantic. Science *283*, 971–975.

McManus, J.F., Francois, R., Gherardi, J.-M., Keigwin, L.D., and Brown-Leger, S. (2004). Collapse and rapid resumption of Atlantic meridional circulation linked to deglacial climate changes. Nature *428*, 834–837.

Menviel, L., Timmermann, A., Mouchet, A., and Timm, O. (2008). Meridional reorganizations of marine and terrestrial productivity during Heinrich events. Paleoceanography *23*.

Milankovitch, M. (1941). Serb. Akad. Beogr. Spec. Publ. 132 (1941) (translated by the Israel Program for Scientific Translations, Jerusalem, 1969 - Google Scholar.

Moffa Sánchez, P.L. (2012). Ocean changes in the North Atlantic over the late holocene: A multi-proxy approach. Cardiff University.

Mohiuddin, M.M., Nishimura, A., and Tanaka, Y. (2005). Seasonal succession, vertical distribution, and dissolution of planktonic foraminifera along the Subarctic Front: Implications for paleoceanographic reconstruction in the northwestern Pacific. Marine Micropaleontology *55*, 129–156.

Mohtadi, M., Steinke, S., Groeneveld, J., Fink, H.G., Rixen, T., Hebbeln, D., Donner, B., and Herunadi, B. (2009). Low-latitude control on seasonal and interannual changes in planktonic foraminiferal flux and shell geochemistry off south Java: A sediment trap study. Paleoceanography *24*.

Monnin, E., Indermühle, A., Dällenbach, A., Flückiger, J., Stauffer, B., Stocker, T.F., Raynaud, D., and Barnola, J.-M. (2001). Atmospheric CO2 concentrations over the last glacial termination. Science *291*, 112–114.

Murray, J., and Renard, A.F. (1891). Deep-sea deposits based on the specimens collected during the voyage of H.M.S. Challenger in the years 1872-1876. Reports Voyage Challenger 525.

NGRIP Members (2004). High-resolution record of Northern Hemisphere climate extending into the last interglacial period. Nature *431*, 147–151.

Niebler, H.-S., and Gersonde, R. (1998). A planktic foraminiferal transfer function for the southern South Atlantic Ocean. Marine Micropaleontology *34*, 213–234.

Ninnemann, U.S., Charles, C.D., and Hodell, D.A. (1999). Origin of global millennial scale climate events: Constraints from the Southern Ocean deep sea sedimentary record. Geophysical Monograph-American Geophysical Union *112*, 99–112.

de Nooijer, L.J., Spero, H.J., Erez, J., Bijma, J., and Reichart, G.J. (2014). Biomineralization in perforate foraminifera. Earth-Science Reviews *135*, 48–58.

Nürnberg, D., Bijma, J., and Hemleben, C. (1996). Assessing the reliability of magnesium in foraminiferal calcite as a proxy for water mass temperatures. Geochimica et Cosmochimica Acta *60*, 803–814.

O'Neil, J.R. (1968). Hydrogen and oxygen isotope fractionation between ice and water. The Journal of Physical Chemistry *72*, 3683–3684.

Oomori, T., Kaneshima, H., Maezato, Y., and Kitano, Y. (1987). Distribution coefficient of Mg 2+ ions between calcite and solution at 10–50 C. Marine Chemistry *20*, 327–336.

Oppo, D.W., and Curry, W.B. (2012). Deep Atlantic circulation during the Last Glacial Maximum and deglaciation. Nature Education Knowledge *3*, 1.

Oppo, D.W., and Fairbanks, R.G. (1987). Variability in the deep and intermediate water circulation of the Atlantic Ocean during the past 25,000 years: Northern Hemisphere modulation of the Southern Ocean. Earth and Planetary Science Letters *86*, 1–15.

Oppo, D.W., McManus, J.F., and Cullen, J.L. (2006). Evolution and demise of the Last Interglacial warmth in the subpolar North Atlantic. Quaternary Science Reviews *25*, 3268–3277.

Orsi, A.H., Whitworth, T., and Nowlin, W.D. (1995). On the meridional extent and fronts of the Antarctic Circumpolar Current. Deep Sea Research Part I: Oceanographic Research Papers *42*, 641–673.

Orsi, A.H., Johnson, G.C., and Bullister, J.L. (1999). Circulation, mixing, and production of Antarctic Bottom Water. Progress in Oceanography *43*, 55–109.

Østerhus, S., Turrell, W.R., Jónsson, S., and Hansen, B. (2005). Measured volume, heat, and salt fluxes from the Atlantic to the Arctic Mediterranean. Geophysical Research Letters *32*.

Overpeck, J.T., Webb, T., and Prentice, I.C. (1985). Quantitative interpretation of fossil pollen spectra: dissimilarity coefficients and the method of modern analogs. Quaternary Research *23*, 87–108.

Paillard, D., Labeyrie, L., and Yiou, P. (1996). Macintosh program performs time-series analysis. Eos, Transactions American Geophysical Union *77*, 379–379.

Parker, F.L. (1960). Living planktonic foraminifera from the equatorial and southeast Pacific.

Parker, F.L. (1962). Planktonic foraminiferal species in Pacific sediments. Micropaleontology 219–254.

Peeters, F.J., Acheson, R., Brummer, G.-J.A., De Ruijter, W.P., Schneider, R.R., Ganssen, G.M., Ufkes, E., and Kroon, D. (2004). Vigorous exchange between the Indian and Atlantic oceans at the end of the past five glacial periods. Nature *430*, 661–665.

Pena, L.D., Calvo, E., Cacho, I., Eggins, S., and Pelejero, C. (2005). Identification and removal of Mn-Mg-rich contaminant phases on foraminiferal tests: Implications for Mg/Ca past temperature reconstructions. Geochemistry, Geophysics, Geosystems *6*.

Petit, J.-R., Jouzel, J., Raynaud, D., Barkov, N.I., Barnola, J.-M., Basile, I., Bender, M., Chappellaz, J., Davis, M., Delaygue, G., et al. (1999). Climate and atmospheric history of the past 420,000 years from the Vostok ice core, Antarctica. Nature *399*, 429–436.

Pflaumann, U., Duprat, J., Pujol, C., and Labeyrie, L.D. (1996). SIMMAX: A modern analog technique to deduce Atlantic sea surface temperatures from planktonic foraminifera in deep-sea sediments. Paleoceanography *11*, 15–35.

Phleger, F.B., Parker, F.L., and Peirson, J.F. (1953). North Atlantic foraminifera. Sediment cores from the North Atlantic Ocean. Swedish Deep-Sea Expedition Reports *7*, 1–122.

Piepgras, D.J., and Wasserburg, G.J. (1982). Isotopic composition of neodymium in waters from the Drake Passage. Science *217*, 207–214.

Piepgras, D.J., and Wasserburg, G.J. (1987). Rare earth element transport in the western North Atlantic inferred from Nd isotopic observations. Geochimica et Cosmochimica Acta *51*, 1257–1271.

Pin, C., and Zalduegui, J.S. (1997). Sequential separation of light rare-earth elements, thorium and uranium by miniaturized extraction chromatography: application to isotopic analyses of silicate rocks. Analytica Chimica Acta *339*, 79–89.

Piotrowski, A.M., Goldstein, S.L., Hemming, S.R., and Fairbanks, R.G. (2004). Intensification and variability of ocean thermohaline circulation through the last deglaciation. Earth and Planetary Science Letters *225*, 205–220.

Piotrowski, A.M., Goldstein, S.L., Hemming, S.R., and Fairbanks, R.G. (2005). Temporal relationships of carbon cycling and ocean circulation at glacial boundaries. Science *307*, 1933–1938.

Piotrowski, A.M., Galy, A., Nicholl, J.A.L., Roberts, N., Wilson, D.J., Clegg, J.A., and Yu, J. (2012). Reconstructing deglacial North and South Atlantic deep water sourcing using foraminiferal Nd isotopes. Earth and Planetary Science Letters *357*, 289–297.

Post, W.M., Peng, T.-H., Emanuel, W.R., King, A.W., Dale, V.H., DeAngelis, D.L., and others (1990). The global carbon cycle. American Scientist *78*, 310–326.

Prell, W.L., Martin, A., Cullen, J., and Trend, M. (1999). The Brown University Foraminiferal Data Base, Data Contribution Series 1999-027.

Rahmstorf, S. (1996). On the freshwater forcing and transport of the Atlantic thermohaline circulation. Climate Dynamics *12*, 799–811.

Rahmstorf, S. (2002). Ocean circulation and climate during the past 120,000 years. Nature *419*, 207–214.

Raymo, M.E. (1997). The timing of major climate terminations. Paleoceanography *12*, 577–585.

Raymo, M.E., Ganley, K., Carter, S., Oppo, D.W., and McManus, J. (1998). Millennial-scale climate instability during the early Pleistocene epoch. Nature *392*, 699–702.

Raymo, M.E., Oppo, D.W., Flower, B.P., Hodell, D.A., McManus, J.F., Venz, K.A., Kleiven, K.F., and McIntyre, K. (2004). Stability of North Atlantic water masses in face of pronounced climate variability during the Pleistocene. Paleoceanography *19*, PA2008.

Roberts, N.L., Piotrowski, A.M., McManus, J.F., and Keigwin, L.D. (2010). Synchronous deglacial overturning and water mass source changes. Science *327*, 75–78.

Rosenthal, Y., and Linsley, B. (2006). Mg/Ca and Sr/Ca paleothermometery from calcareous marine fossils. Encyclopedia of Quaternary Sciences. Elsevier.

Rosenthal, Y., Boyle, E.A., and Labeyrie, L. (1997). Last glacial maximum paleochemistry and deepwater circulation in the Southern Ocean: Evidence from foraminiferal cadmium. Paleoceanography *12*, 787–796.

Rosenthal, Y., Lohmann, G.P., Lohmann, K.C., and Sherrell, R.M. (2000). Incorporation and preservation of Mg in Globigerinoides sacculifer: Implications for reconstructing the temperature and 18O/ 16O of seawater. Paleoceanography *15*, 135–145.

Ruddiman, W.F. (2003). Orbital insolation, ice volume, and greenhouse gases. Quaternary Science Reviews *22*, 1597–1629.

Sabine, C.L., Feely, R.A., Gruber, N., Key, R.M., Lee, K., Bullister, J.L., Wanninkhof, R., Wong, C.S., Wallace, D.W.R., Tilbrook, B., et al. (2004). The oceanic sink for anthropogenic CO2. Science *305*, 367–371.

Sachs, J.P., and Anderson, R.F. (2005). Increased productivity in the subantarctic ocean during Heinrich events. Nature *434*, 1118–1121.

Sarnthein, M. (2011). Northern meltwater pulses, CO2, and changes in Atlantic convection. Science *331*, 156–158.

Sarnthein, M., Winn, K., Jung, S.J., Duplessy, J.-C., Labeyrie, L., Erlenkeuser, H., and Ganssen, G. (1994). Changes in east Atlantic deepwater circulation over the last 30,000 years: Eight time slice reconstructions. Paleoceanography *9*, 209–267.

Scher, H.D., and Delaney, M.L. (2010). Breaking the glass ceiling for high resolution Nd isotope records in early Cenozoic paleoceanography. Chemical Geology *269*, 329–338.

Schlitzer, R. (2009). Ocean data view.

Schmidt, M.W., Vautravers, M.J., and Spero, H.J. (2006). Rapid subtropical North Atlantic salinity oscillations across Dansgaard–Oeschger cycles. Nature *443*, 561–564.

Schmittner, A., and Galbraith, E.D. (2008). Glacial greenhouse-gas fluctuations controlled by ocean circulation changes. Nature *456*, 373–376.

Schwander, J., Jouzel, J., Hammer, C.U., Petit, J.-R., Udisti, R., and Wolff, E. (2001). A tentative chronology for the EPICA Dome Concordia ice core. Geophysical Research Letters *28*, 4243–4246.

Shackleton, N. (1967). Oxygen isotope analyses and Pleistocene temperatures re-assessed.

Shackleton, N.J. (1974). Attainment of isotopic equilibrium between ocean water and the benthonic foraminifera genus Uvigerina: isotopic changes in the ocean during the last glacial.

Shackleton, N.J. (1987). Oxygen isotopes, ice volume and sea level. Quaternary Science Reviews *6*, 183–190.

Shackleton, N.J., Imbrie, J., and Hall, M.A. (1983). Oxygen and carbon isotope record of East Pacific core V19-30: implications for the formation of deep water in the late Pleistocene North Atlantic. Earth and Planetary Science Letters *65*, 233–244.

Shackleton, N.J., Hall, M.A., and Vincent, E. (2000). Phase relationships between millennial-scale events 64,000–24,000 years ago. Paleoceanography *15*, 565–569.

Shackleton, N.J., Sánchez-Goñi, M.F., Pailler, D., and Lancelot, Y. (2003). Marine isotope substage 5e and the Eemian interglacial. Global and Planetary Change *36*, 151–155.

Shipboard Scientific Party (1999). Leg 177 synthesis: insights into Southern Ocean paleoceanography on tectonic to millennial timescales. In Proc. ODP, Sci. Results,.

Sievers, H.A., and Nowlin, W.D. (1984). The stratification and water masses at Drake Passage. Journal of Geophysical Research: Oceans (1978–2012) *89*, 10489–10514.

Sigman, D.M., Hain, M.P., and Haug, G.H. (2010). The polar ocean and glacial cycles in atmospheric CO2 concentration. Nature *466*, 47–55.

Skinner, L.C., Fallon, S., Waelbroeck, C., Michel, E., and Barker, S. (2010). Ventilation of the deep Southern Ocean and deglacial CO2 rise. Science *328*, 1147–1151.

Skinner, L.C., Scrivner, A.E., Vance, D., Barker, S., Fallon, S., and Waelbroeck, C. (2013). North Atlantic versus Southern Ocean contributions to a deglacial surge in deep ocean ventilation. Geology *41*, 667–670.

Staudigel, H., Doyle, P., and Zindler, A. (1985). Sr and Nd isotope systematics in fish teeth. Earth and Planetary Science Letters *76*, 45–56.

Stauffer, B., Blunier, T., Dällenbach, A., Indermühle, A., Schwander, J., Stocker, T.F., Tschumi, J., Chappellaz, J., Raynaud, D., Hammer, C.U., et al. (1998). Atmospheric CO2 concentration and millennial-scale climate change during the last glacial period. Nature *392*, 59–62.

Stichel, T., Hartman, A.E., Duggan, B., Goldstein, S.L., Scher, H., and Pahnke, K. (2015). Separating biogeochemical cycling of neodymium from water mass mixing in the Eastern North Atlantic. Earth and Planetary Science Letters *412*, 245–260.

Stirling, C.H., Esat, T.M., Lambeck, K., and McCulloch, M.T. (1998). Timing and duration of the Last Interglacial: evidence for a restricted interval of widespread coral reef growth. Earth and Planetary Science Letters *160*, 745–762.

Stocker, T.F., and Johnsen, S.J. (2003). A minimum thermodynamic model for the bipolar seesaw. Paleoceanography *18*.

Stramma, L., and England, M. (1999). On the water masses and mean circulation of the South Atlantic Ocean. J. Geophys. Res. *104*, 20863–20883.

Stuiver, M., and Grootes, P.M. (2000). GISP2 oxygen isotope ratios. Quaternary Research *53*, 277–284.

Tanaka, T., Togashi, S., Kamioka, H., Amakawa, H., Kagami, H., Hamamoto, T., Yuhara, M., Orihashi, Y., Yoneda, S., Shimizu, H., et al. (2000). JNdi-1: a neodymium isotopic reference in consistency with LaJolla neodymium. Chemical Geology *168*, 279–281.

Thomas, D.J., Bralower, T.J., and Jones, C.E. (2003). Neodymium isotopic reconstruction of late Paleocene–early Eocene thermohaline circulation. Earth and Planetary Science Letters *209*, 309–322.

Thomson, J., Higgs, N.C., Jarvis, I., Hydes, D.J., Colley, S., and Wilson, T.R.S. (1986). The behaviour of manganese in Atlantic carbonate sediments. Geochimica et Cosmochimica Acta *50*, 1807–1818.

Thornalley, D.J.R. (2008). Palaeoceanography of the South Iceland Rise over the past 21,000 years. University of Cambridge.

Thornalley, D.J., Elderfield, H., and McCave, I.N. (2009). Holocene oscillations in temperature and salinity of the surface subpolar North Atlantic. Nature *457*, 711–714.

Thornalley, D.J., Barker, S., Becker, J., Hall, I.R., and Knorr, G. (2013). Abrupt changes in deep Atlantic circulation during the transition to full glacial conditions. Paleoceanography *28*, 253–262.

Tolderlund, D.S., and Bé, A.W. (1971). Seasonal distribution of planktonic foraminifera in the western North Atlantic. Micropaleontology 297–329.

Urey, H.C. (1947). The thermodynamic properties of isotopic substances. J. Chem. Soc. 562–581.

Vautravers, M.J., and Shackleton, N.J. (2006). Centennial-scale surface hydrology off Portugal during marine isotope stage 3: Insights from planktonic foraminiferal fauna variability. Paleoceanography *21*.

Vautravers, M.J., Shackleton, N.J., Lopez-Martinez, C., and Grimalt, J.O. (2004). Gulf Stream variability during marine isotope stage 3. Paleoceanography *19*.

Vázquez Riveiros, N., Waelbroeck, C., Skinner, L., Roche, D.M., Duplessy, J.-C., and Michel, E. (2010). Response of South Atlantic deep waters to deglacial warming during Terminations V and I. Earth and Planetary Science Letters *298*, 323–333.

Vázquez Riveiros, N., Waelbroeck, C., Skinner, L., Duplessy, J.-C., McManus, J.F., Kandiano, E.S., and Bauch, H.A. (2013). The "MIS 11 paradox" and ocean circulation: Role of millennial scale events. Earth and Planetary Science Letters *371*, 258–268.

Veres, D., Bazin, L., Landais, A., Toyé Mahamadou Kele, H., Lemieux-Dudon, B., Parrenin, F., Martinerie, P., Blayo, E., Blunier, T., Capron, E., et al. (2013). The Antarctic ice core chronology (AICC2012): an optimized multi-parameter and multi-site dating approach for the last 120 thousand years. Climate of the Past *9*, 1733–1748.

Vincent, E., and Berger, W.H. (1981). Planktonic foraminifera and their use in paleoceanography. The Sea *7*, 1025–1119.

Waelbroeck, C., Labeyrie, L., Michel, E., Duplessy, J.C., McManus, J.F., Lambeck, K., Balbon, E., and Labracherie, M. (2002). Sea-level and deep water temperature changes derived from benthic foraminifera isotopic records. Quaternary Science Reviews *21*, 295–305.

Weber, S.L., Drijfhout, S.S., Abe-Ouchi, A., Crucifix, M., Eby, M., Ganopolski, A., Murakami, S., Otto-Bliesner, B., and Peltier, W.R. (2007). The modern and glacial overturning circulation in the Atlantic ocean in PMIP coupled model simulations. Climate of the Past *3*, 51–64.

Weis, D., Kieffer, B., Maerschalk, C., Barling, J., De Jong, J., Williams, G.A., Hanano, D., Pretorius, W., Mattielli, N., Scoates, J.S., et al. (2006). High-precision

isotopic characterization of USGS reference materials by TIMS and MC-ICP-MS. Geochemistry, Geophysics, Geosystems *7*.

Wilson, D.J., Piotrowski, A.M., Galy, A., and Clegg, J.A. (2013). Reactivity of neodymium carriers in deep sea sediments: Implications for boundary exchange and paleoceanography. Geochimica et Cosmochimica Acta *109*, 197–221.

Wilson, T.R.S., Thomson, J., Colley, S., Hydes, D.J., Higgs, N.C., and Sørensen, J. (1985). Early organic diagenesis: the significance of progressive subsurface oxidation fronts in pelagic sediments. Geochimica et Cosmochimica Acta *49*, 811–822.

Wolff, E.W., Fischer, H., and Röthlisberger, R. (2009). Glacial terminations as southern warmings without northern control. Nature Geoscience *2*, 206–209.

Worthington, L.V. (1970). The Norwegian Sea as a mediterranean basin. In Deep Sea Research and Oceanographic Abstracts, (Elsevier), pp. 77–84.

Wright, J., Seymour, R.S., and Shaw, H.F. (1984). REE and Nd isotopes in conodont apatite: variations with geological age and depositional environment. Geological Society of America Special Papers *196*, 325–340.

7 APPENDIX

7.1 APPENDICES FOR CHAPTER 2

Appendix 1. Operating instructions for the CM5130 Acidification Module used in connection with the CM5014 CO_2 Coulometer to provide highly accurate, absolute determination of carbon in any CO_2-containing gas stream.

The % calcium carbonate (% $CaCO_3$) of the bulk sample was measured to align the records from this study to that of previously published records on the same core site using a different splice (Hodell et al., 2003a, 2003b) to allow comparison of the records. The CM5130 Acidification Module is used in connection with the CM5014 CO_2 Coulometer (Figure 7.53) providing highly accurate, absolute determination of carbon in any CO_2-containing gas stream; it is able to detect carbon in the range 0.01μg to 100mg.

Before the samples can be run on coulometry and acidification module to determine the percentage of calcium carbonate ($CaCO_3$) first the samples need to be prepared. This is done by drying approximately 1cm^3 of the bulk sediment by placing them in the oven for approximately 24 hours in fully labeled open vials (n.b. the vials should have a piece of paper over to cover them to prevent dust entering the samples). Once the bulk samples are completely dry they are removed from the oven and placed into a small clean, dry pestle and mortar and are ground down to a finely grained, homogenous dust for analysis, again ensuring that the ground sample is placed in a fully labeled, dry vial with a tight seal.

Once all the samples have been dried out and ground down they can be prepared for analysis (typically prepare 10-20 samples at a time); whereby approximately 30mg of the prepared sediment is weighed out (note the exact amount should be noted down) and placed in a glass test tube with a screw top lid and into a test tube rack.

Once the samples have all been prepared use the cathode and anode compartments of the CM5014 CO_2 coulometer are set up along with the acidification module (see appendix). In the acidification module the samples are acidified in a heated reaction vessel to evolve forms of inorganic carbon (including dissolved CO_2, carbonate ion,

bicarbonate ion and carbonic acid) as CO_2. In the coulometer part of the set the coulometer cell is filled with a proprietary solution containing monoethanolamine and a colourmetric pH indicator. Platinum (cathode) and silver (anode) electrodes are positioned in the cell and the cell assembly is then placed in the coulometer cell compartment between a light source and a photodetector in the coulometer.

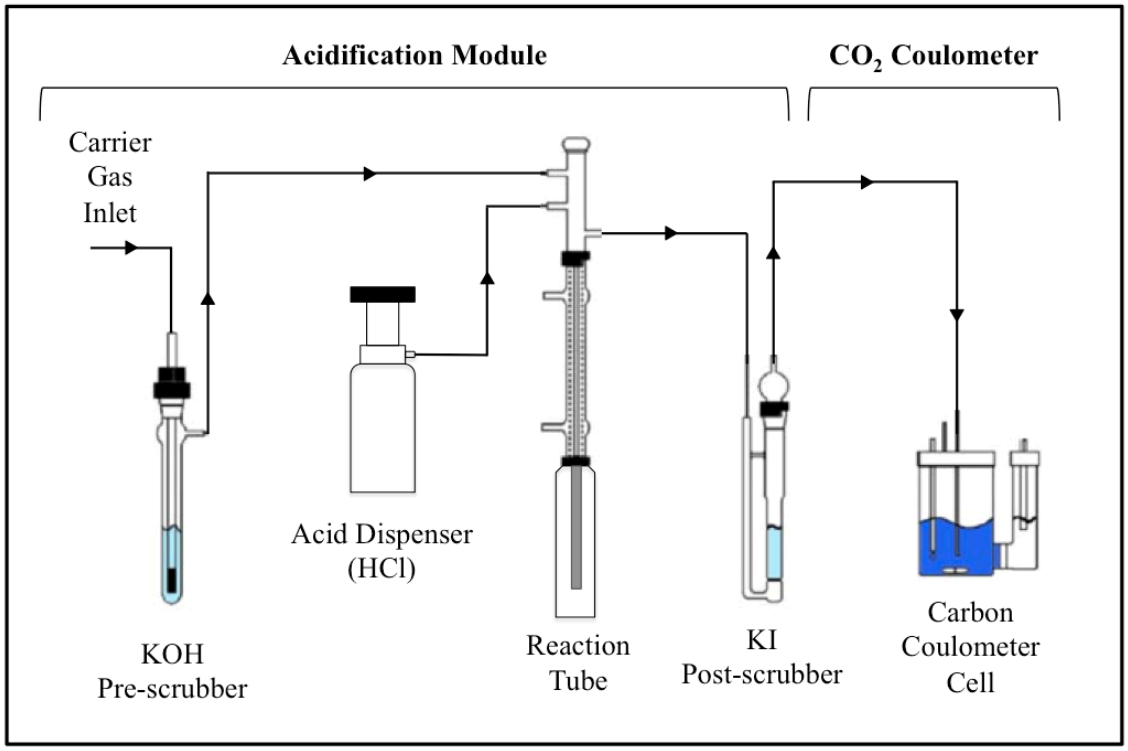

Figure 7.53. A schematic diagram to show the set up of the CM5130 Acidification Module and CM5014 CO_2 Coulometer used for measuring the CO_2 content of an acidified sample. Figure made using resources from the manufacturers (UIC inc.) online resources.

As a CO_2 gas stream passes into the cell the CO_2 is quantitatively absorbed, reacting with the monoethanolamine to form a titratable acid; this causes the colour indicator to fade. Photodetection monitors the change in colour of the solution as a percentage of transmittance (%T). As the %T increases, the titration current is automatically activated to electrochemically generate base at a rate proportional to the %T (approximately 1500µg carbon/minute). When the solution returns to its original colour (original %T), the current stops. The reactions are outlined below in Equation 2.2, Equation 2.3, Equation 2.4 and Equation 2.5.

$CO_2 + HOCH_2CH_2NH_2 \rightarrow HOCH_2CH_2NHCOOH$

Equation 2.2. Absorption of CO_2 by cathode solution (cathode reaction)

$2H_2O + 2e^{-1} \rightarrow H_{2\,(g)} + 2OH^-$

Equation 2.3. Electrochemical generation of OH^- (cathode reaction)

$HOCH_2CH_2NHCOOH + OH^- \rightarrow HOCH_2CH_2NHCOO^- + H_2O$

Equation 2.4. Neutralisation of absorbed CO_2 reaction product by electrochemically generated OH^-

$Ag \rightarrow Ag^+ + e^{-1}$

Equation 2.5. Anode reaction

Cathode compartment set-up

A small Teflon coated stir bar is placed in the bottom of the cell body (cathode compartment – larger section). The body of the coulometer cell is filled with 75-100ml of the carbon cathode solution. The cell is covered with the cell top containing the coiled platinum electrode, positioning the top so that the electrode is opposite the side are and does not block the light path in the coulometer call compartment.

Anode compartment set-up

Approximately ¼″ layer of potassium iodide (KI) is added to the bottom of the side arm (anode compartment) of the cell. The side arm is then filled with carbon anode solution (approximately 12-20ml) ensuring the liquid level is slightly below the liquid level in the cathode compartment. The solid silver electrode is placed in the side arm, making sure the electrode is in the solution and the top containing the anode electrode is in place. Place the completed cell in to the cell compartment.

Pre-scrubber assembly

- The pre-scrubber (KOH) contains 45% solution of potassium hydroxide and is used to remove CO_2 from the air or carrier gas.
- Weigh 45g of KOH into a 100ml volumetric flask. Slowly add DI water* until it all dissolves. *Note this reaction is extremely exothermic and therefore add the water slowly.
- Add 15-20ml of KOH solution to the pre-scrubber body.
- Put the dispersion tube in the pre-scrubber body and tighten the black threaded bushing.
- Place into the acidification module in the correct place. *Note this pre-scrubber solution should be changed once a week.

Post-scrubber assembly

- The post-scrubber removes H_2S and SO_x which may result from the acidification of some materials, I used potassium iodide, 50% (KI) acidified to pH3.
- Weigh out 50g of potassium iodide into a 100ml volumetric flask.
- Fill to the mark with DI water to dissolve.
- Acidify the solution by adding a few drops of acid (sulphuric acid) until a pH of 3 is reached.
- Put into the post-scrubber tube (10-15ml), replace the top on the body and tighten the thread joint connector. *Note this post-scrubber solution should be changed once a week.

Running the CM5014 CO2 coulometer

- Ensure that the CM5130 Acidification Module and CM5014 CO_2 Coulometer are correctly set up (refer to set up figure in chapter 2) below before proceeding.

- Once the CM5130 Acidification Module and CM5014 CO_2 Coulometer set up is complete the following set of instructions are to be followed.

- At this point set up the parameters from the menu screen and print off for clarification, ensure all pipes are connected and that the oxygen is turned on and set to a pressure of 10psig and a flow rate of approximately 100mls/min.

- Enter 'run cell setup' from the home screen using the arrow keys.

- Physically adjust the cell position carefully to get a reading of about 3500-3700 ensuring it does not exceed 3950. Once this value has stabilised in the $3^{rd}/4^{th}$ place press 'F2', this value represents 100%T. *Ensure that the cell isn't moved again for the rest of the experiment.

- Remember to turn the heater block on at this point and turn the cell current switch to 'on' before proceeding.

- Next; 'run analysis' → 'enter' → 'cell operation' screen → 'enter' → (this initiates the cell current in the CM5014 to titrate the cell solution to the 29%T endpoint). Now leave the machine for at least 45 minutes to titrate to 29%T.

- Press 'F2' and 'sample scr-1' appears, enter the number of samples to be analysed. *Note that if the number of samples is less than 10, then an '0' must be entered before the number, i.e. 05 samples.

- Enter the names and weight of each sample, ensuring to use decimal places. The first sample should be 'blank' (no weight) and the second sample should be a standard.

- Once all the sample names and weights have been entered it will automatically go back to the 'run diagnostics' screen.

- Press 'enter' on the machine, add 10ml of 2M hydrochloric acid into the already attached sample, place sample in heater block and wait for the analysis to run.

- Repeat this stage until all samples have been analysed.

Appendix 2. Detailed methodology for sediment processing used for foraminiferal analysis (faunal assemblage/isotope analysis etc)

- Ensure that about 10-20% of the sample is kept as an archive placed in a labelled bag and put back in the fridge.
- Put the majority of the sample in a glass jar, half filled up with deionised water and place on the wheel for 24 hours to break apart the sediment.
- Place a labelled plastic/polythene bag in a glass jar (1 litre?) and weigh on the scale, and record.
- Wash the sample from the glass jar through the >65µm sieve fraction in to the bag in the beaker to ensure that the fine grain size fraction is kept
- Continue to wash until the sample is clear (potentially have a look through the microscope to check that there isn't any mud/sediment still remaining in the foraminifera tests) – this may require up to two litres of water
- What is left in the >65µm sieve fraction is the coarse size fraction; this is left in the sieve and dried overnight in the oven…make sure it is labelled.
- Allow the fine grain size fraction in the bag and beaker to settle for a few days to ensure there is no fine grains size fractions left in suspension.
- Siphon the water off that is left in the top of the fine grain size beaker with water, very carefully to make sure that none of the fine grains go with it. Re-weigh this and subtract that from the original beaker and bag combined weight to get the total fine grain size fraction weight
- Allow this to dry in the oven overnight or until dry – this is my coarse fraction. Weigh this onto a measuring boat/paper, ensuring that the boat/paper has been teared.

- Record this weight and place the sample (carefully) into a labelled glass jar. This is the size fraction that faunal counts are made from.

Appendix 3. Results from the MAT analysis carried out using the Terminal program for Mac OS X. Env1Avg is the average winter SST and Env2Avg is the summer average SST. The down core analysis is compared to the Brown University Foraminiferal Database; (Prell et al., 1999).

CoreID	DissAvg	DissStd	Env1Avg	Env1Std	Env2Avg	Env2Std	MCD
5930	0.1349	0.0441	3.29	1.43	6.17	1.85	59.30
5934	0.3151	0.0743	4.82	2.71	8.3	3.67	59.34
5937	0.208	0.0588	3.75	1.84	6.82	2.38	59.37
6020	0.216	0.0517	6.88	3.01	11.47	4.91	60.20
6024	0.1351	0.0159	3.61	1.53	6.56	1.91	60.24
6028	0.1197	0.0168	3.61	1.53	6.56	1.91	60.28
6033	0.1875	0.0212	5.83	2.25	9.02	2.35	60.33
6037	0.1503	0.0119	3.99	1.94	7.13	2.54	60.37
6041	0.209	0.0546	4.4	2.22	7.33	2.58	60.41
6045	0.255	0.0562	7.85	4.47	13.18	6.91	60.45
6049	0.1762	0.068	6.58	2.37	10.14	2.84	60.49
6054	0.291	0.0242	10.27	6.18	15.26	8.32	60.54
6058	0.2662	0.0593	8.82	5.15	13.99	7.37	60.58
6062	0.3134	0.0502	10.27	6.18	15.26	8.32	60.62
6066	0.1775	0.0528	6.22	2.47	9.78	3.05	60.66
6070	0.406	0.0426	6.96	3.04	12.56	5.7	60.70
6075	0.216	0.0349	13.01	5.41	18.25	6.93	60.75
6079	0.2487	0.0208	7.56	2.56	11.24	2.83	60.79
6083	0.1918	0.0324	5.62	2.15	8.78	2.37	60.83
6087	0.3078	0.0828	2.91	1.12	5.6	1.31	60.87
6091	0.2318	0.0459	8.08	4.19	12.14	5.7	60.91
6096	0.2378	0.0316	10.27	6.18	15.26	8.32	60.96

6100	0.2248	0.0636	8.28	5.1	12.76	6.78	61.00
6104	0.2369	0.0423	13.65	4.63	20.2	6.39	61.04
6108	0.2631	0.0419	9.03	5.05	15.33	7.37	61.08
6112	0.3119	0.0372	11.09	6.09	16.23	7.62	61.12
6116	0.2721	0.0214	10.69	5.47	14.47	5.96	61.16
6121	0.4125	0.0645	21.42	1.28	26.62	1.21	61.21
6125	0.2817	0.0795	7.81	3.17	11.47	3.56	61.25
6129	0.1864	0.0458	9.72	5.24	13.66	5.45	61.29
6133	0.3912	0.0336	10.12	5.65	14.35	6.23	61.33
6137	0.2954	0.0568	16.62	3.97	21.84	5.32	61.37
6142	0.2728	0.0449	15.73	4.43	21.02	5.88	61.42
6146	0.2819	0.043	15.33	5.15	20.5	6.74	61.46
6150	0.2521	0.0328	14.63	5.23	20.09	6.33	61.50
6154	0.2119	0.0455	6.9	2.12	10.71	2.85	61.54
6158	0.3649	0.0561	15.33	5.15	20.5	6.74	61.58
6163	0.2682	0.0535	13.27	5.61	18.62	7.14	61.63
6167	0.3278	0.0468	13.39	5.74	18.58	7.1	61.67
6171	0.3271	0.0597	16.62	3.97	21.84	5.32	61.71
6174	0.2703	0.0654	15.7	4.42	21.44	6.14	61.74
6178	0.3825	0.0617	16.47	3.92	22.3	5.54	61.78
6182	0.3201	0.0346	10.77	5.76	15.56	6.9	61.82
6187	0.2534	0.0472	13.27	5.61	18.62	7.14	61.87
6191	0.2412	0.0569	15.32	4.22	21.11	6.11	61.91
6195	0.2192	0.0622	15.54	4.29	21.43	6.13	61.95
6199	0.2588	0.0867	16.43	3.87	22.25	5.53	61.99
6203	0.1892	0.0515	14.13	4.88	20.23	6.58	62.03
6208	0.306	0.0923	16.65	3.98	21.92	5.33	62.08
6212	0.3281	0.0962	16.59	3.97	22.26	5.54	62.12
6216	0.2845	0.0867	14.13	4.88	20.23	6.58	62.16
6220	0.1761	0.039	9.5	4.87	13.59	5.34	62.20

6224	0.249	0.0697	14.13	4.88	20.23	6.58	62.24
6229	0.242	0.0368	12	5.39	16.65	6.73	62.29
6233	0.273	0.0819	13.19	5.93	17.75	6.99	62.33
6237	0.3174	0.0865	14.16	5.7	19.44	7	62.37
6241	0.1627	0.0548	9.5	4.87	13.59	5.34	62.41
6245	0.248	0.0758	16.53	3.94	22.39	5.55	62.45
6249	0.202	0.0639	16.65	1.19	22.81	3.07	62.49
6254	0.4011	0.0732	8.79	6.38	13.54	8.7	62.54
6258	0.333	0.024	11.19	5.05	15.95	5.43	62.58
6262	0.2832	0.0755	12.41	5.77	17.51	7.53	62.62
6266	0.2872	0.0759	14.13	4.88	20.23	6.58	62.66
6270	0.3662	0.0555	10.47	6.42	15.51	8.55	62.70
6275	0.2321	0.0559	13.15	5.5	19.09	7.53	62.75
6279	0.3105	0.0631	12.1	6.13	17.2	7.91	62.79
6283	0.3479	0.0856	14.16	5.7	19.44	7	62.83
6287	0.2215	0.052	12.41	5.77	17.51	7.53	62.87
6291	0.2183	0.0373	12.99	5.39	18.43	7.06	62.91
6296	0.2407	0.036	11.88	5.91	17.13	7.87	62.96
6300	0.2898	0.0784	16.59	3.97	22.26	5.54	63.00
6304	0.2277	0.0663	16.03	3.76	21.75	5.58	63.04
6308	0.3096	0.0663	15.7	4.42	21.44	6.14	63.08
6312	0.2707	0.0598	14.13	4.88	20.23	6.58	63.12
6317	0.269	0.076	15.51	4.28	21.35	6.11	63.17
6321	0.3376	0.0646	16.47	3.92	22.3	5.54	63.21
6325	0.2363	0.0691	16.58	1.23	23.5	3.04	63.25
6350	0.3292	0.0575	15.33	5.15	20.5	6.74	63.50
6353	0.4039	0.0587	14.44	5.1	20.43	6.6	63.53
6356	0.3569	0.0434	13.2	5.54	18.49	7.04	63.56
6360	0.3349	0.039	13.2	5.54	18.49	7.04	63.60
6363	0.3106	0.0379	13.2	5.54	18.49	7.04	63.63

6366	0.3075	0.0415	16.53	3.93	21.96	5.34	63.66
6369	0.3515	0.0407	15.82	4.2	21.54	4.71	63.69
6372	0.3444	0.0392	11.9	5.93	16.95	7.72	63.72
6376	0.3652	0.0337	13.83	4.72	19.05	5.44	63.76
6379	0.3718	0.0271	11.96	5.8	17.01	6.65	63.79
6382	0.4199	0.0389	13.09	5.72	18.4	7.2	63.82
6385	0.4564	0.0381	9.25	5.85	13.36	6.29	63.85
6388	0.384	0.0483	9.23	5.86	13.44	6.22	63.88
6392	0.4469	0.0385	28.76	0.27	28.91	0.23	63.92
6395	0.4265	0.0186	11.63	5.55	16.34	5.8	63.95
6398	0.4074	0.0288	12.74	4.61	19.33	5.79	63.98
6401	0.3475	0.0536	9.25	5.85	13.36	6.29	64.01
6404	0.451	0.0508	6.22	2.47	9.78	3.05	64.04
6408	0.2904	0.0593	6.58	2.37	10.14	2.84	64.08
6411	0.2309	0.0475	6.71	2.47	10.54	3.12	64.11
6414	0.2321	0.0486	5.96	2.84	9.53	3.42	64.14
6417	0.2003	0.0603	6.22	2.47	9.78	3.05	64.17
6420	0.2867	0.0696	6.14	2.05	9.82	2.89	64.20
6424	0.2546	0.0646	6.58	2.37	10.14	2.84	64.24
6427	0.2109	0.0592	6.58	2.37	10.14	2.84	64.27
6430	0.2478	0.0403	9.05	4.36	13.02	4.69	64.30
6433	0.261	0.0421	10.75	4.76	15.37	5.08	64.33
6436	0.2576	0.0332	8.74	3.8	12.95	4.56	64.36
6440	0.2526	0.031	9.28	4.57	13.5	5.2	64.40
6443	0.2602	0.056	9.05	4.36	13.02	4.69	64.43
6446	0.2243	0.0471	9.72	5.24	13.66	5.45	64.46
6449	0.2547	0.0471	9.5	4.87	13.59	5.34	64.49
6452	0.2156	0.0611	6.58	2.37	10.14	2.84	64.52
6456	0.1463	0.0376	6.61	1.7	10.53	3.04	64.56
6459	0.1778	0.0676	8.27	3.53	13.25	5.07	64.59

6462	0.176	0.0638	6.92	3.02	11.92	5.13	64.62
6465	0.1758	0.0579	6.79	3	11.7	4.99	64.65
6468	0.1848	0.0592	8.47	3.46	13.67	4.65	64.68
6472	0.1804	0.0612	7.79	3.99	12.76	5.37	64.72
6475	0.1874	0.0375	11.95	4.85	17.43	6.44	64.75
6478	0.2157	0.0406	9.7	4.98	14.8	6.45	64.78
6481	0.2382	0.0299	9.97	5.39	16.07	7.5	64.81
6484	0.2318	0.0294	9.09	4.97	15.13	7.36	64.84
6488	0.2339	0.0487	9.12	5.01	15.2	7.42	64.88
6491	0.2369	0.0637	7.85	4.47	13.18	6.91	64.91
6494	0.2338	0.0608	6.37	3.48	10.56	5.38	64.94
6497	0.2308	0.0419	9.14	4.96	14.46	7.08	64.97
6500	0.2375	0.0246	5.38	1.44	8.24	1.44	65.00
6504	0.3141	0.0152	6.05	3.37	10.45	4.54	65.04
6507	0.2649	0.0191	4.89	1.19	8.43	1.4	65.07
6510	0.3429	0.0126	5.89	3.32	10.96	4.46	65.10
6513	0.3305	0.0124	6.05	3.37	10.45	4.54	65.13
6516	0.3384	0.014	6.03	3.39	10.47	4.52	65.16
6520	0.2812	0.0194	4.7	1.54	7.74	1.78	65.20
6523	0.2961	0.0135	8.06	4.45	12.18	5.34	65.23
6526	0.3365	0.012	5.27	1.04	10.06	2.22	65.26
6529	0.3486	0.018	6.18	3.46	10.87	4.69	65.29
6532	0.3674	0.0158	7.28	4.45	11.75	5.41	65.32
6535	0.3521	0.0159	6.03	3.39	10.47	4.52	65.35
6539	0.4558	0.0466	9.88	4.13	16.66	4.6	65.39
6542	0.4269	0.0481	9.43	5.02	14.16	6.18	65.42
6545	0.3842	0.0107	5.93	3.43	9.88	4.61	65.45
6548	0.3171	0.0215	6.42	3.51	11.85	4.74	65.48
6551	0.3072	0.018	9.13	4.5	13.17	6.05	65.51
6555	0.355	0.0363	10.2	4.27	15.93	5.7	65.55

6558	0.3233	0.0413	10.09	4.42	16.12	5.47	65.58
6561	0.309	0.021	5.29	1.53	8.29	1.4	65.61
6564	0.3211	0.021	4.66	1.55	8.03	2.01	65.64
6567	0.3353	0.0203	4.84	0.72	9.58	2.1	65.67
6571	0.301	0.0147	4.62	0.7	8.4	1.16	65.71
6574	0.2854	0.0396	5.65	2.43	10.69	3.32	65.74
6577	0.2229	0.018	4.75	0.64	8.95	1.82	65.77
6580	0.2871	0.0125	4.98	1.15	8.46	1.35	65.80
6583	0.2888	0.0193	4.75	0.64	8.95	1.82	65.83
6587	0.3599	0.0221	5.76	3.34	9.94	4.57	65.87
6590	0.2448	0.0133	4.66	0.92	10.31	2.2	65.90
6593	0.2347	0.0271	4.7	0.89	10.48	1.95	65.93
6596	0.3085	0.0214	4.78	0.74	10.03	2.24	65.96
6599	0.2681	0.0207	4.62	0.73	9.02	1.74	65.99
6603	0.2631	0.0329	5.07	1.23	10.19	2.63	66.03
6606	0.2746	0.0176	4.98	1.35	9.42	1.89	66.06
6609	0.1667	0.0133	4.29	1.73	7.92	2.24	66.09
6612	0.1877	0.0095	4.11	1.22	7.7	2.49	66.12
6615	0.1939	0.0093	4.17	1.32	8.95	2.98	66.15
6619	0.1729	0.011	4.22	1.28	8.12	2.95	66.19
6622	0.1715	0.0123	4.11	1.22	7.7	2.49	66.22
6625	0.1821	0.0071	4.14	1.21	8.08	2.52	66.25
6628	0.1946	0.011	4.16	1.33	8.63	3.02	66.28
6631	0.2226	0.0113	4.35	1.04	9.18	2.6	66.31
6635	0.2016	0.0155	4.31	1.01	9.63	2.47	66.35
6639	0.2197	0.0178	4.19	1.34	9.33	3.21	66.39
6643	0.2018	0.0188	4.59	0.9	10.41	2.02	66.43
6645	0.1769	0.0181	4.59	0.9	10.41	2.02	66.45
6647	0.1614	0.0112	4.29	1.26	8.67	2.86	66.47
6648	0.1754	0.0168	4.5	0.93	10.31	2.18	66.48

6651	0.2177	0.0267	4.43	1.02	10.2	2.4	66.51
6653	0.241	0.0237	4.7	0.92	10.26	2.28	66.53
6655	0.2306	0.0368	4.57	0.9	10.37	2.08	66.55
6656	0.2042	0.0307	5.12	1.35	10.09	1.94	66.56
6659	0.16	0.0163	4.65	0.77	9.92	2.33	66.59
6661	0.1508	0.0181	4.17	0.77	7.78	1.35	66.61
6663	0.1804	0.0276	4	2.2	9.4	2.99	66.63
6664	0.1427	0.015	4.35	1.02	9.34	2.5	66.64
6667	0.1344	0.0239	3.45	2.2	7.29	2.68	66.67
6669	0.0927	0.01	3.19	2.2	6.11	2.56	66.69
6671	0.1226	0.0191	4.46	1.63	8.4	1.7	66.71
6672	0.1127	0.0223	3.82	2.23	8.01	3.09	66.72
6675	0.1556	0.013	4.46	1.63	8.4	1.7	66.75
6677	0.1914	0.0117	4.14	1.84	8.01	2.2	66.77
6679	0.211	0.0347	4.92	1.39	9.07	1.64	66.79
6680	0.1374	0.029	4.45	1.76	9.25	1.55	66.80
6683	0.128	0.0216	4.17	0.77	7.78	1.35	66.83
6685	0.1543	0.0094	3.9	1.1	7.3	1.79	66.85
6687	0.1094	0.0178	4.46	1.63	8.4	1.7	66.87
6688	0.1419	0.0265	4.33	0.74	8.24	1.55	66.88
6690	0.2078	0.0227	4.82	1.64	8.71	2.89	66.90
6693	0.1972	0.0213	4.59	0.94	9.1	2.63	66.93
6695	0.1948	0.0242	4.35	0.78	8.24	1.62	66.95
6696	0.1785	0.0213	4.56	0.92	9.01	2.65	66.96
6699	0.1373	0.0143	4.5	0.93	10.31	2.18	66.99
6701	0.1603	0.0223	4.44	0.87	8.8	2.16	67.01
6703	0.1887	0.0298	4.5	0.93	10.28	2.24	67.03
6704	0.1425	0.0142	3.96	1.12	7.27	1.78	67.04
6707	0.1677	0.0119	4.28	0.79	7.69	1.33	67.07
6709	0.2131	0.0112	4.39	0.73	8.24	1.53	67.09

6711	0.2381	0.0231	4.58	0.65	8.26	1.47	67.11
6712	0.2373	0.0263	4.52	0.67	8.77	1.53	67.12
6715	0.1584	0.0378	4.42	0.54	9.24	1.99	67.15
6717	0.184	0.0412	4.42	0.54	9.24	1.99	67.17
6719	0.1522	0.0246	4.57	0.63	9.19	1.41	67.19
6721	0.2084	0.0438	5.53	2.42	10.73	3.12	67.21
6725	0.1846	0.0356	6.22	2.74	11.01	3.15	67.25
6728	0.1743	0.0378	6.25	2.77	10.96	3.14	67.28
6730	0.1951	0.037	6.13	2.29	11.06	3.05	67.30
6732	0.1517	0.0254	5.5	2.43	10.38	3.3	67.32
6736	0.1295	0.0411	4.74	1.31	9.1	1.77	67.36
6738	0.1754	0.0277	6.39	2.44	10.52	3.09	67.38
6740	0.1748	0.0167	6.46	2.61	10.62	3.43	67.40
6742	0.1478	0.0242	5.71	2.06	9.97	2.02	67.42
6746	0.1345	0.0149	5	1.13	8.41	1.41	67.46
6749	0.1836	0.0606	6	2.18	10.28	3.66	67.49
6751	0.1383	0.0177	5.44	2.16	8.3	1.76	67.51
6753	0.1938	0.0418	6.92	2.02	10.71	3.06	67.53
6757	0.103	0.0273	4.77	1.64	9.64	2.96	67.57
6759	0.0835	0.0091	4.16	1.33	8.86	3.03	67.59
6761	1.5601	0.0028	3.99	1.11	7.42	1.74	67.61
6767	0.077	0.0133	4.13	1.34	8.58	3.04	67.67
6770	0.0932	0.0084	4.14	1.21	8.08	2.52	67.70
6772	0.1824	0.0137	4.65	0.78	8.9	2.03	67.72
6774	0.2096	0.0127	5.16	1.06	9.51	2.02	67.74
6778	0.2315	0.0162	5.01	1.14	8.92	1.84	67.78
6780	0.1931	0.0162	5.03	1.26	10.31	2.2	67.80
6782	0.2065	0.0135	4.98	1.15	8.46	1.35	67.82
6784	0.245	0.0213	6.97	3.79	11.56	5.53	67.84
6789	0.288	0.0193	7.3	3.85	11.52	5.5	67.89

Appendix 4. Results from the MAT analysis carried out using the Terminal program for Mac OS X. Env1Avg is the average winter SST and Env2Avg is the summer average SST. The down core analysis is compared to the Brown University Foraminiferal Database; Atlantic Ocean samples only (Prell et al., 1999).

7.2 APPENDICES FOR CHAPTER 3

Appendix 5. Samples used in the test to determine the cleaning method for mass spectrometry (ultrasonification vs. non-ultrasonification of samples).

Sample	MCD (m)	Clean	Dirty	Code for stable isotope analysis	Box ID number
HB, C4, S5; 48-50cm	36.16	∘		B45 48C	A1
HB, C4, S5; 48-50cm	36.16		∘	B45 48D	A2
HB, C4, S5; 52-54cm	36.20	∘		B45 52C	A3
HB, C4, S5; 52-54cm	36.20		∘	B45 52D	A4
HB, C4, S5; 108-110cm	36.76	∘		B45 108C	A5
HB, C4, S5; 108-110cm	36.76		∘	B45 108D	A6
HB, C4, S5; 112-114cm	36.80	∘		B45 112C	A7
HB, C4, S5; 112-114cm	36.80		∘	B45 112D	A8

Table 3.7. Results of the test to compare cleaning methods for stable isotope analysis (ultrasonification of samples or not).

Sample	Code for stable isotope analysis	$\delta^{13}C$ (VPDB)	1 s.d. internal	$\delta^{18}O$ (VPDB)	1 s.d. internal
HB, C4, S5; 48-50cm	B45 48C	0.069	0.045	0.669	0.039
HB, C4, S5; 48-50cm	B45 48D	-0.033	0.047	0.627	0.052
HB, C4, S5; 52-54cm	B45 52C	-0.053	0.025	0.483	0.054

HB, C4, S5; 52-54cm	B45 52D	-0.067	0.042	0.534	0.075
HB, C4, S5; 108-110cm	B45 108C	0.152	0.051	2.223	0.046
HB, C4, S5; 108-110cm	B45 108D	0.190	0.085	2.393	0.187
HB, C4, S5; 112-114cm	B45 112C	Sample didn't acidify properly, unreliable			
HB, C4, S5; 112-114cm	B45 112D	0.49	0.041	2.576	0.054

Table 3.8. A table showing the average weight of a foraminifera shell to determine the number of specimens required for stable isotope analysis.

Sample	MCD (m)	Boat weight (µg)	Number of *G. inflata*	Boat + foram weight (µg)	Combined weight of forams (µg)	Average individual *G. inflata* weight (µg)
HB, C4, S5;	36.16	44761	29	45380	619	21.34
HB, C4, S5;	36.20	44755	30	45427	672	22.40
HB, C4, S5;	36.76	44756	30	45207	451	15.03
HB, C4, S5;	36.80	44754	29	45161	407	14.03

Appendix 6. The measured weight of each of the standards (Carrara, Estremoz and Atlantis) needed for each of the run matrices for ODP Site 1063 across Termination 2.

Run 1

Run 1 Matrix ideal					
Carrara					
100	130	160	190	220	250
100	130	160	190	220	250

Estremoz	***Atlantis***
130	130
220	220

Run 1 Matrix measured					
Carrara					
C 104	C 129	C 156	C 194	C 219	C 247
C 103	C 126	C 158	C 190	C 228	C 249

Estremoz	***Atlantis***
E 111	A 103
E 247	A 227

Run 2

Run 2 Matrix					
Carrara					
225	260	295	330	365	400
225	260	295	330	365	400

Estremoz	***Atlantis***
260	260
365	365

Run 2 Matrix measured					
Carrara					
C 222	C 257	C 295	C 326	C 365	C 409
C 226	C 266	C 294	C 335	C 369	C 397

Estremoz	***Atlantis***
E 254	A 230
E 375	A 372

Run 3

Run 3 Matrix					
Carrara					
250	280	310	340	370	400
250	280	310	340	370	400

Estremoz	***Atlantis***
280	280
370	370

Run 3 Matrix measured					
Carrara					
C 245	C 281	C 306	C 344	C 367	C 398
C 249	C 278	C 313	C 336	C 370	C 404

Estremoz	***Atlantis***
E 277	A 269
E 377	A 394

Run 4

Run 4 Matrix					
Carrara					
300	340	380	420	460	500
300	340	380	420	460	500

Estremoz	***Atlantis***
340	340
460	460

Run 4 Matrix measured					
Carrara					
C 299	C 339	C 379	C 419	C 463	C 496
C 301	C 344	C 377	C 422	C 458	C 498

Estremoz	***Atlantis***
E 314	A 317
E 482	A 477

Appendix 7. Matrices to show the sample ID and run sequence for stable isotope analysis for the samples from ODP Site 1063

<100µg run matrix

	1	2	3	4	5	6	7	8
A								
B	C53 53	B52 24	B52 44	C54 72	B52 0	B44 32	B52 40	B45 84
C	C53 29	C54 108	C53 65	B52 4	C53 93			
D								
E								
F								
G								
H								

Run 1 matrix

	1	2	3	4	5	6	7	8
A	C 104	C 103	C 129	C 126	C 156	C 158	C 194	C 190
B	C54 36	C54 64	B46 32	B44 24	B52 36	C53 133	B51 113	B52 12
C	B44 28	C54 144	C53 61	B51 149	B46 12	B51 121	B52 32	B44 48
D	B46 88	B44 20	B52 28	B51 145	C54 116	B52 16	C53 101	C53 57
E	C 219	C 228	C 247	C 249	E 111	E 247	A 103	A 227
F	B52 20	C54 48	B51 117	B52 52	B51 125	B51 133	B51 109	C54 32
G	C53 137	C53 149	C54 52	C54 88	C53 145	B51 141	C53 105	C54 12
H	C53 73	B52 8	C53 109	B43 132	B45 92	B46 84	C54 68	B44 96

Run 2 matrix

	1	**2**	**3**	**4**	**5**	**6**	**7**	**8**
A	C 222	C 226	C 257	C 266	C 295	C 294	C 326	C 335
B	B51 137	C53 129	C54 80	B52 48	B44 52	B44 56	C54 112	B44 36
C	B44 44	B44 116	B43 136	B45 88	B44 76	C54 84	B44 72	B45 76
D	B44 112	C54 136	B44 16	B44 92	B44 40	B44 60	B45 80	B44 64
E	C 365	C 369	C 409	C 397	E 254	E 375	A 230	A 372
F	B45 108	C54 132	B45 96	C53 69	C53 77	C54 140	B45 16	B46 36
G	B44 132	B45 104	B44 108	B44 120	B45 112	C53 81	B43 140	B43 144
H	C53 97	B44 128	B44 104	B44 80	B46 0	C53 89	B45 144	B46 68

Run 3 matrix

	1	**2**	**3**	**4**	**5**	**6**	**7**	**8**
A	C 245	C 249	C 281	C 278	C 306	C 313	C 344	C 336
B	B44 12	B44 68	B44 124	B45 72	B44 100	B46 20	C54 44	C54 92
C	C54 56	B52 68	B45 128	B45 148	B52 56	B44 140	C54 100	B44 136
D	C53 37	B44 84	B45 132	B45 4	B45 8	B45 24	B46 80	B45 116
E	C 367	C 370	C 398	C 404	E 277	E 377	A 269	A 394
F	B52 64	C54 0	C54 128	C53 45	B44 88	C53 49	B45 120	B52 60
G	B44 0	B44 4	C54 20	B44 8	B44 148	B46 72	B51 129	B46 4
H	B46 92	C53 125	C54 124	B43 148	B46 52	B45 0	C54 76	C54 104

Run 4 matrix

	1	**2**	**3**	**4**	**5**	**6**	**7**	**8**
A	C 299	C 301	C 339	C 344	C 379	C 377	C 419	C 422
B	C54 28	C54 96	B45 140	B46 8	B46 44	C53 113	B46 24	B46 48
C	C54 16	C54 4	B46 76	C54 24	B45 136	C54 60	B45 12	B45 20
D	B45 124	B46 64	C53 85	B45 28	B45 100	B46 56	B44 144	B46 28
E	C 463	C 458	C 496	C 498	E 314	E 482	A 317	A 477
F	C54 8	C54 40	B46 40	B46 60	C53 121	C53 141	B45 68	C53 33
G	C53 117	C53 41	B46 16	C54 120	B45 32	B45 40	C53 21	B45 56
H	C53 17	B45 48	B45 52	C53 25	B45 36	B45 64	B45 44	B45 60

Appendix 8. Consistency of measurements of individual specimens between laboratories.

In order to ensure consistency when weighing out the samples and standards in different labs, a test weight analysis was performed by comparing the weight of exactly the same samples in both labs to see if the reliability and precision of the scales are accurate enough. This is important as the samples were weighed using one microbalance and the standards a difference balance thus a comparison needed to be carried out to ensure the high precision for the weights being used in the mass spectrometer. The test involved weighing three different samples both as a total sample (29 specimens) to find an average and also individual specimens too for comparison. The results can be found in the table below (Table 9).

Table 9. The differences in measured weights between two different sets of scales in the different labs in the Earth and Ocean Sciences department at Cardiff University.

Sample	Ian's lab scales			Steve's lab scales		
	Combined foram weight (µm)	**Average foram weight (µm)**	**Individual foram weight (µm)**	**Combined foram weight (µm)**	**Average foram weight (µm)**	**Individual foram weight (µm)**
HB, C4, S5; 0-2cm	459	15.83	14	457	15.76	12
HB, C4, S5; 12-14cm	484	16.69	9	482	16.62	12
HB, C4,	459	16.39	12	456	16.29	11

S5; 24-26cm							

The results of this test weighing show that when comparing the scales between the two labs there isn't that much difference in the numbers and thus it is fine to weigh the foram samples in one lab and then the standards in a different lab (the reason for the different labs being used it purely a logistical one) as the weight comparison between the two of them is minimal and within the error of the balance.

Appendix 9. Initial cleaning procedure used for the fish teeth/debris

The following procedure (

Table 10) was followed in a clean lab in Cardiff University prior to transporting the samples to Imperial College, London for the column chemistry and analysis – note this was carried out using acid-cleaned tubes (see Table 12. A table to show the individual composition of each of the samples run for neodymium analysis.

Sample Number	**Weighted MCD**	**Sample Composition**
1	34.05	Mainly debris/fragments; 20x frags and 2x teeth
2	34.25	Mainly debris/fragments; 15x frags, 2x long teeth, 1x 3-pronged teeth
3	34.38	All fragments; 11x frags
4	34.61	Mainly fragments, some bones; 20x frags, 3x long teeth, 2x 'shark-like' teeth, 2x fish bones

5	34.79	Mainly fragments; 15x frags, 1x very long, bent tooth
6	35.02	Mainly fragments; 25x frags, 1x fish jaw with 3 teeth attached
7	35.21	All fragments; 25x frags
8	35.34	Mainly fragments; 20x frags, 3x large, thin fish teeth
9	35.54	Mainly fragments, some bones; 15x frags, 3x long , thin teeth, 1x long bent tooth, 2x fish bones
10	35.93	All fragments; 25x frags
11	36.04	Mainly fragments, some bones; 20x frags, 3x long teeth, 2x fish bones
12	36.19	Mainly fragments; 30x frags, a bit of bone
13	36.42	Mainly fragments, a few teeth and bones; 15x frags, 3x bent teeth, 2x long teeth, 3x fish bones
14	36.74	Mainly fragments; 10x frags, 1x very large tooth
15	37.03	Mainly fragments, some bones; 12x frags, 3x fish bones
16	37.47	50% fragments, 50% fish teeth/bones; 6x frags, 2x fish bones, 6x long bent fish teeth
17	37.78	Mainly fragments; 10x frags, 1x bent tooth, 1x price of fish jaw, a piece of bone
18	38.15	Mainly fragments; 10x frags, 1x ‘shark-like’ tooth

19	38.81	Mainly fragments; 5x frags, 1x bent tooth, 1x fish tooth
20	39.12	Mainly fragments; 8x frags, 1x fish bone
21	39.49	All fragments; 4x frags
22	39.74	All fragments; 10x frags

Table 10. Initial stages of fish teeth/debris cleaning methods (these were carried out prior to traveling to Imperial College, London for the full analyses.

	Turn the flow bench on 15 minutes before starting work and wash well with D.I. water.
	Ensure that pipettes and tips as well as the tip rinse (10% HCl and 18.2 mΩ DI H_2O) and waste bucket are set up in the flow bench.
	Place the fish teeth into a labeled 5ml acid-cleaned centrifuge tube using a fine haired paintbrush and 18.2 mΩ DI H_20.
	Attach a pipette tip to the pipette and clean the tip 6 times with 10%HCl and a further 6 times with 18.2 mΩ DI H_2O.
	Next pipette approximately 350µl of 18.2 mΩ DI H_2O into 3 or 4 tubes.
	Allow the fish teeth to settle for a few seconds ensuring that all the fish teeth are at the bottom of the tube (this can be done by tapping the tube on the bench or by flicking the tube).

	Pipette out about 300µl of the 18.2 mΩ DI H_2O from each of the tubes – ensuring to clean the pipette tip with two rinses of the 10% HCl and followed by two rinses of the pipette with 18.2 mΩ DI H_2O between each sample.
	Repeat this with 3 or 4 tubes at time until all the tubes have had the 18.2 mΩ DI H_2O added and the majority of it then removed.
	Once the 18.2 mΩ DI H_2O has been removed from each of the samples the rack can then be placed in the ultrasonciate bath for 1minute.
	Repeat stages VII-XI three times.
	Next, with a clean – fully washed pipette tip (see point 2 above) add approximately 300µl of methanol to the tubes and allow to settle.
	Place the rack of samples in to the ultrasoncaite bath for 1 minute.
	Next, pipette out the majority of the methanol from the tube and then instantly re-suspend the sample by squirting the same methanol back in to the tube. Allow this to settle for 2-3 seconds and then remove the methanol.
	Once stage 10 has been carried out on all the samples, repeat stages 8-10 three times.
	Finally the tubes needs to be rinsed three times with 18.2 mΩ DI H_2O allowing only a few seconds each time of re-suspension of the fish teeth before removing the 18.2 mΩ DI H_2O with a pipette.

	Finally once repeating stage XIII three times all the water needs to be taken off of the samples before they are transported for analysis – this is done using a finer pipette tip found on a smaller volume pipette.
	Ensure that all the caps are tightly placed on the tubes and place in a rack and two, clean ziplock bags for transportation.

Table 11. An easy tick-box summary of the steps and number of repeats required to clean the fish teeth/debris in the clean lab.

	Repeat 1	**Repeat 2**	**Repeat 3**
Fill 3 or 4 tubes with approximately 350µl 18.2 mΩ DI H_2O			
Allow contents to settle and then remove approximately 300µl of the 18.2 mΩ DI H_2O			
Ultrasonicate the samples for 1 minute			
Add approximately 300µl of methanol to all the tubes			
Ultrasonicate the samples for 1 minute			
Pipette out 250µl methanol and then instantly re-suspend, allow this to settle for 2-3 seconds and then			
Add 350µl of 18.2 mΩ DI H_2O			
Allow the fish debris to settle and then remove all the 18.2 mΩ DI H_2O			

Table 12. A table to show the individual composition of each of the samples run for neodymium analysis.

Sample Number	Weighted MCD	Sample Composition
1	34.05	Mainly debris/fragments; 20x frags and 2x teeth
2	34.25	Mainly debris/fragments; 15x frags, 2x long teeth, 1x 3-pronged teeth
3	34.38	All fragments; 11x frags
4	34.61	Mainly fragments, some bones; 20x frags, 3x long teeth, 2x 'shark-like' teeth, 2x fish bones
5	34.79	Mainly fragments; 15x frags, 1x very long, bent tooth
6	35.02	Mainly fragments; 25x frags, 1x fish jaw with 3 teeth attached
7	35.21	All fragments; 25x frags
8	35.34	Mainly fragments; 20x frags, 3x large, thin fish teeth
9	35.54	Mainly fragments, some bones; 15x frags, 3x long , thin teeth, 1x long bent tooth, 2x fish bones
10	35.93	All fragments; 25x frags
11	36.04	Mainly fragments, some bones; 20x frags, 3x long teeth, 2x fish bones
12	36.19	Mainly fragments; 30x frags, a bit of bone

13	36.42	Mainly fragments, a few teeth and bones; 15x frags, 3x bent teeth, 2x long teeth, 3x fish bones
14	36.74	Mainly fragments; 10x frags, 1x very large tooth
15	37.03	Mainly fragments, some bones; 12x frags, 3x fish bones
16	37.47	50% fragments, 50% fish teeth/bones; 6x frags, 2x fish bones, 6x long bent fish teeth
17	37.78	Mainly fragments; 10x frags, 1x bent tooth, 1x price of fish jaw, a piece of bone
18	38.15	Mainly fragments; 10x frags, 1x 'shark-like' tooth
19	38.81	Mainly fragments; 5x frags, 1x bent tooth, 1x fish tooth
20	39.12	Mainly fragments; 8x frags, 1x fish bone
21	39.49	All fragments; 4x frags
22	39.74	All fragments; 10x frags

7.3 APPENDICES FOR CHAPTER 4

Appendix 10. Acid cleaning centrifuge tubes method

I	**Turn the flow bench on 15 minutes before starting work and wash well with D.I. water.**
II	Rinse the large glass beaker and watch glass well with 18.2 mΩ DI H_2O.
III	Fill the beaker about ¾ full with 10% HCl.
IV	While in the fume cupboard fill each individual 5.0ml centrifuge tube with the acid from the large beaker ensuring that there are no air bubbles in the
V	Carefully drop/place the rubes into the beaker of acid – you should be able to
VI	Once you have repeated until the beaker is full of tubes, check to see if any
VII	Place the watch glass on the beaker and leave in the fume cupboard.
VIII	First thing in the morning place the beaker full of tubes with the watch glass on top on to the hot plate (in the fume cupboard) and set the hotplate to; 100 for >1 hour 150 for a further >1 hour 200, at which point bubbles will start to form. Leave the beaker at this temperature for the rest of the day remembering to TURN THE HOTPLATE OFF at the end of the day.
IX	Leave the tubes in the acid overnight (remember to leave the fume cupboard on).

X	The next day, turn the flow benches on for 15 minutes and clean again with 18.2 mΩ DI H_2O before starting work.
XI	In the fume cupboard return the acid back to the container taking care not to allow any of the tubes to fall back in with the acid (Do this by inverting the watch glass on the top of the beaker).
XII	Fill the beaker with 18.2 mΩ DI H_2O and swirl around/gently shake the tubes around, pour the dilute acid to waste.
XIII	Repeat stage XII three times.
X1V	Carefully pick up an emptied centrifuge tube by the pointy end (i.e. furthest point from the lid), flick out any remaining liquid into the sink.
XV	Place the tube between your index and middle finger and repeat XIII and XIV until you have 6 tubes held between your fingers.
XVI	Using the already acid cleaned squeezy bottle containing 18.2 mΩ DI H_2O squirt 18.2 mΩ DI H_2O into each of the tubes and lids making sure you rinse the hinges and top of the cap too.
XVII	Next the water needs to be removed from the tube. This is done by using a quick flick of the wrist towards the sink (note this shouldn't be done too close to the sink to ensure that none of the contents of the tube are able to return back into the tube.
XV111	Repeat stages XV and XVI five times
	Place the now emptied centrifuge tubes on the pre-cleaned flow bench to dry.
	Repeat stages XIII-XVII until all the tubes have been cleaned and none remain in the beaker.

	Once the tube are dried (this doesn't take long), carefully close the caps avoiding touching any part of the tube and place in a clean ziplock bag and label with name, what they are, the date and number of tubes in the bag.
	Clean the flow bench, fume cupboard and work surface with 18.2 mΩ DI H_2O, remembering to clean the beaker and watch glass too.
	Once all the tubes have been cleaned and put away the fume cupboard can be turned off.

Appendix 11. The number of inflata used in the paired Mg/Ca-$\delta^{18}O$ analysis. Estimated weight being analysed for both the stable isotope and Mg/Ca analysis also indicated.

MCD	Hole	Core	Section	Top Depth (cm)	Bottom Depth (cm)	Number of Inflata	Estimated Weight Isotopes (mg)	Estimated Weight Mg/Ca (mg)
44.79	A	5	3	8	10	12	102	204
44.81	A	5	3	10	12	8	68	136
44.83	A	5	3	12	14	2	26	26
44.85	A	5	3	14	16	12	98	196
44.87	A	5	3	16	18	15	88	265
44.89	A	5	3	18	20	14	91	273
44.93	A	5	3	22	24	10	98	196
44.97	A	5	3	26	28	12	77	154
45.01	A	5	3	30	32	4	45	45
45.05	A	5	3	34	36	20	142	283

45.09	A	5	3	38	40	7	72	72
45.13	A	5	3	42	44	26	142	425
45.17	A	5	3	46	48	6	74	74
45.21	A	5	3	50	52	4	36	36
45.25	A	5	3	54	56	5	50	50
45.29	A	5	3	58	60	4	41	41
45.33	A	5	3	62	64	5	55	55
45.37	A	5	3	66	68	7	64	64
45.41	A	5	3	70	72	6	72	72
45.45	A	5	3	74	76	15	110	221
45.49	A	5	3	78	80	6	64	64
45.53	A	5	3	82	84	4	44	44
45.57	A	5	3	86	88	15	107	215
45.61	A	5	3	90	92	12	103	207
45.65	A	5	3	94	96	16	109	219
45.69	A	5	3	98	100	30	154	462
45.73	A	5	3	102	104	18	129	257
45.77	A	5	3	106	108	18	113	339
45.81	A	5	3	110	112	14	95	191
45.85	A	5	3	114	116	15	120	240
45.89	A	5	3	118	120	30	164	492
45.93	A	5	3	122	124	18	133	265
45.97	A	5	3	126	128	16	117	234
46.01	A	5	3	130	132	30	167	501

46.05	A	5	3	134	136	8	62	125
46.09	A	5	3	138	140	28	144	574
46.13	A	5	3	142	144	8	66	131
46.17	A	5	3	146	148	4	54	54
46.21	A	5	4	0	2	10	78	156
46.25	A	5	4	4	6	12	108	215
46.29	A	5	4	8	10	26	166	499
46.33	A	5	4	12	14	22	146	438
46.37	A	5	4	16	18	10	94	187
46.41	A	5	4	20	22	17	110	329
46.45	A	5	4	24	26	27	151	603
46.49	A	5	4	28	30	11	101	201
46.53	A	5	4	32	34	16	139	278
46.57	A	5	4	36	38	9	87	174
46.61	A	5	4	40	42	18	131	263
46.65	A	5	4	44	46	20	131	392
46.69	A	5	4	48	50	21	135	406
46.73	A	5	4	52	54	30	135	541
46.77	A	5	4	56	58	30	146	583
46.81	A	5	4	60	62	15	107	215
46.85	A	5	4	64	66	15	125	249
46.89	A	5	4	68	70	30	145	579
46.93	A	5	4	72	74	30	148	592
46.97	A	5	4	76	78	30	156	623

47.01	A	5	4	80	82	29	138	552
47.03	A	5	4	82	84	30	163	490
47.07	A	5	4	86	88	30	142	567
47.11	A	5	4	90	92	30	165	494
47.15	A	5	4	94	96	30	137	547
47.19	A	5	4	98	100	30	141	563
47.23	A	5	4	102	104	30	173	519
47.27	A	5	4	106	108	30	169	508
47.31	A	5	4	110	112	30	168	505
47.35	A	5	4	114	116	30	168	504
47.39	A	5	4	118	120	30	167	500
47.43	A	5	4	122	124	30	171	514
47.47	A	5	4	126	128	30	171	512
47.51	A	5	4	130	132	30	168	505
47.55	A	5	4	134	136	30	168	504
47.59	A	5	4	138	140	30	156	468
47.63	A	5	4	142	144	30	139	557
47.67	A	5	4	146	148	30	162	486
47.71	A	5	5	0	2	30	137	549
47.75	A	5	5	4	6	30	161	482
47.79	A	5	5	8	10	30	149	595
47.83	A	5	5	12	14	30	154	614
47.87	A	5	5	16	18	29	174	521
47.91	A	5	5	20	22	30	172	515

47.95	A	5	5	24	26	27	164	492
47.99	A	5	5	28	30	20	144	288
48.03	A	5	5	32	34	30	167	502
48.05	A	5	5	34	36	30	163	488
48.07	A	5	5	36	38	30	162	485
48.09	A	5	5	38	40	30	163	488
48.11	A	5	5	40	42	30	144	579
48.13	A	5	5	42	44	24	132	397
48.15	A	5	5	44	46	20	131	263
48.17	A	5	5	46	48	30	149	446
48.19	A	5	5	48	50	30	161	482
48.21	A	5	5	50	52	30	152	456
48.23	A	5	5	52	54	29	146	438
48.25	A	5	5	54	56	23	143	286
48.27	A	5	5	56	58	30	141	423
48.29	A	5	5	58	60	29	151	451
48.31	A	5	5	60	62	29	151	452
48.33	A	5	5	62	64	30	150	450
48.35	A	5	5	64	66	28	138	415
48.37	A	5	5	66	68	30	155	465
48.39	A	5	5	68	70	27	134	401
48.41	A	5	5	70	72	30	156	467
48.43	A	5	5	72	74	30	163	490
48.45	A	5	5	74	76	30	151	451

48.47	A	5	5	76	78	30	168	503
48.49	A	5	5	78	80	30	146	438
48.51	A	5	5	80	82	30	155	466
48.53	A	5	5	82	84	30	172	515
48.55	A	5	5	84	86	15	128	256
48.57	A	5	5	86	88	25	141	423
48.59	A	5	5	88	90	19	137	275
48.61	A	5	5	90	92	30	142	570
48.63	A	5	5	92	94	30	163	490
48.65	A	5	5	94	96	30	168	507
48.67	A	5	5	96	98	30	168	503
48.69	A	5	5	98	100	30	175	525
48.73	A	5	5	102	104	30	169	506
48.77	A	5	5	106	108	30	164	492
48.81	A	5	5	110	112	30	167	500
48.85	A	5	5	114	116	30	164	493
48.89	A	5	5	118	120	30	165	495
48.93	A	5	5	122	124	30	164	493
48.97	A	5	5	126	128	30	156	467
49.01	A	5	5	130	132	30	158	473
49.05	A	5	5	134	136	30	151	454
49.09	A	5	5	138	140	30	146	437
49.13	A	5	5	142	144	30	144	431
49.17	A	5	5	146	148	30	154	463

49.21	A	5	6	0	2	19	129	258
49.25	A	5	6	4	6	28	148	443
49.29	A	5	6	8	10	15	117	235
49.33	A	5	6	12	14	30	160	480
49.37	A	5	6	16	18	30	142	427
49.39	A	5	6	18	20	16	109	219
49.41	A	5	6	20	22	16	100	199
49.43	A	5	6	22	24	20	137	275
49.45	A	5	6	24	26	30	150	451
49.47	A	5	6	26	28	30	183	366
49.49	A	5	6	28	30	30	162	487
49.51	A	5	6	30	32	30	184	367
49.53	A	5	6	32	34	30	159	477
49.55	A	5	6	34	36	30	141	424
49.57	A	5	6	36	38	30	149	448
49.59	A	5	6	38	40	30	150	449
49.61	A	5	6	40	42	30	150	451
49.63	A	5	6	42	44	29	143	428
49.65	A	5	6	44	46	15	104	209
49.67	A	5	6	46	48	30	150	449
49.69	A	5	6	48	50	30	150	449
49.71	A	5	6	50	52	20	143	285
49.73	A	5	6	52	54	22	167	334
49.75	A	5	6	54	56	22	153	305

49.77	A	5	6	56	58	28	196	393
49.81	A	5	6	60	62	27	195	389
49.85	A	5	6	64	66	29	163	489
49.89	A	5	6	68	70	18	132	264
49.93	A	5	6	72	74	30	155	465
49.97	A	5	6	76	78	30	143	430
50.01	A	5	6	80	82	30	161	483
50.05	A	5	6	84	86	30	203	406
50.09	A	5	6	88	90	21	145	289
50.13	A	5	6	92	94	16	122	245
50.17	A	5	6	96	98	22	118	355
50.19	A	5	6	98	100	27	165	494
50.21	A	5	6	100	102	20	147	293
50.23	A	5	6	102	104	30	168	503
50.25	A	5	6	104	106	17	128	257
50.27	A	5	6	106	108	15	112	224
50.29	A	5	6	108	110	14	116	232
50.31	A	5	6	110	112	10	63	126
50.33	A	5	6	112	114	8	65	130
50.35	A	5	6	114	116	7	49	98
50.37	A	5	6	116	118	7	56	112
50.39	A	5	6	118	120	3	31	31

Appendix 12. Magnesium/calcium methods

Before work can start on preparing any of the reagents or cleaning any tubes for Ma/Ca analysis the whole clean lab needs to be cleaned. That is to say, that all the sides need to be washed down with DI water (note the squeezy bottle is called 'DI water for lab cleaning'). Not only to the sides need to be cleaned out but so too does the back panel of the fume cupboards as well as the sides and surfaces of everything in the clean lab. The reason for this is to simply remove any dust particles that might be in the lab that if present, will alter the results. As well as washing down all the sides of the lab, the floor also needs to be cleaned thoroughly with DI water. For this the bucket and mop in the clean lab should be used, not only does the floor in the far clean lab need to be done, but so too does the middle clean lab room. The final thing to do is to pull off one of the sheets of the silver sticky flooring mat that you have to walk across to get in to the clean lab (as this removes any additional dirt). At any time in the clean lab white lab coats must be worn and outdoor shoes must be taken off and replaced by the specific clean lab shoes.

This lab cleaning should be done the night before the lab is needed to ensure that the whole lab is clean and the floors are dry before you use it.

If at any point I you need to poor away the previous remains of the regents, i.e. they are too old then instead of just pouring this down the sink, it is important that you pour the liquid into the cap of the bottle first and then out in to the sink from the cap and sinks are made of a lot of magnesium which is obviously no ideal and is likely to contaminate the samples.

Appendix 13. Table to show the dilutions of OPTIMA to DI water needed for each of the acids used during Mg/Ca analysis.

Concentration of nitric acid	**Neogene bottle capacity**	**Volume of DI water* to be used**	**Volume of OPTIMA nitric acid to be used**
0.5M	1 litre	9400ml	31ml
0.065M	500ml	498ml	2.072ml
0.002M	500ml	400ml	2g

⌘ Note that the acid bottles should not only be kept in neogene bottles but these bottles should also be kept in see through 'ziplock' bags to prevent any dust getting in the acids. *The DI water that should be used for making up the reagents should be >18 (units????)

Before using the pipettes for anything (such as making up the reagents as above) the tips need to be rinsed and washed out properly. For this the tip needs to be set to the amount (volume) needed and then used to pipette 10%HCL 6 times into a waste tub. This process then needs to be followed by pipetting out DI water 6 times.

Appendix 14. Cleaning procedure steps for lab

The following steps (Appendix 15) were followed based on the cleaning procedure outlined by Barker et al., 2003. These points were followed in the clean lab for each of the samples, the samples were cleaned in sets of 30 which included 28 samples to be analysed and 2 procedural blanks. The cleaning steps were aimed at removing as many potential contaminants as possible; (i) the clay removal steps involved repeated UHQ water and methanol rinses with intervals of ultrasonification; (ii) the oxidation step aided the removal of organic matter by using alkali (NaOH 0.01M) buffered 1% H2O2; (iii) silicates that had not been removed during the previous cleaning steps were removed by hand (as was any obviously discoloured foraminiferal calcite) using

a single-lash brush; and (iv) the dilute acid leach step (0.002M HNO) is carried out to remove Authigenic Mn-Fe coatings. Finally, once these cleaning steps were completed, the samples were dissolved in 120µl of 0.065M HNO3 and centrifuged to remove any remaining silicate particles.

Appendix 15. A table to show the procedural cleaning steps used for Mg/Ca analysis. Note; these steps should all be carried out in a fume cupboard (turned on) in a clean lab that has been washed down with DI water. Procedure outlined by Barker et al., 2003.

Stage	Process	Complete
CLAY REMOVAL **Only do 3-4 tubes at a time as to ensure the clays don't all settle again**	Add a squeeze of 18.2mΩ DI H_2O to all samples, briefly allow time to settle, remove H_2O with a pipette – remember to leave 20µl or so.	
	Ultrasonicate for 2 minutes.	
	Add a squeeze of 18.2mΩ DI H_2O to all samples, briefly allow time to settle, remove H_2O with a pipette – remember to leave 20µl or so.	
	Ultrasonicate for 2 minutes.	
	Add a squeeze of 18.2mΩ DI H_2O to all samples, briefly allow time to settle, remove H_2O with a pipette – remember to leave 20µl or so.	
	Ultrasonicate for 2 minutes.	
	Add a squeeze of 18.2mΩ DI H_2O to all samples, briefly allow time to settle, remove H_2O with a pipette – remember to leave 20µl or so.	
	Ultrasonicate for 2 minutes.	
	Add a squeeze of 18.2mΩ DI H_2O to all samples, briefly allow time to settle, remove H_2O with a pipette – remember to leave 20µl or so.	

	Ultrasonicate for 2 minutes.	
CLAY REMOVAL	Add 250µl of methanol.	
	Ultrasonicate for 1-2 minutes.	
	One at a time, remove the methanol and then squirt back into the tube, allow sample to settle for just a few seconds and remove methanol.	
	Add 250µl of methanol to all samples.	
	Ultrasonicate for 1-2 minutes.	
	One at a time, remove the methanol and then squirt back into the tube, allow sample to settle for just a few seconds and remove methanol.	
WATER RINSE	Add 18.2mΩ DI H_2O, allow to settle, remove 18.2mΩ DI H_2O.	
	Add 18.2mΩ DI H_2O, allow to settle, remove 18.2mΩ DI H_2O.	
REMOVAL OF ORGANIC MATTER	Add 250µl of alkali buffered 1% H_2O_2 to each tube .	
	Place in boiling H2O bath for 10 minutes At 2.5 minutes remove rack and tap on bench At 5 minutes ultrasonicate in the bath for a 2-5 seconds At 7.5 minutes remove rack and tap on bench	
	Remove the H_2O_2	
	Add 250µl of alkali buffered 1% H_2O_2 to each tube	

	Place in boiling H2O bath for 10 minutes (detail as above)	
	Remove the H_2O_2	
WATER RINSE	Add 18.2mΩ DI H_2O, allow to settle, remove 18.2mΩ DI H_2O.	
	Add 18.2mΩ DI H_2O, allow to settle, remove 18.2mΩ DI H_2O.	
SILICATE REMOVAL	Using a 50µl pipette move the sample to a slide or just remove the silicates with the cow's eyelash brush.	
	Once removed all the silicates put the sample into a new, clean tube and remove any excess 18.2mΩ DI H_2O.	
WATER RINSE	Add 18.2mΩ DI H_2O, allow to settle, remove 18.2mΩ DI H_2O.	
	Add 18.2mΩ DI H_2O, allow to settle, remove 18.2mΩ DI H_2O.	
DILUTE ACID LEACH	**Only do this with a row of samples (10) at a time** Add 250µl of 0.002M HNO_3 Optima to each sample.	
	Ultrasonicate for 30 seconds.	
	Remove 0.002M HNO_3 Optima with pipette.	
WATER RINSE	Add 18.2mΩ DI H_2O, allow to settle, remove 18.2mΩ DI H_2O.	
	Add 18.2mΩ DI H_2O, allow to settle, remove 18.2mΩ DI H_2O.	
	Using a 10µl pipette to remove as much of the 18.2mΩ DI H_2O as possible.	

Appendix 16. A table to show the results of the Ca run for the samples from ODP Site 983. Before the samples can be analysed for their trace metal content their Ca concentration needs to be established so that the standard can be matrix matched.

Day	Sample number	Ca conc. In 350µl	Vol. of original 100µl 'TM' sample	Vol. of 0.5M HNO3 Optima to add	Standard number	Vol. of 4mM standard (µl)	Vol. 0.5M HNO3 Optima (µl)
1	**MD_176**	0.00	100.0	250.0	**-**	-	-
1	**MD_174**	0.10	100.0	250.0	**STD_1**	8.7	341.3
1	**MD_16**	0.11	100.0	250.0	**STD_2**	9.3	340.7
1	**MD_172**	0.18	100.0	250.0	**STD_3**	16.4	333.6
1	**MD_03**	0.20	100.0	250.0			
1	**MD_14**	0.28	100.0	250.0	**STD_4**	24.4	325.6
1	**MD_173**	0.44	100.0	250.0	**STD_5**	39.2	310.9
1	**MD_18**	0.46	100.0	250.0			
1	**MD_13**	0.52	100.0	250.0	**STD_6**	45.3	304.7
1	**MD_15**	0.62	100.0	250.0	**STD_7**	54.9	295.1
1	**MD_09**	0.64	100.0	250.0			
1	**MD_38**	0.70	100.0	250.0	**STD_8**	61.5	288.6
1	**MD_175**	0.71	100.0	250.0			
1	**MD_19**	0.75	100.0	250.0	**STD_9**	65.7	284.3
2	**MD_22**	0.78	100.0	250.0	**STD_10**	68.4	281.6
2	**MD_166**	0.92	100.0	250.0	**STD_11**	80.7	269.3
2	**MD_171**	0.95	100.0	250.0	**STD_12**	83.3	266.7

2	**MD_17**	1.01	100.0	250.0	**STD_13**	88.8	261.2
2	**MD_137**	1.07	100.0	250.0	**STD_14**	94.4	255.7
2	**MD_21**	1.08	100.0	250.0			
2	**MD_37**	1.21	100.0	250.0	**STD_15**	106.2	243.8
2	**MD_170**	1.24	100.0	250.0	**STD_16**	108.1	241.9
2	**MD_167**	1.41	100.0	250.0	**STD_17**	123.8	226.2
2	**MD_11**	1.44	100.0	250.0	**STD_18**	125.8	224.2
2	**MD_91**	1.58	100.0	250.0	**STD_19**	138.3	211.7
2	**MD_155**	1.67	100.0	250.0	**STD_20**	145.7	204.3
2	**MD_08**	1.70	100.0	250.0	**STD_21**	149	201
2	**MD_47**	1.74	100.0	250.0	**STD_22**	152.4	197.6
2	**MD_163**	1.78	100.0	250.0	**STD_23**	156.5	193.6
2	**MD_169**	1.80	100.0	250.0			
2	**MD_39**	1.84	100.0	250.0	**STD_24**	160.9	189.1
2	**MD_133**	1.92	100.0	250.0	**STD_25**	168.3	181.7
2	**MD_136**	1.93	100.0	250.0			
2	**MD_43**	2.01	100.0	250.0	**STD_26**	177.7	172.4
2	**MD_02**	2.05	100.0	250.0			
2	**MD_160**	2.18	100.0	250.0	**STD_27**	191.2	158.8
2	**MD_35**	2.18	100.0	250.0			
2	**MD_152**	2.20	100.0	250.0			
2	**MD_164**	2.37	100.0	250.0	**STD_28**	208	142.1
2	**MD_29**	2.38	100.0	250.0			
2	**MD_165**	2.48	100.0	250.0	**STD_29**	216.9	133.1

3	**MD_40**	2.52	100.0	250.0	**STD_30**	220.1	129.9
3	**MD_158**	2.67	100.0	250.0	**STD_31**	234.6	115.5
3	**MD_149**	2.69	100.0	250.0			
3	**MD_28**	2.73	100.0	250.0	**STD_32**	238.7	111.3
3	**MD_07**	2.76	100.0	250.0	**STD_33**	242.5	107.6
3	**MD_55**	2.78	100.0	250.0			
3	**MD_01**	2.81	100.0	250.0	**STD_34**	246.1	103.9
3	**MD_48**	2.82	100.0	250.0			
3	**MD_96**	2.87	100.0	250.0	**STD_35a + b**	253	97
3	**MD_138**	2.89	100.0	250.0			
3	**MD_44**	2.89	100.0	250.0			
3	**MD_151**	2.91	100.0	250.0			
3	**MD_154**	2.97	100.0	250.0	**STD_36**	262	88
3	**MD_32**	2.99	100.0	250.0			
3	**MD_140**	3.02	100.0	250.0			
3	**MD_84**	3.11	100.0	250.0	**STD_37**	273.1	76.9
3	**MD_153**	3.11	100.0	250.0			
3	**MD_145**	3.15	100.0	250.0			
3	**MD_49**	3.23	100.0	250.0	**STD_38**	284	66
3	**MD_33**	3.26	100.0	250.0			
3	**MD_135**	3.30	100.0	250.0	**STD_39**	288.7	61.3
3	**MD_142**	3.43	100.0	250.0	**STD_40**	299.8	50.2
3	**MD_124**	3.48	100.0	250.0	**STD_41**	306.9	43.1
3	**MD_54**	3.51	100.0	250.0			

3	**MD_148**	3.53	100.0	250.0			
3	**MD_150**	3.59	100.0	250.0	**STD_42**	315.8	34.1
3	**MD_24**	3.63	100.0	250.0			
3	**MD_129**	3.69	100.0	250.0	**STD_43a + b**	325.1	24.9
3	**MD_134**	3.71	100.0	250.0			
3	**MD_143**	3.71	100.0	250.0			
3	**MD_30**	3.74	100.0	250.0			
3	**MD_27**	3.81	100.0	250.0	**STD_44**	333.5	16.5
3	**MD_23**	3.92	100.0	250.0	**STD_45**	343.5	6.5
3	**MD_125**	3.93	100.0	250.0			
4	**MD_26**	3.97	100.0	247.5	**STD_46_4mM**		
4	**MD_69**	3.98	100.0	248.4			
4	**MD_25**	3.98	100.0	248.5			
4	**MD_103**	4.00	100.0	250.1			
4	**MD_161**	4.02	100.0	251.9			
4	**MD_46**	4.03	100.0	252.5	**STD_47_4mM**		
4	**MD_06**	4.07	100.0	256.0			
4	**MD_156**	4.07	100.0	256.5			
4	**MD_146**	4.08	100.0	256.7			
4	**MD_04**	4.10	100.0	258.4			
4	**MD_10**	4.12	100.0	260.2	**STD_48_4mM**		
4	**MD_157**	4.13	100.0	261.7			
4	**MD_131**	4.21	100.0	268.1			
4	**MD_20**	4.26	100.0	273.0			

4	**MD_162**	4.30	100.0	275.9	
4	**MD_34**	4.33	100.0	278.7	**STD_49_4mM**
4	**MD_147**	4.36	100.0	281.6	
4	**MD_58**	4.41	100.0	286.0	
4	**MD_111**	4.45	100.0	289.7	
4	**MD_117**	4.47	100.0	291.0	
4	**MD_104**	4.51	100.0	294.4	**STD_50_4mM**
4	**MD_127**	4.53	100.0	296.1	
4	**MD_113**	4.60	100.0	302.2	
4	**MD_36**	4.72	100.0	312.6	
4	**MD_128**	4.77	100.0	317.2	
4	**MD_168**	4.80	100.0	320.3	**STD_51_4mM**
4	**MD_121**	4.84	100.0	323.2	
4	**MD_85**	4.86	100.0	325.6	
4	**MD_132**	4.96	100.0	334.3	
4	**MD_115**	4.96	100.0	334.4	
4	**MD_126**	4.97	100.0	334.9	**STD_52_4mM**
4	**MD_108**	4.97	100.0	335.2	
4	**MD_130**	5.00	100.0	337.7	
4	**MD_50**	5.00	100.0	337.8	
4	**MD_42**	5.01	100.0	338.2	
4	**MD_78**	5.03	100.0	339.9	**STD_53_4mM**
4	**MD_05**	5.07	100.0	343.2	
4	**MD_53**	5.07	100.0	343.4	

4	**MD_51**	5.13	100.0	349.3	
4	**MD_106**	5.27	100.0	361.1	
4	**MD_144**	5.31	100.0	364.9	**STD_54_4mM**
4	**MD_57**	5.33	100.0	366.2	
4	**MD_94**	5.41	100.0	373.1	
4	**MD_12**	5.42	100.0	374.5	
4	**MD_31**	5.50	100.0	381.0	
4	**MD_116**	5.54	100.0	384.8	**STD_55_4mM**
4	**MD_90**	5.55	100.0	385.3	
4	**MD_70**	5.60	100.0	389.7	
4	**MD_75**	5.75	90.0	362.5	
4	**MD_139**	5.78	90.0	364.8	**STD_56_4mM**
5	**MD_100**	5.85	90.0	370.5	**STD_57_4mM**
5	**MD_41**	5.85	90.0	370.9	
5	**MD_45**	5.87	90.0	372.6	
5	**MD_112**	5.90	90.0	375.0	
5	**MD_62**	5.90	90.0	375.0	
5	**MD_86**	5.93	90.0	377.3	**STD_58_4mM**
5	**MD_56**	5.98	90.0	380.7	
5	**MD_61**	6.00	90.0	382.6	
5	**MD_81**	6.05	90.0	386.4	
5	**MD_92**	6.09	90.0	389.2	
5	**MD_101**	6.12	90.0	392.2	**STD_59_4mM**
5	**MD_119**	6.16	90.0	395.4	

5	**MD_59**	6.16	90.0	395.5	
5	**MD_123**	6.17	90.0	395.7	
5	**MD_97**	6.17	90.0	396.2	
5	**MD_105**	6.18	90.0	396.4	
5	**MD_52**	6.19	90.0	397.6	
5	**MD_141**	6.21	90.0	399.2	**STD_60_4mM**
5	**MD_93**	6.30	70.0	316.1	
5	**MD_79**	6.35	70.0	319.0	
5	**MD_159**	6.36	70.0	319.3	
5	**MD_74**	6.42	70.0	322.9	
5	**MD_99**	6.43	70.0	324.0	**STD_61_4mM**
5	**MD_109**	6.47	70.0	326.6	
5	**MD_77**	6.50	70.0	327.9	
5	**MD_110**	6.50	70.0	328.4	
5	**MD_83**	6.51	70.0	329.0	
5	**MD_76**	6.54	70.0	330.8	**STD_62_4mM**
5	**MD_122**	6.55	70.0	331.0	
5	**MD_60**	6.58	70.0	332.8	
5	**MD_66**	6.59	70.0	333.9	
5	**MD_68**	6.60	70.0	334.4	
5	**MD_118**	6.64	70.0	336.7	**STD_63_4mM**
5	**MD_63**	6.69	70.0	340.0	
5	**MD_87**	6.86	70.0	350.1	
5	**MD_98**	6.93	70.0	354.5	**STD_64_4mM**

5	**MD_120**	6.99	70.0	358.4	
5	**MD_72**	7.04	70.0	361.2	
5	**MD_102**	7.30	70.0	377.4	
5	**MD_73**	7.39	70.0	382.6	
5	**MD_88**	7.43	70.0	385.3	
5	**MD_95**	7.45	70.0	386.2	
5	**MD_67**	7.46	70.0	386.7	**STD_65_4mM**
5	**MD_82**	7.61	70.0	396.4	
5	**MD_65**	7.63	70.0	397.3	
5	**MD_107**	7.63	70.0	397.5	
5	**MD_71**	7.67	70.0	399.5	
5	**MD_80**	7.72	50.0	287.6	**STD_66_4mM**
5	**MD_114**	7.72	50.0	287.8	
5	**MD_89**	7.89	50.0	295.3	
5	**MD_64**	8.09	50.0	304.1	**STD_67_4mM**

Appendix 17. The breakdown of samples used to test the cleaning methods. 'd' and 'c' notation indicates samples that have not/have had the additional silicate removal step added respectively.

Sample Code	Total weight (µm)	Number of *G. inflata* crushed	All silicates removed?	Sample left 'dirty'
S1d1	**1188**	49		•
S1d2				•
S1d3				•
S1c1			•	
S1c2			•	
S1c3			•	
S2d1	**1204**	49		•
S2d2				•
S2d3				•
S2c1			•	
S2c2			•	
S2c3			•	
S3d1	**1195**	50		•
S3d2				•
S3d3				•
S3c1			•	
S3c2			•	
S3c3			•	

Appendix 18. A table to show the breakdown of samples used to test the different morphotypes of G.inflata, both 'glassy' and 'porcellaneous' foraminifera were picked from the same sample for comparison. It should be noted that all the silicates were removed during this test as to ensure only one variable was being tested. 'G' and 'P' notation indicates samples that have specimens with glassy (non-encrusted)/porcellaneous (encrusted) foraminiferal composition.

Sample Code	Total weight (µm)	Number of *G. inflata* crushed	Glassy *G.inflata*	Porcellaneous *G.inflata*
S4aG	**1166**	50	•	
S4bG			•	
S4cG			•	
S4dG			•	
S4eG			•	
S4aP	**998**	50		•
S4bP				•
S4cP				•
S4dP				•
S4eP				•
S5aG	**1169**	50	•	
S5bG			•	
S5cG			•	
S5dG			•	
S5eG			•	
S5aP	**883**	50		•

S5bP				•
S5cP				•
S5dP				•
S5eP				•

Appendix 19. The simplified sample number and corresponding sample details for sample from ODP Site 983 used for paired isotope and Mg/Ca isotope analysis.

Sample	MCD	Hole	Core	Section	Top	Bottom	Sample
A53_8	44.79	A	5	3	8	10	**1**
A53_10	44.81	A	5	3	10	12	**2**
A53_12	44.83	A	5	3	12	14	**3**
A53_14	44.85	A	5	3	14	16	**4**
A53_16	44.87	A	5	3	16	18	**5**
A53_18	44.89	A	5	3	18	20	**6**
A53_22	44.93	A	5	3	22	24	**7**
A53_26	44.97	A	5	3	26	28	**8**
A53_30	45.01	A	5	3	30	32	**9**
A53_34	45.05	A	5	3	34	36	**10**
A53_38	45.09	A	5	3	38	40	**11**
A53_42	45.13	A	5	3	42	44	**12**
A53_46	45.17	A	5	3	46	48	**13**
A53_50	45.21	A	5	3	50	52	**14**
A53_54	45.25	A	5	3	54	56	**15**

A53_58	45.29	A	5	3	58	60	**16**
A53_62	45.33	A	5	3	62	64	**17**
A53_66	45.37	A	5	3	66	68	**18**
A53_70	45.41	A	5	3	70	72	**19**
A53_74	45.45	A	5	3	74	76	**20**
A53_78	45.49	A	5	3	78	80	**21**
A53_82	45.53	A	5	3	82	84	**22**
A53_86	45.57	A	5	3	86	88	**23**
A53_90	45.61	A	5	3	90	92	**24**
A53_94	45.65	A	5	3	94	96	**25**
A53_98	45.69	A	5	3	98	100	**26**
A53_102	45.73	A	5	3	102	104	**27**
A53_106	45.77	A	5	3	106	108	**28**
A53_110	45.81	A	5	3	110	112	**29**
A53_114	45.85	A	5	3	114	116	**30**
A53_118	45.89	A	5	3	118	120	**31**
A53_122	45.93	A	5	3	122	124	**32**
A53_126	45.97	A	5	3	126	128	**33**
A53_130	46.01	A	5	3	130	132	**34**
A53_134	46.05	A	5	3	134	136	**35**
A53_138	46.09	A	5	3	138	140	**36**
A53_142	46.13	A	5	3	142	144	**37**
A53_146	46.17	A	5	3	146	148	**38**
A54_0	46.21	A	5	4	0	2	**39**

A54_4	46.25	A	5	4	4	6	**40**
A54_8	46.29	A	5	4	8	10	**41**
A54_12	46.33	A	5	4	12	14	**42**
A54_16	46.37	A	5	4	16	18	**43**
A54_20	46.41	A	5	4	20	22	**44**
A54_24	46.45	A	5	4	24	26	**45**
A54_28	46.49	A	5	4	28	30	**46**
A54_32	46.53	A	5	4	32	34	**47**
A54_36	46.57	A	5	4	36	38	**48**
A54_40	46.61	A	5	4	40	42	**49**
A54_44	46.65	A	5	4	44	46	**50**
A54_48	46.69	A	5	4	48	50	**51**
A54_52	46.73	A	5	4	52	54	**52**
A54_56	46.77	A	5	4	56	58	**53**
A54_60	46.81	A	5	4	60	62	**54**
A54_64	46.85	A	5	4	64	66	**55**
A54_68	46.89	A	5	4	68	70	**56**
A54_72	46.93	A	5	4	72	74	**57**
A54_76	46.97	A	5	4	76	78	**58**
A54_80	47.01	A	5	4	80	82	**59**
A54_82	47.03	A	5	4	82	84	**60**
A54_86	47.07	A	5	4	86	88	**61**
A54_90	47.11	A	5	4	90	92	**62**
A54_94	47.15	A	5	4	94	96	**63**

A54_98	47.19	A	5	4	98	100	**64**
A54_102	47.23	A	5	4	102	104	**65**
A54_106	47.27	A	5	4	106	108	**66**
A54_110	47.31	A	5	4	110	112	**67**
A54_114	47.35	A	5	4	114	116	**68**
A54_118	47.39	A	5	4	118	120	**69**
A54_122	47.43	A	5	4	122	124	**70**
A54_126	47.47	A	5	4	126	128	**71**
A54_130	47.51	A	5	4	130	132	**72**
A54_134	47.55	A	5	4	134	136	**73**
A54_138	47.59	A	5	4	138	140	**74**
A54_142	47.63	A	5	4	142	144	**75**
A54_146	47.67	A	5	4	146	148	**76**
A55_0	47.71	A	5	5	0	2	**77**
A55_4	47.75	A	5	5	4	6	**78**
A55_8	47.79	A	5	5	8	10	**79**
A55_12	47.83	A	5	5	12	14	**80**
A55_16	47.87	A	5	5	16	18	**81**
A55_20	47.91	A	5	5	20	22	**82**
A55_24	47.95	A	5	5	24	26	**83**
A55_28	47.99	A	5	5	28	30	**84**
A55_32	48.03	A	5	5	32	34	**85**
A55_34	48.05	A	5	5	34	36	**86**
A55_36	48.07	A	5	5	36	38	**87**

A55_38	48.09	A	5	5	38	40	**88**
A55_40	48.11	A	5	5	40	42	**89**
A55_42	48.13	A	5	5	42	44	**90**
A55_44	48.15	A	5	5	44	46	**91**
A55_46	48.17	A	5	5	46	48	**92**
A55_48	48.19	A	5	5	48	50	**93**
A55_50	48.21	A	5	5	50	52	**94**
A55_52	48.23	A	5	5	52	54	**95**
A55_54	48.25	A	5	5	54	56	**96**
A55_56	48.27	A	5	5	56	58	**97**
A55_58	48.29	A	5	5	58	60	**98**
A55_60	48.31	A	5	5	60	62	**99**
A55_62	48.33	A	5	5	62	64	**100**
A55_64	48.35	A	5	5	64	66	**101**
A55_66	48.37	A	5	5	66	68	**102**
A55_68	48.39	A	5	5	68	70	**103**
A55_70	48.41	A	5	5	70	72	**104**
A55_72	48.43	A	5	5	72	74	**105**
A55_74	48.45	A	5	5	74	76	**106**
A55_76	48.47	A	5	5	76	78	**107**
A55_78	48.49	A	5	5	78	80	**108**
A55_80	48.51	A	5	5	80	82	**109**
A55_82	48.53	A	5	5	82	84	**110**
A55_ 84	48.55	A	5	5	84	86	**111**

A55_86	48.57	A	5	5	86	88	**112**
A55_88	48.59	A	5	5	88	90	**113**
A55_90	48.61	A	5	5	90	92	**114**
A55_92	48.63	A	5	5	92	94	**115**
A55_94	48.65	A	5	5	94	96	**116**
A55_96	48.67	A	5	5	96	98	**117**
A55_98	48.69	A	5	5	98	100	**118**
A55_102	48.73	A	5	5	102	104	**119**
A55_106	48.77	A	5	5	106	108	**120**
A55_110	48.81	A	5	5	110	112	**121**
A55_114	48.85	A	5	5	114	116	**122**
A55_118	48.89	A	5	5	118	120	**123**
A55_122	48.93	A	5	5	122	124	**124**
A55_126	48.97	A	5	5	126	128	**125**
A55_130	49.01	A	5	5	130	132	**126**
A55_134	49.05	A	5	5	134	136	**127**
A55_138	49.09	A	5	5	138	140	**128**
A55_142	49.13	A	5	5	142	144	**129**
A55_146	49.17	A	5	5	146	148	**130**
A56_0	49.21	A	5	6	0	2	**131**
A56_4	49.25	A	5	6	4	6	**132**
A56_8	49.29	A	5	6	8	10	**133**
A56_12	49.33	A	5	6	12	14	**134**
A56_16	49.37	A	5	6	16	18	**135**

A56_18	49.39	A	5	6	18	20	**136**
A56_20	49.41	A	5	6	20	22	**137**
A56_22	49.43	A	5	6	22	24	**138**
A56_24	49.45	A	5	6	24	26	**139**
A56_26	49.47	A	5	6	26	28	**140**
A56_28	49.49	A	5	6	28	30	**141**
A56_30	49.51	A	5	6	30	32	**142**
A56_32	49.53	A	5	6	32	34	**143**
A56_34	49.55	A	5	6	34	36	**144**
A56_36	49.57	A	5	6	36	38	**145**
A56_38	49.59	A	5	6	38	40	**146**
A56_40	49.61	A	5	6	40	42	**147**
A56_42	49.63	A	5	6	42	44	**148**
A56_44	49.65	A	5	6	44	46	**149**
A56_46	49.67	A	5	6	46	48	**150**
A56_48	49.69	A	5	6	48	50	**151**
A56_50	49.71	A	5	6	50	52	**152**
A56_52	49.73	A	5	6	52	54	**153**
A56_54	49.75	A	5	6	54	56	**154**
A56_56	49.77	A	5	6	56	58	**155**
A56_60	49.81	A	5	6	60	62	**156**
A56_64	49.85	A	5	6	64	66	**157**
A56_68	49.89	A	5	6	68	70	**158**
A56_72	49.93	A	5	6	72	74	**159**

A56_76	49.97	A	5	6	76	78	**160**
A56_80	50.01	A	5	6	80	82	**161**
A56_84	50.05	A	5	6	84	86	**162**
A56_88	50.09	A	5	6	88	90	**163**
A56_92	50.13	A	5	6	92	94	**164**
A56_96	50.17	A	5	6	96	98	**165**
A56_98	50.19	A	5	6	98	100	**166**
A56_100	50.21	A	5	6	100	102	**167**
A56_102	50.23	A	5	6	102	104	**168**
A56_104	50.25	A	5	6	104	106	**169**
A56_106	50.27	A	5	6	106	108	**170**
A56_108	50.29	A	5	6	108	110	**171**
A56_110	50.31	A	5	6	110	112	**172**
A56_112	50.33	A	5	6	112	114	**173**
A56_114	50.35	A	5	6	114	116	**174**
A56_116	50.37	A	5	6	116	118	**175**
A56_118	50.39	A	5	6	118	120	**176**

Appendix 20. The estimated weights used for both the stable isotope analysis and the Mg/Ca analysis, based on the total weight and split of the sample.

Sample number	MCD	Total weight (µm)	Split for isotopes	Estimated weight (µg)	Split for Mg/Ca	Estimated weight for Mg/Ca	Average foram weight (µm)
1	44.79	335	0.33	**102**	0.67	**204**	27.92
2	44.81	224	0.33	**68**	0.67	**136**	28.00
3	44.83	56	0.50	**26**	0.50	**26**	28.00
4	44.85	323	0.33	**98**	0.67	**196**	26.92
5	44.87	387	0.25	**88**	0.75	**265**	25.80
6	44.89	399	0.25	**91**	0.75	**273**	28.50
7	44.93	323	0.33	**98**	0.67	**196**	32.30
8	44.97	253	0.33	**77**	0.67	**154**	21.08
9	45.01	99	0.50	**45**	0.50	**45**	24.75
10	45.05	466	0.33	**142**	0.67	**283**	23.30
11	45.09	157	0.50	**72**	0.50	**72**	22.43
12	45.13	622	0.25	**142**	0.75	**425**	23.92
13	45.17	162	0.50	**74**	0.50	**74**	27.00
14	45.21	78	0.50	**36**	0.50	**36**	19.50
15	45.25	110	0.50	**50**	0.50	**50**	22.00
16	45.29	89	0.50	**41**	0.50	**41**	22.25
17	45.33	120	0.50	**55**	0.50	**55**	24.00
18	45.37	140	0.50	**64**	0.50	**64**	20.00
19	45.41	157	0.50	**72**	0.50	**72**	26.17

20	45.45	363	0.33	**110**	0.67	**221**	24.20
21	45.49	141	0.50	**64**	0.50	**64**	23.50
22	45.53	97	0.50	**44**	0.50	**44**	24.25
23	45.57	353	0.33	**107**	0.67	**215**	23.53
24	45.61	340	0.33	**103**	0.67	**207**	28.33
25	45.65	360	0.33	**109**	0.67	**219**	22.50
26	45.69	676	0.25	**154**	0.75	**462**	22.53
27	45.73	423	0.33	**129**	0.67	**257**	23.50
28	45.77	496	0.25	**113**	0.75	**339**	27.56
29	45.81	314	0.33	**95**	0.67	**191**	22.43
30	45.85	395	0.33	**120**	0.67	**240**	26.33
31	45.89	720	0.25	**164**	0.75	**492**	24.00
32	45.93	436	0.33	**133**	0.67	**265**	24.22
33	45.97	385	0.33	**117**	0.67	**234**	24.06
34	46.01	732	0.25	**167**	0.75	**501**	24.40
35	46.05	205	0.33	**62**	0.67	**125**	25.63
36	46.09	787	0.20	**144**	0.80	**574**	28.11
37	46.13	216	0.33	**66**	0.67	**131**	27.00
38	46.17	118	0.50	**54**	0.50	**54**	29.50
39	46.21	256	0.33	**78**	0.67	**156**	25.60
40	46.25	354	0.33	**108**	0.67	**215**	29.50
41	46.29	730	0.25	**166**	0.75	**499**	28.08
42	46.33	640	0.25	**146**	0.75	**438**	29.09
43	46.37	308	0.33	**94**	0.67	**187**	30.80

44	46.41	481	0.25	**110**	0.75	**329**	28.29
45	46.45	826	0.20	**151**	0.80	**603**	30.59
46	46.49	331	0.33	**101**	0.67	**201**	30.09
47	46.53	458	0.33	**139**	0.67	**278**	28.63
48	46.57	287	0.33	**87**	0.67	**174**	31.89
49	46.61	432	0.33	**131**	0.67	**263**	24.00
50	46.65	573	0.25	**131**	0.75	**392**	28.65
51	46.69	593	0.25	**135**	0.75	**406**	28.24
52	46.73	742	0.20	**135**	0.80	**541**	24.73
53	46.77	799	0.20	**146**	0.80	**583**	26.63
54	46.81	353	0.33	**107**	0.67	**215**	23.53
55	46.85	410	0.33	**125**	0.67	**249**	27.33
56	46.89	793	0.20	**145**	0.80	**579**	26.43
57	46.93	812	0.20	**148**	0.80	**592**	27.07
58	46.97	855	0.20	**156**	0.80	**624**	28.50
59	47.01	756	0.20	**138**	0.80	**552**	26.07
60	47.03	717	0.25	**163**	0.75	**490**	23.90
61	47.07	777	0.20	**142**	0.80	**567**	25.90
62	47.11	722	0.25	**165**	0.75	**494**	24.07
63	47.15	750	0.20	**137**	0.80	**547**	25.00
64	47.19	772	0.20	**141**	0.80	**563**	25.73
65	47.23	759	0.25	**173**	0.75	**519**	25.30
66	47.27	742	0.25	**169**	0.75	**508**	24.73
67	47.31	739	0.25	**168**	0.75	**505**	24.63

68	47.35	737	0.25	**168**	0.75	**504**	24.57
69	47.39	731	0.25	**167**	0.75	**500**	24.37
70	47.43	751	0.25	**171**	0.75	**514**	25.03
71	47.47	748	0.25	**171**	0.75	**512**	24.93
72	47.51	739	0.25	**168**	0.75	**505**	24.63
73	47.55	737	0.25	**168**	0.75	**504**	24.57
74	47.59	684	0.25	**156**	0.75	**468**	22.80
75	47.63	763	0.20	**139**	0.80	**557**	25.43
76	47.67	710	0.25	**162**	0.75	**486**	23.67
77	47.71	753	0.20	**137**	0.80	**549**	25.10
78	47.75	704	0.25	**161**	0.75	**482**	23.47
79	47.79	816	0.20	**149**	0.80	**595**	27.20
80	47.83	842	0.20	**154**	0.80	**614**	28.07
81	47.87	761	0.25	**174**	0.75	**521**	26.24
82	47.91	753	0.25	**172**	0.75	**515**	25.10
83	47.95	720	0.25	**164**	0.75	**492**	26.67
84	47.99	474	0.33	**144**	0.67	**288**	23.70
85	48.03	734	0.25	**167**	0.75	**502**	24.47
86	48.05	713	0.25	**163**	0.75	**488**	23.77
87	48.07	709	0.25	**162**	0.75	**485**	23.63
88	48.09	714	0.25	**163**	0.75	**488**	23.80
89	48.11	792	0.20	**144**	0.80	**578**	26.40
90	48.13	581	0.25	**132**	0.75	**397**	24.21
91	48.15	432	0.33	**131**	0.67	**263**	21.60

92	48.17	652	0.25	**149**	0.75	**446**	21.73
93	48.19	704	0.25	**161**	0.75	**482**	23.47
94	48.21	667	0.25	**152**	0.75	**456**	22.23
95	48.23	641	0.25	**146**	0.75	**438**	22.10
96	48.25	470	0.33	**143**	0.67	**286**	20.43
97	48.27	618	0.25	**141**	0.75	**423**	20.60
98	48.29	659	0.25	**150**	0.75	**451**	22.72
99	48.31	661	0.25	**151**	0.75	**452**	22.79
100	48.33	658	0.25	**150**	0.75	**450**	21.93
101	48.35	606	0.25	**138**	0.75	**415**	21.64
102	48.37	680	0.25	**155**	0.75	**465**	22.67
103	48.39	586	0.25	**134**	0.75	**401**	21.70
104	48.41	683	0.25	**156**	0.75	**467**	22.77
105	48.43	716	0.25	**163**	0.75	**490**	23.87
106	48.45	660	0.25	**150**	0.75	**451**	22.00
107	48.47	735	0.25	**168**	0.75	**503**	24.50
108	48.49	641	0.25	**146**	0.75	**438**	21.37
109	48.51	682	0.25	**155**	0.75	**466**	22.73
110	48.53	753	0.25	**172**	0.75	**515**	25.10
111	48.55	421	0.33	**128**	0.67	**256**	28.07
112	48.57	619	0.25	**141**	0.75	**423**	24.76
113	48.59	452	0.33	**137**	0.67	**275**	23.79
114	48.61	781	0.20	**142**	0.80	**570**	26.03
115	48.63	716	0.25	**163**	0.75	**490**	23.87

116	48.65	736	0.25	**168**	0.75	**503**	24.53
117	48.67	734	0.25	**167**	0.75	**502**	24.47
118	48.69	768	0.25	**175**	0.75	**525**	25.60
119	48.73	740	0.25	**169**	0.75	**506**	24.67
120	48.77	720	0.25	**164**	0.75	**492**	24.00
121	48.81	731	0.25	**167**	0.75	**500**	24.37
122	48.85	721	0.25	**164**	0.75	**493**	24.03
123	48.89	724	0.25	**165**	0.75	**495**	24.13
124	48.93	721	0.25	**164**	0.75	**493**	24.03
125	48.97	683	0.25	**156**	0.75	**467**	22.77
126	49.01	691	0.25	**158**	0.75	**473**	23.03
127	49.05	664	0.25	**151**	0.75	**454**	22.13
128	49.09	639	0.25	**146**	0.75	**437**	21.30
129	49.13	630	0.25	**144**	0.75	**431**	21.00
130	49.17	677	0.25	**154**	0.75	**463**	22.57
131	49.21	424	0.33	**129**	0.67	**258**	22.32
132	49.25	647	0.25	**148**	0.75	**443**	23.11
133	49.29	386	0.33	**117**	0.67	**235**	25.73
134	49.33	702	0.25	**160**	0.75	**480**	23.40
135	49.37	624	0.25	**142**	0.75	**427**	20.80
136	49.39	360	0.33	**109**	0.67	**219**	22.50
137	49.41	328	0.33	**100**	0.67	**199**	20.50
138	49.43	452	0.33	**137**	0.67	**275**	22.60
139	49.45	660	0.25	**150**	0.75	**451**	22.00

140	49.47	602	0.33	**183**	0.67	**366**	20.07
141	49.49	712	0.25	**162**	0.75	**487**	23.73
142	49.51	604	0.33	**184**	0.67	**367**	20.13
143	49.53	697	0.25	**159**	0.75	**477**	23.23
144	49.55	620	0.25	**141**	0.75	**424**	20.67
145	49.57	655	0.25	**149**	0.75	**448**	21.83
146	49.59	656	0.25	**150**	0.75	**449**	21.87
147	49.61	660	0.25	**150**	0.75	**451**	22.00
148	49.63	625	0.25	**143**	0.75	**428**	21.55
149	49.65	343	0.33	**104**	0.67	**209**	22.87
150	49.67	657	0.25	**150**	0.75	**449**	21.90
151	49.69	656	0.25	**150**	0.75	**449**	21.87
152	49.71	469	0.33	**143**	0.67	**285**	23.45
153	49.73	550	0.33	**167**	0.67	**334**	25.00
154	49.75	502	0.33	**153**	0.67	**305**	22.82
155	49.77	646	0.33	**196**	0.67	**393**	23.07
156	49.81	640	0.33	**195**	0.67	**389**	23.70
157	49.85	715	0.25	**163**	0.75	**489**	24.66
158	49.89	435	0.33	**132**	0.67	**264**	24.17
159	49.93	680	0.25	**155**	0.75	**465**	22.67
160	49.97	628	0.25	**143**	0.75	**430**	20.93
161	50.01	706	0.25	**161**	0.75	**483**	23.53
162	50.05	667	0.33	**203**	0.67	**406**	22.23
163	50.09	476	0.33	**145**	0.67	**289**	22.67

164	50.13	399	0.33	**121**	0.67	**243**	24.94
165	50.17	519	0.25	**118**	0.75	**355**	23.59
166	50.19	722	0.25	**165**	0.75	**494**	26.74
167	50.21	482	0.33	**147**	0.67	**293**	24.10
168	50.23	736	0.25	**168**	0.43	**288**	24.53
169	50.25	422	0.33	**128**	0.67	**257**	24.82
170	50.27	368	0.33	**112**	0.67	**224**	24.53
171	50.29	382	0.33	**116**	0.67	**232**	27.29
172	50.31	207	0.33	**63**	0.67	**126**	20.70
173	50.33	213	0.33	**65**	0.67	**130**	26.63
174	50.35	162	0.33	**49**	0.67	**98**	23.14
175	50.37	184	0.33	**56**	0.67	**112**	26.29
176	50.39	68	0.50	**31**	0.50	**31**	22.67

Appendix 21. Summary of results from the paired δ^{18}O-Mg/Ca analysis from ODP Site 983 across MIS 11.

		Mg/Ca [mmol/mol]		Fe/Ca [µmol/mol]		Mn/Ca [µmol/mol]	
		mean	**range**	**mean**	**range**	**mean**	**range**
Silicate removal stage excluded	1	2.04	0.13	310.15	197.11	398	121
	2	2.25	0.54	349.32	152.04	357	32
	3	1.91	0.18	224.19	34.22	368	107
Silicate removal stage included	1	2.04	0.22	207.49	54.55	392	48
	2	1.99	0.05	229.51	68.39	372	28
	3	1.99	0.13	223.64	23.77	423	87
		Al/Ca [µmol/mol]		**Fe/Mg [mol/mol]**		**Mn/Mg [mol/mol]**	
		mean	**range**	**mean**	**range**	**mean**	**range**
Silicate removal stage excluded	1	26	14	0.15	0.10	0.19	0.07
	2	52	14	0.16	0.11	0.16	0.05
	3	22	6	0.12	0.01	0.19	0.04
Silicate removal stage included	1	167	275	0.10	0.03	0.20	0.03
	2	45	52	0.12	0.04	0.19	0.01
	3	33	53	0.11	0.01	0.21	0.03

		Mg/Ca [mmol/mol]		Fe/Ca [µmol/mol]		Mn/Ca [µmol/mol]	
		mean	**range**	**mean**	**range**	**mean**	**range**
Porcellaneous	1	1.88	0.82	184.59	123.12	698	208
	2	1.69	0.30	229.81	291.78	648	194
Glassy	1	2.04	0.21	242.73	194.00	367	87
	2	2.01	0.21	291.30	58.51	368	58
		Al/Ca [µmol/mol]		**Fe/Mg [mol/mol]**		**Mn/Mg [mol/mol]**	
		mean	**range**	**mean**	**range**	**mean**	**range**
Porcellaneous	1	304	1200	0.10	0.05	0.38	0.20
	2	245	383	0.14	0.18	0.39	0.09
Glassy	1	23	29	0.12	0.09	0.18	0.05
	2	20	16	0.15	0.02	0.18	0.03

Appendix 22. A table to show the results of the Ca run and the Mg/Ca results for the test samples from ODP Site 983.

Sample number	Ca conc. In 350µl ratio sample	Standard	Volume of 4mM standard to pipette (µl)	Volume of 0.5M HNO3 Optima to pipette (µl)	Mg25/Ca43
MD_S4bP	0.11	STD_1	10.0	340.0	**2.35**

MD_S4cP	0.22	STD_2	19.2	331.0	**1.53**
MD_S5aP	0.34	STD_3	29.6	320.0	**1.77**
MD_S4aP	0.39	STD_4	34.5	315.0	**2.06**
MD_S5dP	0.48	STD_5	42.0	308.0	**1.64**
MD_S5cP	0.53	STD_7	46.4	304.0	**1.62**
MD_S5eP	0.58	STD_8	50.7	299.0	**1.86**
MD_S5bP	0.70	STD_10	61.2	289.0	**1.56**
MD_S4eP	0.96	STD_13	84.8	265.0	**1.79**
MD_S3c3	1.42	STD_14	124.2	226.0	**1.96**
MD_S3d3	1.72	STD_15	150.6	199.0	**1.85**
MD_S3d2	1.85	STD_17	162.4	188.0	**2.03**
MD_S4dP	1.86				**1.66**
MD_S3d1	1.86				**1.85**
MD_S1c3	1.88	STD_18	164.2	186.0	**1.89**
MD_S3c2	1.98	STD_19	173.9	176.0	**2.08**
MD_S5cG	2.00				**1.92**
MD_S4eG	2.26	STD_20	199.4	151.0	**2.08**
MD_S1d3	2.30				**2.04**
MD_S5eG	2.53	STD_21	222.4	128.0	**2.02**
MD_S1d1	2.56				**1.97**
MD_S4dG	2.60	STD_22	228.8	121.0	**1.96**
MD_S1c2	2.63				**2.01**
MD_S2c2	2.76	STD_23	241.4	109.0	**1.99**
MD_S5bG	3.06	STD_24	269.0	81.0	**2.12**

MD_S5dG	3.09				**1.92**
MD_S2d3	3.13	STD_25	272.0	78.0	**2.52**
MD_S4bG	3.21	STD_26	283.3	68.0	**2.13**
MD_S1c1	3.26				**2.11**
MD_S4cG	3.31	STD_27	290.3	60.0	**1.92**
MD_S5aG	3.32				**2.08**
MD_S2d2	3.33				**2.24**
MD_S2d1	3.36	STD_28	295.4	55.0	**1.98**
MD_S1d2	3.38				**2.11**
MD_S4aG	3.63	STD_29	371.4	33.0	**2.10**
MD_S2c1	3.92	4mM STD	-	243.0	**1.97**
MD_S3c1	4.06	4mM STD	-	255.0	**1.94**
MD_S2c3	4.91	4mM STD	-	329.0	**2.02**

Appendix 23. A table to show the results of the stable isotope analysis run at Cardiff University.

Sample code	**MCD**	**$\delta^{13}C$ (VPDB)**	**$\delta^{18}O$ (VPDB)**	**Sample code**	**MCD**	**$\delta^{13}C$ (VPDB)**	**$\delta^{18}O$ (VPDB)**
A53_8	44.79	1.239	2.085	**A55_40**	48.11	0.927	1.954
A53_10	44.81	1.203	2.427	**A55_42**	48.13	0.827	1.891
A53_12	44.83	1.085	2.257	**A55_44**	48.15	0.976	1.882
A53_14	44.85	1.244	2.388	**A55_46**	48.17	0.764	1.761

A53_16	44.87	1.150	2.228	**A55_48**	48.19	0.745	1.74
A53_18	44.89	1.262	2.356	**A55_50**	48.21	0.770	1.694
A53_22	44.93	1.273	2.407	**A55_52**	48.23	0.741	1.751
A53_26	44.97	0.993	2.213	**A55_54**	48.25	0.631	1.749
A53_30	45.01	1.233	2.311	**A55_56**	48.27	0.793	1.792
A53_34	45.05	1.090	2.095	**A55_58**	48.29	0.711	1.734
A53_38	45.09	1.235	2.400	**A55_60**	48.31	0.681	1.825
A53_42	45.13	1.119	2.149	**A55_62**	48.33	0.834	1.757
A53_46	45.17	1.321	2.314	**A55_64**	48.35	0.711	1.766
A53_50	45.21	0.755	1.818	**A55_66**	48.37	0.797	1.711
A53_54	45.25	1.489	1.908	**A55_68**	48.39	0.710	1.827
A53_58	45.29	1.113	2.114	**A55_70**	48.41	0.789	1.956
A53_62	45.33	1.215	2.046	**A55_72**	48.43	0.800	1.760
A53_66	45.37	1.365	2.078	**A55_74**	48.45	0.680	1.796
A53_70	45.41	1.011	1.873	**A55_76**	48.47	0.645	1.803
A53_74	45.45	0.957	1.92	**A55_78**	48.49	0.714	1.741
A53_78	45.49	1.073	2.20	**A55_80**	48.51	0.723	1.833
A53_82	45.53	0.791	1.904	**A55_82**	48.53	0.718	1.886
A53_86	45.57	0.923	1.941	**A55_ 84**	48.55	0.831	2.081
A53_90	45.61	1.210	2.154	**A55_86**	48.57	0.710	1.899
A53_94	45.65	1.106	1.941	**A55_88**	48.59	0.797	1.933
A53_98	45.69	1.069	2.024	**A55_90**	48.61	0.788	2.126
A53_102	45.73	1.013	2.056	**A55_92**	48.63	0.639	1.933
A53_106	45.77	1.217	2.167	**A55_94**	48.65	0.585	1.735

A53_110	45.81	0.992	2.081	**A55_96**	48.67	0.731	1.897
A53_114	45.85	1.035	2.14	**A55_98**	48.69	0.730	1.997
A53_118	45.89	1.061	2.123	**A55_102**	48.73	0.538	2.082
A53_122	45.93	1.009	2.018	**A55_106**	48.77	0.776	1.905
A53_126	45.97	1.078	1.995	**A55_110**	48.81	0.743	1.969
A53_130	46.01	1.040	1.989	**A55_114**	48.85	0.580	2.039
A53_134	46.05	0.902	2.062	**A55_118**	48.89	0.636	1.869
A53_138	46.09	1.105	2.134	**A55_122**	48.93	0.654	1.930
A53_142	46.13	1.018	2.028	**A55_126**	48.97	0.717	1.965
A53_146	46.17	1.009	2.070	**A55_130**	49.01	0.621	2.068
A54_0	46.21	0.924	2.023	**A55_134**	49.05	0.687	2.001
A54_4	46.25	1.123	2.148	**A55_138**	49.09	0.532	1.901
A54_8	46.29	0.987	1.911	**A55_142**	49.13	0.596	1.992
A54_12	46.33	1.000	2.078	**A55_146**	49.17	0.566	1.960
A54_16	46.37	1.087	2.088	**A56_0**	49.21	0.485	2.004
A54_20	46.41	1.013	2.045	**A56_4**	49.25	0.604	1.886
A54_24	46.45	0.97	1.946	**A56_8**	49.29	0.742	1.913
A54_28	46.49	0.949	2.000	**A56_12**	49.33	0.532	1.978
A54_32	46.53	1.018	1.935	**A56_16**	49.37	0.609	2.046
A54_36	46.57	0.970	1.924	**A56_18**	49.39	0.694	2.124
A54_40	46.61	0.923	1.963	**A56_20**	49.41	0.633	2.224
A54_44	46.65	1.059	2.039	**A56_22**	49.43	0.579	2.02
A54_48	46.69	0.825	1.979	**A56_24**	49.45	0.579	2.002
A54_52	46.73	0.912	1.949	**A56_26**	49.47	0.550	1.810

A54_56	46.77	0.844	1.856	**A56_28**	49.49	0.701	1.896
A54_60	46.81	0.862	1.969	**A56_30**	49.51	0.557	2.053
A54_64	46.85	1.027	1.944	**A56_32**	49.53	0.669	2.100
A54_68	46.89	0.817	1.673	**A56_34**	49.55	0.464	2.144
A54_72	46.93	1.194	2.121	**A56_36**	49.57	0.474	2.078
A54_76	46.97	0.781	1.953	**A56_38**	49.59	0.478	2.071
A54_80	47.01	0.931	1.749	**A56_40**	49.61	0.588	2.162
A54_82	47.03	0.852	1.882	**A56_42**	49.63	0.510	2.190
A54_86	47.07	0.837	1.839	**A56_44**	49.65	0.643	2.064
A54_90	47.11	0.883	1.735	**A56_46**	49.67	0.514	2.194
A54_94	47.15	0.993	1.817	**A56_48**	49.69	0.500	2.001
A54_98	47.19	0.875	1.830	**A56_50**	49.71	0.459	2.164
A54_102	47.23	0.927	1.889	**A56_52**	49.73	0.605	2.224
A54_106	47.27	0.861	1.783	**A56_54**	49.75	0.571	2.146
A54_110	47.31	0.925	1.614	**A56_56**	49.77	0.561	2.253
A54_114	47.35	0.746	2.004	**A56_60**	49.81	0.530	2.423
A54_118	47.39	0.950	1.864	**A56_64**	49.85	0.547	2.230
A54_122	47.43	0.986	1.843	**A56_68**	49.89	0.363	2.327
A54_126	47.47	0.940	1.947	**A56_72**	49.93	0.404	2.386
A54_130	47.51	0.871	1.832	**A56_76**	49.97	0.409	2.388
A54_134	47.55	0.778	1.840	**A56_80**	50.01	0.197	2.538
A54_138	47.59	0.884	1.881	**A56_84**	50.05	0.355	2.376
A54_142	47.63	0.915	1.964	**A56_88**	50.09	0.437	2.26
A54_146	47.67	0.895	1.873	**A56_92**	50.13	0.437	2.651

A55_0	47.71	1.044	1.965	**A56_96**	50.17	0.434	2.581
A55_4	47.75	0.973	1.906	**A56_98**	50.19	0.497	2.633
A55_8	47.79	0.978	1.686	**A56_100**	50.21	0.539	2.468
A55_12	47.83	-	-	**A56_102**	50.23	0.337	2.527
A55_16	47.87	0.933	2.046	**A56_104**	50.25	0.440	2.524
A55_20	47.91	0.878	1.921	**A56_106**	50.27	0.468	2.560
A55_24	47.95	1.024	2.027	**A56_108**	50.29	0.557	2.345
A55_28	47.99	0.972	1.930	**A56_110**	50.31	0.317	2.605
A55_32	48.03	0.954	1.718	**A56_112**	50.33	0.757	1.826
A55_34	48.05	0.934	1.778	**A56_114**	50.35	0.650	2.167
A55_36	48.07	1.008	1.677	**A56_116**	50.37	0.311	2.211
A55_38	48.09	0.882	1.951	**A56_118**	50.39	0.176	2.669

Appendix 24. Methods of rate of change calculations.

The rate of change was calculated by linearly interpolating between data points to obtain equally spaced ages down core (1kyr spacing). The associated data point was calculated using the 'FORECAST' and 'MATCH' functions in Microsoft's excel; these functions were able to interpolate the correct data point given the distance of the interpolated age to a 'real' age, original data point. From here I was able to smooth the data to remove some of the noise of the signal by sampling the data at a 3, 5 and 7 point running mean. Following this analysis, the 7 points running mean was used to calculate the rate of change as this represented a 7000 year smooth; this time bracket was used to 'filter out' orbital timescale variability following numerous authors (Alley et al., 2002; Schmittner et al., 2003; Barker and Knorr, 2007; Barker et al., 2011). Taking the difference in the 'rise' between two data points and dividing it by the different in the 'run' of the same two data points calculated the rate of change (i.e. for example the difference in CO_2 divided by the difference in time for that change).